UC Berkeley
UC Berkeley Electronic Theses and Dissertations

Title

A Panchromatic Study of the Metal-poor Massive Stars in the Local Group

Permalink

https://escholarship.org/uc/item/7zh304cj

ISBN

9798297601444

Author

Gull, Maude

Publication Date

2025-08-01

Peer reviewed|Thesis/dissertation

eScholarship.org Powered by the California Digital Library
University of California

A Panchromatic Study of the Metal-poor Massive Stars in the Local Group

By

Maude Gull

A dissertation submitted in partial satisfaction of the

requirements for the degree of

Doctor of Philosophy

in

Astrophysics

in the

Graduate Division

of the

University of California, Berkeley

Committee in charge:

Associate Professor Daniel R. Weisz, Chair
Associate Professor Jessica Lu
Associate Professor Raffaella Margutti
Associate Professor Anna McLeod

Summer 2025

A Panchromatic Study of the Metal-poor Massive Stars in the Local Group

Copyright 2025
by
Maude Gull

Abstract

A Panchromatic Study of the Metal-poor Massive Stars in the Local Group

by

Maude Gull

Doctor of Philosophy in Astrophysics

University of California, Berkeley

Associate Professor Daniel R. Weisz, Chair

Metal-poor massive stars are central to a wide range of astrophysics. They are thought to give rise to exciting transients and explosive enrichment in the early Universe, power cosmic reionization, and to pump large amounts of kinetic energy into the interstellar medium, thereby shaping the evolution of galaxies. They are the most likely progenitors of gravitational wave events and dominate the evolution and spectral energy distribution (SEDs) of star-forming galaxies across cosmic time. Despite their importance, observing and studying populations of metal-poor massive stars is challenging. Luckily, the Local Group (z=0, our cosmic neighborhood) harbors dozens of metal-poor star-forming dwarf galaxies that meet the sub-SMC metallicity threshold and are home to extremely metal-poor massive stars.In this thesis, I will presents the results of HST and JWST photometric and Keck and MMT optical spectroscopic studies in three of these dwarf galaxies; Leo A ($Z \sim 5\% \, Z_{\odot}; D \sim 800$ kpc), Wolf–Lundmark–Melotte (WLM, $Z \sim 14\% \, Z_{\odot}; D \sim 970$ kpc) and Sextans A ($Z \sim 6\% \, Z_{\odot}; \; D \sim 1.32$ Mpc).

In Leo A, the spectroscopic sample of eighteen massive stars comprises a significant fraction of all known metal-poor massive stars with high-quality optical spectra at sub-SMC metallicities. More than half the stars in the sample show emission lines not associated with surrounding H II regions, and half the stars can be considered isolated star candidates (not within $\sim$ 40 pc of the nearest H II region). I adapt the `The Payne`, a highly efficient, multi-dimensional interpolator, to train a neural net on the TLUSTY non-local thermodynamic equilibrium (non-LTE) models, creating an infrastructure to fit metal-poor massive stars rapidly. I show that there are early indications that near-ultraviolet/optical/near-infrared photometry fitted using the `BEAST` can be used to reliably characterize massive main-sequence star properties relative to low-resolution optical spectroscopy. I present six spectroscopically identified Be stars, representing the first sub-SMC Be stars to have both

photometric and spectroscopic analysis. I postulate that Be stars may contaminate parts of the core helium burning branch in the optical CMD.

In WLM, I present the lowest metallicity massive contact binary candidate to date. Identified through optical HST time-series photometry, I supplement these light-curves with novel JWST and UV HST photometry, providing light-curve data across six bands. Using machine learning, I emulate the eclipsing binary modeling software (PHysics Of Eclipsing BinariEs; `PHOEBE`), integrating it within a nested sampling framework to simultaneously fit the multi-band light curves. The best fit model consists of two hot massive stars stars ($T_1 = 29800^{+2300}_{-1700}$ K, $M_1 = 16^{+2}_{-3}\ M_\odot$, and $T_2 = 18000^{+5000}_{-5000}$ K, $M_2 = 7^{+5}_{-3}\ M_\odot$). The contact system candidate shows a mass-ratio of $q = 0.41^{+0.24}_{-0.14}$, which provides an important observational data point, as theoretically predicted mass ratio ranges are sensitive to model assumptions that drive our current binary population models. We expect time series imaging from LSST, BlackGEM, etc., to uncover similar objects in nearby galaxies and aid us in constraining the population of massive metal-poor binaries.

In Sextans A, I analyze bright stars (F475W <24) using panchromatic photometry and identify 369 massive star candidates ($M_{act,p50} > 8$ and $Logg_{p50} > 3.7$). I compare the derived stellar parameters to existing spectral typing of a subset of the stars, based on existing low-resolution optical spectroscopy. Overall, I find good agreement, with outliers explainable by binarity, binary interaction, or low-quality spectra. I discuss the shortcomings of SED fitting when it comes to capturing binaries and binary products, and showcase the importance of UV photometry in studying massive stars accurately. I identify promising stripped star candidates and find an increasing fraction of OBe stars at low metallicity.

Pour Mami, Papi, Morgane, Mario, la Yaye, Barbara, le Nonno, Tschuli et toute la famille,
Grace a votre soutiens, votre confiance en moi, vos sacrifice et surtout
Dank eurer unterstützig, euem vertraue i mir, eurne sacrifice und vorallem
votre amour inconditionnelle j'ai pus affronter ce parcour avec tel
eui unkonditonelli liebi hani mit so viel zuversicht chönne durch die etappe
confiance et sûreté en moi que j'allais réussir.
i mim lebe gah mit de überzügig dass ichs schaffe.
Pour moi, la motivation que j'ai trouvée à chaque pas de cette étape est
Für mich isch d'motivation woni immer wieder gfunde han
profondément liée à l'importance de pouvoir étudier et à l'éducation pour
tüüf demit verbunde wie wichtig lerne und bildig mir
moi et la familie et qu'il n'est pas toujours une donnée qu'on peut
und i eusere familie isch und dass d'möglichkeit sinere neugir und
poursuivre sa curiosité et sa connaissance. Je vous aime tous très fort. <3
em wüsse nach zgha nie garantiert isch. Han eu alli ganz fescht lieb. <3
For Aidan,
I cannot put into words how much your love, patience, and support mean to me and how they helped "carry me" to the finish line. :) I love you.
And for my friends,
In the spirit of misusing or altering English sayings, "It takes a village to do a PhD," and you all are my village. From proofreading my applications to hanging out in the ER to late-night talks in the rain, driving to nowhere, and being my fans even when you had no idea what I was talking about, I am so incredibly thankful to have you all in my life.

Contents

List of Figures v

List of Tables xvi

Acknowledgments xix

1 Introduction 1
- 1.0.1 Mass loss of Metal-poor Massive Stars . . . 2
- 1.0.2 Rotation of Metal-poor Massive Stars . . . 4
- 1.0.3 Binarity of Metal-poor Massive Stars . . . 4

1.1 Thesis Chapters . . . 5

2 A Panchromatic Study of Massive Stars in the Extremely Metal-Poor Local Group Dwarf Galaxy Leo A 6
- 2.1 Chapter Abstract . . . 6
- 2.2 Introduction . . . 7
- 2.3 Sample selection, Observations, and Data Reduction . . . 10
  - 2.3.1 *HST* Observations and Photometry . . . 10
  - 2.3.2 Spectroscopic Target Selection . . . 11
  - 2.3.3 Spectroscopic Normalization . . . 15
- 2.4 Measuring Stellar Parameters From Panchromatic Photometry . . . 15
- 2.5 Measuring Stellar Parameters From Optical Spectroscopy . . . 18
  - 2.5.1 The Payne . . . 19
  - 2.5.2 Equivalent Widths . . . 21
  - 2.5.3 Analysis of emission line stars . . . 21
- 2.6 Results . . . 23
  - 2.6.1 Stellar Parameters from Photometry . . . 23
  - 2.6.2 Radial Velocities from Spectroscopy . . . 25
  - 2.6.3 Stellar Parameters from Spectroscopic Analysis . . . 26
  - 2.6.4 The Utility of Panchromatic Photometry for Massive Star Studies . 32

2.7 Discussion . . . 37
2.7.1 Stars in H II regions . . . 37
2.7.2 Field OB-stars . . . 39
2.7.3 Purity of the Blue Core Helium Burning Sequence . . . 41
2.7.4 Extremely metal-poor environments . . . 42
2.7.5 Finding Be stars in low metallicity environments . . . 45
2.8 Conclusions . . . 45
2.9 Acknowledgments . . . 61
2.10 Appendix . . . 61
2.10.1 The Effects of Stellar Model Choice on Photometric Fitting Results 61
2.10.2 Detailed discussion of individual stars . . . 63

3 A Low Metallicity Massive Contact Binary Star System Candidate in WLM identified by Hubble and James Webb Space Telescope imaging 75
3.1 Chapter Abstract . . . 75
3.2 Introduction . . . 76
3.3 Photometry . . . 78
3.3.1 *HST* Imaging and Photometry . . . 78
3.3.2 *JWST* Imaging and Photometry . . . 81
3.4 Analysis . . . 81
3.4.1 Discovery . . . 82
3.4.2 Period and Temperature Estimation . . . 83
3.4.3 Neural Net training and Setup . . . 84
3.4.4 Fitting using `UltraNest` . . . 86
3.5 Results . . . 88
3.6 Stellar Evolution Modeling of WLM-CB1 Using `MESA` . . . 89
3.7 Discussion . . . 93
3.7.1 WLM-CB1: a contact binary candidate . . . 93
3.8 Acknowledgments . . . 94

4 Photometric study of the massive star content in Sextans A 102
4.1 Chapter Abstract . . . 102
4.2 Introduction . . . 103
4.3 HST Photometry . . . 104
4.4 Analysis . . . 106
4.4.1 BEAST fitting . . . 107
4.4.2 The Importance of the UV . . . 108
4.4.3 Shortcomings of the BEAST in regards to massive binaries . . . 110
4.5 Massive stars in Sextans A . . . 111
4.6 Comparison to Literature . . . 113

4.6.1 Spectral Types 113
4.6.2 S3 – s029 115
4.7 Stripped star and OBe star candidates 117
4.7.1 Stripped star candidates 117
4.7.2 Be stars fraction and candidates 119
4.8 Conclusion 121
4.9 Acknowledgments 122

5 Concluding Remarks **132**

Bibliography **136**

List of Figures

1.1 Overview of the observational progress of metal-poor massive stars (circles scale with sample size) with spectroscopic mass measurements (Gull et al. 2022; Evans et al. 2006; Telford et al. 2021; Ramachandran et al. 2021). This figure does not include stars with only qualitative analysis or $M_* > 100\ M_\odot$. The shaded area indicates the metallicity range of most galaxies observed in the high-redshift Universe. This thesis (red circles) increased the number of quantitatively analyzed stars in the lowest metallicity regime by an order of magnitude. 3

2.1 Select *HST*-based UV-optical (left), NUV-optical (left middle), optical-only (right middle), and NIR (right) CMDs of Leo A. Colored points indicate stars observed with LRIS (Keck) (navy triangles), Binospec (MMT) (red dots) and both telescopes (magenta squares). For reference, we overplot select MIST tracks ([Fe/H] =−1.0, v/vcrit=0.4, $A_v = 0.03$). There are fewer stars on the NIR CMD because WFC3/IR has a smaller field of view and does not entirely overlap the UV and optical imaging. All spectroscopic stars are massive stars (i.e. $M > 8M_\odot$). The NUV CMD shows that the stars in our spectroscopic sample are not very evolved. 12

2.2 This plot is identical to Fig. 4.2, only zoomed in on luminous blue stars selected for spectroscopy in the UV and optical CMDs. We label the stars by the names in Table 2.1, where K stands for stars with Keck and B for stars with Binospec spectra. For reference, we overplot select MIST tracks ([Fe/H] =−1.0, v/vcrit=0.4, $A_v = 0.03$). Interestingly, a handful of stars that appear on the main sequence in the UV-optical CMDs appear in the blue core helium burning region of the F475W-F814W CMD. We discuss this in §2.6.3. 13

2.3 The Leo A *HST* ACS/F475W image zoomed in on the central region of the galaxy. Stars with spectroscopic observations are color-coded by telescope: Keck/LRIS (blue triangles), MMT/Binospec (red circles), both (magenta squares). Contours of Hα emission from ground-based imaging (Local Volume Legacy Survey; Kennicutt et al. 2007) are overplotted in green. Note that many of the massive stars are not obviously associated with cataloged H II regions including one O-star (K7). 14

2.4 Example normalized spectra of massive stars in Leo A shown from 4000-5100Å with key features labeled. Top two panels: Keck/LRIS ($R \sim 1800$) spectra of an O-type (top) and a Be-type star (bottom) in Leo A. The O-star exhibits He I (dark blue) and He II (light blue) absorption lines and a clear Balmer series in absorption. These are typical of a late-type O star. The Be star shows He I (dark blue) absorption but no He II (light blue). The Balmer series is primarily in emission. Bottom two panels: Binospec spectra ($R \sim 1250$) of an early B-type (top) and a B(e)-type (bottom) in Leo A. The B star shows primarily He I (dark blue) absorption features, while He II (light blue) absorption is minimal. The Balmer lines show absorption features, although there appears to be weak emission within the feature. The bottom panel shows a B0.5-type star. Though the low SNR makes identification of clear features more challenging, we still find clear He I (dark blue) absorption features. The Balmer lines are a mix of absorption and emission features. We note the star is a potentially a Be star as well 17

2.5 Example SED fits in each category of χ^2: good (top), decent (middle), and poor (lower). The data are shown as black points. The median fit stellar (pink), stellar+dust (purple), and stellar+dust+bias (cyan) are overplotted. The subpanels show the residuals in units of σ. The top panel shows all residuals of the best model (cyan) within 4σ. The middle panel shows residuals of the best model (cyan) within 12 σ (note that for 5 bands the value is closer to 4 σ). The bottom panel shows the largest deviations in the residual with the best model (cyan) being within 15 σ. For the good and decent fit we report $\log(T_{\rm eff})$, $\log(g)$, and $A_{\rm V}$. 48

2.6 A panchromatic gallery of CMDs for Leo A ranging from UV-optical on the left to NIR on the right. Points in each row are color-coded by results from SED fitting with the `the BEAST`. From top to bottom, the rows reflect: χ^2, $\log(T_{\rm eff})$, $\log(g)$, M_{ini}, and $A_{\rm V}$. For χ^2, we divide the fits into three categories: good (pink), decent (purple), poor (cyan). Stars that have spectroscopic data are plotted as squares. 49

2.7 The distribution of radial velocities for stars in Leo A. Our LRIS (blue) and Binospec (pink) velocities are consistent with the the Keck/DEIMOS-based velocities of red giants (RG) measured by Kirby et al. (2017), and the average velocity measured from the Supergiants (SG) by Brown et al. (2007). Each sample is normalized by counts. 50
2.8 Keck/LRIS and MMT/Binospec normalized spectra (with an arbitrary offset added for clarity) for all 18 stars in the spectroscopic sample. For stars with both Keck and MMT data, we show the Keck spectra in the 4000-5100 Å region. If there is no LRIS spectrum, we show the Binospec (1000 lpmm) spectrum. The spectra in the 6520-6610 Å region are from the Binospec 270 lpmm grating and are shown for all stars that have Binospec spectra. The spectra are sorted by spectral type from O-type stars at the top to B-type and Be-type stars at the bottom. This is one of the largest set of optical spectra for sub-SMC metallicity massive dwarf stars. 51
2.9 Comparison between the parameters derived for K1 using full spectral fitting and SED fitting. We show a plot of the observed spectra (black dots), the TLUSTY-based model generated by the median parameters derived from the full spectral fitting (pink), and the TLUSTY-based model generated by the median parameters derived from the SED fitting (blue). While both models reasonably replicate the observed He I 4471 and He II 4541 fits, both struggle to fully fill the absorption feature of the helium lines. This shortcoming is potentially due to the fixed resolution, metallicity, or macroturbulence. We see the effect of the different $\log(g)$ values between the methods most prominently in the Balmer lines (see the Hβ feature). The grey bar shows the part of the spectrum that we masked. 52
2.10 Models for K6 from adapted composite SED fitting (See §2.5.3). The data (black dots) are matched by scaling and combining the stellar models. The star (blue line) and the disk (red line) are combined for the composite SED (black line). The star and the disk models are both varied to find the median SED. We note that the error bars of the data are smaller than the dots representing the data point. 53
2.11 Corner plot of stellar parameters from the adapted double SED fitting of K6. The first two columns show the contours for the derived $\log(T_{\rm eff})$ and radius of the star. The next two columns show the contours for the derived $\log(T_{\rm eff})$ and radius of the disk. The last column shows E(B-V). 54

2.12 A comparison between the parameters derived from the BEAST using the models with v/vcrit=0.4 (PHOT) and the parameters derived from the PAYNE (SPEC). The top panel compares log($T_{\rm eff}$). The middle panel compares log($L/L_{\odot}$). The bottom panel compares log(g). The comparison between the two methods shows that panchromatic photometry can be used to recover reliable stellar parameters at least for "normal" single stars. 55
2.13 Top panel: The Leo A *HST* ACS/F475W image zoomed in on two H II regions. Stars with spectroscopic observations are labeled by their reference names. Contours of Hα emission from ground-based imaging are overplotted in green. The H II regions are overplotted with the stars color-coded by log(Age)< 7.5 dex from the BEAST fits and include only good fits from the UV-optical catalog. Bottom panel: The optical CMDs are overplotted with the stars shown in the top panel and using the same color-coding for both regions. 56
2.14 UV-optical (left) and optical (right) *HST*-based CMDs of Leo A. The pink colored circles are stars that appear in the BHeB region both in the UV and the optical CMD. The blue colored circles are stars that are stars that are on the MS in the UV CMD, but appear on or near the BHeB region in the optical CMD. The cyan squares are the stars identified as Be stars in our spectroscopic sample. This shows candidate Be stars could possibly pollute the BHeB in the optical CMD, and that we can filter for candidate Be stars in panchromatic photometry studies. 57
2.15 Properties of the OB-stars in Leo A. log($T_{\rm eff}$) is plotted vs. Spectral Type for early-type (O-B3) stars in our sample. The spectroscopically derived log($T_{\rm eff}$) are indicated by the solid markers, while the photometrically derived log($T_{\rm eff}$) are the fainter bigger markers. The O-stars in Leo A are blue circles, the B-stars purple circles, and the Be stars are purple squares. We compare our stars ($\chi^2 \leq 100$) with SMC results and Sextans A late-type O stars. For the SMC O-stars we fit a best line to the V type stars in Massey et al. (2009) (left-most black dashed line, M09). For the B-type stars we plot the O V and B V spectral types to the log($T_{\rm eff}$) scale derived by Dufton et al. (2019) (dashed line, D19). We also plot the fit to the Be stars in the SMC from Dunstall et al. (2011) (dotted line, D11). Furthermore, we plot the two late-type O stars observed by Telford et al. (2021) (dark green, T21) and Camacho et al. (2016) (light green, C16) in Sextans A, for which there is a log($T_{\rm eff}$) measurement for the spectral type. 58

2.16 The HR diagrams of massive sub-SMC metallicity stars in the Local Group with derived stellar parameters. We overplot MIST tracks. **Top**: All the stars with temperatures and luminosities in the metal-poor galaxies: WLM (~ 15 % $Z_\odot$; aqua triangle), IC 1613 (~ 14 % $Z_\odot$; blue circles), and NGC 3109 (~ 11 % $Z_\odot$; purple-blue squares). The WLM stars are from Bresolin et al. (2006), Tramper et al. (2011), Tramper et al. (2014), and Telford et al. (2021); the IC 1613 stars are from Bresolin et al. (2007), and the NGC 3109 stars are from Evans et al. (2007), Tramper et al. (2014), and Hosek et al. (2014). **Bottom**: All stars with temperatures and luminosities in the extremely metal-poor galaxies Sextans A (~ 6 % $Z_\odot$; purple triangle) and Leo P (~ 3 % $Z_\odot$; rose squares). As well as the stars in our spectroscopic sample (~ 5 % $Z_\odot$; pink circles). The Sextans A stars are from Kaufer et al. (2004), Camacho et al. (2016), and Telford et al. (2021); the Leo P star is from Telford et al. (2021). Our sample represents the first extended sample of MS stars at sub-SMC metallicities with derived stellar parameters. Furthermore it is the largest sample at sub-10% $Z_\odot$ with derived stellar parameters. 59

2.17 Three panels comparing the different masses derived throughout the study; M_{ini} and M_{act} from the photometry, M_0, M_{evo}, and M_{spec} from the spectroscopy. The top left panel compares the initial masses derived from each method (M_{ini} vs M_0). The top right panel compares the present-day masses derived from each method using evolutionary tracks and isochrones (M_{act} vs M_{evo}). The bottom panel compares the present-day masses derived from spectroscopy (M_{spec} vs M_{evo}). We show all stars with $\chi^2 < 100$ in both photometry and spectroscopy. . 60

2.18 The figure shows a direct comparison between the parameters derived from the `BEAST`using the different available evolutionary models. The left panels compare the MIST models with v/vcrit=0.4 (MR) and v/vcrit=0.0 (MNR). The right panels compare the MIST models with v/vcrit=0.4 (MR) to the PARSEC models (P). We plot the values for the stars in both our spectroscopic and photometric sample. The top two panels compare $\log(T_{\rm eff})$. The second two panels compare the $\log(g)$. The third two panels compare M_{ini}. The fourth panels compare $\log(L/L_\odot)$. The fifth panels compare $\log(A)$. The bottom panels compare the A_V. Stars with $\chi^2 < 20$ for both fits are pink (good fits), stars with $\chi^2 > 80$ in either fits are cyan (poor fits), all other stars are purple (decent fits). 74

3.1 An optical ground-based image of WLM (credit: NOIRLab/NSF/AURA/CTIO/Local Group Survey Team and T.A. Rector (University of Alaska Anchorage)) with the *HST*/ACS, *HST*/WFC3, and *JWST*/NIRCAM footprints overplotted. The location of WLM-CB1 (RA: 00 02 00.23, DEC:15 31 05.20) is shown as a pink star. It falls within all three footprints. 79

3.2 Select *HST* and *JWST* CMDs of WLM, zoomed in the upper MS: UV-optical (left), optical-only (middle), near-IR (right). WLM-CB1 is shown as a star symbol. The optical and near-IR values of WLM-CB1 reflect the maximum point on the optical and near-IR light curves i.e., maximum brightness of the system. Since we have no direct constraint initially on the the phase of the UV data point, we indicate likely CMD position by the shaded oval. We overplot select MIST tracks ([Fe/H]=−0.82, v/vcrit = 0.4, A_v = 0.10) for reference. Note that the 5 $M_\odot$ track falls off in the UV-optical CMD, due to its faintness in F275W. A visual comparison with the single-star models suggests a lower limit of ∼ 10 $M_\odot$ on the current mass of WLM-CB1. 80
3.3 All *HST* and *JWST* observations of the WLM-CB1 used in this paper, shown in chronological order. Even without phase-folding, variability in the light curves is visible for the optical and near-IR bands. A constant offset has been added to the two UV data points in order to improve the dynamic range of the y-axis for illustrative purposes. 83
3.4 Synthetic F475W light-curves generated by the neural network trained on PHOEBE. The solid light-curve in each panel is the baseline model. Each panel shows the effects of a singular parameter being varied on the light-curve. It is evident that the mass-ratio has the smallest effect in the light-curve and can only be constrained by high-precision photometry such *HST* and *JWST*. We note that since this is in phase space, the effects of the period on the fitting is not fully captured, as it also folds the data into phase space. 86
3.5 A corner plot showing samples of the posterior from our "ultranest" fitting of WLM-CB1. For the marginalized 1D distributions, we indicate the median and 25th and 75th percentiles. The period clearly shows the mutli-modal nature of the posterior distribution. The lack of any data in the secondary dip, along with a paucity of UV data, contribute to broad constraints on temperature ratio, mass, and mass-ratio. This would be better recovered with the addition of spectroscopy. There is a correlation between temperature of the primary, mass of the primary and dust, as all parameters affect the light-curve similarly (See Figure 3.4).Because the fill-out factor is hitting the edge of its parameter space we consider this to be a minimal contact binary. 96
3.6 Multi-band observed (points) and model light curves (black lines) for WLM-CB1. We also plot 300 draws from the posterior as individual colored lines. Residuals for each set of filters are plotted below the light curves. The models generally provide an excellent fit to the observed light curves. The largest uncertainties are near the minima and the UV, for which there is sparse sampling. 97

3.7 Evolutionary tracks yielded by MESA for our best match evolutionary path with initial primary mass (M_p) of 11.25 $M_\odot$ for the more massive component at ZAMS, initial mass-ratio (q_i) of 0.8, and initial binary separation (a_i) of 10.75 $R_\odot$. **Left:** The evolutionary tracks of WLM-CB1a (blue) and WLM-CB1b (red, M_p) are shown compared to MIST single star evolutionary tracks (grey lines). The pink dots indicate the area where the current observables match. It is evident from the figure that the initial mass exchange occurs soon after the ZAMS, that the second mass exchanges also occurs on the MS and that in this particular scenario the system merges on the MS. We also overplot the evolutionary tracks computed by MESA assuming the Björklund et al. (2021) wind prescription (black dashed line) to illustrate that in this very weak wind regime the binary interaction dominates the evolution of the stars. **Center and Right:** The evolutionary tracks yielded by MESA for a system with the aforementioned initial conditions (M_p=11.25 $M_\odot$, q_i=0.8, a_i=10.75 $R_\odot$) at different metallicities of 14% $Z_\odot$ (WLM), 10% $Z_\odot$(metal-poor), and 20% $Z_\odot$(SMC). While the evolutionary tracks are qualitatively similar between the 14% $Z_\odot$ and 10% $Z_\odot$ track, there is a clear difference to the higher metallicity (20% $Z_\odot$) track, which experiences an additional mass transfer. The sensitivity to metallicity in binary evolution is clearly illustrated here, emphasizing the need for systematic exploration of binaries in the sub-SMC metallicity regime. It also shows that caution is necessary when extrapolating from the SMC to lower metallicity regimes. 98

3.8 Best model of the evolutionary path WLM-CB1 that is consistent with current observations. The initial parameters of this model are the Mass of the primary (Mp) = 11.25 $M_\odot$, mass-ratio (q) = 0.8 and binary separation (a_i) = 10.75. The instance of overlap between the models and the observational parameters are marked by black dots. The limits given by the observational uncertainties are horizontal solid lines (crimson for WLM-CB1a and navy for WLM-CB1b). As seen in the 4th row, each evolutionary path suggests that both stars have filled their Roche Lobe ($R/R_L \geq 1$ at the observed point of their evolution). The scenario suggest a previous drastic short-lived mass transfer/contact phase, where the mass-ratio is flipped (light pink vertical line). The matches between models and observation suggest that WLM-CB1 just re-entered a contact phase (pink) after a prolonged near contact phase (semi-detached, grey), hence why the definitive nature of WLM-CB1 is hard to determine. 99

3.9 Overview of the observed mass ratio (q) and period (top) and of the observed total mass and period (bottom) of the contact binaries (circles) or semi-detached binaries (squares) in the LMC (blue hues) and SMC (purple/pink hues). We also plot system that are not clearly distinguished between the two (diamonds). WLM-CB1 (black star) appears to be in a regime where the transition from semi-detached to contact binary occurs based on the current observational sample. In the top panel, the gray line indicated $P = 1.2$ days, to illustrate that the majority of the systems below that line are contact binaries. In the bottom panel, the gray line is a visual guide to show that if a line is draw through the marginal contact binaries in literature (V382 Cyg (MW green), $f \sim 0.1$; Abdul-Masih et al. 2021) and SSN 7 ($R_1/R_{RL} = 1.01$ and $R_1/R_{RL} = 1.03$; Rickard & Pauli 2023) all observed contact system to this date fall on or below that line. We further note that the SMC appears to show a wider range of observed mass-ratios, though this may be an effect introduced by observational bias or the small sample. 100

3.10 Synthetic Radial Velocity curves obtained by the PHOEBE code. We compute the expected radial velocity curves using the parameters obtained by the analysis. The solid lines represent the expected curves yielded by the contact fit, whereas the dotted lines are the expected curves yielded by the semi-detached fit. The velocity of the primary is more affected by the difference in parameters, since the difference is primarily introduces by the mass-ratio, i.e., in the semi-detached case the secondary is more massive than in the contact case, therefore the orbital velocity of the primary is larger. 101

4.1 Optical image (left: color, right:bw) of Sextans A with the Nicholas U. Mayall 4-meter Telescope at Kitt Peak National Observatory. Left: We indicate the directions of North and East and a distance scale of 500pc. Middle: Footprints of the HST imaging produced by the LUVIT Survey (Gilbert et al. 2025) and JWST/NIRCAM observations (JW 2391 PI: Roman-Duval and JW 1619 PI: Boyer) are overlaid on the optical image. The turquoise footprint shows the HST UV observations, the green and black footprint shows the HST optical observations, the red footprint denotes the HST IR footprint, and the yellow footprint indicates the JWST/NIRCAM observations. Right: We plot the filter coverage with corresponding coordinates. Stars filter coverage is color-coded in the following way: pink;7, blue;6, green; 5 and purple;4. (credit: KPNO/NOIRLab/NSF/AURA Data obtained and processed by: P. Massey (Lowell Obs.), G. Jacoby, K. Olsen, & C. Smith (AURA/NSF) Image processing: T.A. Rector (University of Alaska Anchorage/NSF NOIRLab), M. Zamani (NSF NOIRLab) & D. de Martin (NSF NOIRLab) 105

4.2 Select *HST*-based UV-optical (top) and optical-only (bottom) CMDs of Sextans A. For reference, we overplot select MIST tracks ([Fe/H] =−1.0, v/vcrit=0.4, A_v = 0.09). We also indicate the typical errors for each CMD in the left-hand of each subplot. 106
4.3 The medium $\pm 1\sigma$ difference between the BEAST output (Output) and simulated parameters (Input) for 45'000 stars. We compare the difference as a function of removing a filter in the NUV until we have only optical and IR bands. For single stars, we recover the parameters (M_{act},M_{ini},log(g),log(L),Av) for massive stars up to 55 $M_\odot$ consistently. We find that even with 7-bands available, the BEAST tends to fit slightly younger ages to the oldest stars in the population (Age > 500 Myr). Additionally, we find that at the hot end of log(T), the BEAST starts to underestimate the temperature, which is unsurprising as the hotter temperature pushes the SED of the star into a regime less sensitive to the NUV-Optical photometry. The output parameters struggle to recover the true parameters as blue filters get removed. In particular, the BEAST underestimates mass, which was also noted in Lindberg et al. (2025). Especially when no UV filters are available (No F225W, F275W, F336W), recovering the properties of massive stars is not realistic. 124
4.4 We show synthetic spectra of massive stars and binaries. The top panel shows the spectra of a twin binary system consisting of two 10 $M_\odot$ MS stars, each with T_{eff} = 30kK (purple). We overplot the spectra of a single 17 $M_\odot$ MS star with T_{eff} = 30kK (blue). The two spectra are nearly indistinguishable; inspecting the residual, we see nearly no difference between the two SEDs. Only if we were to zoom in on the spectral features would we see minimal differences in the depth of the lines, which is unlikely to be captured by photometry alone. The middle and lower panel repeat the exercise, but the companion is once cooler (middle), once hotter (bottom). We note that in the optical (λ > 4000 Angstrom), there is nearly no difference between the binary and the single star. However, the UV reveals a deviation covered by our HST photometry and will yield a less-than-optimal χ^2. 125

4.5 Hertzsprung-Russel diagram of the main-sequence massive stars in Sextans A. We overplot Parsec evolutionary tracks. The circles are stars where the BEAST yields $\chi^2 < 10$, whereas the squares represent $10 < \chi^2 < 100$. The stars are color-coded by their mass range, and the size of the stars is scaled to their mass. Additionally, we overplot the stars in Lorenzo et al. (2022) sample with their spectral and luminosity type. O-stars are in light blue, while B stars are in dark blue. We also circle stars marked as potential binary candidates by the author. We note that several stars that appear at odd locations for their spectral type are amongst the faintest stars in the sample, and the low S/N may have complicated the spectral typing. 126
4.6 The Sextans A HST WFC3/F475W footprint overplotted with the stars fitted with the BEAST that yield a good fit ($\chi^2 < 10$) color-coded by$\log(A)_{p50} < 7.50$. Intensity maps of Hα emission from ground-based imaging are overplotted in the left plot, color-coded by intensity. Intensity maps of the UV as observed by GALEX are overplotted in the right plot. The HII regions (A, B, C, D) overlap with the young stellar population and the high intensity part of the UV map; however, some young stars appear in the field. 127
4.7 $\log(T_{\rm eff})$ is plotted vs. Spectral Type for early-type (O-B3) stars in our sample. The $\log(T_{\rm eff})$ values are taken from our BEAST fit, while the Spectral Types are the types reported in (Lorenzo et al. 2022). We classify stars with $\log(g)_{p50} > 3.70$ as dwarfs (left), and $2.50 < \log(g)_{p50} < 3.70$ as giants. We note that these classifications are based on the photometry alone and must be confirmed by spectra. The stars are color-coded by the number of filters they were observed in. We compare our stars ($\chi^2 \leq 100$) with the theoretical $\log(T_{\rm eff})$ is plotted vs. Spectral Type relation derived by (Lorenzo et al. 2025) as well as the $\log(T_{\rm eff})$ scale derived by Dufton et al. (2019) (dashed line, D19). The stars appear to follow the relationship within error bars, except for four dwarfs and six sub-giants. 128
4.8 We show NUV-Optical (top) and Optical-only (middle and bottom) CMDs of Sextans A. The stars are color-coded by the $\log(g)_{p50}$ values obtained by the BEAST fit. Furthermore, we overplot the stars observed in Telford et al. (2021) (star) and Lorenzo et al. (2022) (squares), the latter of which are color-coded by their Luminosity class based on the R$\sim$ 1000 spectra in Lorenzo et al. (2022). In the optical, distinguishing between surface gravity and luminosity class is challenging; however, the NUV-Optical CMD paints a clearer picture. Most stars are placed on the CMD as expected based on their luminosity class, with a couple of outliers. 129

4.9 UV-optical (both top and bottom left) and optical (bottom right) *HST*-based CMDs of Sextans A. We overplot the ZAMS (pink, solid) as well as the stripped star core He burning (cHeb) sequence (black, dashed Götberg et al. 2018). Stars to the left of the ZAMS in the NUV-optical are plotted as purple (F225W-F475W), light blue (F275W-F475W), and green (F336W-F475W). Lastly, we plot the stars identified as stripped star candidates by Lorenzo et al. (2022). Additionally, three stars to the left of the cHeb (black) appear to be true sources upon further investigation. Two sources identified by Lorenzo et al. (2022) appear bluer than the ZAMS in the optical-only, but otherwise on the ZAMS in the other CMDs. However, two stars appear on top of the cHeb in all other CMDs. Higher S/N and resolution optical or UV spectra are necessary to ultimately confirm these stars' nature. 130
4.10 UV-optical (left) and optical (right) *HST*-based CMDs of Sextans A. Using the `BEAST` fit, we identify the area of the CMD where main-sequence OB stars show up in the UV-optical CMD and color-code the stars with navy. We additionally plot the emission-line stars identified by Massey et al. (2007a) (pink) and stars identified as strong Hα emission in GO-17438 (PI: Gull) (purple). Using the `BEAST` fit, we identify stars on the MS in the UV and show more than 2σ difference between the observed F814W flux and the `BEAST` predicted F814W flux. Additionally, we apply color cuts to identify stars with potential IR excess in the CMD. These two groups of stars are our OBe star candidates. In Gull et al. (2022), some stars showing this behavior were identified as Be-type stars, while one was identified as a partially stripped star candidate with a companion (Senchyna, Götberg, Gull et al. in prep). We find a OBe fraction of $\sim 15\%$ in Sextans A for stars $F275W > 22.9$, a OBe fraction of $\sim 25\%$ for stars $F275W > 21$ and a OBe fraction of $\sim 63\%$ for stars $F275W > 19.5$. Although confirmation through deep Hα imaging (GO-17438 PI: Gull) or spectroscopic follow-up is needed. 131

List of Tables

2.1 Observing details of the spectroscopic data taken with LRIS (KECK) and Binospec (MMT). The columns are: (1) The name of each star used throughout the paper; (2) Alternative ID; (3) Right Ascension; (4) Declination; (5) Observing date; (6) slit width; (7) Integration time; (8)-(10) select *HST* magnitudes and colors; (11) & (12) SNR at specified wavelength 16
2.2 Basic information on the TLUSTY model grids used for The Payne. The columns are: (1) Grid name;(2) number of models in grid used to train the neural net; (3) temperature range in log space; (4) temperature range in kilo-Kelvin; (5) surface gravity range and (6) fixed microturbulence value. 19
2.3 List of equivalent widths used in analysis to determine the spectral type of each star. 33
2.4 Spectroscopic parameters determined using The Payne. The columns are: (1) star name; (2) spectroscopic mass; (3) initial mass; (4) evolutionary mass; (5) effective temperature; (6) surface gravity; (7) luminosity; (8) rotational velocity; (9) heliocentric corrected radial velocity from full spectral fitting; (10) heliocentric corrected radial velocity measurements using Gaussian profile fitting. Columns (4), (5), (7), and (8) are the stellar parameters that directly resulted from the full spectral fitting with The Payne. Columns (2) and (6) are derived using the previous stellar parameters in addition to the SED. Column (3) lists the evolutionary mass determined by eye. 34

2.5 Stellar parameters determined using the adapted methods. The table list the results from the adapted spectroscopic and photometric analysis. The columns are: (1) name; (2) spectroscopic temperature of the star; (3) photometric temperature of the star; (4) photometric radius of the star; (5) rotational velocity; (6) reddening value from the SED fitting; (7) photometric temperature of the disk; (8) photometric radius of the disk; (9) present-day mass picked for the combined SED fitting; (10) heliocentric corrected radial velocity from full spectral fitting; (11) heliocentric corrected radial velocity measurements using gaussian fitting; (12) reduced χ^2 value from the composite photometric fitting. Columns (2), (5), (10) and (11) are the stellar parameters derived from the adapted spectroscopic analysis. Columns (3), (4), (6), (7), (8), and (12) are the stellar parameters derived from the composite photometric analysis. 35

2.6 Photometric parameters determined using the BEAST and the MIST models with $v/v_{crit} = 0.4$. The columns are: (1) star name; (2) initial mass; (3) actual mass; (4) temperature; (5) surface gravity; (6) luminosity; (7) extinction parameter; (8) stellar age in log-space; (9) χ^2 yielded by the BEAST; (10) number of *HST* bands used for the SED fitting (when the value is 4 we observed F275W, F336W, F475W and F814W, and when the value is 6, we additionally observed F110W and F160W); (11) spectral type derived from EW analysis. Columns (2), (7), and (8) list primary parameters, while columns (4), (5), and (6) list derived parameters. 36

2.7 Parameters of isolated stars in Leo A. The columns are: (1) star name; (2) initial mass (photometry); (3) initial mass (spectroscopy); (4) Spectral Type; (5) stellar age in Myr; (6) radial velocity; (7) approximate distances to the closest H II region or cluster for each star; (8) approximate velocity derived from taking the values (7) and dividing it by the values in (5). When available we list the initial mass, otherwise we list the evolutionary mass. 40

2.8 Photometric parameters determined using the BEAST and the PARSEC models. The columns are:(1) star name; (2) initial mass; (3) temperature; (4) surface gravity; (5) luminosity; (6) extinction parameter; (7) stellar age in log-space; (8) reduced χ^2 yielded by the BEAST; (9) number of *HST* bands used for the SED fitting, when the value is 4 we observed F275W, F336W, F475W and F814W. When the value is 6, we additionally observed F110W and F160W. Columns (2), (6) and (7) lists primary parameters, while columns (3), (4) and (5) list derived parameters. 64

2.9 Photometric parameters determined using the BEAST and the MIST models with $v/vcrit = 0.0$. The columns are:(1) star name; (2) initial mass; (3) temperature; (4) surface gravity; (5) luminosity; (6) extinction parameter; (7) stellar age in log-space; (8) reduced χ^2 yielded by the BEAST; (9) number of *HST* bands used for the SED fitting, when the value is 4 we observed F275W, F336W, F475W and F814W. When the value is 6, we additionally observed F110W and F160W. Columns (2), (6) and (7) lists primary parameters, while columns (3), (4) and (5) list derived parameters. 65

3.1 Time-stamps of individual WLM-CB1 observations. 82
3.2 Basic information on the PHOEBE model grids used for the neural network. The columns are: (1) Model type; (2) Temperature of the primary (T_1); (3) Mass of the primary (M_1); (4) Temperature Ratio (T_2/T_1); (5) Inclination (Inc);(6) Mass ratio ($q = M_2/M_1$); (7) Period (P); (8) fillout-factor (f); (9) extinction (A_V); (10) Temperature of the secondary (T_2); (11) Radius of the Primary (R_1); (12) Radius of the secondary (R_2) 85
3.3 Parameters yielded by the contact binary model of WLM-CB1 binary system. . 88
3.4 Parameter ranges of the different initial binary parameter sweeps and zoom-ins for the MESA models. 91

4.1 Filter Combinations 108

Acknowledgments

Thank you, Dan Weisz, for entrusting me to take the lead in this project and giving me the room to grow as an independent scientist. I appreciate that you never outright shut down any of my ideas, no matter how out there or ambitious, or if sent at 3 am on a random Tuesday, but instead pushed and challenged me to flesh out my arguments and help me be a better researcher. And for being an incredibly understanding advisor and mentor, I really enjoyed working with and learning from you these past six years.

Thank you, Anna Frebel, Anna McLeod, and Moni Hamolksi, for showing me what it means to be a woman in STEM, each in their own way, and for being a source of mentorship and, more importantly, role models.

Thanks you, Alan Guth and Ted Gull, for taking time to share with me their science and stories, and always looking out for me.

Thank you to Alessandro Savino, Yumi Choi, Meredith Durbin, Nathan Sanford, and Ryan Cooke for essentially teaching me most of what I know about HST/JWST reductions, Artifical Star Tests, LRIS and KCWI reductions.

Thank you to my fellow graduate students, particularly my cohort, for sharing this part of my academic journey. You all made Campbell a homely place from the science chats to the laughter to the MIND Coffee breaks.

Thank you to the Shining Lights, MPS Scholars program and the binary banter discord, who all provided such an incredible community. I learned so much from these scientist and hope I was able to help as much as they helped me.

Thank you to the faculty, staff, and everyone who makes UC Berkeley Astro run! I am incredibly grateful to have spent my PhD in such an intellectually stimulating environment and appreciate the feedback and comments that have helped me become a better scientist.

Thank you to the committee for helpful feedback on the manuscript.

Thank you to the Cranor fellowship and the Schweizerische Studienstiftung for the financial support that supported this thesis.

Chapter 1

Introduction

At cosmic dawn, the Universe was chemically composed of three elements: hydrogen, helium, and a dash of lithium. The first stars, thought to have been very massive ($M_* > 100$ $M_\odot$), were born in this primordial gas mixture, free of any other elements on the periodic table. The energy and momentum released by their tumultuous lives and violent deaths shaped the evolution of the first galaxies in the Universe and enriched them with heavier elements. Together with the subsequent generations of massive stars, these engines are responsible for building the rest of the periodic table and driving the evolution of galaxies.

Despite their importance, observing and studying populations of metal-poor massive stars is challenging. For every massive star with a mass of ~20 $M_\odot$, there are ~100,000 stars like our sun, and even the most luminous of metal-poor massive stars in star-forming Local Group dwarf galaxies can only be resolved by the most powerful telescopes. As a consequence, metal-poor massive stars remain poorly constrained, and high uncertainty persists in the physics governing their evolution, final fates, and impact on their host galaxies.

Metal-poor massive stars ($M_* > 8$ $M_\odot$ and $Z_* < 0.2$ $Z_\odot$) are central to a wide range of astrophysical phenomena. They are thought to give rise to transients and explosive enrichment in the early Universe (e.g., Smartt 2009; Frebel & Norris 2015; Ji et al. 2019), to power cosmic reionization (e.g., Robertson et al. 2015; Götberg et al. 2017; Robertson 2021), and to inject large amounts of kinetic energy into the interstellar medium (e.g., Hopkins et al. 2011), shaping the evolution of galaxies. They are likely progenitors of gravitational wave (GW) events (e.g., Spera et al. 2015; Abbott et al. 2016; Marchant & Bodensteiner 2024) and dominate the evolution and spectral energy distribution (SED) of star-forming galaxies at high-redshift (Eldridge & Stanway 2022). To understand the various connections between metal-poor massive stars and these physical phenomena, it is imperative to understand their formation, evolution, and deaths. Six key factors mark stellar evolution: 1. mass, 2. metallicity, 3. mass-loss, 4. rotation, 5. internal structure, and 6. binarity. The importance of the interplay between these factors is evident by the tremendous

effort put into studying metal-poor massive stars and their evolutionary paths in the Small Magellanic Cloud (SMC; $\sim 0.2\ Z_{\odot}$). Only recently did the Ultraviolet Legacy Library of Young Stars as Essential Standards (ULLYSES), a major community initiative, conclude its 500 orbits of HST observations of massive stars in the SMC (Roman-Duval et al. 2020), making it the largest ultraviolet (UV) spectroscopy sample of metal-poor massive stars to this date (Crowther 2022; Vink et al. 2023; Sana et al. 2024; Hawcroft et al. 2023; Sander et al. 2024; Martins et al. 2024; Ramachandran et al. 2024). In combination with previous studies (e.g., VLT-FLAMES Survey Evans et al. 2006; Mokiem et al. 2006; Ritchie et al. 2012; Dunstall et al. 2011; Hunter et al. 2007, 2008, 2009; Trundle et al. 2007; Evans et al. 2006, 2011; Ramírez-Agudelo et al. 2015; Evans et al. 2015; Patrick et al. 2019), the SMC currently sets the standard for the field of metal-poor massive stars. While the proximity of the SMC gives us the unique advantage of looking at these stars up close, the SMC metallicity is not representative of most galaxies past redshift = 1 (Madau & Dickinson 2014; Eldridge & Stanway 2022). While theoretical frameworks exist (e.g., Meynet & Maeder 2002; Ekström et al. 2008; Eldridge et al. 2017; Groh et al. 2019; Liu et al. 2021; Martins & Palacios 2021; Sibony et al. 2024), there is a need to observationally explore and study extremely metal-poor regimes (sub-SMC, $Z_{*} < 0.2\ Z_{\odot}$) to bridge the gap across cosmic time all the way to the metal-free very massive stars post Big Bang. The Local Group (z=0, our cosmic neighborhood) harbors dozens of metal-poor star-forming dwarf galaxies that meet the sub-SMC metallicity threshold [37], home to extremely metal-poor massive stars. This thesis comprises one of the largest quantitative studies of metal-poor massive stars, aiming to fill this knowledge gap (See Fig. 1.1). It increased the number of in-detail studied stars in this regime by an order-of-magnitude. The result suggests that rotation and binarity play a significant role in the evolution of massive stars in the lowest metallicity regime. It demonstrates the potential of panchromatic photometry to extend our observational reach beyond our current spectroscopic capabilities. The combined studies of SMC and sub-SMC metal-poor massive stars have yielded insights into the interplay between the metallicity and mass of these stars with their mass loss, rotation, internal structure, and binarity. While internal structure is essential, it remains the most challenging aspect to study observationally for massive stars outside the Milky Way, as it primarily relies on asteroseismology (Maeder & Meynet 2002; Degroote et al. 2010; Noels et al. 2015; Godart et al. 2017; Ekström 2021; Sibony et al. 2023; Bellinger et al. 2024) and is currently beyond the observational reach for extremely metal-poor stars. I will briefly summarize the current knowledge of mass-loss, rotation, and binarity.

1.0.1 Mass loss of Metal-poor Massive Stars

Mass loss plays a significant role in the evolution of massive stars, especially for stars $M_{*} > 60 M_{\odot}$ (Puls et al. 2008; Vink 2022, 2024) and occurs in different forms across various

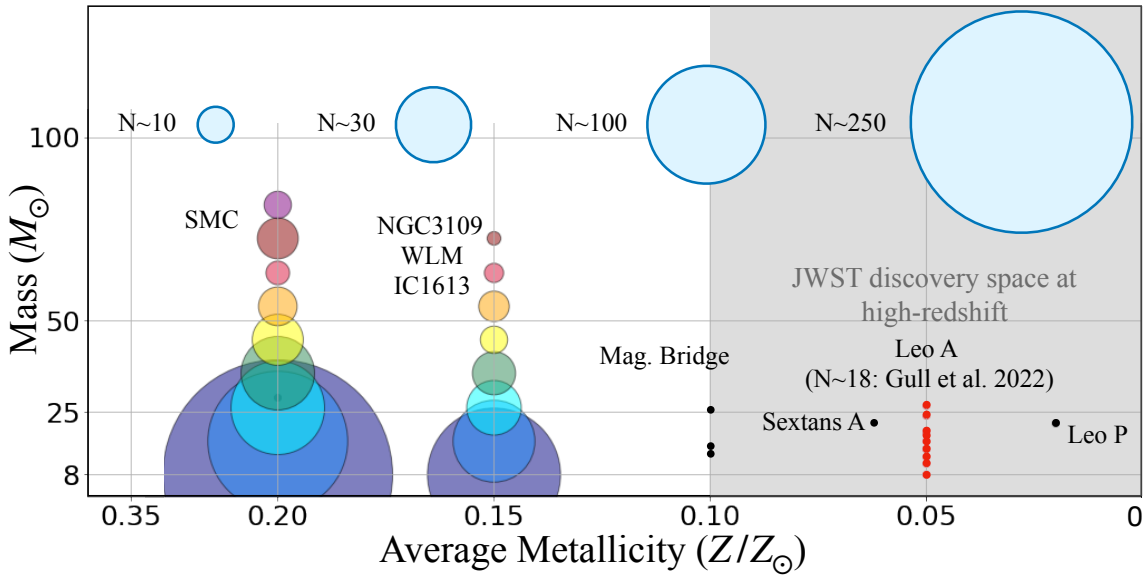


Figure 1.1: Overview of the observational progress of metal-poor massive stars (circles scale with sample size) with spectroscopic mass measurements (Gull et al. 2022; Evans et al. 2006; Telford et al. 2021; Ramachandran et al. 2021). This figure does not include stars with only qualitative analysis or $M_* > 100\ M_\odot$. The shaded area indicates the metallicity range of most galaxies observed in the high-redshift Universe. This thesis (red circles) increased the number of quantitatively analyzed stars in the lowest metallicity regime by an order of magnitude.

stages of stellar evolution (Smith 2014). On the main sequence, where stars spend most of their lifetime, most mass loss occurs through stellar winds (excluding binaries) driven by the metals in their stellar atmosphere. For decades, studies focused on understanding and constraining this mass loss. One of the primary motivators for the surveys in the SMC has been constraining mass loss (VLT-FLAMES; (Evans et al. 2006), ULLYSES; (Roman-Duval et al. 2020)). A few studies on extremely metal-poor stars also focus on UV observations to measure mass-loss rates (Ramachandran et al. 2021; Telford et al. 2021; Ramachandran et al. 2024). These observations suggest that massive stars in the $\sim 8 - 25\ M_\odot$ regimes have weak winds, meaning that their evolution is more affected by other parameters (e.g., rotation, binarity). In the extremely metal-poor regime, observations show that stellar winds are not the main contributing factor to the evolution of the stars (Gull et al. 2022; Telford et al. 2021; Ramachandran et al. 2024). While they are still an important parameter to understand and constrain due to their ubiquity, it is evident that for most extremely metal-poor massive stars, stellar winds are not the dominant factor that will shape a star's evolution on the main sequence. Rotation and binarity are likely more dominant factors in their evolution, which is supported by the findings in this thesis.

1.0.2 Rotation of Metal-poor Massive Stars

Rotation is an intrinsic parameter of massive stars and plays a significant role in their evolution, especially at low metallicity (Maeder & Meynet 2000; Heap et al. 2006a; de Mink et al. 2013; Sander et al. 2024). Rotation affects massive stars in two distinct ways: (1) the centrifugal force of fast-spinning stars will make the star deviate from its spherical shape, and (2) the internal mixing induced by rotation can set off various internal mechanisms. The former forces the star to act like a lower mass non-rotating star early in its evolution, while the latter forces it to act like a higher mass non-rotating star later. At low metallicity, massive stars are predicted to spin faster throughout their lifetime (Maeder & Meynet 2000; Heap et al. 2006a; de Mink et al. 2013). Studies of O ($> 15\ M_{\odot}$) and B stars ($\sim 8 - 15\ M_{\odot}$) in the SMC recently confirmed these predictions (Hunter et al. 2008; Sander et al. 2024). Even at extremely low metallicity, some initial indications indicate this trend holds (Gull et al. 2022; Telford et al. 2021). The distribution of rotation rates of metal-poor massive stars is central to several outstanding mysteries surrounding them. The distribution of rotation rates of stars on the zero-age main sequence (ZAMS) hints towards their formation, which is currently under investigation (Zinnecker & Yorke 2007). During the lifetime of stars, high rotation rates can give rise to exotic phenomena such as Be stars, which are B-type stars showing emission lines in their spectra, likely due to a decretion disk originating from their fast spins (Rivinius et al. 2013). Lastly, their high rotation rates allow them to conserve more of their core mass during their lifetime; this implies that the "traditional" mass cut-offs for different final fates might shift to slightly lower ZAMS masses (Groh et al. 2019; Sibony et al. 2024). The higher rotation rates allow us to investigate the chemical transport inside stars since rotation induces mixing processes that bring elements like carbon (C), nitrogen (N), and oxygen (O) to the surface of the star. While this suggests that mixing is more efficient at lower metallicity, the link to how this enrichment will alter the star's evolution is currently predominantly theoretical (Meynet & Maeder 2002; Groh et al. 2019; Sibony et al. 2024). Studies in the Milky Way, Large Magellanic Cloud, and SMC have already shown the increase in importance of rotation with decreasing metallicity. This thesis further supports these findings, particularly the high incidence of the Be star phenomenon, which is described in Chapter 2, Section 2.6.3.3 .

1.0.3 Binarity of Metal-poor Massive Stars

The vast majority of massive stars live in binary systems (Marchant & Bodensteiner 2023; Sana et al. 2012; Moe & Di Stefano 2017; Offner et al. 2023). On top of that, most of them interact with their companions at some point during their lifetimes (de Mink et al. 2007; de Mink et al. 2014; Marchant & Bodensteiner 2023). While these interactions are expected to drastically change the stars' evolutionary path and final fates, significant uncertainties on the degree and mechanism of interaction remain (Willcox et al. 2023;

Marchant & Bodensteiner 2023). Yet, interactions are believed to lead to products such as stellar mergers (e.g., de Mink et al. 2014; Henneco et al. 2024), various supernovae (e.g., Chevalier 2012; Metzger 2022), and potential progenitors to detectable gravitational wave emission (e.g., Tauris et al. 2017; Mandel & Farmer 2022). Understanding the distribution of binary parameters is crucial for stellar evolution and the study of galaxies across cosmic time. Since metal-poor massive binaries dominate distant star-forming galaxies' spectral energy distribution and spectra, constraining their fraction has significant implications for studying galaxies (Eldridge & Stanway 2022). Observationally, there have been concrete efforts to study the binary populations (e.g., Aasi et al. 2014; Gaia Collaboration et al. 2023, 2024; Shenar et al. 2024) and search for binary products (Bodensteiner et al. 2021, 2022; Ramachandran et al. 2024). At sub-SMC, there are mostly individual observations of binary candidates (Gull et al. 2022; Telford et al. 2024) and one observed contact binary candidate system (Gull et al. 2024). Although there are concrete efforts to study binaries in the SMC, we are still quite far from completing the census of massive binaries in the SMC. To address these data needs, several synoptic surveys will be conducted to observe the SMC and sub-SMC galaxies in the next few years. While no dedicated time-series photometry program has yet focused on sub-SMC metallicity binaries, such programs exist for other variable objects (e.g., RR Lyrae, Cepheids). Exploiting these types of datasets, this thesis presents the lowest metallicity contact binary to date in Chapter 3. Additionally, in Chapter 4, this thesis presents binary product candidates identified through panchromatic photometry.

1.1 Thesis Chapters

This thesis is organized as follows. After the introduction in Chapter 1, Chapter 2 presents a joint HST UV/optical/IR photometric and Keck and MMT optical spectroscopic study of massive stars in the nearest low-metallicity star-forming galaxy Leo A. Chapter 3 shows a novel use of JWST and HST imaging data to identify and characterize metal-poor massive binaries and discusses the lowest metallicity massive contact binary candidate to date found in WLM. Chapter 4 presents an in-depth HST UV/optical/IR photometric study of the massive stars in Sextans A. Finally, Chapter 4 summarizes the findings in this thesis and discusses future directions.

Chapter 2

A Panchromatic Study of Massive Stars in the Extremely Metal-Poor Local Group Dwarf Galaxy Leo A

An earlier version of this article was previously published as Gull,Maude; Weisz,Daniel R. ; Senchyna,Peter ; Sandford,Nathan R. ; Choi,Yumi ; McLeod,Anna F. ; El-Badry,Kareem ; Götberg,Ylva ; Gilbert,Karoline M. ; Boyer,Martha ; Dalcanton,Julianne J. ; GuhaThakurta,Puragra ; Goldman,Steven ; Marigo,Paola ; McQuinn,Kristen B.W. ; Pastorelli,Giada ; Stark,Daniel P. ; Skillman,Evan ; Ting,Yuan-sen ; Williams, Benjamin F. (2022) 'A Panchromatic Study of Massive Stars in the Extremely Metal-Poor Local Group Dwarf Galaxy Leo A', The Astrophysical Journal,Volume 941, Issue 2, id.206, 35 pp. Available at: https://doi.org/10.3847/1538-4357/aca295. Co-authors contributed the following parts: Binospec reductions (Senchyna, Peter), HST reductions as part of LUVIT (PIs: Gilbert and Boyer) products (Williams, Benjamin F.), and the ASTs as part of LUVIT products (Choi Yumi). The remaining co-authors provided feedback and comments on the manuscript. The first author (Gull, Maude) led, performed, created, and wrote the remaining reductions, analysis, figures, and texts.

2.1 Chapter Abstract

We characterize massive stars ($M > 8\ M_{\odot}$) in the nearby ($D \sim 0.8$ Mpc) extremely metal-poor (Z$\sim$ 5% $Z_{\odot}$) galaxy Leo A using *Hubble Space Telescope* ultra-violet (UV), optical, and near-infrared (NIR) imaging along with Keck/LRIS and MMT/Binospec optical spectroscopy for 18 main sequence OB stars. We find that: (a) 12 of our 18 stars show emission lines, despite not being associated with an H II region, suggestive of stellar activity (e.g., mass loss, accretion, binary star interaction), which is consistent with previ-

ous predictions of enhanced activity at low metallicity; (b) 6 are Be stars, which are the first to be spectroscopically studied at such low metallicity — these Be stars have unusual panchromatic SEDs; (c) for stars well-fit by the TLUSTY non-local thermodynamic equilibrium (non-LTE) models, the photometric and spectroscopic values of $\log(T_{\rm eff})$ and $\log(g)$ agree to within $\sim$ 0.01 dex and $\sim$ 0.18 dex, respectively, indicating that NUV/optical/NIR imaging can be used to reliably characterize massive (M$\sim$ 8 – 30 $M_\odot$) main sequence star properties relative to optical spectroscopy; (d) the properties of the most massive stars in H II regions are consistent with constraints from previous nebular emission line studies; and (e) 13 stars with $M > 8M_\odot$ are >40 pc from a known star cluster or H II region. Our sample comprises $\sim$ 50% of all known massive stars at $Z \lesssim 10\%\ Z_\odot$with derived stellar parameters, high-quality optical spectra, and panchromatic photometry.

2.2 Introduction

Metal-poor ($Z \lesssim 10\%\ Z_\odot$) massive stars ($M \gtrsim 8\ M_\odot$) are central to a wide variety of astrophysics. In low-mass galaxies, their feedback (i.e., stellar winds, supernovae) regulates star formation, enriches the interstellar medium (ISM), and may drive the formation of dark matter cores (e.g., Mac Low & Ferrara 1999; Stinson et al. 2007; Governato et al. 2010; El-Badry et al. 2016; Emerick et al. 2018; Eldridge & Stanway 2022). At low metallicity, those processes are expected to change significantly in comparison to higher metallicity environments (e.g., decreased line-driven winds, properties of supernovae; Heger et al. 2003; Eldridge & Tout 2004; Young et al. 2008; Smartt 2009; Vink & Sander 2021) due to changes in stellar properties (e.g., rotation, opacity, internal mixing; Maeder et al. 2005; Meynet et al. 2008, 2017; Sanyal et al. 2017; Groh et al. 2019). For example, in the early Universe, ionizing photons from early generations of massive metal-poor stars may power cosmic reionization, since they experience very high effective temperatures over a sizable fraction of their lives, resulting in an extreme ionizing ultra-violet (UV) radiation field (e.g., Wang 2013; Madau & Dickinson 2014; Stark et al. 2014; Robertson et al. 2015; Robertson 2021). At all redshifts, single and binary massive metal-poor stars are thought to be the progenitors to many explosive transients, including gravitational wave sources (e.g., Smartt 2009; Smith 2014; Spera et al. 2015).

Due to their close proximity, which enables resolved star studies, nearby star-forming dwarf galaxies are among the best targets for studies of individual massive stars and their environments at extremely low metallicities (e.g., Dalcanton et al. 2009; Hunter et al. 2012; Ott et al. 2012). However, despite substantial observational investments in resolving gas and stars in nearby dwarf galaxies, our detailed knowledge of their resolved massive star content has been limited. Many massive stars are hot ($\gtrsim 15,000$ K) meaning their spectral energy distributions peak at UV wavelengths. Massive stars are not always the brightest, most easily identifiable stars in the optical (e.g., Massey 2003), which limits the utility of

the existing optical imaging. Older *Hubble Space Telescope* (*HST*) UV imaging (e.g., with WFPC2) exists for some local dwarf galaxies, but the data quality is modest relative to the optical and the resulting studies are generally limited to the hottest and/or brightest objects (e.g., Bianchi et al. 2012). Other UV imaging surveys focus on the ensemble population of star-forming regions and young clusters as hosts of massive stars, but are less focused on the properties of the individual stars (e.g. LEGUS; Calzetti et al. 2015).

There is a similar paucity of spectra for massive metal-poor stars. While high-resolution optical and UV spectra of massive stars has improved our understanding of massive stars in the metal-rich environments (e.g., Bianchi & Garcia 2002; Bouret et al. 2003; Heap et al. 2006b; Sota et al. 2011, 2014; Barbá et al. 2017; Russeil et al. 2017; Li 2021), data of similar quality is less abundant at lower metallicities. Much of our understanding of metal-poor massive stars is based primarily on studies of the the Small Magellanic Cloud (SMC; Z $\sim$ 1/5$Z_{\odot}$, Martins et al. 2004; Castro et al. 2018; Ramachandran et al. 2019). However, the metallicity of the SMC does not probe the extremely metal-poor regime. One example of the need for extremely low-metallicity spectra is the need to calibrate the relative strengths of He I absorption lines that underlie He I emission lines in nebular spectra. This is an important correction for the determination of the primordial helium abundance and currently relies entirely on simulated spectra (e.g., Aver et al. 2021). Existing stellar models for lower metallicities predict significant differences in evolutionary pathways with implications for time-integrated feedback, final fates, and compact remnants (e.g., Meynet & Maeder 2002; Eldridge et al. 2008; Chen et al. 2015; Costa et al. 2021). Lastly, spectral atmosphere models for massive metal-poor stars are currently calibrated from higher metallicity environments. However, at lower metallicities, models predict, for example, more emission features due to increased stellar activity and deeper absorption features due to the increased effective temperature for a given spectral type, or broader absorption feature at a given spectra type (e.g., Kubátová et al. 2019; Martins & Palacios 2021).

Historically, the study of metal-poor massive stars has been challenging, since most star-forming metal-poor dwarf galaxies are located at distances of $\gtrsim$ 1 Mpc, meaning that even the most luminous massive stars are often faint and crowded. The limiting factors above have typically confined the study of low metallicity massive stars to a small number of stars in the closest dwarf galaxies. While providing important insights into chemical evolution and massive stars physics, the challenge of acquiring these data limited the sample sizes and homogeneity required for systematic progress in understanding metal-poor massive star evolution and how these stars impact their surroundings. Several recent efforts have sought to improve this situation. For example, only recently has there been a large survey published of $\sim$ 150 low-resolution spectra ($R \sim 1000$, SNR$\sim 8-256$ with a majority SNR$\sim 30-100$; Lorenzo et al. 2022). The study currently only provides spectra and spectral type identifications, but no stellar parameters. This is currently the only study of its kind at such low metallicties. Other than this low-resolution optical spectroscopy

is only available for a handful of massive stars in several sub-SMC dwarf galaxies within $\sim$ 1.5 Mpc (e.g., Venn et al. 2004; Bresolin et al. 2007; Kudritzki et al. 2008; Tramper et al. 2014; Hosek et al. 2014; Berger et al. 2018; Evans et al. 2019; Garcia et al. 2019; Telford et al. 2021). In these same systems, there are also concerted efforts to obtain UV spectroscopy of O-type stars with *HST* (e.g., García et al. 2015; Wofford et al. 2021; Telford et al. 2021), including a dozen stars as part of the Hubble UV Legacy Library of Young Stars as Essential Standards (ULLYESES) program (e.g., Roman-Duval et al. 2020, 2021).

Motivated by the need for a panchromatic photometric and high-quality spectroscopic inventory, we use Leo A as a test-bed galaxy. We pursue following aims: (a) to characterize the population of massive stars in Leo A and (b) test the reliability of photometric-only techniques in this metallicity regime. The latter is especially important as there are few extremely metal-poor systems in which individual massive stars can be resolved and high quality spectra can be acquired. Leo A is an ideal test-bed as it is the closest of the star-forming extremely metal-poor dwarf galaxies known in the local Universe ($D \sim 760$ kpc, $Z \sim 5\%$ $Z_{\odot}$) (e.g., van Zee et al. 2006; Nagarajan et al. 2021). Despite its favorable distance, low metallicity, and sizable massive star population (e.g., Cole et al. 2007), there has not yet been a systematic investigation of massive metal-poor star properties in Leo A. Existing studies that focus on Leo A's young stars do so in the context of H II region physics or as dynamical tracers of dark matter (e.g., Skillman et al. 1989; van Zee et al. 2006; Brown et al. 2007; Cole et al. 2007; Ruiz-Escobedo et al. 2018; Stonkutė & Vansevičius 2022; Leščinskaitė et al. 2022; Ricotti et al. 2022).

Recently, Leo A was observed as part of the *HST* Local Ultra Violet Infrared Treasury program (LUVIT; GO-15275, PI Gilbert and GO-16162, PI Boyer). This survey has obtained new *HST* ultra-violet (UV), optical, and near-IR (NIR) imaging with *HST* for 19 nearby dwarf galaxies in GO-16162 and 21 nearby dwarf galaxies in GO-15275 (overlap between the two programs consist of 19 galaxies). Combined with archival *HST* optical imaging, it provides broad information about the spectral energy distribution (SED) for a variety metal-poor stars across the H-R diagram.

Using LUVIT imaging for target selection, we acquired optical spectroscopy with the Low-Resolution Imaging Spectrograph (LRIS) on Keck and Binospec on MMT for two dozen of the most UV luminous stars in Leo A. This is one of the largest uniform collections of high-quality optical spectroscopy for extremely low-metallicity massive stars. Between the panchromatic *HST* imaging and the high fidelity optical spectra, we undertake here a systematic study of hot, massive, metal-poor stars in Leo A and their relationship to the broader galactic environment.

This paper is organized as follows. In §4.3, we describe the multi-wavelength *HST* observations and data reduction, along with target selection, observations, and data reduction for the Keck/LRIS and MMT/Binospec optical spectroscopy. In §2.4, we detail the process of measuring stellar properties from the *HST*-based spectral energy distributions (SEDs).

In §2.5, we expand on how we measure the stellar properties from modeling the optical spectra, and from the conventional approach of measuring equivalent widths (EWs). We present the results of each method in §2.6 and present a detailed discussion of the spectrum for each star along with a comparison of the photometric and spectroscopic parameters we measure. In §3.7, we discuss our results in the context of nebular studies of H II regions, field OB-stars, Be stars, and stars in the extremely metal-poor environments, as well as a comparison of SED fitting to full spectral fitting.

2.3 Sample selection, Observations, and Data Reduction

2.3.1 *HST* Observations and Photometry

We make use of *HST* UV, optical, and NIR broad-band imaging for selecting the spectroscopic sample and for measuring stellar properties based on *HST* photometry. Deep optical imaging was acquired in the ACS/WFC F475W and F814W filters as part of GO-10590 (Cole et al. 2007). WFC3/UVIS F275W and F336W and WFC3/IR F110W and F160W imaging was collected as part of LUVIT. We note that the ACS/WFC imaging has the largest spatial coverage of Leo A, followed by WFC3/UVIS imaging, while WFC3/IR imaging covers the smallest area. We only focus on stars for which we have at least 4-band UV+optical imaging, and include NIR when possible.

The LUVIT data are reduced by utilizing the photometric reduction pipelines that have been developed and improved for *HST* simultaneous *N*-band photometry (Williams et al. 2014, 2021). We refer the readers to the LUVIT survey paper (Gilbert, K. M., in prep) for the details of data collection and reduction for the entire LUVIT sample. Here we provide some of the Leo A specific details. We first aligned all `flc` (ACS/WFC, WFC3/UVIS) and `flt` (WFC3/IR) images to the Gaia DR2 astrometric solution following Bajaj (2017)[1] and combine images in each band weighted by exposure time using `AstroDrizzle` (Hack et al. 2020) after flagging and masking bad pixels and cosmic rays on input exposures. These aligned images, as well as the individual exposures with updated data quality extensions, are processed via the DOLPHOT package (Dolphin 2000, 2016) for photometry. We use the combined full-depth F475W image as the astrometric reference image for our final photometry.

DOLPHOT reports measurements of point-spread-function photometry for every object detected on any exposures within the reference image footprint. These include the flux, flux uncertainty, magnitude in the Vega system, SNR, and various photometry quality metrics. A raw output catalog of all objects identified by DOLPHOT is then subjected to quality cuts in each filter to include objects: 1) with SNR ≥ 4; (2) with crowding < 1.3 and < 2.25 for

[1] https://github.com/spacetelescope/gaia_alignment

UV and optical/IR filters, respectively; and (3) with square of sharpness ($SHARP^2$) < 0.15 and < 0.2 for UV/IR and optical filters, respectively, producing the "GST" catalog. These quality cuts were applied in each band independently. To remove objects that are associated with diffraction spikes after performing the GST cuts, we first identified individual tiny regions with severe diffraction spike feature using the median filter technique and then culled objects belonging to those regions (Gilbert, K. M., in prep). To construct an initial spectroscopic target sample, we further required SNR in F475W and F814W to be > 15 and $F475W^2_{SHARP} + F814W^2_{SHARP}$ to be ≤ 0.3. Additional criteria for the final spectroscopic target selection are presented in § 2.3.2. Even though the photometric depth reaches a couple of magnitudes fainter than the old main-sequence turn-off, we limited our stellar SED modeling to the bright targets of our interest. We note that we did not use the NIR medium-band photometry (F127M, F139M, and F153M) in this study, since it does not provide any further significant constraints in this stellar regime.

Photometric accuracy, precision, and completeness were computed from artificial star tests (ASTs). We generated ~135,000 dust-extinguished SED models in our UV, optical, and NIR bands that cover the entire H-R diagram, but more heavily populate the observed color and magnitude ranges (Choi et al. 2020). We assigned more input ASTs in higher stellar density regions of Leo A to better capture non-linear trends in photometric characteristics as a function of source crowding. Photometric measurements for input artificial stars were made in the exact same way as we did for real objects, and then identical quality cuts were applied to determine if the injected artificial stars were recovered. Comparisons of the input and output magnitudes are used to quantify our photometry uncertainty. The 50% completeness limits for F275W, F336W, F475W, F814W, F110W, and F160W are 24.97, 25.89, 29.10, 27.89, 26.58, and 25.27, respectively.

Fig. 4.2 shows select UV, optical, and NIR CMDs of Leo A, with the spectroscopic sample highlighted, as described in §2.3.2. The NIR CMD contains a smaller sample because the NIR imaging field of view covers a smaller spatial area of Leo A. The CMDs are close to 50% or above of the completeness limit. We overplot the rotating (v/vcrit=0.4) MESA Isochrones & Stellar Tracks (MIST) (Dotter 2016; Choi et al. 2016) for reference. We shift the tracks to the *Gaia* eDR3-anchored distance modulus of μ=24.40 mag reported by Nagarajan et al. (2021) and A_v = 0.03 mag, consistent with the foreground maps of Schlafly & Finkbeiner (2011). We do not apply any further dust corrections, since Leo A shows little internal redding (Skillman et al. 1989; van Zee et al. 2006).

2.3.2 Spectroscopic Target Selection

We observed Leo A for one night using Keck/LRIS in the 2020A semester. To fill the slit mask, we prioritized the stars brightest in the *HST* $F336W - F475W$ CMD (Fig. 4.2). We were able to place 9 UV bright stars on the LRIS slitmask. This number was limited

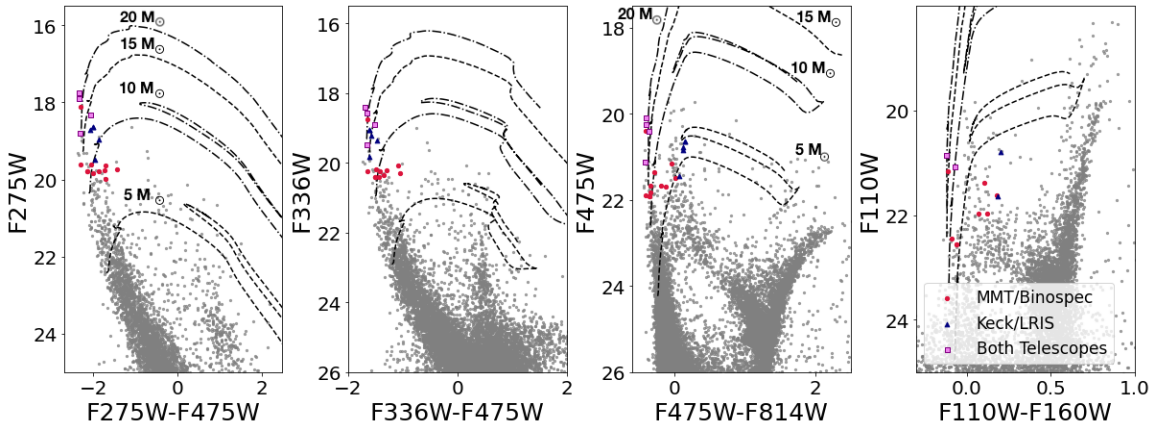


Figure 2.1: Select *HST*-based UV-optical (left), NUV-optical (left middle), optical-only (right middle), and NIR (right) CMDs of Leo A. Colored points indicate stars observed with LRIS (Keck) (navy triangles), Binospec (MMT) (red dots) and both telescopes (magenta squares). For reference, we overplot select MIST tracks ([Fe/H] =−1.0, v/vcrit=0.4, A_v = 0.03). There are fewer stars on the NIR CMD because WFC3/IR has a smaller field of view and does not entirely overlap the UV and optical imaging. All spectroscopic stars are massive stars (i.e. $M > 8M_{\odot}$). The NUV CMD shows that the stars in our spectroscopic sample are not very evolved.

by crowding, LRIS slit mask alignment constraints, and science goals. The remaining slits were filled with filler stars (i.e., bright stars in ground-based photometric observations of Leo A). To achieve sufficient SNR (see below) we integrated for a full night on this single slit mask.

We also observed Leo A on MMT/Binospec in the 2020A semester. Targets were selected using the Binospec mask software with following criteria as input: $F475W - F814W \leq -0.1$, F275W ≤ 20, and $-0.8 \leq F275W - F336W \leq -0.2$, thereby selecting the bluest and brightest sources.

The two spectroscopic datasets have stars in common, which allows us to check for systematic changes and gauge consistency. Fig. 4.2 shows the LRIS and Binospec spectroscopic samples overplotted on the *HST* CMDs. The majority of the brightest UV stars have spectroscopic coverage from at least one of the telescopes. The handful that do not were excluded due to slitmask and/or crowding constraints. We plan to target them in a future observing run.

Fig. 2.2 shows zoomed-in CMDs that highlight the spectroscopic sample. We label them based on the origin of the spectra used for analysis (i.e., Keck stars: K, Binospec stars: B) and in decreasing F475W magnitude. In the UV-optical CMD (left panel), we see that the stars appear to have masses of at least 8 $M_{\odot}$, since they pool around the 10 $M_{\odot}$ track. In the optical CMD (right panel) the picture is not as clear as in the UV-optical

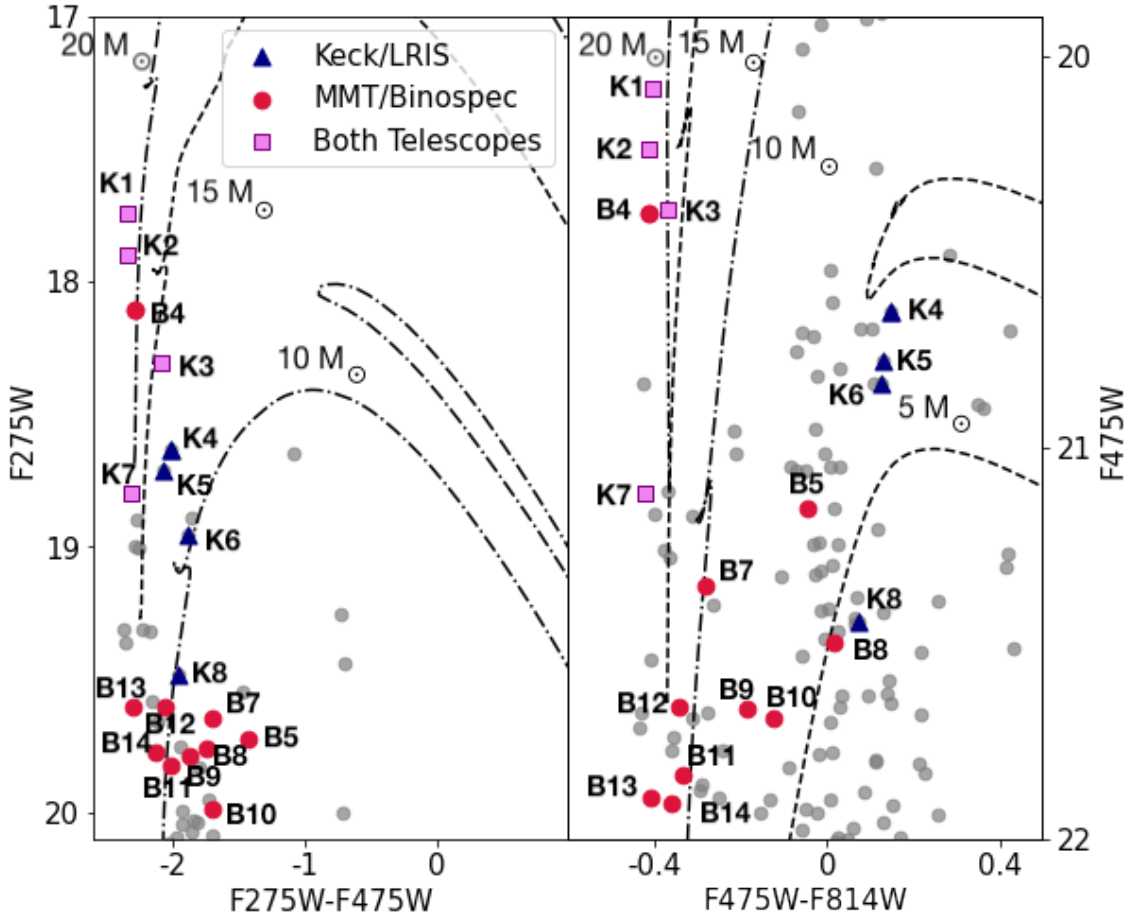


Figure 2.2: This plot is identical to Fig. 4.2, only zoomed in on luminous blue stars selected for spectroscopy in the UV and optical CMDs. We label the stars by the names in Table 2.1, where K stands for stars with Keck and B for stars with Binospec spectra. For reference, we overplot select MIST tracks ([Fe/H] =−1.0, v/vcrit=0.4, A_v = 0.03). Interestingly, a handful of stars that appear on the main sequence in the UV-optical CMDs appear in the blue core helium burning region of the F475W-F814W CMD. We discuss this in §2.6.3.

CMD. Interestingly, a handful of stars (K4,K5,K6,K8,B5,B8) visually appear to be main sequence (MS) stars in the UV-optical CMD, but appear on the blue core helium burning (BHeB) sequence in the optical CMD. We discuss these stars in detail in §2.6.3. In total, we have spectroscopic observations for 18 stars. Observational properties of these stars are listed in Table 2.1. We now describe the details of each spectroscopic dataset.

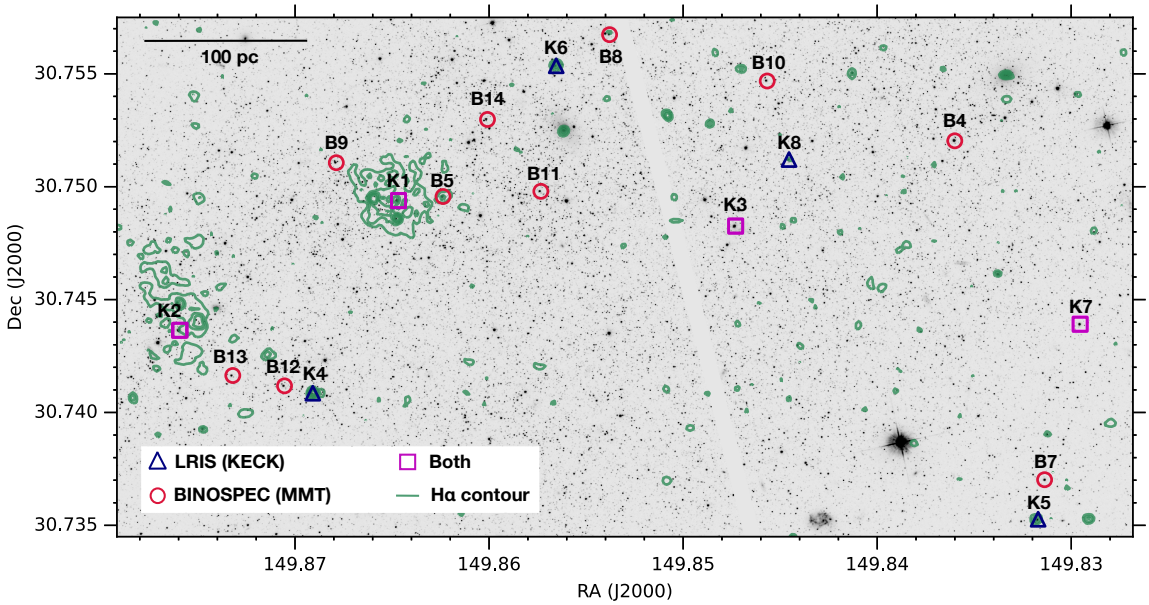


Figure 2.3: The Leo A *HST* ACS/F475W image zoomed in on the central region of the galaxy. Stars with spectroscopic observations are color-coded by telescope: Keck/LRIS (blue triangles), MMT/Binospec (red circles), both (magenta squares). Contours of Hα emission from ground-based imaging (Local Volume Legacy Survey; Kennicutt et al. 2007) are overplotted in green. Note that many of the massive stars are not obviously associated with cataloged H II regions including one O-star (K7).

2.3.2.1 LRIS and Binospec Observation

We observed Leo A on the night of February 20th 2020 using LRIS (Schulte-Ladbeck et al. 1995) at the Keck telescope at W.M. Keck Observatory in Hawaii, and February 23th, 24th, and 29th 2020 using the Binospec instrument, mounted on the 6.5m MMT telescope. For LRIS, we obtained spectra using a custom made 0.7″ slit-mask. The gratings for the LRIS red channel were set to 1200/7500, covering 7224−8855 Å. The grism for the LRIS blue channel was set to 600/4000, covering 3330−5910 Å and the dichroic was set to D680, yielding a nominal resolution of R∼1800. For Binospec, we observed two nights using the 1000 lpmm grating, providing spectra from 3900−5400 Å at a nominal resolution of $R \sim 3600$. The last night, we used the 270 lpmm grating and obtained spectra spanning 3900 to 9240 Å, with a resolution of $R \sim 1250$.

For LRIS, we integrated for a total of 6.3 hours using multiple 1200-1800s exposures. We reduced the spectra using the `Pypelt` pipeline (Prochaska et al. 2019) and then co-added each single epoch spectrum. The resulting SNRs range from ∼ 30 to ∼ 83 per Å at ∼ 5000 Å and ∼ 5 to ∼ 17 per Å at ∼ 8000 Å. For Binospec, we integrated for a total of 2

hours on night 1, 1 hour on night 2, and 1 hour on night 3, in intervals of 1200s exposures. We observed the same stars all three nights. We reduced the spectra with the Binospec Data Reduction Pipeline (Kansky et al. 2019). We co-added single exposure spectra for each star from the first two nights. The co-added spectra from the first two nights have SNRs ranging from ~ 9 to ~ 31 per Å at ~ 5000 Å. Spectra from the third night have SNRs ranging from ~ 11 to ~ 40 per Å.

Table 2.1 lists the basic properties of our LRIS and Binospec targets. As noted in the Table, four stars were observed with both Binospec and LRIS: K1/B1, K2/B2, K3/B3 and K7/B6. For simplicity, we refer to the Keck stars as K1-K8. We note that a second star fell into the same slit K2, however, K2 is unaffected by this. This was the only slit to do so, we do not include the second star in the sample.

2.3.3 Spectroscopic Normalization

We normalize all spectroscopic observations using PySpecKit (Ginsburg & Mirocha 2011). We exclude the parts of the spectrum showing strong absorption or emission features. We normalize all our spectra using a fifth-order polynomial, in order to avoid over fitting. We show examples of normalized sample spectra with a detailed indication of spectral features in Fig. 2.4.

2.4 Measuring Stellar Parameters From Panchromatic Photometry

We use the Bayesian Extinction and Stellar Tool (`BEAST`; Gordon et al. 2016) to infer physical properties of luminous blue stars in Leo A from the *HST* broad-band multi-wavelength imaging (F275W, F336W, F475W, F814W, F110W, F160W). The `BEAST` is a probabilistic approach to simultaneously modeling the stellar and line-of-sight dust properties of individual stars in nearby galaxies by carefully considering observational uncertainties arising from photon noise and crowding. Here, we briefly summarize how the `BEAST` works and its application to stars in Leo A. Detailed descriptions of the `BEAST` technical underpinnings and its application to a nearby low-metallicity dwarf galaxy can be found in Gordon et al. (2016) and Choi et al. (2020), respectively.

Briefly, the `BEAST` creates a physics model grid by mapping a stellar evolution library onto a stellar atmospheric model using stellar evolutionary parameters (initial mass M_{ini}, age A, and metallicity Z) and stellar atmospheric parameters (effective temperature $\log(T_{\rm eff})$, surface gravity $\log(g)$ and metallicity Z). Lower temperature stars (i.e., A type and

Table 2.1: Observing details of the spectroscopic data taken with LRIS (KECK) and Binospec (MMT). The columns are: (1) The name of each star used throughout the paper; (2) Alternative ID; (3) Right Ascension; (4) Declination; (5) Observing date; (6) slit width; (7) Integration time; (8)-(10) select *HST* magnitudes and colors; (11) & (12) SNR at specified wavelength

Star	Alternative ID	α (J2000)	δ (J2000)	UT dates	slit (arcsec)	t_{exp} (hr)	$F475W$	$F475W-F814W$	$F366W$	SNR (4500 Å)	SNR (8000 Å)
LRIS (KECK)											
K1	J095927.52+304457.82	09 59 27.52	+30 44 57.82	20/02/21	0.7	6.3	20.1	−0.40	18.4	82.5	11.5
K2	J095930.22+304437.14[A]	09 59 30.22	+30 44 37.14	20/02/21	0.7	6.3	20.2	−0.41	18.6	68.9	16.6
K3	J095923.35+304453.76	09 59 23.35	+30 44 53.76	20/02/21	0.7	6.3	20.4	−0.36	18.9	73.5	10.8
K4	J095928.58+304427.08	09 59 28.58	+30 44 27.08	20/02/21	0.7	6.3	20.7	0.15	19.0	47.8	4.9
K5	J095919.61+304406.98	09 59 19.61	+30 44 06.98	20/02/21	0.7	6.3	20.8	0.12	19.2	56.1	13.3
K6	J095925.57+304519.29	09 59 25.57	+30 45 19.29	20/02/21	0.7	6.3	20.8	0.13	19.4	52.2	5.8
K7	J095919.09+304438.11	09 59 19.09	+30 44 38.11	20/02/21	0.7	6.3	21.1	−0.42	18.5	46.3	5.6
K8	J095922.69+304504.34	09 59 22.69	+30 45 04.34	20/02/21	0.7	6.3	21.5	0.00	19.8	29.7	5.8
Binospec (MMT)											
B1/K1	J095927.52+304457.76	09 59 27.52	+30 44 57.76	20/01 23+24/29	1.0	2/1+1	20.1	−0.40	18.4	35.1/40.6	-/10.9
B2/K2	J095930.23+304437.08[A]	09 59 30.23	+30 44 37.08	20/01 23+24/29	1.0	2/1+1	20.2	−0.41	18.6	34.0/40.0	-/10.3
B3/K3	J095923.35+304453.70	09 59 23.35	+30 44 53.70	20/01 23+24/29	1.0	2/1+1	20.4	−0.37	18.9	30.4/36.6	-/11.8
B4	J095920.64+304507.32	09 59 20.64	+30 45 07.32	20/01 23+24/29	1.0	2/1+1	20.4	−0.41	18.8	29.3/35.8	-/9.3
B5	J095926.97+304458.44	09 59 26.97	+30 44 58.44	20/01 23+24/29	1.0	2/1+1	21.2	−0.04	20.1	19.8/24.0	-/8.1
B6/K7	J095919.09+304438.05	09 59 19.09	+30 44 38.05	20/01 23+24/29	1.0	2/1+1	21.1	−0.42	18.5	19.5/22.8	-/5.5
B7	J095919.53+304413.28	09 59 19.53	+30 44 13.28	20/01 23+24/29	1.0	2/1+1	21.4	−0.29	20.3	17.0/19.2	-/5.3
B8	J095924.91+304524.25	09 59 24.91	+30 45 24.25	20/01 23+24/29	1.0	2/1+1	21.5	0.02	20.2	24.2/28.1	-/8.0
B9	J095928.29+304503.83	09 59 28.29	+30 45 03.83	20/01 23+24/29	1.0	2/1+1	21.7	−0.18	20.2	16.2/17.0	-/6.6
B10	J095922.96+304516.86	09 59 22.96	+30 45 16.86	20/01 23+24/29	1.0	2/1+1	21.7	−0.12	20.4	12.2/14.4	-/3.5
B11	J095925.76+304459.27	09 59 25.76	+30 44 59.27	20/01 23+24/29	1.0	2/1+1	21.7	−0.43	20.4	9.4/11.0	-/2.2
B12	J095928.93+304428.25	09 59 28.93	+30 44 28.25	20/01 23+24/29	1.0	2/1+1	21.7	−0.35	20.2	11.9/14.0	-/3.5
B13	J095929.57+304429.90	09 59 29.57	+30 44 29.90	20/01 23+24/29	1.0	2/1+1	21.9	−0.41	20.2	11.5/13.5	-/3.1
B14	J095926.42+304510.73	09 59 26.42	+30 45 10.73	20/01 23+24/29	1.0	2/1+1	21.9	−0.36	20.4	14.7/17.3	-/4.9

Note. — A- Same star, with different name in the observing logs. K - Keck, B - Binospec

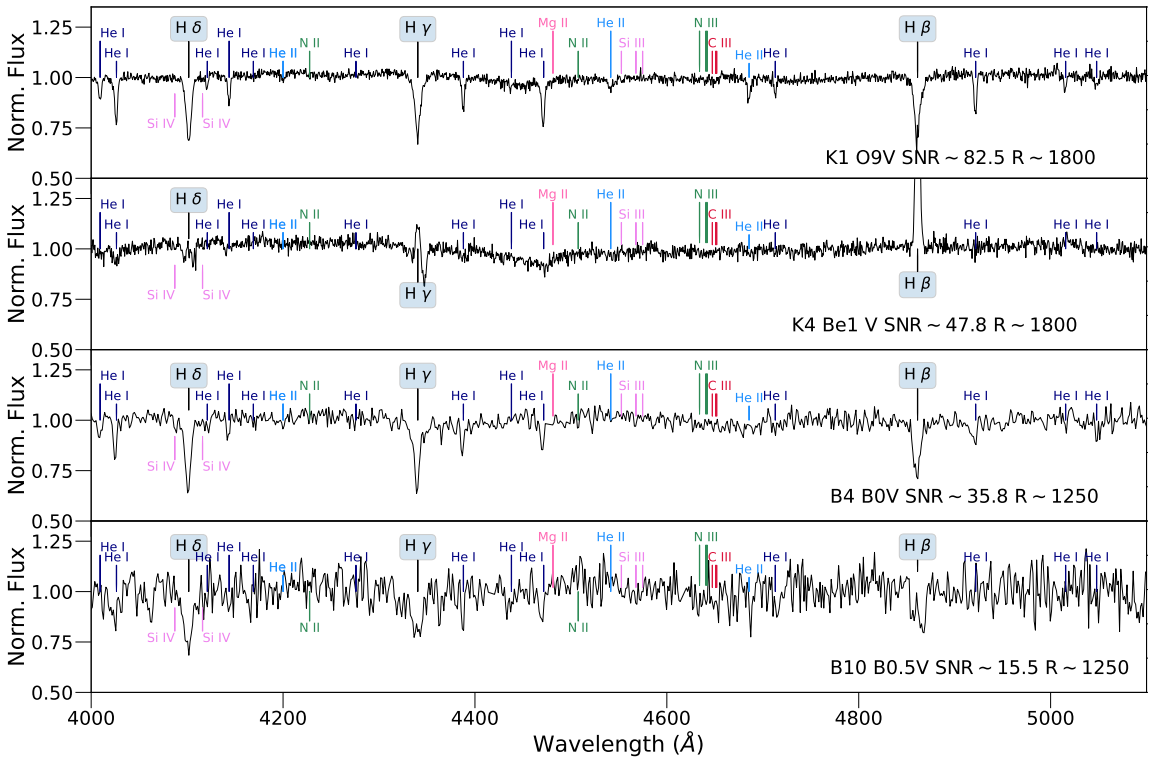


Figure 2.4: Example normalized spectra of massive stars in Leo A shown from 4000-5100Å with key features labeled. Top two panels: Keck/LRIS ($R \sim 1800$) spectra of an O-type (top) and a Be-type star (bottom) in Leo A. The O-star exhibits He I (dark blue) and He II (light blue) absorption lines and a clear Balmer series in absorption. These are typical of a late-type O star. The Be star shows He I (dark blue) absorption but no He II (light blue). The Balmer series is primarily in emission. Bottom two panels: Binospec spectra ($R \sim 1250$) of an early B-type (top) and a B(e)-type (bottom) in Leo A. The B star shows primarily He I (dark blue) absorption features, while He II (light blue) absorption is minimal. The Balmer lines show absorption features, although there appears to be weak emission within the feature. The bottom panel shows a B0.5-type star. Though the low SNR makes identification of clear features more challenging, we still find clear He I (dark blue) absorption features. The Balmer lines are a mix of absorption and emission features. We note the star is a potentially a Be star as well

cooler) are paired with local thermodynamic equilibrium models from Castelli & Kurucz (2004) while hotter stars are paired with non-local thermodynamic equilibrium (non-LTE) atmospheres from the TLUSTY OSTAR and BSTAR grids (Lanz & Hubeny 2003, Lanz & Hubeny 2007). This process covers intrinsic properties for each star. Stars are then moved to the distance of the galaxy of interest (or can be left as a free parameter) and then the

intrinsic light is extinguished by a dust model. The dust model used by the BEAST is a flexible mixture model that allows for smooth variation between average Milky Way-like and SMC-like attenuation curves, including the curve steepness and changes in the 2175Å bump strength (Gordon et al. 2022). For each of resultant dust extinguished stellar models, a observational noise model is determined based on artificial star tests (ASTs).

For our analysis of stars in Leo A, we adopt the following priors on various physical parameters. First, we fix the distance modulus to $\mu = 24.40$ mag, which is the *Gaia* eDR3-anchored RR Lyrae distance reported by Nagarajan et al. (2021). Second, we use the MIST stellar evolutionary models with rotation (v/vcrit=0.4) in preference over the MIST non-rotation (v/vcrit=0.0) models and the PARSEC Bressan et al. (2012) models. This choice is primarily made due to the evidence of rotation in the spectra, which is accounted for in the MIST rotation model. In Appendix 2.10.1, we discuss the difference between the two MIST models as well as the PARSEC models. Third, we adopt an SMC-like average extinction curve with $R_V = 2.74$ (Gordon et al. 2003), and allow A_V to vary from a minimum of $A_V = 0.00$ mag to a maximum of $A_V = 0.5$ mag, which is the amount of internal dust needed to match the width of the upper MS in nearby dwarf galaxies based on fitting optical CMDs (e.g., Dolphin et al. 2003). We note that some stars can have higher A_V values than the typical value set by the width of the MS. Finally, we adopt a metallicity of $Z = 0.1\ Z_\odot$ throughout the paper. This is slightly higher than the H II region metallicity of Leo A, but it is: (a) the minimum value for both of the publicly available TLUSTY OSTAR and BSTAR high resolution spectral grids; and (b) may be more appropriate for the massive stars, which have been found to be more metal-rich (from iron absorption lines) than gas-phase metallicities (from oxygen emission lines) in other nearby dwarf galaxies (Bouret et al. 2015; Garcia et al. 2014; Telford et al. 2021) . Adopting this single metallicity ensures uniform analysis of the spectra and photometry. We report the median value (_p50) and the uncertainty computed from the 68% confidence interval (i.e., 0.5∗(_p84-_p16)) of a marginalized 1D posterior probability distribution function (PDF) for each parameter. We show example BEAST fits in Fig. 2.5 and discuss them in §2.6.1.

2.5 Measuring Stellar Parameters From Optical Spectroscopy

We use two methods to characterize the stars from spectroscopy. The first, which also derives stellar parameters (e.g., $\log(T_{\rm eff})$, $\log(g)$, $v \sin i$, A_V, mass), is through an adaptation of the full spectral fitting code, "The Payne" (Ting et al. 2019) for massive stars. The Payne has primarily been used for cool stars in the Galaxy, but its flexibility makes it readily adaptable to different types of stellar spectra including massive stars (e.g., Xiang et al. 2022). The second is through the measurement of equivalent widths (EWs). EWs

Table 2.2: Basic information on the TLUSTY model grids used for `The Payne`. The columns are: (1) Grid name;(2) number of models in grid used to train the neural net; (3) temperature range in log space; (4) temperature range in kilo-Kelvin; (5) surface gravity range and (6) fixed microturbulence value.

Grid	Nr. of models	$\log(T_{\rm eff})$ dex	$\log(T_{\rm eff})$ kK	$\log(g)$ dex	$v_{\rm micro}$ kms^{-1}
(1)	(2)	(3)(4)	(5)	(6)	
OSTAR	69	4.44-4.74	27.5-55	3.00-4.75	10
BSTAR	105	4.18-4.48	15-30	3.25-4.75	2

are conventionally used in the field of metal-poor massive stars (e.g., Bresolin et al. 2006; Evans et al. 2007; Tramper et al. 2011, 2014; Camacho et al. 2016; Evans et al. 2019; Garcia et al. 2019), and provide a sanity check on our quantitative fitting. The extreme metal-poor nature of Leo A means there ia a lack of empirical low-metallicity templates for comparison, while the low-resolution nature of the spectroscopy means that the EWs cannot always be as cleanly determined compared to higher resolution spectroscopy. We use the EWs to provide guidance rather than rigorous parameter determination.

2.5.1 The Payne

For quantitative spectral fitting, we have adapted `The Payne` (Ting et al. 2019) for use with the TLUSTY non-LTE massive star model atmospheres (Lanz & Hubeny 2003). Specifically, we use the public OSTAR and BSTAR grids available on the TLUSTY website[2]. At its core, `The Payne` is a highly efficient, multi-dimensional interpolator that can generate accurate models based on sparse pre-computed grid points by using a neural net (see Ting et al. 2019 for details).

We train two different neural nets that separately cover O-stars (Lanz & Hubeny 2003) and B-stars (Lanz & Hubeny 2007). Spectral features in these stars are sufficiently different, and the public TLUSTY grids are sufficiently sparse, that training nets based on separate models lead to more accurate synthetic spectra when compared to trying to interpolate across both model grids at once.

The two pre-computed TLUSTY model grids are not uniform in their coverage of parameter space. For consistency, we adopt a fixed metallicity of $Z/Z_{\odot} = 0.1$ in both grids, similarly to the `BEAST` models chosen. Lastly, we note that a solar Helium abundance is assumed and by number is fixed to $He/H = 0.1$. We list all other parameters in Table 2.2.

Beyond $\log(T_{\rm eff})$ and $\log(g)$, we also fit for radial velocity, $V_{\rm R}$, and rotational velocity, $v \sin i$, of each star. For $v \sin i$, we use the Fourier method as outlined by Simón-Díaz &

[2] http://tlusty.oca.eu/Tlusty2002/tlusty-frames-models.html

Herrero 2007; however, it is currently not a label we train the neural net on. Furthermore, we note that the accuracy of $v \sin i$ is limited by the resolution of the spectra. The resolution limit on $v \sin i$ is $\sim$ 170 kms^{-1} for Keck and $\sim$ 80 kms^{-1} for Binospec. For stars where we have both Binospec and Keck spectra, we report the Binospec derived $v \sin i$ value. We fix the macroturblent velocity to $V_{\rm macro}$ = 20 kms^{-1}, which is motivated by various literature studies of hot, massive stars in the SMC (e.g., Mokiem et al. 2006, Penny & Gies 2009, Grassitelli et al. 2016). We further fix the instrumental resolution to $R \sim 1800$ for the Keck spectra and $R \sim 3600$ for the Binospec data. We note that having fixed resolution, $V_{\rm macro}$ = 20 kms^{-1} and $V_{\rm micro}$ = 20 kms^{-1}, all might slightly bias $\log(g)$ and $v \sin i$, since they all influence the line profile.

We use `The Payne` to find best fit stellar parameters for our spectra via χ^2 minimization. We only fit LRIS and Binospec spectra blueward of 7500A, the red edge of the TLUSTY grid, and mask emission lines, which are not included in TLUSTY, as described in §2.6.3.

We use the optimization results to initialize a Markov chain Monte Carlo (MCMC) sampler that explores the posterior probability distribution for each star. We use a Gaussian log-likelihood function and adopt uniform priors for $\log(T_{\rm eff})$, $\log(g)$, $v \sin i$ and $V_{\rm R}$. The ranges of allowed values for each are the grid edges for $\log(T_{\rm eff})$ and $\log(g)$ of the respective model grid and [0,1000] kms^{-1} for $v \sin i$ and [-50,150] kms^{-1} for $V_{\rm R}$.

We use the MCMC sampler `emcee` (Foreman-Mackey et al. 2013) to sample the posterior. We first use 512 walkers to first burn in our sample for 200 steps. We then initialize 512 walkers, applying a Gaussian scatter of 0.001 and set a maximum step number of 10^5 steps. However, the sampling stops if one of our convergence criteria is reached: 1) the auto-correlation time, τ, has changed by $< 1\%$ over the last 100 steps; or 2) the sampler has run for $> 20\tau$ steps. To remove any residual effects of burn-in or corrected samples, we discard the first 5τ samples from each walker and thin each chain's samples by a factor of $\sim \tau/2$.

For each star, we report the median value of the marginalized posterior PDFs along with the 16th and 84th percentiles as a measurement of uncertainty. If the uncertainty is less than 0.01, we round it to 0.01.

Once we have the parameters from the full spectral fitting, we use those to determine the luminosity ($\log(L)$), the evolutionary mass (M_{evo}), the initial mass (M_0) and the spectroscopic mass (M_{spec}). We note that both M_{evo} and M_{spec} are present day masses. The luminosity is determined by using both the spectroscopic parameters as well as the photometric data. Based on the spectroscopic parameters, we choose the appropriate model to scale in order to fit to the observed and dust-corrected photometric SED from the *HST* photometry. We use the ratio between the observed dust-corrected SED, f_ν, to the intrinsic

SED (i.e., the model: F_ν) and the distance to Leo A to obtain the spectroscopic radius R

$$R = \sqrt{\frac{f_\nu}{F_\nu} \times d^2} \tag{2.1}$$

Using the spectroscopic radius, $\log(T_{\rm eff})$, and the Stefan-Boltzmann constant ($\sigma_{\rm SB}$), we calculate the luminosity.

$$L = 4\pi R^2_{spec} \times \sigma_{\rm SB} \times T^4_{eff} \tag{2.2}$$

We use the spectroscopic radius and $\log(g)$ value to determine M_{spec}:

$$M_{spec} = 10^{log(g)} R^2_{spec}/G \tag{2.3}$$

Finally, we use the derived $\log(L)$ and spectroscopically $\log(T_{\rm eff})$ and the rotating MIST stellar models to find the mass track that the star falls on to determine M_0. The models are spaced at 1 $M_\odot$ and we determine the mass by visual inspection. For M_{evo} we use the stellar parameters to find the stellar mass of the MIST stellar models by looking at the mass at the current position on the track.

2.5.2 Equivalent Widths

To support our qualitative analysis, we measure the equivalent widths of each spectral line from the one-dimensional spectrum for the stars in our sample. After normalizing the spectrum as described in §2.3.3, we combine the `specutils` (an extensible spectroscopic analysis toolkit for astronomy; Earl et al. 2019) package with `scipy` (Virtanen et al. 2020) to determine the EWs. We use the `CLOUDY` linelist (Ferland et al. 2017) to identify the correct wavelengths. We specify the region of the spectral lines of interest and provide initial guesses for the line centre, amplitude, and width. We choose to fit a Gaussian profile to all our lines. In the scenario of a mixed absorption-emission feature, we employ a Gaussian fit to the emission component and subtract it out of the spectra before fitting the absorption feature for the equivalent width. The results are used in §2.6.3 to support the commentary and in Table 2.3.

2.5.3 Analysis of emission line stars

For a subset of stars (K4, K5, K6, K8, B5, B8), both the spectroscopic method and photometric method described above yield high reduced χ^2 ($\geq$150) values. These stars also have unusual SEDs such that they are bright in the UV, red-optical, and NIR (when available), i.e. their SEDs are not well-approximated by a blackbody as expected for normal stars. Their spectra usually feature strong emission, despite not being in close proximity to an H II region (except B5). They further show no or little extended emission beyond the

stellar trace in the 2D spectra. We posit that these stars may have circumstellar disks (e.g., Iqbal & Keller 2013; Lazzarini et al. 2021) causing both the emission features seen in the spectra as well as the IR-excess in the photometry leading to unusual SEDs. We use an alternative fitting technique to constrain the properties of the star and disk.

We fit emission lines stars in two different ways. First, we use full spectral fitting, which enables the recovery of $v \sin i$ and $\log(T_{\rm eff})$. Second, we fit the photometric SEDs, which provides $\log(T_{\rm eff})$ and $A_{\rm V}$. For spectroscopic fitting, we use `The Payne` but emphasize the He I/He II features by inflating uncertainties on other features, such that they effectively only provide continuum constraints. For Be stars, we mask the Balmer lines owing to strong emission. We recover $\log(T_{\rm eff})$ and $v \sin i$ but not $\log(g)$ which is derived from the Balmer lines.

Photometrically, we opt to fit a dual model of a star and potential disk to the UV-optical-NIR SEDs. We use `pystellibs`[3] to interpolate between model SEDs, and `pyphot`[4] to calculate synthetic photometry. Only stellar models are currently publicly available, hence we opt to use stellar models for the disk as well, since the disk is a nuisance parameter. This will still allow us to capture the essential underlying parameters, temperature and extinction, although we might miss the broader physics (e.g., density, velocity, chemical composition). For the stellar component, we continue to use the TLUSTY models, similarly to the `BEAST`, while for the potential disk component we use the BaSeL (Lejeune 2002) library, since we need cooler temperatures than TLUSTY can provide. We fit the following parameters: $\log(T_{\rm eff})_{star}$, $\rm R_{star}$, $\log(T_{\rm eff})_{disk}$, $\rm R_{disk}$, and E(B-V). We adopt the same extinction curve as used in the `BEAST` fitting. We keep distance as well as mass constant ($M_{star} = 10 M_{\odot}$ for K4, K5, K6 and K8, and $M_{star} = 8 M_{\odot}$ for B5 and B8). We use the MCMC sampler `emcee` to determine the median value. We first use 64 walkers to first burn in our sample. We burn in the sample with 50 steps and use 128 walkers, we then set a maximum step number of 1000 steps. We determine convergence by the same criteria as `The Payne` fitting. We use a log-Gaussian likelihood function and use a Gaussian prior for each parameter. We allow a broad range of priors so that we can simultaneously check whether the SED could also be explained by a companion star. We allow the parameters to sample over following ranges for $\log(T_{\rm eff})_{star}$ = [4,5.7] $\log(K)$, $\rm R_{star}$ = [0.8,42] $R_{\odot}$, $\log(T_{\rm eff})_{disk}$= [2,4] $\log(K)$, $\rm R_{disk}$ = [0.8,127] $R_{\odot}$, and E(B-V)= [0,0.5] dex. We note that we use the same extinction value for both components, since we are only interested in the stellar component. Lastly, we initialize the sampler by using the spectroscopic values. The results are used in §2.6.3.3 to support the commentary.

[3]https://github.com/mfouesneau/pystellibs
[4]https://mfouesneau.github.io/pyphot/

2.6 Results

2.6.1 Stellar Parameters from Photometry

For comparison with our spectroscopic sample, we only ran `the BEAST` on stars with $F475W < 22$ and $F475W - F814W < 0.5$ (i.e., $M \gtrsim 5M_{\odot}$ on the MS). For select science cases (e.g., §2.6.1) we used `the BEAST` on slightly fainter stars.

To facilitate discussion and comparison, we divide the resulting photometric SED fits into 3 groups based on the χ^2 values. Fits with $\chi^2 < 20$ are considered good fits, $20 \leq \chi^2 < 80$ are decent fits, and $\chi^2 \geq 80$ are poor fits. These χ^2 divisions are based on qualitative assessment of the fits, following other BEAST papers in the literature (e.g., Van De Putte et al. 2020). They are only meant to be used qualitatively to facilitate discussion. Furthermore we note that the uncertainties are likely underestimated, since they take the models at face value.

Fig. 2.5 shows three example SEDs in each of our χ^2 categories. These examples all have spectroscopic data enabling further evaluation. The top panel illustrates the case of a good SED fit for star K1 ($\chi^2 \sim 18$ for the stellar, dust, and crowding bias fit). All SED points for the median model (combined star, dust, and bias model) are consistent with the observed SED within 4-σ. The derived physical parameters ($\log(T_{\rm eff})$, $\log(g)$, $A_{\rm V}$, initial mass M_{ini}, present day mass M_{act}, $\log(L)$; see Table 2.6) all appear reasonable given the star's location on the observed CMDs. Overall, they indicate that K1 is a late type O dwarf. We compare the SED and spectroscopically determined parameters in §2.6.3.

The middle panel of Fig. 2.5 illustrates a decent SED fit using star B10 ($\chi^2 \sim 72$). The residuals show that the median model SED is within $\sim$ 4-σ for 5 bands and $\sim$ 12-σ of the observed SED for one NIR band. Like the good χ^2 for K1, the stellar parameters for B10 are in reasonable agreement with its position on the CMD and a B0.5 dwarf. The star, however, appears to have quite high extinction ($A_{\rm V}$= 0.49), which is puzzling. We compare the SED and spectroscopically determined parameters in §2.6.3.

The bottom panel of Fig. 2.5 displays an example of a poor SED fit ($\chi^2 \sim 1259$) for star K6. In general, the median model values range in agreement from $\sim$ 5-σ for the two UV SED points to $\sim$ 15-σ for the F475W SED point. K5 falls into the category of stars that show an unusual SED, bright in the UV and red-optical, possibly due to the presence of a disk (See §2.6.3.3). Hence, it is not surprising that a single star model cannot be well fit to the SED.

Having illustrated our SED fitting with a few examples, we now consider general trends in the SED fits of luminous stars in Leo A. Fig. 2.6 shows observed CMDs in Leo A color-coded by the results of our photometric SED fitting for select stellar parameters ($\log(T_{\rm eff})$, $\log(g)$, M_{ini}, $A_{\rm V}$) along with the χ^2 value of the fit. The values assigned to these points reflect the median of the posterior distributions reported by the BEAST.

In general, as expected, the temperature decreases for redder CMD colors (second row

of Fig. 2.6). This is particularly evident in the UV-optical CMDs, where the hottest stars are located at the blue edge of the MS. We find that $\log(T_{\rm eff})$ only weakly depends on χ^2; poor fits seem to have a qualitatively reasonable correspondence between UV-optical color and $\log(T_{\rm eff})$(i.e., the redder the stars, the cooler the stars).

However, the situation changes slightly when considering optical-only colors. Here, while the majority still follow the expected trend, we find several outliers. Namely, several decently fit stars that appear on the MS in the UV-optical CMDs and have hot SED-based values of $\log(T_{\rm eff})$ appear to be cooler stars (i.e., BHeB region stars) in the optical only CMD. In the NIR CMD we see, similarly to the optical-only CMD, that the outliers are primarily the same stars that are displaying odd temperature to color combinations.

For a subset of these color outliers, we have spectra that we use to cross-check the reasonability of the photometrically determined parameters. In many cases, these color outliers appear to have emission features that suggest they are not nebular in origin and instead may indicate these are Be stars. We compare spectroscopic and photometric parameters for this subset in §2.6.3 and discuss the candidate Be stars in §2.7.3. Similar to $\log(T_{\rm eff})$, trends in $\log(g)$ (third row of Fig. 2.6) are generally consistent with expectations. The bluest stars should have the highest values of $\log(g)$, which is what we find. For redder stars, we expect and observe a decrease in $\log(g)$. We find that several of the stars causing discrepancies in $\log(T_{\rm eff})$ in the optical-only CMD show questionable values for $\log(g)$ as well. In the UV CMD, we observe the same outliers as in the optical CMD. In the NIR CMD, we similarly observe that the outliers in $\log(T_{\rm eff})$ are outliers in $\log(g)$.

We observe a broad trend between M_{ini} and $\log(g)$, expected from stellar models, with a few exceptions. The most massive stars are generally the brightest and hottest, while fainter stars are less massive. Stars with poor fits in $\log(g)$ are exceptions. Their values of M_{ini} are higher than one expects from their location on the panchromatic CMDs. Stars in the BHeB region of the optical CMD have $M_{ini} \lesssim 13 M_{\odot}$, but are all poor fits, suggesting we should use caution in taking their masses at face value.

Several studies of Leo A find it has very little dust (e.g., van Zee et al. 2006; Ruiz-Escobedo et al. 2018). This is reflected in the `BEAST` fitting as well. The MS stars all show little to no dust ($A_{\rm V} \lesssim 0.08$), though the BHeB sequence shows higher $A_{\rm V}$ values. This difference can potentially be explained by elevated dust production in supergiants (e.g., Waters 2010; de Wit et al. 2014), but we note that several of the high $A_{\rm V}$ stars also have poor fits, as is especially visible in the NIR CMD. Several of the previously mentioned outliers (i.e., the stars with peculiar colors) may have higher extinction, since the `BEAST` is trying to fit the excess IR emission created by the disk as we discuss in §2.6.3. Another highly probable explanation for the poor fits of stars appearing on the BHeB sequence in the optical CMD with unphysically high dust is the lack of calibration of stellar models for BHeB stars at the extreme low metallicity (e.g., McQuinn et al. 2012).

2.6.2 Radial Velocities from Spectroscopy

We determined the radial velocity (V_R) of the co-added spectra for each star using two methods. First, we model the full spectrum of each star using `The Payne`, for which V_R is a free parameter as described §2.5. Second, we measure the Doppler displacement of specific spectral lines using a Gaussian-fitting method to obtain the radial velocity. The latter method is more commonly used in the literature (e.g., Sana et al. 2013; Camacho et al. 2016; Evans et al. 2019) and we use it as a check on the full spectral fitting approach. We follow the cited literature studies and fit Gaussian line profiles to a collection of Balmer absorption lines (Hα, Hβ, Hγ, Hδ) and He absorption lines (He I 4387, He I 4713, and He II 4686) that have been identified as only mildly impacted by winds in the temperature regime. We exclude any lines that show strong emission. If the emission is small relative to the absorption feature, we mask out pixels with an emission component. Hα is only measured for stars in the Binospec sample, since it is not in the wavelength range of the Keck spectra. We report the radial velocity of each star as the error-weighted mean of the velocities measured for each line. We apply heliocentric corrections of $v_{helio} = -5.08$ kms^{-1} to our Keck measurements and $v_{helio} = -6.49$ kms^{-1} to our Binospec measurements.

We find that all stars agree within 1-σ between the two methods (see Table 2.4). This confirms that full spectral fitting can provide accurate V_R measurements for SNRs as low as ~10 (lowest SNR in sample). V_R measurements may be accurately measured at lower SNRs as well, but will be investigated in future work. We further find that the measurements yielded by the full spectral fitting are more precise ($\sigma_{Gauss} \lesssim 32$ kms^{-1}, $\sigma_{Payne} \lesssim 11$ kms^{-1}). For the remainder of the analysis, we use the V_R measurements derived from the full spectral fitting and reported in Table 2.4.

Fig. 2.7 shows the distribution of measured radial velocities with select literature measurements overplotted for comparison. For our 8 Keck stars, we find a mean radial velocity of $V_R = 23.7 \pm 16.3$ kms^{-1}. For our 10 Binospec stars, we find a mean radial velocity of $V_R = 29.4 \pm 16.2$ kms^{-1}. They are consistent with each other and agree well with radial velocities of supergiants in Leo A ($V_R = 22.9 \pm 10.2$ kms^{-1}; Brown et al. 2007) and of the old red giant branch stars ($V_R = 26.2 \pm 9.0$ kms^{-1}; Kirby et al. 2017). Our combined Keck and Binospec samples for non-overlapping stars yields a mean $V_R = 26.9 \pm 12.3$ kms^{-1}. The stellar measurements are inline with previous gas velocity studies (Young & Lo 1996; Hunter et al. 2012).

Three of the four stars observed with both telescopes yield consistent velocities. The Keck spectrum of the fourth star (K2) yields $V_R = -13 \pm 2$ kms^{-1}, whereas the Binospec spectrum yields $V_R = 16 \pm 4$ kms^{-1}. There is no obvious issue with the data that would cause this level of discrepancy. One possibility is that this is a binary star, and that the different velocities are the result of observing the system at different points in the orbital phase. We are in the process of obtaining time resolved spectroscopy to better quantify the degree of binarity in the massive stars of Leo A.

2.6.3 Stellar Parameters from Spectroscopic Analysis

We present discussion of our spectroscopic sample. This section includes an example of each stellar type found in the study, a detailed individual discussion of all stars can be found in the Appendix 2.10.2. We determine these stellar parameters for the stars using full spectral fitting via `The Payne` and via photometric SED fitting with `the BEAST`. We also use EWs to provide spectral types using conventional stellar classification schemes in the literature. We discuss agreement between the methods. The spectrum of each star is shown in Fig. 2.8, and Table 2.3 provides a full list of lines we detect and measure in each spectrum. For guiding the discussion, we group the stars into broad categories (e.g., O-stars, B(e)-stars) and, for brevity, focus only on the most salient features in the spectra and photometry.

2.6.3.1 O-Type Stars

We classify 4 stars as O-type star in our sample (K1/B1, K2/B2, K7/B6, B13) based on their EW measurements. Overall the parameters derived from spectroscopy and photometry yield consistent values with the EW classification. We present a detailed example of the analysis of K1 and highlight interesting features of the other stars.

K1/B1: K1/B1 is the brightest star in our Leo A sample ($F475W_{VEGA}$ = 20.09 and $F336W_{VEGA}$ = 18.36). Its locations in the optical and UV CMDs are typical of an O-star. Its spectrum is shown in Fig. 2.8. We list its EW measurements in Table 2.3 and comment only on a subset of those features.

The spectrum shows the characteristics of a typical late-type O-star: strong absorption of He I and He II. Most of the Balmer series is in absorption, though Hβ appears to exhibit weak emission, likely due to K1's location in an H II region (See Fig. 2.3).

We first estimate the stellar type of K1 using the relevant EWs, which are listed in Table 2.3. We use both Galactic (Conti & Alschuler 1971, Sota et al. 2011, Martins 2018) and sub-Solar metallicity classification schemes (Castro et al. 2008), prioritizing the latter whenever possible. From the EW(He I λ4471)/EW(He II λ4542) ratio, we find that K1 is of spectral type O9, or perhaps later, in the traditional spectral classification scheme of Conti & Alschuler (1971). We also consider EW ratios of the (He I λ4471/He II λ4542) and (He I λ4388/He II λ4542) in the classification scheme of Martins (2018). They indicate a star of type O8.5-9. The He II λ4542 to He I λ4388 comparison yields a spectral type O9.5 in the Sota et al. (2011) classification scheme. Lastly, using Castro et al. (2008) classification scheme we find the star to be an O9. K1 could be either a dwarf or a subgiant star based on the comparison with the Martins (2018) classification scheme using (log(EW(He II λ4686))+log(EW(He I λ4388))), since its value falls within both ranges. However, using Castro et al. (2008), we determine the star is likely a dwarf. Our best estimate from spectroscopy is that K1 is an O9V star. We employ the same EW classification

scheme for our other O stars.

We fit the full Keck spectrum of K1 using `The Payne`. The median parameters for the spectral fitting are listed in Table 2.4. For K1, we find $\log(T_{\rm eff})= 4.49 \pm 0.01$ dex and $\log(g)= 3.69 \pm 0.01$ dex, which, like the EW ratios, indicates that K1 is a late-type O star. Using equations 1-3, we derive $M_{spec} = 17 \pm 3 M_{\odot}$ and $M_0 = 19 \pm 1 M_{\odot}$, and $\log(L/L_{\odot}) = 4.90 \pm 0.09$ dex. All of these values agree with the classifications derived from the EW measurements and location in the CMD. The photometric analysis yields $\log(T_{\rm eff})= 4.52 \pm 0.02$ dex and $\log(g)= 3.92 \pm 0.05$ dex. While $\log(T_{\rm eff})$ is consistent, $\log(g)$ shows a 0.23 dex difference. This difference may be explainable by three different reasons: (1) keeping the instrument resolution, micro- and macroturbulence constant might impact $\log(g)$ since they all affect the line widths; (2) subtraction of the nebular emission during data reduction; if the Balmer lines are slightly over/under-subtracted, then the line width and $\log(g)$ can be affected; and (3) assumptions within stellar atmosphere models give rise to systematic differences (~0.2 dex; Markova et al. 2018, Dufton et al. 2019). Computing our own systematic uncertainties requires delving into stellar atmosphere physics for very metal-poor stars, and is beyond the scope of this paper. We find that M_0 and M_{ini} are consistent with each other as seen in Tables 2.4 and 2.6.

We show the spectrum of K1 with the models generated from the two different methods in Fig. 2.9; we overplot synthetic spectra of K1 from our spectroscopy (pink) and photometric (blue) parameters. Both synthetic spectra provide a similar match to the He I/He II feature, as expected since our $\log(T_{\rm eff})$ is in agreement. We find the difference in $\log(g)$ is best displayed in the Hβ feature, primarily in the wings. The Balmer lines are well fit by the models, which we highlight by showing a zoom in on Hβ. However, while the model appears to match the He I/He II ratio, it struggles with the recovering the depth of the He I lines, in that the model is shallow. This is clear from He I λ4471. A lower temperature may improve the He I fit, but this would make the fit to He II worse. This difference could be due to the fixed resolution of the spectra or, alternatively, could be due to the H to He ratio that is expected to change at lower metallicity (e.g., Martins & Palacios 2021), but is currently fixed at the Solar value. Despite some modest disagreements, the model spectrum appears to provide a good overall characterization of K1. Our formal fitting consistently suggests K1 is a late-type O dwarf.

K2/B2: K2/B2 is a O9.7 V type star. We find a small mismatch in $\log(g)$ between spectroscopy and photometry. The emission line contamination of the Balmer lines may affect our spectroscopic determination of $\log(g)$. The discrepancy in $\log(g)$ is likely why M_{spec} is in disagreement with M_{act}. We further note that $M_0 < M_{spec}$, which is physically impossible.

We find a > 3-σ discrepancy between the RV measured for K2/B2 with Keck ($-13 \pm$

2 kms^{-1}) and Binospec (16 ± 4 kms^{-1}). We do not observe this effect in any other star in our sample. We suggest that K2 may be a binary star system. This is potentially further supported by the odd present day to initial mass relation(See §2.17). Currently it is not possible to verify the binary status with our limited time information. We are in the process of acquiring time series spectra with Keck to further investigate this possibility.
K7/B6: K7/B6 is a O9.5 V type star and yields consistent parameters from photometry and spectroscopy. Although K7 is classified as an O-type star, it is not near any of the known H II regions in Leo A. We discuss the possibility of it being a runaway star in §2.7.2.
B13: B13 yields a SNR of ∼ 12 making the classification challenging. The star is likely a O9.7 V type star, but could be consistent with a B0 V type star as well. It's Hα feature is fully in emission, and the remaining Balmer lines are in absorption with some light emission within the feature. Given that the star shows narrow emission features, poor spectroscopic fitting, and extended emission in the 2D spectra, we postulate that the star must have some nebular contamination.

2.6.3.2 B-Type Stars

We classify 8 stars as B-type star in our sample (K3/B3, B4, B7, B9, B10, B11, B12, B14) based on their EW measurements. Overall the parameters derived from spectroscopy and photometry yield consistent values with the EW classification. We present a detailed example of the analysis of K3/B3 and highlight interesting features of the other stars.
K3/B3: K3 is the 3rd brightest star in our sample ($F336W_{VEGA}$ = 18.87 and $F475W_{VEGA}$ = 20.4). Its locations in the optical and UV CMDs are typical of a MS star. Its spectrum is shown in Figure 2.8. We list its EW measurements in Table 2.3 and comment only on a subset of those features.

The spectrum broadly suggests the star is a B-type star: He I, Mg II, Si II, and Si III are in absorption. The Balmer series shows no Hα, while Hβ is primarily in absorption. For Hβ, there is emission in the red wing, which could either be consistent with the wavelength of two O II features at λ4865Å and λ4872Å and the forbidden [Fe IV] emission at λ4868Å, or the kinematic components of some Hβ emission. The remaining Balmer lines appear to have little to no emission in their red wings. The Hβ in the 2D spectra shows that the emission is spatially extended with a slope towards redder wavelengths, as opposed to perpendicular to the trace. The features appear to spatially extend to ∼ 5.5 pc. We find Fe II at λ6540Å in emission to the blue side of where Hα should be. We further find Fe II in emission at λ8617Å and [S IV] at λ8575Å. Based on the EW, we use the Castro et al. (2008) and Evans et al. (2015) classification schemes and find that K3 is most likely a B1.5 V star.

From full spectral fitting, we find K3 has median values of log($T_{\rm eff}$)= 4.42±0.01 dex and log(g)= 3.75 ± 0.05 dex, which, like the EW ratios, indicate that K3 is a early-type B star. Using equations 1-3, we derive $M_{spec} = 20 \pm 5 M_{\odot}$, $M_0 = 13 \pm 1 M_{\odot}$, and $\log(L/L_{\odot}) = 4.53 \pm$

0.12 dex. These are all in line with the classification derived from the EW measurements and location in the CMD. The spectroscopic parameters are consistent with the results from SED fitting, which yield $\log(T_{\rm eff})= 4.41 \pm 0.01$ dex, $\log(g)= 3.66 \pm 0.01$ dex and $M_{ini} = 12.9 \pm 0.17 M_{\odot}$.

We postulate that the majority of the emission is due to nebula southwest of the star, which appears to fall into our slit based on the HST imaging. The nebula can explain the emission features near Hβ as well as Fe II and other emission at redder wavelengths. The 2D spectra further supports this scenario, since the emission primarily extends to only one side of the stellar trace. Furthermore, the nebula shape suggest that we may be observing a bow shock nebula (e.g., Gull & Sofia 1979; van Buren & McCray 1988; Meyer et al. 2014). This is supported by the following: K3 is a runaway candidate (See §2.7.2), the nebula is the most visible in the F110W and F160W imaging, and the absence of Hα. To capture the intrinsic characteristics of the nebula, its formation, and the star-nebula interaction, follow-up observations are necessary, ideally with an IFU instrument.

B4: B4 is a B0 V type star and yields consistent parameters from photometry and spectroscopy. The presence of emission lines coupled with the star not being near an H II region suggest the emission is not gaseous in origin. Instead, this may indicate the presence of a circumstellar nebula or of stellar winds. Given that Hα shows only weak emission and He II 4686 in absorption, the stellar wind scenario seems unlikely (e.g., Lamers & Cassinelli 1999). Alternatively, the star could have a companion that provides the emission components to the spectra.

B7:B7 is a P-Cyg B1 V or a Be1 V type star. The star resembles the traditional P Cyg star (Rivet et al. 2020, and references therein). We do not observe metal lines with P-Cygni profiles. This is not surprising given the Leo A's low metallicity. However, the lines are narrower than what would be expected from stellar wind emission lines. Alternatively, the star could be a Be star, whose disk is oriented so that we coincidentally capture the emission resembling the P-Cygni profile. This could also explain the lower $v \sin i$ value, since Be stars typically have higher $v \sin i$ values (e.g., Rivinius et al. 2013; Iqbal & Keller 2013; Arcos et al. 2018). Potentially this could also explain why, in comparison to the other Be stars in this sample (See §2.6.3.3), the star does not show signs of potential NIR excess in the optical CMD. Extended spectroscopic coverage into the UV could help shed light on wind parameters or photometric coverage into the NIR could shed light on a potential disk. We discuss a more clear example in §2.6.3.3.

B9:B9 is a B1.5 V type star. Hα appears in emission, and all other Balmer lines are in absorption. B9 yields consistent parameters from photometry and spectroscopy.

B10:B10 is a B0.5/Be0.5 V type star. The photometric parameters and spectroscopic parameters are consistent. Both methods yield decent to high χ^2 values (See Tables 2.4 and 2.6) suggesting that potentially a circumstellar disk or nebulae could affect the star. The stellar emission and the high $v \sin i$ value would support a Be star scenario. We discuss

more clear examples in §2.6.3.3.
B11:B11 is a B2 V type star. Most Balmer lines are in absorption with variable amounts of emission. Since the B11 spectrum shows a SNR of <10, we cannot reliably recover the spectroscopic parameters. Given the SNR is ∼10, we refrain from making any further speculations as to the origin of the emission.
B12:B12 is a B1.5 V type star. The star shows signs of stellar emission, but the low SNR (∼12) prohibits detailed analysis. We do note that we only have 4 bands in the photometry. B12 is one of the few stars that we do not find consistency between the two methods, although both χ^2 values would suggest they are good or decent fits.
B14:B14 is a B3 V type star. Hα is in absorption, while the other Balmer lines show potential emission in their wings. Due to the low SNR (∼ 15) of the spectrum, the weak emission in the Balmer lines could be artifacts of the data. $\log(T_{\rm eff})$ is consistent between the two methods, while $\log(g)$ shows a discrepancy likely due to the affected Balmer lines.

2.6.3.3 Classical Be stars

Our sample contains several objects that appear to be classical Be stars: rapidly rotating, main-sequence B stars with emission lines that originate in a circumstellar accretion disk (Rivinius et al. 2013). The key spectroscopic feature is emission in the Balmer lines (usually strongest in Hα), while the key photometric feature is an IR excess due to the extended circumstellar disk. We provide the analysis of the clearest example (K6) in this section. In total we find 6 stars (K4, K5, K6, K8, B5, B8) for which we can identify both key features. They all show strong Balmer emission lines, and their particular SEDs cannot be reproduced by a "normal" single star model.
K6: K6 ($F475W_{VEGA}$ = 20.84 and $F336W_{VEGA}$ = 19.35) is located on the BHeB sequence in the optical CMD, but appears on the MS in the UV-optical CMD. Its spectrum is shown in Figure 2.8. We list its EW measurements in Table 2.3 and comment only on a subset of those features. Stars K4, K5, K8, and B5 share similar CMD characteristics. The Keck spectrum of K6 is shown in Fig. 2.8.

The spectral features suggest K6 is a fast rotating early B-type star. K6 shows He I in absorption and emission, and Mg II, S II, and Si IV in absorption. He II appears to potentially be a mix of emission with absorption. We find strong emission in Hβ. We find an emission feature within an absorption feature for Hγ and Hδ. However, Hϵ appears to be mostly in absorption. All of the features are very shallow, which is typical of fast rotators. The signs of strong rotation and emission means that detection of equivalent widths might be harder to recover for certain features (e.g., Si, Mg, He II), since they become so shallow that they are indistinguishable from the noise. Based on Lennon (1997); Castro et al. (2008); Evans et al. (2015), we classify it as a Be2 V star.

The strong emission appears to be associated with the star, as opposed to being gaseous in origin. K6 is not near the known H II regions (See Fig. 2.3). Moreover, the lack of typical

nebular emission lines further suggests it is not from an H II region. Leščinskaitė et al. (2022) identified K6 as a strong Hα emitter based on the Subaru/Suprime-Cam narrowband imaging, postulating that it might be an emission star.

Due to the strong emission in the Balmer lines, the likely presence of a disk and the high χ^2 in the photometry, we adopt here the alternative fitting methods introduced in §2.5.3.

Using this adapted spectroscopic method, we determine that the star has $\log(T_{\rm eff})$= 4.43 ± 0.02 dex and a $v \sin i$= 220 ± 10 kms^{-1}. This is in line with an early type Be star (Rivinius et al. 2013). The high $v \sin i$ is a key indicator that the star has to be a rotating MS star as opposed to a BHeB star. An evolved star would break apart at such high $v \sin i$. As previously mentioned, the star is amongst the bluest in the UV CMD but amongst the reddest in the optical CMD.

Using our composite photometry fitting (See §2.5.3), we determine that $\log(T_{\rm eff})_{star}$ = $4.48\pm^{0.04}_{0.03}$ dex, which is in line with our spectroscopic measurement. The disk $\log(T_{\rm eff})_{disk}$ = 3.73 ± 0.03 dex. This serves primarily as an estimate, since we use the model of a cool star to mimic the disk spectra.

Figs. 2.10 and 2.11 show the median photometric model along with samples from the posterior. In Fig. 2.10 we can clearly see that the UV photometry is fitted well by a rotating MS B-type star. In the NIR, the fit is not as good. However, since we are not actually fitting a disk model, this could explain the discrepancy. Overall the fit yields a good χ^2 value (See Table 2.5).

We considered other explanations for the unusual photometric SED. The first possibility could be dust giving rise to NIR excess. However, given how blue the star is in the UV CMD, we believe dust is unlikely. A second possibility is an unresolved red stellar companion. We tried fitting two stellar models simultaneously. However, one of the stars always yields nonphysical parameters (i.e., a temperature and radius combination that is not expected for any star). Given that there is no evidence for a red star in the spectra and we are not able to fit a physically reasonable star to the photometric data, this scenario is unlikely.

We note here that this does not mean that the star is necessarily a single star, simply that there is no evidence for a secondary polluting our current data.

Based on the present evidence, we suggest this is a Be star. This provides the first spectroscopic confirmation for Be stars in Leo A.

K4: K4 is a Be1 V type star. Due to the strong emission in the Balmer lines and the high χ^2 (> 300) in the BEAST fitting, we postulate it is a star surrounded by a disk. Another possibility is an unresolved red stellar companion. For this particular star, we cannot completely exclude this possibility, since we do not have the NIR photometry to determine the nature of the excess. However, given that for other Be stars in our sample we find the same characteristics as for K4, we postulate that extinction occurring in the photometry is due to

a disk.
K5: K5 is a Be2 V type star. Similar to K4, we assume that the star is a Be star whose photometry is affected by extinction/reddening due to the disk, as opposed to extensive dust or a red companion.
B5: B5 is a Be3 V type star. The 2D spectra show extended emission, which suggest it is due to nebular emission from the nearby H II region. However, the Hα/ Hβ emission ratio suggests that the Hα emission cannot be purely gaseous. While our data cannot exclude a binary influencing the star (e.g., we need time series spectra), the spectroscopic features and SED fit are consistent with a circumstellar disk.
K8: K8 is a Be2 V type star. Similar to K6, the star is a Be star whose photometry is affected by extinction/reddening due to the disk as opposed to extensive dust or a red companion.
B8: B8 is a shell Be3 V type star. Hα and Hβ are in emission and both show a double peaked line profile. The distinct Balmer profiles suggest that the star is most likely a shell star (i.e., a Be star viewed edge-on). Despite the low $v \sin i$, the strong emission and spectral shape supports the classification of the star as a shell star.

2.6.4 The Utility of Panchromatic Photometry for Massive Star Studies

We have shown the first extensive and quantitative comparison between stellar parameters for massive stars derived from optical spectroscopy and UV-optical-NIR broad-band photometry at low metallicity. Fig. 2.12 shows the comparison between photometric and spectroscopic $\log(T_{\rm eff})$, $\log(g)$, and $\log(L/L_\odot)$ for stars that have $\chi^2 < 100$ in both methods. We find that a median absolute deviation (MAD) between the two $\log(T_{\rm eff})$ of < 0.01 dex and a median difference of -0.03 dex (1600 K). The 16th and 84th percentiles of the difference span 0.05 dex (i.e., ± 0.025 dex around the median), indicating that the observed differences are slightly smaller than scatter in the data. For $\log(g)$, the MAD is 0.18 dex and the median difference is 0.06 ± 0.20 dex. Lastly, for $\log(L/L_\odot)$, we find a MAD of 0.05 dex and a median difference of -0.03 ± 0.06 dex. The clear outlier in each panel is B12. B12 is among the lowest SNR stars in our spectroscopic sample (SNR $\sim$ 12) and has modest emission, though not as strong as other stars, which could explain the larger differences between the photometric and spectroscopic parameters. In general, these findings show that for "normal" O/B type MS stars in our sample (i.e., those with no or little emission), photometric and spectroscopic parameters are consistent with each other.

This comparison clearly shows that panchromatic photometric studies can yield reliable stellar parameters at least for "normal" single stars, which is encouraging especially when spectra are not available. For example, most of the LUVIT sample consist of galaxies too far away for acquiring optical spectra with the current generation of telescopes. Poor

Table 2.3: List of equivalent widths used in analysis to determine the spectral type of each star.

Star	He I 4121	He I 4144	He I 4388	He I 4471	He I 4713	He I+ II 4026	He II 4200	He II 4542	He II 4686	Mg II 4481	Si II 4128	Si III 4553	Si IV 4089
	Å	Å	Å	Å	Å	Å	Å	Å	Å	Å	Å	Å	Å
(1)	(2)	(3)	(4)	(5)	(6)	(7)	(8)	(9)	(10)	(11)	(12)	(13)	(14)
K1	0.16 ± 0.10	0.13 ± 0.10	0.43 ± 0.10	1.08 ± 0.10	0.61 ± 0.10	0.56 ± 0.10	0.18 ± 0.20	0.44 ± 0.20	0.71 ± 0.10	...	...	0.15 ± 0.10	0.15 ± 0.10
K2	0.20 ± 0.10	0.37 ± 0.05	0.81 ± 0.10	0.81 ± 0.10	0.50 ± 0.04	0.65 ± 0.10	...	≤0.30	0.41 ± 0.15	...	...	0.21 ± 0.15	≤0.30
K3	0.40 ± 0.10	0.54 ± 0.10	0.76 ± 0.10	1.09 ± 0.20	0.45 ± 0.10	0.99 ± 0.05	...	...	≤0 0.17	0.40 ± 0.15	0.22 ± 0.10	≤ 0.32	≤ 0.21
K4	0.37 ± 0.20	0.43 ± 0.20	0.58 ± 0.20	0.73 ± 0.20	...	0.64 ± 0.20	...	...	0.17 ± 0.15	≤ 0.11	...	0.19 ± 0.10	≤ 0.12
K5	≤0.13*	≤ 0.54*	0.62 ± 0.25	0.68* ± 0.25	...	0.46 ± 0.20	...	...	...	≤ 0.21	...	≤ 0.15	...
K6	0.27* ± 0.15	0.42 ± 0.20	0.53 ± 0.20	0.87 ± 0.20	...	0.84 ± 0.20	...	...	≤ 0.85*	≤ 0.27*	≤ 0.10	...	0.24 ± 0.15
K7	0.42 ± 0.10	0.66 ± 0.10	0.68 ± 0.10	1.30 ± 0.20	0.60 ± 0.20	1.10 ± 0.20	0.21 ± 0.15	0.32 ± 0.15	0.34 ± 0.15	0.48 ± 0.10	...	...	≤ 0.15
K8	...	0.62 ± 0.25	0.75 ± 0.25	1.21 ± 0.15	...	0.93 ± 0.30	...	...	...	≤ 0.28	...	≤ 0.30	≤ 0.16
B4	0.38 ± 0.15	0.71 ± 0.15	0.73 ± 0.15	0.88 ± 0.10	0.24 ± 0.15	0.88 ± 0.20	...	...	0.28 ± 0.15	...	0.17 ± 0.10	0.24 ± 0.10	0.28 ± 0.10
B5	0.48 ± 0.25	0.49 ± 0.20	0.39 ± 0.30	0.92 ± 0.20	0.48 ± 0.15	1.24 ± 0.30	...	...	...	0.30 ± 0.20	0.35 ± 0.15	...	≤ 0.30
B7	0.75 ± 0.15	0.90* ± 0.20	0.68* ± 0.20	0.59 ± 0.15	...	0.50 ± 0.10	...	≤ 0.17	...	...	...	0.32 ± 0.10	≤ 0.16
B8	...	≤ 0.33	≤ 0.40	0.72 ± 0.20	0.56 ± 0.20	≤0.98	...	...	...	≤ 0.28	...	...	≤0.22
B9	0.83 ± 0.20	0.82 ± 0.20	0.78 ± 0.20	1.10 ± 0.20	1.02 ± 0.20	1.80 ± 0.30	...	...	...	0.23 ± 0.10	≥ –0.48	0.38 ± 0.10	≤ 0.26
B10	0.55 ± 0.15	0.80 ± 0.25	0.77 ± 0.20	1.09 ± 0.25	...	0.80 ± 0.25	...	...	...	...	...	≤0.55	0.34 ± 0.10
B11	1.26± 0.30	1.04± 0.30	1.16 ± 0.30	2.46 ± 0.40	...	2.17 ± 0.25	...	...	...	...	0.87 ± 0.40	≤ 1.61	0.40 ± 0.20
B12	0.72 ± 0.20	0.79 ± 0.20	1.38 ± 0.30	1.20 ± 0.30	...	2.20 ± 0.25	...	...	...	...	...	≤ 0.77	≤ 0.32
B13	1.04 ± 0.30	0.81 ± 0.25	0.79 ± 0.20	2.15 ± 0.35	0.83 ± 0.15	1.94 ± 0.40	...	1.20 ± 0.30	1.46 ± 0.40	...	...	0.53 ± 0.20	0.63 ± 0.20
B14	0.50 ± 0.30	0.37 ± 0.10	0.81* ± 0.20	0.65 ± 0.30	...	1.34 ± 0.30	...	...	...	0.61 ± 0.20	...	0.31 ± 0.10	...

Note. — The * denotes lines that have emission components that had to be masked out to determine the EW.

Table 2.4: Spectroscopic parameters determined using The Payne. The columns are: (1) star name; (2) spectroscopic mass; (3) initial mass; (4) evolutionary mass; (5) effective temperature; (6) surface gravity; (7) luminosity; (8) rotational velocity; (9) heliocentric corrected radial velocity from full spectral fitting; (10) heliocentric corrected radial velocity measurements using Gaussian profile fitting. Columns (4), (5), (7), and (8) are the stellar parameters that directly resulted from the full spectral fitting with The Payne. Columns (2) and (6) are derived using the previous stellar parameters in addition to the SED. Column (3) lists the evolutionary mass determined by eye.

Star	M_{spec}	M_0	M_{evo}	$\log(T_{eff})$	$\log(g)$	$\log(L/L_\odot)$	v_{sini}	V_R	V_{RGauss}	χ^2	Spectral Type
	$M_\odot$	$M_\odot$	$M_\odot$				kms^{-1}	kms^{-1}	kms^{-1}		
(1)	(2)	(3)	(4)	(5)	(6)	(7)	(8)	(9)	(10)	(11)	(12)
K1	17 ± 3	19 ± 1	19 ± 1	4.49 ± 0.01	3.69 ± 0.01	4.90 ± 0.09	< 80	21 ± 2	18 ± 8	15	O9V
K2	27 ± 6	17 ± 1	17 ± 1	4.50 ± 0.01	4.10 ± 0.02	4.72 ± 0.09	95 ± 20	−13 ± 2	−25 ± 13	21	O9.7 V
K3	20 ± 5	13 ± 1	13 ± 1	4.42 ± 0.01	3.75 ± 0.05	4.53 ± 0.12	< 80	37 ± 2	27 ± 21	17	B1.5 V
K7	13 ± 3	13 ± 1	13 ± 1	4.48 ± 0.01	4.04 ± 0.02	4.38 ± 0.08	103 ± 20	24 ± 3	19 ± 21	18	O9.5 V
B4	15 ± 2	15 ± 1	15 ± 1	4.46 ± 0.01	3.75 ± 0.04	4.65 ± 0.04	< 80	29 ± 3	33± 8	67	B0V
B9	15 ± 5	12 ± 1	12 ± 1	4.45 ± 0.02	4.18 ± 0.06	4.25 ± 0.04	115 ± 20	20 ± 8	5 ± 32	47	B1.5 V
B10	11 ± 6	11 ± 1	11 ± 1	4.43 ± 0.02	3.92 ± 0.11	4.24 ± 0.04	141 ± 25	31 ± 11	31 ± 24	100	B0.5 V / Be0.5 V
B12	8 ± 4	11 ± 1	11 ± 1	4.44 ± 0.05	4.00 ± 0.10	4.07 ± 0.05	< 80	30 ± 8	27 ± 28	48	B1.5V
B13	19 ± 4	12 ± 1	12 ± 1	4.50 ± 0.02	4.64 ± 0.06	4.07 ± 0.08	< 80	24 ± 8	18 ± 29	141	O9.7 V
B14	24 ± 5	8 ± 1	8 ± 1	4.39 ± 0.02	4.41 ± 0.08	3.87 ± 0.08	80 ± 15	20 ± 5	32 ± 19	78	B3 V

Table 2.5: Stellar parameters determined using the adapted methods. The table list the results from the adapted spectroscopic and photometric analysis. The columns are: (1) name; (2) spectroscopic temperature of the star; (3) photometric temperature of the star; (4) photometric radius of the star; (5) rotational velocity; (6) reddening value from the SED fitting; (7) photometric temperature of the disk; (8) photometric radius of the disk; (9) present-day mass picked for the combined SED fitting; (10) heliocentric corrected radial velocity from full spectral fitting; (11) heliocentric corrected radial velocity measurements using gaussian fitting; (12) reduced χ^2 value from the composite photometric fitting. Columns (2), (5), (10) and (11) are the stellar parameters derived from the adapted spectroscopic analysis. Columns (3), (4), (6), (7), (8), and (12) are the stellar parameters derived from the composite photometric analysis.

Star	$\log(T_{eff,spec})$	$\log(T_{eff,SED*})$	R_{SED*}	v_{sini}	E(B-V)	$\log(T_{eff,DISK})$	R_{DISK}	M_{model}	$V_{Rheliocorr}$	V_{RGauss}	χ^2	Spectral Type
				kms^{-1}				$M_\odot$	kms^{-1}	kms^{-1}		
(1)	(2)	(3)	(4)	(5)	(6)	(7)	(8)	(9)	(10)	(11)	(12)	(13)
K4	4.45 ± 0.01	...	...	339 ± 10	...	...	...	10	29 ± 10	16 ± 16	...	Be1 V
K5	4.46 ± 0.02	...	...	370 ± 90	...	...	...	10	46 ± 11	31 ±25	...	Be2 V
B7	4.44 ± 0.02	...	...	125 ± 11	...	...	...	10	44 ± 6	36 ± 30	...	P-Cyg B1 V / Be1 V
K6	4.43 ± 0.02	$4.48 \pm^{0.04}_{0.03}$	$8.0 \pm^{0.6}_{0.6}$	220 ± 5	0.17 ± 0.02	$3.73 \pm^{0.03}_{0.03}$	$21.5 \pm^{1.2}_{1.0}$	10	18 ± 6	18 ± 18	3	Be2 V
K8	4.44 ± 0.03	$4.51 \pm^{0.04}_{0.06}$	$5.9 \pm^{0.5}_{0.5}$	290 ± 10	0.18 ± 0.04	$3.64 \pm^{0.04}_{0.04}$	$12.6 \pm^{1.9}_{1.7}$	10	28 ± 8	38 ± 17	19	Be2 V
B5	4.40 ± 0.01	$4.38 \pm^{0.06}_{0.08}$	$9.0 \pm^{0.8}_{1.1}$	165 ± 15	0.13 ± 0.03	3.74 ± 0.17	$12.0 \pm^{8.7}_{1.7}$	8	36 ± 10	22 ± 15	12	Be3 V
B8	4.42 ± 0.03	$4.37 \pm^{0.15}_{0.03}$	6.9 ±1.0	135 ± 80	0.12 ± 0.06	$3.74 \pm^{0.06}_{0.10}$	13.7 ±1.7	8	28 ± 4	23 ± 24	20	shell Be3 V

Table 2.6: Photometric parameters determined using the BEAST and the MIST models with v/v_{crit} = 0.4. The columns are: (1) star name; (2) initial mass; (3) actual mass; (4) temperature; (5) surface gravity; (6) luminosity; (7) extinction parameter; (8) stellar age in log-space; (9) χ^2 yielded by the BEAST; (10) number of *HST* bands used for the SED fitting (when the value is 4 we observed F275W, F336W, F475W and F814W, and when the value is 6, we additionally observed F110W and F160W); (11) spectral type derived from EW analysis. Columns (2), (7), and (8) list primary parameters, while columns (4), (5), and (6) list derived parameters.

Star	$M_{ini,Exp}$	$M_{act,Exp}$	$\log(T_{eff})$	$\log(g)$	$\log(L/L_\odot)$	A_v	log(Age)	χ^2	Nr. of filters	Spectral Type
	$M_\odot$	$M_\odot$	kK							
(1)	(2)	(3)	(4)	(5)	(6)	(7)	(8)	(9)	(10)	(11)
K1	20.1±1.29	19.99±1.19	4.53±0.02	3.92±0.05	4.88±0.05	0.05±0.01	6.9±0.08	11	6	O9V
K2	16.81±0.21	16.74±0.30	4.50±0.01	3.85±0.01	4.74±0.01	0.06±0.02	7.0±0.07	4	4	O9.7 V
K3	12.89±0.17	12.87±1.24	4.41±0.01	3.66±0.02	4.50±0.01	0.07±0.02	7.2±0.08	7	6	B1.5 V
K7	14.69±1.06	14.68±1.0	4.52±0.02	4.23±0.05	4.45±0.04	0.06±0.03	6.8±0.15	17	4	O9.5 V
B4	16.38±0.18	16.32±0.27	4.50±0.01	3.91±0.01	4.68±0.01	0.04±0.01	7.0±0.07	10	6	B0V
B9	10.87±6.13	9.96±7.5	4.49±0.05	4.12±0.68	4.39±0.14	0.42±0.08	7.0±0.85	83	6	B1.5 V
B10	12.2±1.21	12.19±1.24	4.47±0.03	4.02±0.07	4.35±0.1	0.49±0.04	7.1±0.11	73	6	B0.5 V / Be0.5 V
B11	6.26±0.69	6.26±0.64	4.27±0.04	3.81±0.06	3.45±0.13	0.07±0.01	7.8±0.13	2	6	B2 V
B12	6.61±1.21	6.61±1.14	4.34±0.05	3.86±0.08	3.73±0.19	0.05±0.03	7.6±0.16	3	4	B1.5V
B13	12.45±0.5	12.45±0.42	4.50±0.01	4.37±0.03	4.11±0.02	0.06±0.02	6.5±0.22	3	4	O9.7 V
B14	9.22±0.99	9.22±0.91	4.42±0.02	4.12±0.06	3.92±0.08	0.06±0.02	7.3±0.16	15	6	B3 V

photometric fits with `the BEAST` are often due to stellar activity (e.g., binarity, disks) that are not captured by single star models. We find that with full UV through NIR broad-band SEDs it is possible to identify such candidates by their poor χ^2 values, providing an invaluable way to identify unusual objects for future follow up (e.g., with *JWST*, ELT, GMT, and TMT). We note that the BEAST is in development of including more models.

2.7 Discussion

2.7.1 Stars in H II regions

Leo A hosts several known H II regions (see Fig. 1 of van Zee et al. 2006), two of which are included in the *HST* and the spectroscopic data set. Previous analysis of these H II region ionized gas abundance patterns have placed indirect constraints on the properties of the ionization fields, and in turn, the underlying types of ionizing sources (e.g., the spectral type of the OB stars, Skillman et al. 1989; van Zee et al. 2006; Ruiz-Escobedo et al. 2018). There have been a few direct studies of the massive stars that power H II regions at such low metallicities (e.g., Garcia et al. 2014; Camacho et al. 2016; Evans et al. 2019; Telford et al. 2021). In most cases, these studies have found that a singular star is responsible for powering most of the H II region.

In this section, we discuss the results of our stellar spectroscopic and SED fitting in the context of literature nebular line analysis of the H II regions in Leo A.

Fig. 2.13 shows the two H II regions that are covered by our UV and optical *HST* data along with their corresponding optical CMDs. Stars located approximately within each H II region are color-coded by their age from our SED fitting, while the CMD of the entire Leo A field population is shown for reference in grey. For clarity of discussion, we label the two H II regions: Region A and Region B. We have 6 band coverage for Region B, and 4 band (2 UV and 2 optical) coverage for Region A.

2.7.1.1 Region A

Region A is the left H II region in Fig. 2.13. It is listed as Leo A +069˘018 in van Zee et al. (2006). Region A is a diffuse H II region with weak [OIII]λ5007, which suggests a low ionization scenario (van Zee et al. 2006). After correcting for extinction ($E(B-V) = 0.021$; Schlegel et al. 1998), they determine a B0 - O9.5 Zero-age MS (ZAMS) star to be the likely source of ionizing photons.

The brightest star in Region A is K2. From our spectra and photometry, we find that K2 is an O9.7V type star with a $\log(T_{\rm eff})= 4.50 \pm 0.01$ dex, which is very similar to what van Zee et al. (2006) suggest. Furthermore, K2 has an age of $\log(t) = 7.0 \pm 0.07$ (yr), $M_{ini} = 16.81 \pm 0.21 M_{\odot}$ and $A_{\rm V}= 0.06 \pm 0.02$. For K2, we are able to calculate the intrinsic

ionizing photon production rate using the BEAST (Choi et al. 2020). We derive a median rate of $10^{47.6\pm0.1}$ photons s^{-1}. Using the Hα value reported in van Zee et al. (2006), we compute the photoionization rate required to produce the Hα luminosity (Hummer & Storey 1987; Storey & Hummer 1995; Kennicutt 1998; Choi et al. 2020). We derive a rate of $10^{47\pm0.05}$ photons s^{-1}. This is consistent with the value derived for K2 from the BEAST. This suggests that K2 could be responsible for a majority of the ionization in the H II-region. Furthermore, this finding supports the, thus far, low extinction from dust along the line of sight, since we would otherwise expect our derived stellar value to be larger than the value reported in literature.

2.7.1.2 Region B

Region B is the right region in Fig 2.13. It is described as the East H II region in Ruiz-Escobedo et al. (2018), who also note it is faint and appears to have low-extinction ($c(H_\beta) = 0.08 \pm 0.05$).

Ruiz-Escobedo et al. (2018) detect only the hydrogen Balmer series in emission as well as [O II] λ3727Å, [N II] λ6583Å, and [S II] λ6717, 6731Å. Since they are only able to obtain an upper limit for [O III]λ5007Å, they determine that a star with $\log(T_{\rm eff})\geq 4.45$ is necessary and an ionising photon production rate of $10^{48.0}$ photons s^1 is required to produce the observed H II region size of 1.5 pc, assuming an electron density of 100 cm^{-3}.

Star K1 is located in Region B. From our spectra, we find K1 is a O9V type star. We find $\log(T_{\rm eff})=4.49 \pm 0.01$ from our spectroscopic analysis and $\log(T_{\rm eff})=4.52 \pm 0.02$ from SED fitting. Both are in reasonable agreement with the estimate of $\log(T_{\rm eff})\geq 4.45$ from Ruiz-Escobedo et al. (2018). Our SED fitting shows that K1 has $\log(t) = 6.9 \pm 0.08$ (yr), $M_{ini} = 20.1 \pm 1.29 M_\odot$, and $A_{\rm V}= 0.05 \pm 0.01$. The age and mass of this star are comparable to what is expected for an H II region, while the extinction is similar to what is derived from the nebular emission analysis. We find that B5 is in the H II region as well. However, B5 is a Be star, which makes the age and mass determination more difficult. For K1, we are able to calculate the intrinsic ionizing photon rate using the BEAST. We derive a median rate of $10^{48.1\pm0.1}$ photons s^{-1}, which is consistent with the derivation from Ruiz-Escobedo et al. (2018). This supports that the majority of the ionization is likely coming from K1. Again, our results suggest that dust along the line-of-sight in Leo A has to be low to negligible.

Overall, we find consistency between previous studies of the H II regions in Leo A and our study of massive stars in those regions. van Zee et al. (2006) considers whether the lack of hotter O-type stars can be explained by either a truncated IMF or that the H II regions are evolved. To explore this, we consider the ages derived by the BEAST of the stars (K1,K2,B5) in those regions (Fig. 2.13). Given that those stars are high mass stars, they are already at the end of their lifetime on the MS. In Fig 2.13, we can clearly see that Region B is more evolved H II region than Region A, since the average age of the massive stars in the region is older. However, we also find very few massive stars in both H II regions.

Lastly, the results suggest that in both H II regions a majority of the ionization is coming from a singular O-star.

2.7.2 Field OB-stars

It is well-established that most stars form in clustered environments (e.g., Lada & Lada 2003; Krumholz et al. 2019). Accordingly, OB-stars are expected to be found in or near H II regions or star clusters as their short lifetimes imply they do not have time to wander to significant distances before ending their stellar lives.

However, a subset (20-30 %) of massive stars are found in the "field" with no clear association to clusters or H II regions (e.g., Jones et al. 2020). The existence of those stars pose a dilemma for stellar kinematics, star formation theory, IMF sampling, etc. (e.g., Blaauw 1961; Clarke & Pringle 1992; Hoogerwerf et al. 2000; Oey et al. 2004; de Wit et al. 2005; Renzo et al. 2019). This has led to major differing theories to the formation of those stars; in situ star formation (Oey et al. 2013) and ejection (Oey et al. 2018; Jones et al. 2020). Recent studies (e.g., Oey et al. 2018; Vargas-Salazar et al. 2020; Jones et al. 2020) favor the latter scenario in most cases, which is further broken down into two different type of ejections; a dynamical ejection scenario (DES) and a binary supernova scenario (BSS). While both require massive star binaries, in the DES a close encounter with a binary system ejects the star (or binary) at high velocity out of the cluster or H II region. In the BSS scenario, a core-collapse supernova of the more evolved star ejects its OB companion or sometimes the entire system (Jones et al. 2020).

The majority (~70%, 13 stars) of the stars in our spectroscopic sample are not within $d \sim 40$ pc of any H II region. To obtain a rough understanding of which mechanism is responsible for the position of the stars, we derive estimated required velocities from the age estimate yielded by the `BEAST` and distances from the H II region map (Fig. 2.3). We summarize the derived values in Table 2.7. In this discussion, we take advantage of the coincidence that 1 pc Myr^{-1} is 0.98 km s^{-1}.

K3, K7, B4, and B10 can be considered runaway candidates, since their lower limit for velocity suggest that the stars could have been ejected. All four stars are at least 200 pc from the nearest H II region or cluster. They are amongst the youngest field stars (with the following ages in Myr: K3: 15.8 $\pm^{2.7}_{2.4}$, K7: 6.3 $\pm^{2.6}_{1.8}$, B4: 10 $\pm^{1.7}_{1.5}$, B10: 12.6 $\pm^{3.6}_{2.8}$). Although recent studies (e.g., Renzo et al. 2019; Schoettler et al. 2020; Vargas-Salazar et al. 2020) suggest a cutoff for runaways around $\sim$ 30 kms^{-1}, we still can consider those four stars runaway candidates, since we only report lower limits. Due to the lack of precise velocity measurements it is currently not possible to distinguish whether the stars were ejected through DES or BSS.

B11, B12, and B14 are more likely walkaway candidates (de Mink et al. 2014; Renzo et al. 2019; Schoettler et al. 2020; Vargas-Salazar et al. 2020). Overall, the stars are on

Table 2.7: Parameters of isolated stars in Leo A. The columns are: (1) star name; (2) initial mass (photometry); (3) initial mass (spectroscopy); (4) Spectral Type; (5) stellar age in Myr; (6) radial velocity; (7) approximate distances to the closest H II region or cluster for each star; (8) approximate velocity derived from taking the values (7) and dividing it by the values in (5). When available we list the initial mass, otherwise we list the evolutionary mass.

Star	M_{ini}	M_0	Spectral Type	Age	V_R	Dist. to nearest H II region/cluster	Velocity (Dist./Age)
	$M_\odot$	$M_\odot$		Myr	kms^{-1}	pc	pc/Myr
(1)	(2)	(3)	(4)	(5)	(6)	(7)	(8)
K3	12.9 ± 0.17	...	B1.5V	$15.8 \pm^{2.7}_{2.4}$	27 ± 2	> 200	> 11-15
K7	15.3 ± 1.06	...	O9.5V	$6.3 \pm^{2.6}_{1.8}$	24 ± 23	> 200	> 22-45
B4	16.2 ± 0.18	...	B0V	$10 \pm^{1.7}_{1.5}$	30 ± 3	> 200	> 17-23
B11	5.9 ± 0.69	...	B2V	$63 \pm^{22}_{16.3}$	...	> 40	> 1
B12	7.3 ± 1.21	...	B1.5V	$39.8 \pm^{17.7}_{12.3}$	30 ± 8	~ 40	~ 1-2
B14	9.3 ± 0.99	...	B3V	$20 \pm^{8.9}_{6.1}$	20 ± 5	~ 50	~ 2-3
B10	12.8 ± 1.21	...	B0.5V/Be0.5V	$12.6 \pm^{3.6}_{2.8}$	31 ± 11	> 200	> 12-20
B7	...	11 ± 2	B1V/Be1V	5−50	44 ± 6	~ 70	~ 1-14
K4	...	13 ± 2	Be1V	5−50	30 ± 10	~ 60	~ 1-12
K5	...	14 ± 2	Be2V	5−50	35 ± 11	~ 80	~ 2-16
K6	...	12 ± 2	Be2V	5−50	18 ± 6	~ 100	~ 2-20
K8	...	17 ± 2	Be2V	5−50	28 ± 8	~ 200	~ 4-40
B8	...	10 ± 2	Be3V	5−50	28 ± 4	~ 230	~ 5-46

Note. — 1 - The star has a really high χ^2-value making the age unreliable and therefore the velocity unreliable as well.

average $\sim 40-70$ pc to the closest H II region or nearest H II region. In comparison to the other group they are older in age (with the following ages in Myr: B11: $63 \pm^{22}_{16.3}$, B12: 39.8 $\pm^{17.7}_{12.3}$, B14: $20 \pm^{8.9}_{6.1}$). Their estimated velocities are of the order a couple of pc Myr^{-1}. This is in-line with intermediate mass runaway velocities (Renzo et al. 2019). However, these type of walkaways remain rare (Renzo et al. 2019), and therefore are impossible to confirm without precise velocity measurements, much less to associate with different mechanisms.

Five of our Be stars (K4, K5, K6, K8, and B8) and B7 are also in the field. Since we do not have age measurements, we can only present rough velocity ranges in Table 2.7. All five stars show velocity limits consistent with runaway stars. In the literature, Be stars in the field have been associated with BSS (Jones et al. 2020). However, we cannot exclude that DES could be responsible for the ejection and velocity of these stars.

Further studies of OB-stars in Leo-A would likely provide better understanding on the overall distribution of the mechanism responsible for runaway stars at extremely low metallicity.

2.7.3 Purity of the Blue Core Helium Burning Sequence

BHeB stars provide important constraints on stellar evolution and serve as excellent tracers of recent star formation (Langer & Maeder 1995; Dohm-Palmer et al. 2002a; Dolphin et al. 2003; Larsen et al. 2011; Leščinskaitė et al. 2022). In particular, the extent of the blue loop and the ratio of blue to red core helium burning stars are sensitive to several poorly constrained aspects of massive stars physics (e.g., rotation, convective overshoot; Alongi et al. 1991; Ritossa 1996; McQuinn et al. 2011; Jie et al. 2015; Georgy et al. 2021; Farrell et al. 2022; Eldridge & Stanway 2022). The lumionsities and spatial positions of BHeBs in nearby galaxies have been used to construct spatially resolved maps of star formation over the past few hundred Myr (Dohm-Palmer et al. 2002a; McQuinn et al. 2012; Leščinskaitė et al. 2022).

However, some of the data and findings presented in this paper suggest that not all stars that reside in the BHeB region of an optical CMD are *bona fide* BHeBs. This has been previously suggested by Stonkutė & Vansevičius (2022) and Leščinskaitė et al. (2022). In our combined photometric and spectroscopic sample we find that indeed, six stars in our sample out of seven that appear to be in the BHeB region on the optical CMD (K4, K5, K6, K8, B5, B8) are, in fact, spectroscopically Be-type stars. This provides the first spectroscopic confirmation for Be stars in Leo A.

We compare the UV and optical CMDs to see if any other stars that appear to be in the MS region in the UV CMD are in the BHeB region in the optical. We compare stars that are brighter than 23.5 mag in the F475W filter. We further apply following cuts; F475W-F814W > 0.2, F475W-F814W < -0.15, and F275W-F475W < 0.0. Lastly, we apply cuts by eye on stars that are on the MS region. These cuts are visualized in Fig. 2.14. We

find that ~5-10 % of the stars in the BHeB region above 23.5 mag in F475W exhibit this behaviour. This finding suggests that when taking the BHeB/RHeB-ratio from photometric surveys, we have to take into account that the BHeB region could be contaminated by Be stars. However, since we can disentangle the Be star candidates in the UV, corrections can be applied when multi-wavelength coverage is available. Lastly, the findings propose a new avenue to potentially search for and detect Be star candidates through photometry.

2.7.4 Extremely metal-poor environments

2.7.4.1 Spectral Type vs Effective Temperature

Spectroscopic studies of sub-SMC metallicity massive stars continues to be challenging, because of the large distances to the nearest galaxies that host them. Though tremendous efforts have gone into characterizing metal-poor massive stars in nearby dwarf galaxies (e.g., Kaufer et al. 2004; Venn et al. 2004; Bresolin et al. 2006; Evans et al. 2007; Bresolin et al. 2007; Garcia & Herrero 2013; Tramper et al. 2014; Hosek et al. 2014; Camacho et al. 2016, 2017; Garcia 2018; Evans et al. 2019; Garcia et al. 2019a,b; Telford et al. 2021; Lorenzo et al. 2022) most our knowledge remains based on larger studies in the SMC (e.g., Heap et al. 2006b; Mokiem et al. 2006; Penny & Gies 2009; Hunter et al. 2009; Dunstall et al. 2011; Bouret et al. 2013; Dufton et al. 2019; Ramachandran et al. 2019; Bouret et al. 2021).

In Fig. 4.6, we compare our spectroscopic sample stellar types to other samples of massive stars with spectra at SMC and sub-SMC metallicities with published temperature and spectral type. We compare the 4 O-stars to the best fit of the Massey et al. (2009) sample and the Dufton et al. (2019) $\log(T_{\rm eff})$ to spectral type relation. We further compare the stars to two stars in Sextans A; S3 Telford et al. (2021) and OB521 Camacho et al. (2016). We note that two of our stars (K2 and B13: $\log(T_{\rm eff})$= 4.50 dex and SpT is O9.7V) fall on top of each other in the $\log(T_{\rm eff})$ vs. spectral type plot, which is why we only see three O-stars in the plot.

We find that our O-stars are consistent with the sub-SMC stars S3 & OB521. When comparing to the SMC trend lines, we see that our parameters are consistent with Massey et al. (2009), but find lower $\log(T_{\rm eff})$ for the same spectral type than Dufton et al. (2019). However, O-stars in Sextans A and Leo A appear to have similar $\log(T_{\rm eff})$ to the SMC sample from Massey et al. (2009). They are also all lower in $\log(T_{\rm eff})$ than the relation derived by Dufton et al. (2019), contradictory to expectations (see e.g., Mokiem et al. 2004). One possibility is the difference in the underlying models. While Telford et al. (2021) and our work use the `TLUSTY` models, other groups use other models (e.g., `CMFGEN` (Hillier & Lanz 2001), `FASTWIND` (Santolaya-Rey et al. 1997)), introducing at least some uncertainty.

For the photomerically determined values of $\log(T_{\rm eff})$, we find that for two of the stars (K2 and B13) we derived hotter $\log(T_{\rm eff})$ while for the other two (K1 and K7) the photom-

etry yields the same $\log(T_{\rm eff})$.

We compare our B-stars to the SMC relation for B-stars from Dufton et al. (2019) for the dwarfs and to Dunstall et al. (2011) for the Be stars. For the B0-B1 stars we find that we are cooler than the Dufton et al. (2019) derived relation. For stars after B1, the stars seem to be closer to the derived relation and hotter. We find that all of our Be stars are hotter than the derived relationship from the SMC for Be stars, both spectroscopically and photometrically. We did not find any sub-SMC B V stars to compare our sample to. While, for the O-stars, the slope between our points appears similar to the literature, we find that we have a flatter fall off for our B-stars. Since the B stars in our sample represent the first MS stars we have both spectral type and photometry for, they provide the first insight into the scale at sub-SMC. Overall, we find that at later spectral types $\log(T_{\rm eff})$ decreases in our sample as expected. However, there is a large spread, which is likely due to decreasing data quality. Increasing our sample of sub-SMC stars is crucial to obtain a full understanding of the relation between spectral type and $\log(T_{\rm eff})$.

2.7.4.2 Current Observational Knowledge of Metal-Poor Massive Stars

In Fig. 4.5, we plot HR diagrams for the entire sub-SMC metallicity star sample in the literature with temperatures and luminosities that have been derived from spectroscopy. We note that recently Lorenzo et al. (2022) collected $\sim$ 150 spectra of metal-poor massive stars; however, currently there are no stellar parameters for this sample, and we cannot include them on this plot. We overplot the MIST stellar tracks at select masses for reference. We indicate the gas-phase metallicities for each galaxy after placing them on a common scale using Grevesse et al. (2010) for the Solar abundance ($12 + \log(O/H) = 8.69$).

The top panel shows metal-poor galaxies WLM ($Z \sim 15$ % $Z_\odot$; Bresolin et al. 2006, Tramper et al. 2011, Tramper et al. 2014 and Telford et al. 2021), IC 1613 ($Z \sim 14$ % $Z_\odot$; Bresolin et al. 2007) and NGC 3109 ($Z \sim 13$ % $Z_\odot$; Evans et al. 2007, Tramper et al. 2014 and Hosek et al. 2014). The bottom panel shows extremely metal-poor galaxies Sextans A ($Z \sim 10$ % $Z_\odot$; Kaufer et al. 2004, Camacho et al. 2016 and Telford et al. 2021), and Leo P ($Z \sim 3$ % $Z_\odot$; Telford et al. 2021), along with stars in our Leo A spectroscopic sample.

We clearly see that the literature thus far has populated mostly the very upper area of the HR diagram. This is not surprising, since the most luminous stars are more accessible to observe. In comparison, our sample extends to fainter luminosities, later types, and less evolved stars.

We double the number of OB-stars thus far with spectroscopically derived stellar parameters at sub-10% solar metallicity. It also contains the the first sample of spectroscopically confirmed sub-SMC Be stars and the largest sample of sub-SMC B-type dwarf stars.

2.7.4.3 Initial and present-day masses across analysis methods

The mass of a star is among its most fundamental parameters. Here, we examine the masses we have measured from photometric SED fitting and from spectroscopy. SED fitting yields an initial mass of M_{ini} and a present day mass of M_{act}. Spectroscopic fitting provides an initial mass of M_0 and present day masses of M_{evo} and M_{spec}. As a reminder, M_{evo} is determined by using $\log(T_{\rm eff})$, $\log(L/L_\odot)$ and evolutionary tracks, whereas M_{spec} is determined using the Eqns. (1)-(3) as explained in §2.3.2. The exact derivation of each of these masses is given in §2.6.1 and 2.5. The different masses are listed in Tables 2.4 and 2.6 and comparison plots are presented in Fig. 2.17. We note that the comparison includes stars that have $\chi^2 < 100$ in both methods.

For the initial masses, M_{ini} and M_0, we find a median absolute deviation between the two masses of $0.59 M_\odot$ and a median difference of $1.1 \pm 1.1 M_\odot$. Overall, the M_{ini} values are slightly larger than M_0, but they are all roughly within the uncertainty except for B12 (which was pointed out as an outlier in §2.6.4). B12 shows a difference ~ 3 times larger than the uncertainty and shows a significantly higher initial mass ($M_0 \sim 11\ \ M_\odot$) for spectroscopy. For the present-day masses of the stars in the sample, we find overall that M_{act} and M_{evo} are consistent with each other. We find a median absolute deviation between the two masses of $0.69 M_\odot$ and a median difference of $0.99 \pm 1.42 M_\odot$. Similar to the initial masses, the M_{act} values are slightly larger than M_{evo}, but within the uncertainty. We find B12 remains an outlier.

In Fig. 2.17, we also compare M_{evo} and M_{spec}. We do not include M_{act}, since the values agree well with M_{evo}. In principle, M_{evo} and M_{spec} should be the same, and differences between them are used as a consistency check for evolutionary models. For example, as first noted by Herrero et al. (1992), there have been multiple studies (e.g., Herrero et al. 2002; Massey et al. 2005; Weidner & Vink 2010; Mahy et al. 2015; Markova & Puls 2015; McEvoy et al. 2015; Ramírez-Agudelo et al. 2017; Sabín-Sanjulián et al. 2017; Markova et al. 2018; Schneider et al. 2018; Castro et al. 2021) that discuss the the tension between M_{evo} and M_{spec} for O-type stars. The tension rises from M_{evo} being larger than M_{spec}, although they should be the same. Most of these studies suggest that the discrepancy is the most significant at $M > 40 M_\odot$. We do not have any stars this massive, but we can examine differences in the $\sim 10 - 20 M_\odot$ range. For all the stars in our sample, we find a median absolute deviation between the two masses of $3.0 M_\odot$ and a median difference of $< 0.01 \pm 5.3 M_\odot$. To get a sense of typical differences for stars that agree, we consider stars that agree within the uncertainty measurement, and we find a median absolute deviation between the two masses of $1.5 M_\odot$ and a median difference of $0.0 \pm 2.2 M_\odot$. We find three outliers in our comparison, K2 (~ 1.5 times larger), K3 (~ 1.5 times larger), and B14 (~ 3 times larger). In §2.6.3, we noted that these stars show a slightly higher than expected $\log(g)$ value which is likely driving up the mass, in comparison to the stars' photometry. We note that these stars also show $M_{spec} > M_0$, which is not physical, and is likely due to

a high $\log(g)$ value or $\log(L/L_{\odot})$ value. It is interesting that K2 and K3 are outliers, since the K2 observations suggest it could be a binary candidate, while K3 has a peculiar spectra, which can be explained by a binary scenario. Overall, we find that for "normal" single stars, the evolutionary model derived masses and spectra derived masses are in agreement at the level of 1-2 $M_{\odot}$.

2.7.5 Finding Be stars in low metallicity environments

We provide the first confirmation of Be stars in Leo A. We also spectroscopically observed the lowest metallicity Be stars to date. We confirm 6 Be stars (K4, K5, K6, K8, B5, B8) and label two B stars as potential Be stars (B7, B10). Excluding the last two stars, we find that for our spectroscopic sample $\sim 45\%$ of B-type stars are Be stars. This is high compared to the Be fraction in the Milky Way ($\approx 17\%$; Zorec & Briot 1997), LMC ($\approx 20\%$; Martayan et al. 2006), and SMC ($\approx 30\%$; Martayan et al. 2007a,b), and appears in line with the expected trend of an increased Be star fraction at low metallicity due to weaker winds and faster rotation rates. However, our sample is also biased toward early spectral types, where the Be occurrence rate is higher; further study is needed to confirm this trend.

Furthermore, we show that Be stars in Leo A can be photometrically identified by a strong IR excess relative to stars near the main-sequence in UV colors, even without spectroscopic follow-up. We show that the panchromatic SED allows us to put some constraints on both the stellar and disk parameters. While we explore the simplest parameters for the Be stars, the combination of our obtained spectra and photometry presents the unique opportunity to gain first insights on the disk physics at low metallicity. Lastly, the identification through a NIR excess is especially promising with *JWST*. *HST* UV and Hα imaging surveys can now be combined with the NIR imaging to identify and characterize Be stars.

2.8 Conclusions

We have presented the first combined stellar spectroscopy and *HST* photometry analysis of the extremely metal-poor OB-stars in Leo A, a low luminosity, dwarf galaxy at a distance modulus of $\mu = 24.40$ mag. Our findings from the LUVIT *HST*, LRIS (KECK), and Binospec (MMT) observations include:

- We analyze the brightest OB-stars ($F475W < 22$ and $F475W - F814W < 0.5$) in Leo A using the LUVIT *HST* photometry. We spectroscopically observe and analyze a total of 18 stars within the photometric sample. We find 4 O-type dwarfs, 8 B-type dwarfs, and 6 Be stars.

- We derive stellar parameters of the photometric sample using the `BEAST`. We find that for good fits ($\chi^2 < 80$) $\log(T_{\rm eff})$ and $\log(g)$ increase for bluer F475W−F814W

colors as expected from stellar models. For stars on the MS region of the CMD, M_{ini} trends as expected; the brightest stars (e.g., F275W< 18) have the highest M_{ini} with masses up to $M_{ini} \sim 20 M_{\odot}$. Similarly, $A_{\rm V}$ matches findings from previous studies, which suggest little to no dust in Leo A ($A_{\rm V} \lesssim 0.08$). However, for stars on the BHeB region of the CMD, the trends do not appear quite as clear, which we expand upon below.

- We use `The Payne` and two different publicly available TLUSTY spectroscopic grids for O-stars and B-stars to measure spectroscopic parameter for 18 stars. We measure $\log(T_{\rm eff})$, $\log(g)$, $V_{\rm R}$, and $v \sin i$ for each star. We use MCMC sampling to obtain the uncertainties on all parameters. We find our spectroscopic sample has a $\log(T_{\rm eff})$ range of 4.39 to 4.50, a $\log(g)$ range of 3.69 to 4.64, and a $v \sin i$ range of < 80 to 370. We find $V_{\rm R}$ variation for K2 with Keck (-13 ± 2 kms^{-1}) and Binospec (16 ± 4 kms^{-1}), making it a viable binary system candidate.

- The photometrically and spectroscopically derived parameters ($\log(T_{\rm eff})$, $\log(g)$, and $\log(L/L_{\odot})$) are consistent to within 1σ for stars with $\chi^2 < 100$ in both methods. We find a MAD of < 0.01 dex for $\log(T_{\rm eff})$, 0.18 dex for $\log(g)$, and 0.05 dex for $\log(L/L_{\odot})$. When we find disagreement it is usually due to stars with signs of emission, peculiar SED colors (i.e., IR excess), or high χ^2 values. This is a promising avenue to study more distant low metallicity galaxies for which resolved star spectra cannot be obtained.

- We compute and compare both initial masses and present-day masses with photometry and spectroscopy. The initial stellar masses (M_{ini} (photometry) and M_0 (spectroscopy)) determined by the two techniques are consistent within 1σ. M_{ini} ranges from $6.26 M_{\odot}$ to $20.1 M_{\odot}$ and M_0 ranges from $8.0 M_{\odot}$ to $19\ M_{\odot}$. Similarly, the present-day masses derived from the stellar parameters in combination with evolutionary tracks (M_{act} (photometry) and M_{evo} (spectroscopy)) are consistent within 1σ. M_{act} ranges from $6.26 M_{\odot}$ to $19.99 M_{\odot}$ and M_{evo} ranges from $8.0 M_{\odot}$ to $19 M_{\odot}$. We further compare M_{evo} to the spectroscopic present-day mass (M_{spec}), and find that the stars are consistent to 1σ when excluding stars with $M_{spec} > 20 M_{\odot}$ (K2, K3 and B14). These stars show disagreements larger than $5 M_{\odot}$. M_{spec} ranges from $8.0 M_{\odot}$ to $27 M_{\odot}$

- We find that the gas, RGB and stellar velocities are consistent within 1σ. We further are able to show that full spectral fitting is reliable at recovering RV measurements to higher precision.

- Overall, we find that our study of massive stars in two H II regions is consistent with previous gas-phase studies of these H II regions in Leo A. The O-type stars (K1 and K2) in the H II regions provide the expected ionization power for each ($10^{48.1 \pm 0.1}$

photons s^1 and $10^{47.6\pm0.1}$ photons s^1, respectively), and suggest little dust along the line-of-sight.

- We find a total of 13 isolated stars in our spectroscopic sample, i.e., they are not within $d \sim 40$ pc of any H II region. For seven stars, we are able to use the derived ages and approximate distances to the nearest H II region to estimate velocities. Four stars yield velocities consistent with runaway stars (i.e., $V \gtrsim 30$ kms^{-1}), while three are consistent with walkaway stars (i.e., $V < 30$ kms^{-1}).

- We confirm that six of our spectroscopically observed stars are Be stars; these are the first at sub-10% solar metallicity. We further find that these stars are photometrically contaminating the BHeB region in the optical CMD. We unexpectedly find that $\sim 5 - 10\%$ of stars in the BHeB region above 23.5 mag (F475W) in the optical CMD appear to be on the MS region in the UV CMD.

- We find the observed sub-SMC metallicity late-type O dwarfs and our O dwarfs to be consistent in $\log(T_{\rm eff})$ within 1σ for a given spectral type. We increase the sample of O dwarfs in the sub-10% solar metallicity regime with derived stellar parameters from five to nine. We provide the largest sub-SMC metallicity B dwarfs sample. We also spectroscopically observe the first sub-10% solar metallicity Be stars. We present the largest spectroscopic sample of MS stars at sub-SMC metallicity with derived stellar parameters.

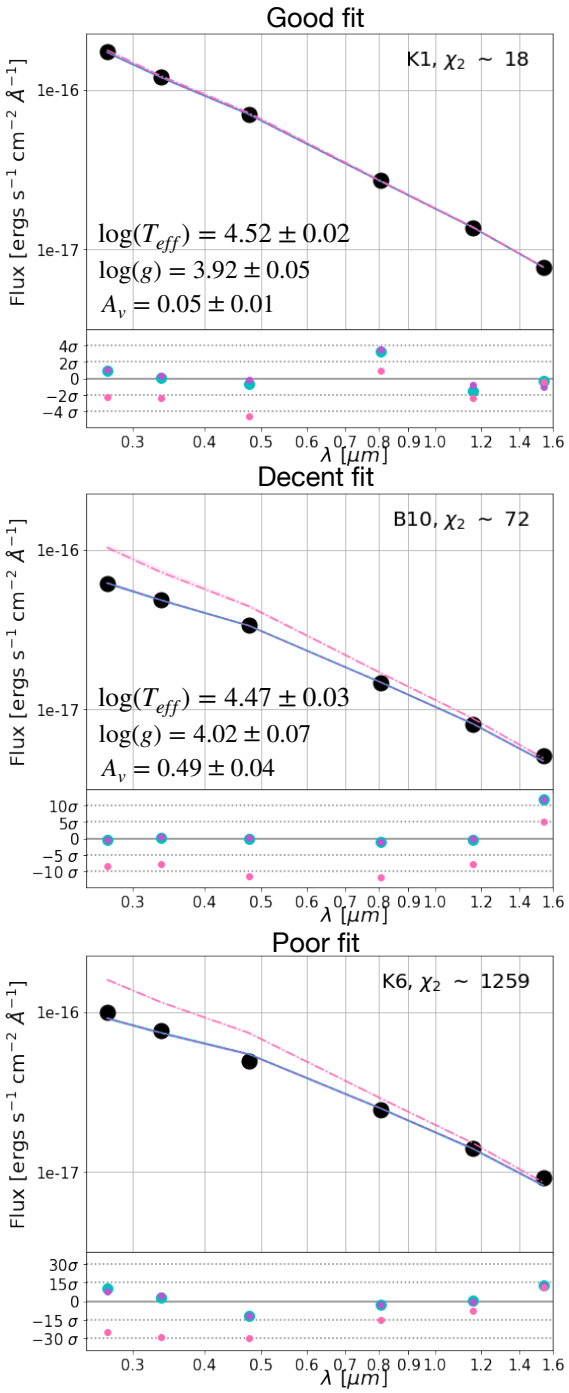


Figure 2.5: Example SED fits in each category of χ^2: good (top), decent (middle), and poor (lower). The data are shown as black points. The median fit stellar (pink), stellar+dust (purple), and stellar+dust+bias (cyan) are overplotted. The sub-panels show the residuals in units of σ. The top panel shows all residuals of the best model (cyan) within 4σ. The middle panel shows residuals of the best model (cyan) within 12 σ (note that for 5 bands the value is closer to 4 σ). The bottom panel shows the largest deviations in the residual with the best model (cyan) being within 15 σ. For the good and decent fit we report $\log(T_{\rm eff})$, $\log(g)$, and $A_{\rm V}$.

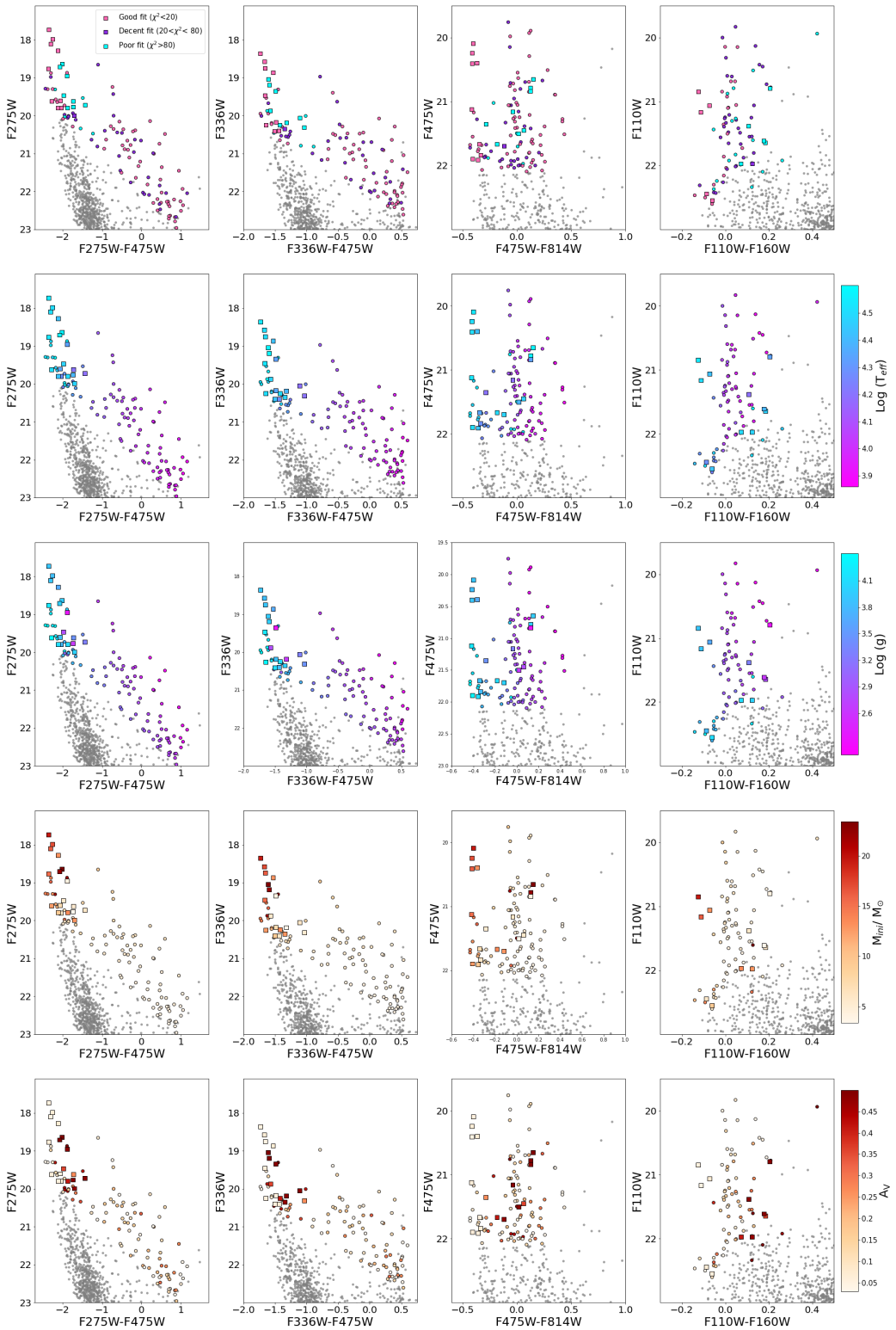


Figure 2.6: A panchromatic gallery of CMDs for Leo A ranging from UV-optical on the left to NIR on the right. Points in each row are color-coded by results from SED fitting with the `the BEAST`. From top to bottom, the rows reflect: χ^2, log($T_{\rm eff}$), log(g), M_{ini}, and $A_{\rm V}$. For χ^2, we divide the fits into three categories: good (pink), decent (purple), poor (cyan). Stars that have spectroscopic data are plotted as squares.

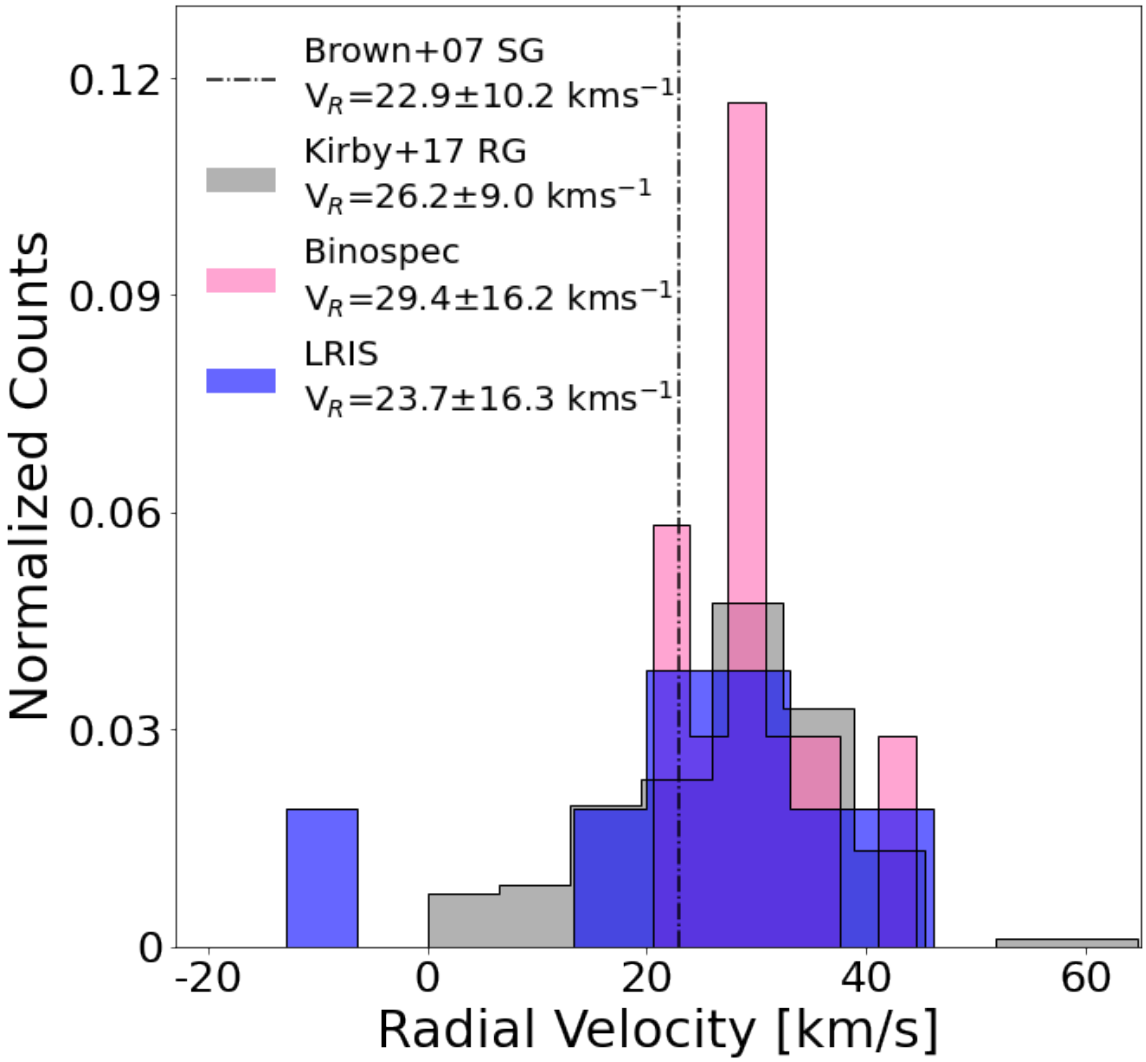


Figure 2.7: The distribution of radial velocities for stars in Leo A. Our LRIS (blue) and Binospec (pink) velocities are consistent with the the Keck/DEIMOS-based velocities of red giants (RG) measured by Kirby et al. (2017), and the average velocity measured from the Supergiants (SG) by Brown et al. (2007). Each sample is normalized by counts.

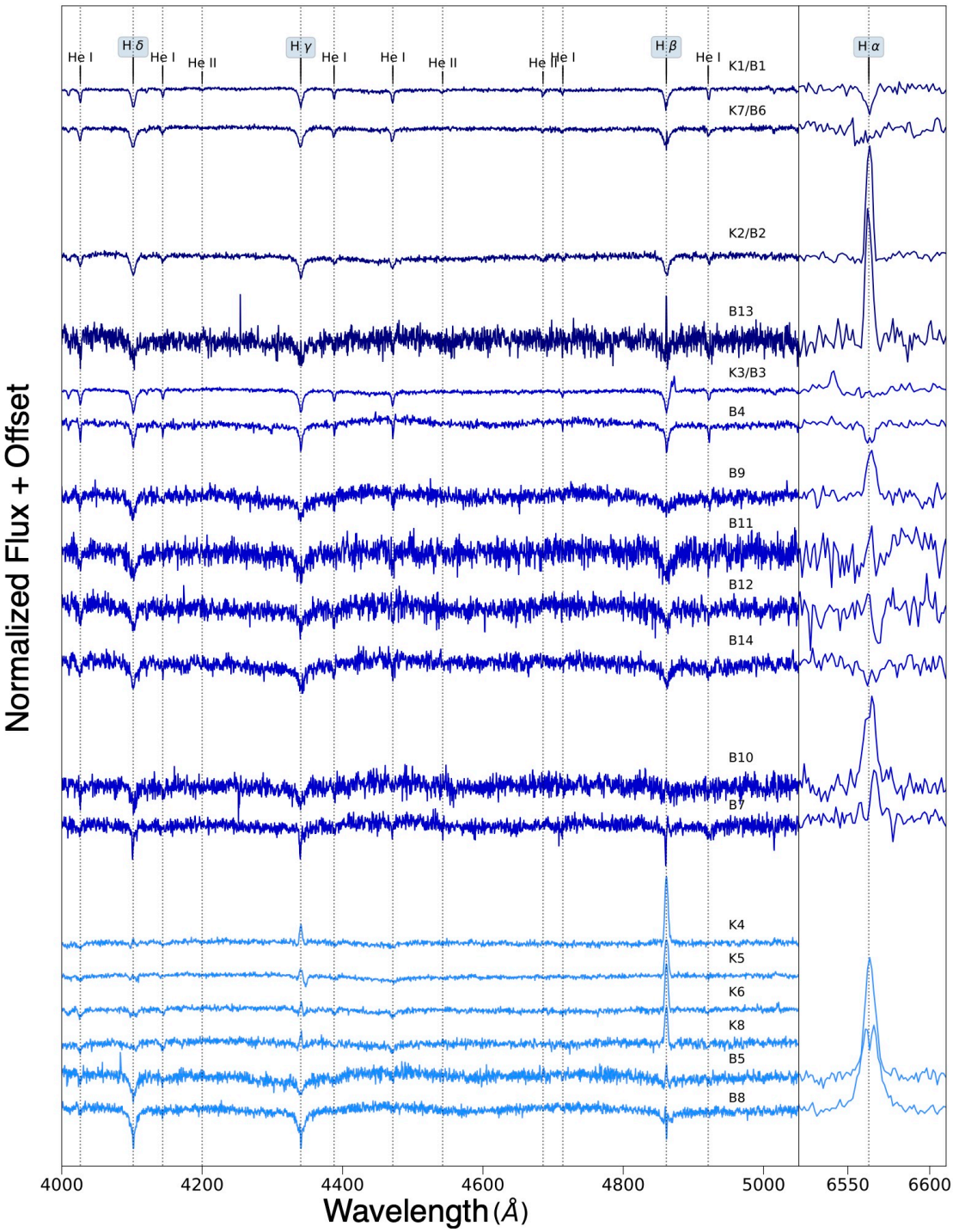


Figure 2.8: Keck/LRIS and MMT/Binospec normalized spectra (with an arbitrary offset added for clarity) for all 18 stars in the spectroscopic sample. For stars with both Keck and MMT data, we show the Keck spectra in the 4000-5100 Å region. If there is no LRIS spectrum, we show the Binospec (1000 lpmm) spectrum. The spectra in the 6520-6610 Å region are from the Binospec 270 lpmm grating and are shown for all stars that have Binospec spectra. The spectra are sorted by spectral type from O-type stars at the top to B-type and Be-type stars at the bottom. This is one of the largest set of optical spectra for sub-SMC metallicity massive dwarf stars.

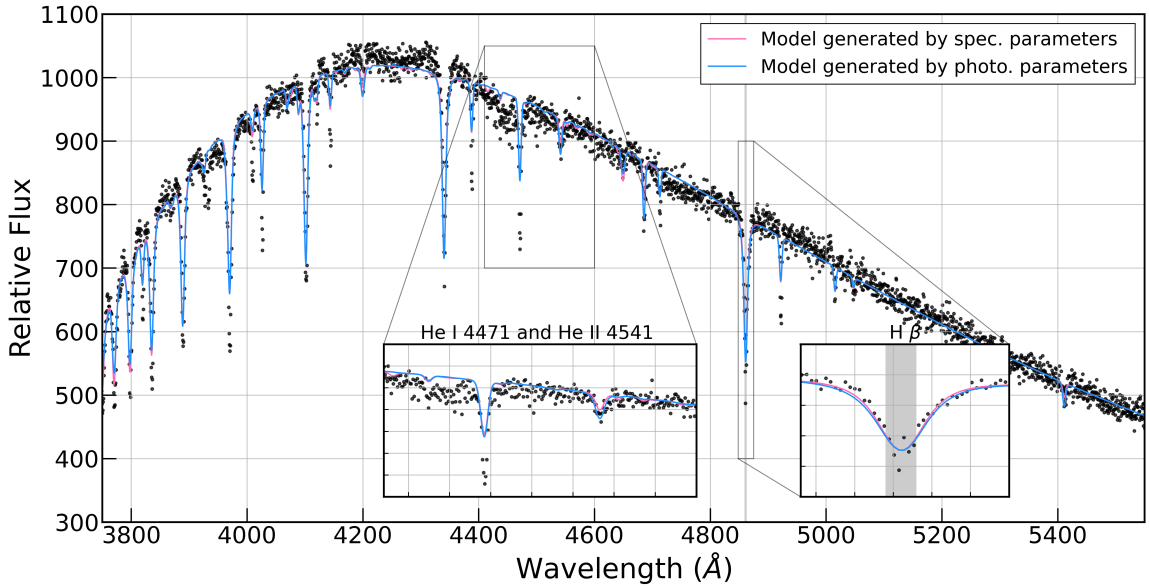


Figure 2.9: Comparison between the parameters derived for K1 using full spectral fitting and SED fitting. We show a plot of the observed spectra (black dots), the TLUSTY-based model generated by the median parameters derived from the full spectral fitting (pink), and the TLUSTY-based model generated by the median parameters derived from the SED fitting (blue). While both models reasonably replicate the observed He I 4471 and He II 4541 fits, both struggle to fully fill the absorption feature of the helium lines. This shortcoming is potentially due to the fixed resolution, metallicity, or macroturbulence. We see the effect of the different $\log(g)$ values between the methods most prominently in the Balmer lines (see the Hβ feature). The grey bar shows the part of the spectrum that we masked.

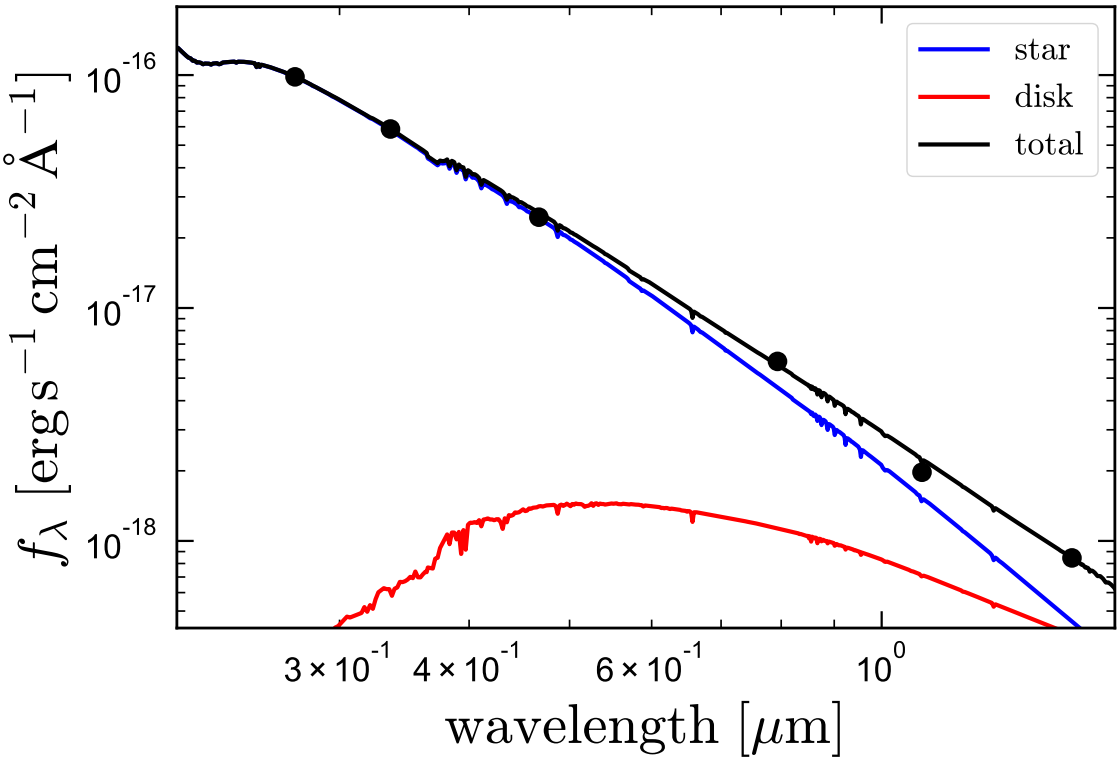


Figure 2.10: Models for K6 from adapted composite SED fitting (See §2.5.3). The data (black dots) are matched by scaling and combining the stellar models. The star (blue line) and the disk (red line) are combined for the composite SED (black line). The star and the disk models are both varied to find the median SED. We note that the error bars of the data are smaller than the dots representing the data point.

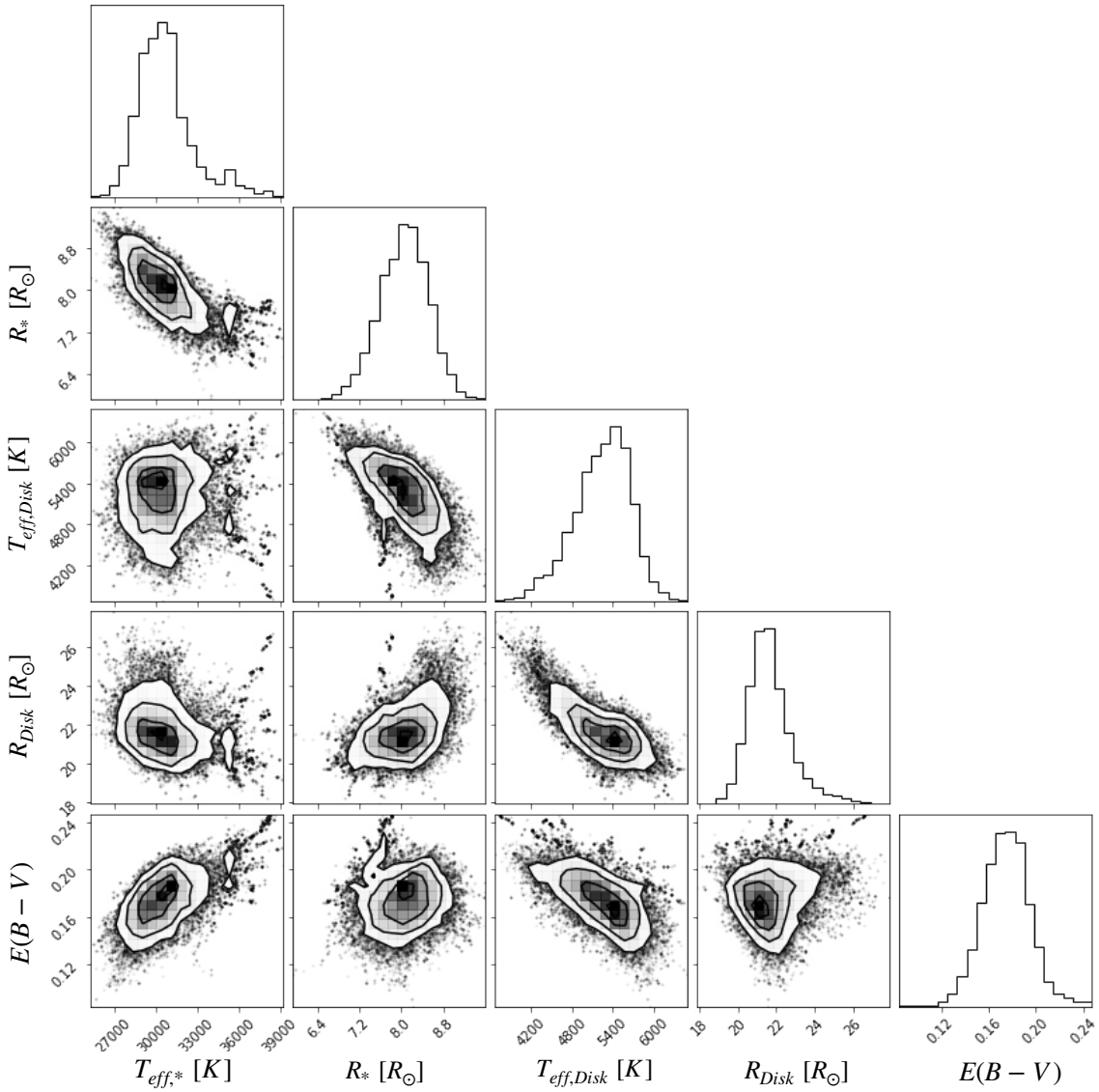


Figure 2.11: Corner plot of stellar parameters from the adapted double SED fitting of K6. The first two columns show the contours for the derived $\log(T_{\rm eff})$ and radius of the star. The next two columns show the contours for the derived $\log(T_{\rm eff})$ and radius of the disk. The last column shows E(B-V).

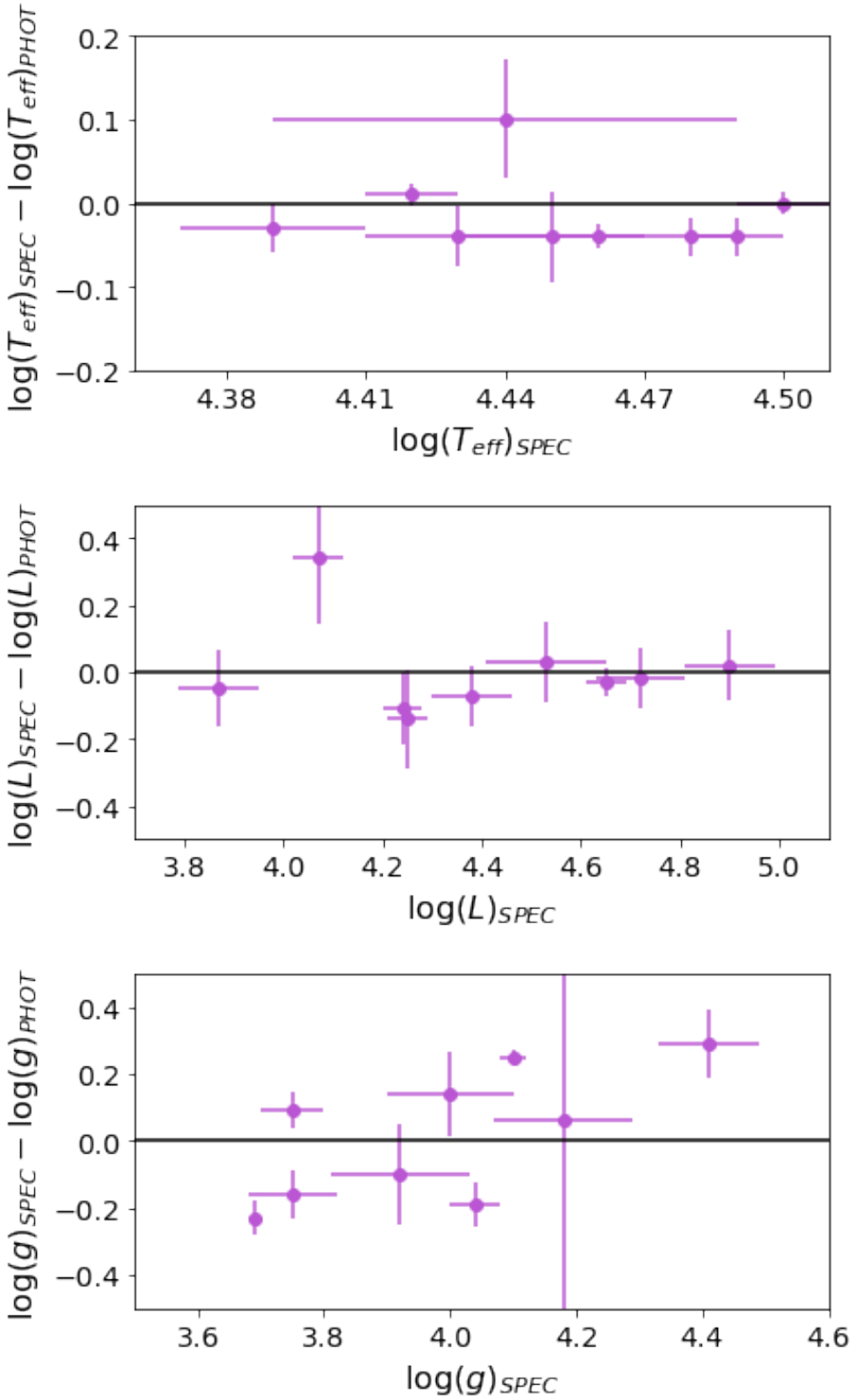


Figure 2.12: A comparison between the parameters derived from the `BEAST` using the models with v/vcrit=0.4 (PHOT) and the parameters derived from the `PAYNE` (SPEC). The top panel compares $\log(T_{\rm eff})$. The middle panel compares $\log(L/L_{\odot})$. The bottom panel compares $\log(g)$. The comparison between the two methods shows that panchromatic photometry can be used to recover reliable stellar parameters at least for "normal" single stars.

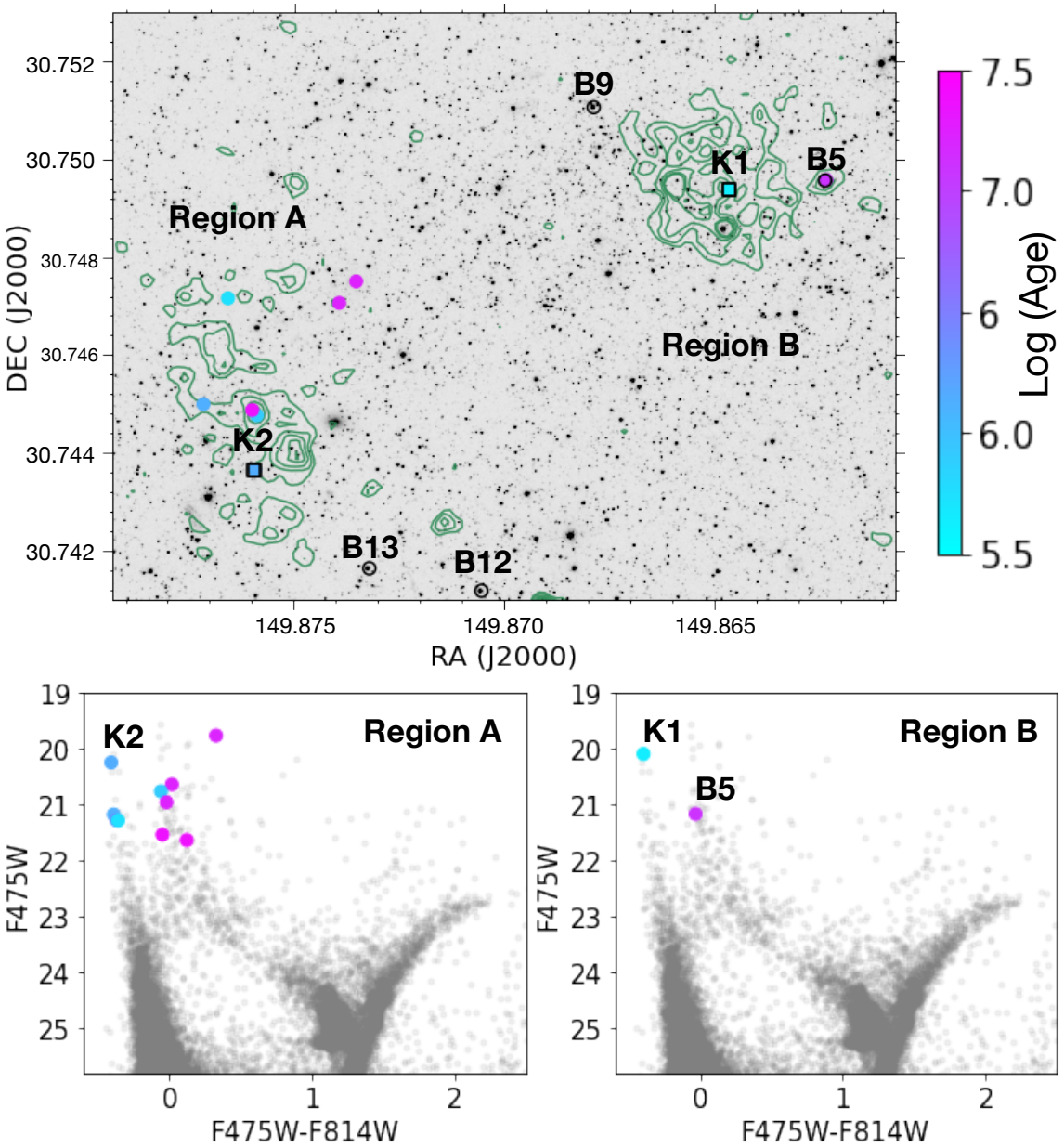


Figure 2.13: Top panel: The Leo A *HST* ACS/F475W image zoomed in on two H II regions. Stars with spectroscopic observations are labeled by their reference names. Contours of Hα emission from ground-based imaging are overplotted in green. The H II regions are overplotted with the stars color-coded by log(Age)< 7.5 dex from the `BEAST` fits and include only good fits from the UV-optical catalog. Bottom panel: The optical CMDs are overplotted with the stars shown in the top panel and using the same color-coding for both regions.

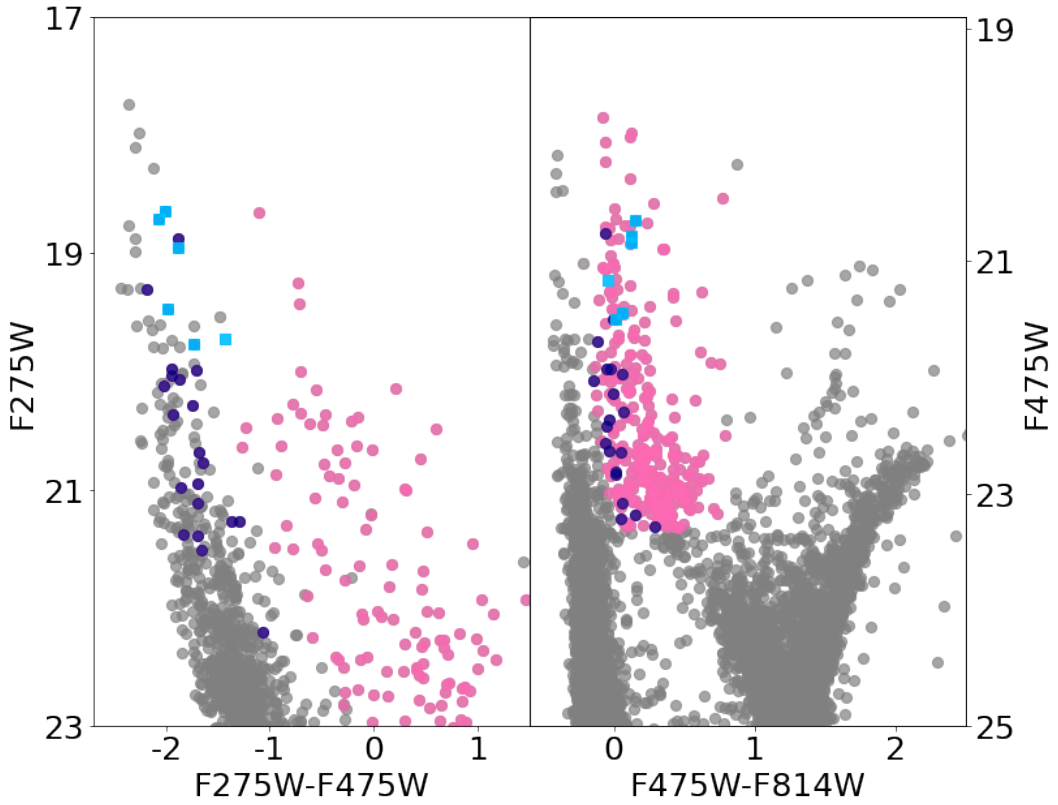


Figure 2.14: UV-optical (left) and optical (right) *HST*-based CMDs of Leo A. The pink colored circles are stars that appear in the BHeB region both in the UV and the optical CMD. The blue colored circles are stars that are stars that are on the MS in the UV CMD, but appear on or near the BHeB region in the optical CMD. The cyan squares are the stars identified as Be stars in our spectroscopic sample. This shows candidate Be stars could possibly pollute the BHeB in the optical CMD, and that we can filter for candidate Be stars in panchromatic photometry studies.

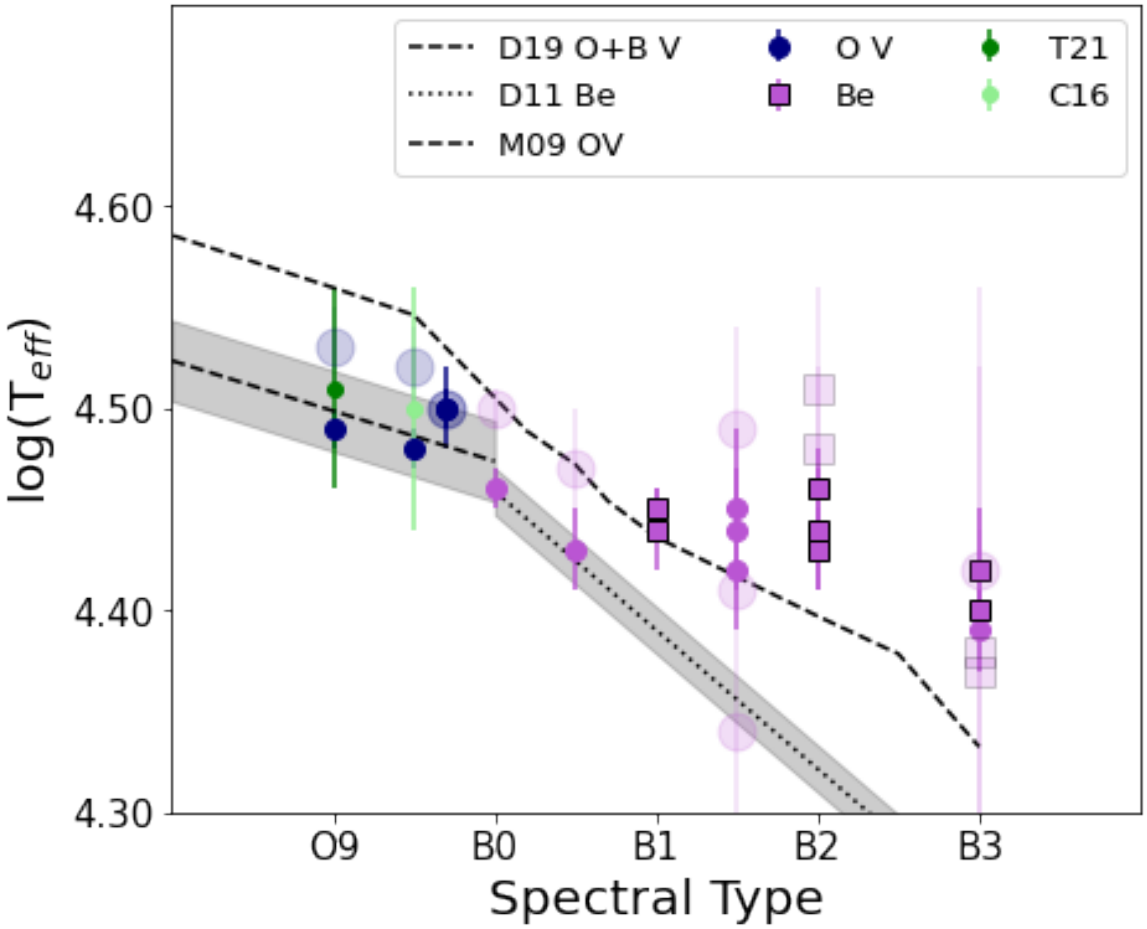


Figure 2.15: Properties of the OB-stars in Leo A. $\log(T_{\rm eff})$ is plotted vs. Spectral Type for early-type (O-B3) stars in our sample. The spectroscopically derived $\log(T_{\rm eff})$ are indicated by the solid markers, while the photometrically derived $\log(T_{\rm eff})$ are the fainter bigger markers. The O-stars in Leo A are blue circles, the B-stars purple circles, and the Be stars are purple squares. We compare our stars ($\chi^2 \leq 100$) with SMC results and Sextans A late-type O stars. For the SMC O-stars we fit a best line to the V type stars in Massey et al. (2009) (left-most black dashed line, M09). For the B-type stars we plot the O V and B V spectral types to the $\log(T_{\rm eff})$ scale derived by Dufton et al. (2019) (dashed line, D19). We also plot the fit to the Be stars in the SMC from Dunstall et al. (2011) (dotted line, D11). Furthermore, we plot the two late-type O stars observed by Telford et al. (2021) (dark green, T21) and Camacho et al. (2016) (light green, C16) in Sextans A, for which there is a $\log(T_{\rm eff})$ measurement for the spectral type.

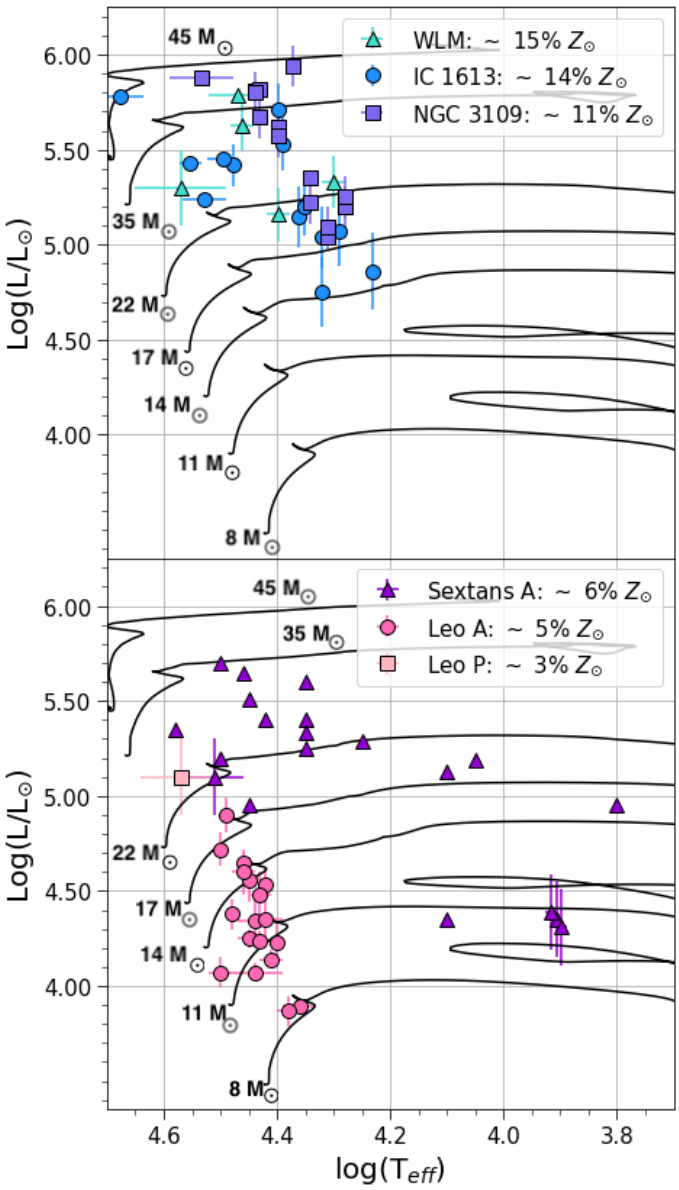


Figure 2.16: The HR diagrams of massive sub-SMC metallicity stars in the Local Group with derived stellar parameters. We overplot MIST tracks. **Top**: All the stars with temperatures and luminosities in the metal-poor galaxies: WLM (~ 15 % $Z_\odot$; aqua triangle), IC 1613 (~ 14 % $Z_\odot$; blue circles), and NGC 3109 (~ 11 % $Z_\odot$; purple-blue squares). The WLM stars are from Bresolin et al. (2006), Tramper et al. (2011), Tramper et al. (2014), and Telford et al. (2021); the IC 1613 stars are from Bresolin et al. (2007), and the NGC 3109 stars are from Evans et al. (2007), Tramper et al. (2014), and Hosek et al. (2014). **Bottom**: All stars with temperatures and luminosities in the extremely metal-poor galaxies Sextans A (~ 6 % $Z_\odot$; purple triangle) and Leo P (~ 3 % $Z_\odot$; rose squares). As well as the stars in our spectroscopic sample (~ 5 % $Z_\odot$; pink circles). The Sextans A stars are from Kaufer et al. (2004), Camacho et al. (2016), and Telford et al. (2021); the Leo P star is from Telford et al. (2021). Our sample represents the first extended sample of MS stars at sub-SMC metallicities with derived stellar parameters. Furthermore it is the largest sample at sub-10% $Z_\odot$ with derived stellar parameters.

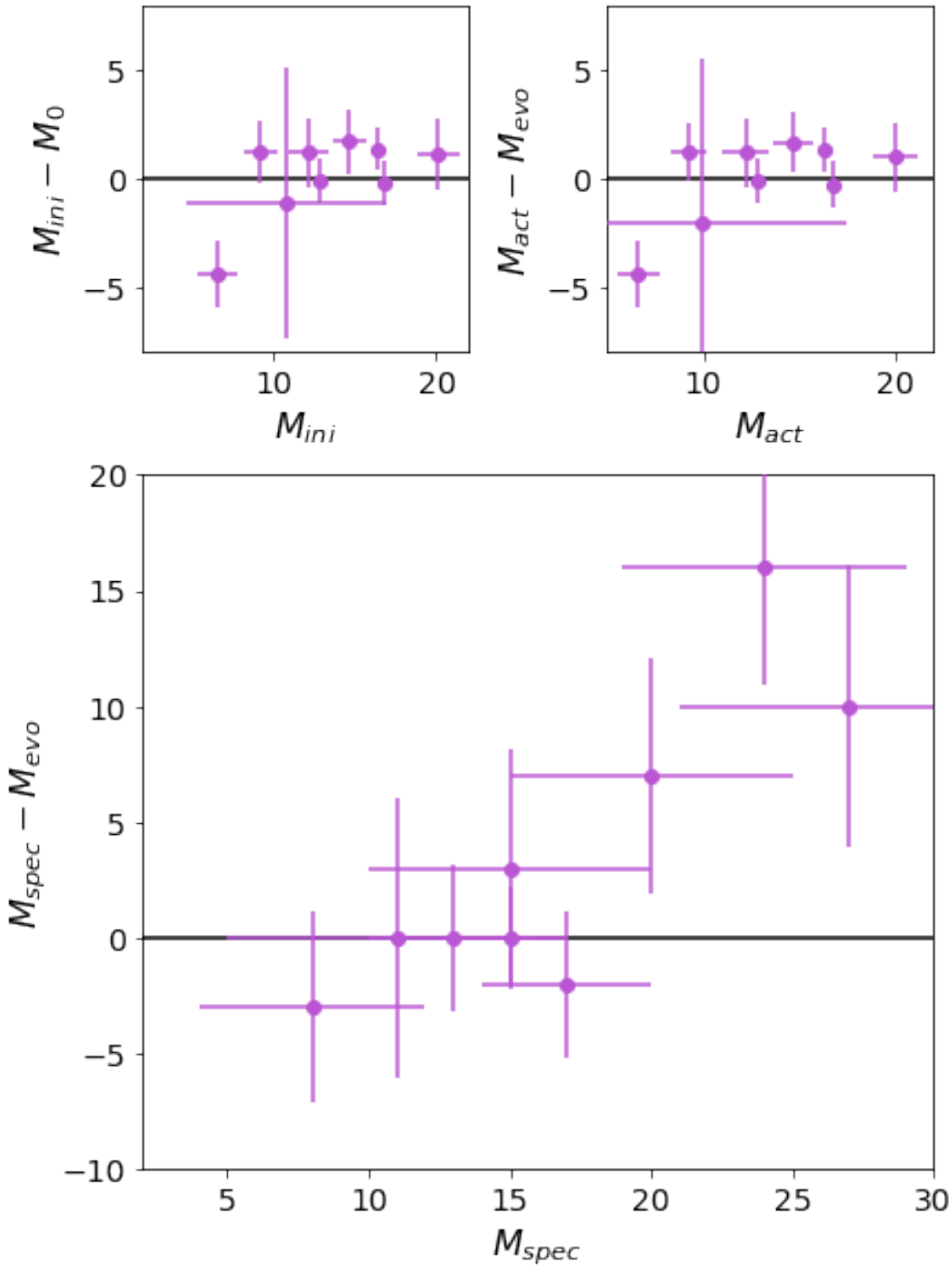


Figure 2.17: Three panels comparing the different masses derived throughout the study; M_{ini} and M_{act} from the photometry, M_0, M_{evo}, and M_{spec} from the spectroscopy. The top left panel compares the initial masses derived from each method (M_{ini} vs M_0). The top right panel compares the present-day masses derived from each method using evolutionary tracks and isochrones (M_{act} vs M_{evo}). The bottom panel compares the present-day masses derived from spectroscopy (M_{spec} vs M_{evo}). We show all stars with $\chi^2 < 100$ in both photometry and spectroscopy.

2.9 Acknowledgments

MG thanks Miriam Garcia, Chris Evans, Sally Oey, Nate Bastian, Morgan Fouseneau, Dietrich Baade and the referee for helpful discussions, feedback or comments. MG acknowledges support of the "Schweizerische Studienstiftung" and UC Berkeley Cranor Fellowship. Support for this work was provided by NASA through grants GO-15275, GO-15921, GO-16162, GO-16717, AR-15056, AR-16120, and HST-HF2-51457.001-A from the Space Telescope Science Institute, which is operated by AURA, Inc., under NASA contract NAS5-26555.

The authors wish to recognize and acknowledge the very significant cultural role and reverence that the summit of Maunakea has always had within the indigenous Hawaiian community. We are most fortunate to have the opportunity to conduct observations from this mountain.

Part of the data presented herein were obtained at the W. M. Keck Observatory, which is operated as a scientific partnership among the California Institute of Technology, the University of California and the National Aeronautics and Space Administration. The Observatory was made possible by the generous financial support of the W. M. Keck Foundation. Further, this data was made accessible by the Keck Observatory Archive (KOA), which is operated by the W. M. Keck Observatory and the NASA Exoplanet Science Institute (NExScI), under contract with the National Aeronautics and Space Administration.

Part of the data presented here were obtained at the MMT Observatory, a joint facility of the University of Arizona and the Smithsonian Institution.

This work is based on photometric observations made with the NASA/ESA Hubble Space Telescope, obtained from the data archive at the Space Telescope Science Institute. STScI is operated by the Association of Universities for Research in Astronomy, Inc. under NASA contract NAS 5-26555.

This work made extensive use of NASA's Astrophysics Data System Bibliographic Services.

2.10 Appendix

2.10.1 The Effects of Stellar Model Choice on Photometric Fitting Results

We compare the stellar parameters derived from the `BEAST` using the different stellar models models it has available. They are: (i) MIST models with no rotation (MIST_{NR}; Choi et al. 2016); (ii) MIST models with rotation (MIST_{R}; Choi et al. 2017); (iii) the PARSEC models that do not have rotation (PARSEC; Bressan et al. 2012). We limited this

comparison to massive stars that fall within our spectroscopy color and magnitude limits ($F475W < 22$ and $F475W - F814W < 0.5$). This selects MS stars with $M \gtrsim 5M_{\odot}$

We compare parameters derived for the same stars from two different models. We divide the photometric SED fits into 3 groups based on the reduced χ^2 values. Fits with $\chi^2 < 20$ for models being compared are considered good fits. Values of $\chi^2 \geq 80$ in either of the evolutionary models are considered poor fits. All other fits are fits of decent quality. These categories are only meant to be used qualitatively to facilitate discussion. When comparing the agreement between different parameters we only use stars deemed to have good or decent fits.

Fig.,2.18 shows a comparison between MIST$_R$ and MIST$_{NR}$ in the left column and the between MIST$_R$ and PARSEC in the right column. The y-axis is the difference between parameter values for the two models and the x-axis is the MIST$_R$ parameter values.

For $\log(T_{\rm eff})$ (top row), the MIST$_R$ versus MIST$_{NR}$ we find a median absolute deviation (MAD) of 0.01 dex and median difference of -0.01 dex. The 16th and 84th percentiles of the difference span 0.04 dex (i.e., $\pm$0.02 dex around the median). This indicates that the differences are smaller than scatter in the data. In general, these findings show that for decent and good fit stars the rotational and non-rotational models are generally consistent with each other. We note that the scatter is larger for stars with $\log(T_{\rm eff})> 4.0$, where we find a MAD of 0.03 dex and scatter of 0.05 dex. As discussed in Choi et al. (2017), at this $\log(T_{\rm eff})$ the MIST models change mass loss prescriptions, which offers on possibility for the increased scatter. For MIST$_R$ versus PARSEC we find a MAD of 0.01 dex and a median difference of 0.00 ± 0.02 dex. The two models provide consistent values of $\log(T_{\rm eff})$.

The second row shows $\log(g)$. For the MIST$_R$ versus MIST$_{NR}$ we find a MAD of 0.05 dex and a median of -0.11 ± 0.09 dex. This implies that MIST$_{NR}$ has systematically larger $\log(g)$ values than MIST$_R$. It is possible that rotation may affect $\log(g)$ (e.g., due to line broadening), which could contribute to the disagreement. For the MIST$_R$ versus PARSEC we find a MAD of 0.02 and a median difference of 0.00 dex. The 16th and 84th percentiles of the difference span 0.08 dex ($\pm$0.04 dex), indicating that MIST$_R$ versus PARSEC are consistent with each other.

The third row shows M_{ini}. For the MIST$_R$ versus MIST$_{NR}$ we find a MAD of $0.46M_{\odot}$ and a median of $-0.78 \pm 0.97M_{\odot}$. The two models are consistent, but MIST$_{NR}$ return slightly larger values of M_{ini} values for more massive stars. For the MIST$_R$ versus PARSEC, we find a MAD of $0.06M_{\odot}$ and and median difference of $0.05 \pm 0.29M_{\odot}$. MIST$_R$ and PARSEC are consistent with each other. There is one clear outlier, which appears to be a good fit (i.e. $\chi^2 < 20$) for both model fits. Interestingly, for all other parameters the fits are consistent with each other. We currently do not have spectra to further investigate this star.

The fourth row shows $\log(L/L_{\odot})$. For the MIST$_R$ versus MIST$_{NR}$ we find a MAD of 0.04 dex and and median of 0.15 ± 0.14 dex. In this case MIST$_R$ returns slightly higher luminosities than MIST$_{NR}$. For the MIST$_R$ versus PARSEC we find a MAD of 0.02 dex and

median difference of -0.01 ± 0.09 dex. Showing that MIST$_R$ versus PARSEC are consistent.

The fifth row shows log(A). For the MIST$_R$ versus MIST$_{NR}$ we find a MAD of 0.10 dex and and median of 0.20 ± 0.42 dex. We find the two models are consistent. For the MIST$_R$ versus PARSEC we find a MAD of 0.00 dex and median difference of 0.00 ± 0.06 dex. The MIST$_R$ versus PARSEC models also yield values that are consistent.

The bottom row shows A_V. For the MIST$_R$ versus MIST$_{NR}$ we find a MAD of 0.04 dex and and median of -0.01 ± 0.05 dex. Interestingly, most of the high A_V values in either models are also associated with poor fits. The presence of larger A_v values in a galaxy wit minimal dust may be an indicator that we are not observing "normal" stars. Overall, the A_V values from both models are consistent. For the MIST$_R$ versus PARSEC we find a MAD of 0.02 dex and median difference of -0.02 ± 0.04 dex, indicating that MIST$_R$ versus PARSEC derived parameters are consistent.

We list all the parameters for the stars covered by the spectroscopic sample in Tables 2.8 and 2.9. We note that between all three evolutionary models the MIST$_R$ models yield the best reduced χ^2 values for all stars. Overall, MIST$_R$ versus PARSEC yields consistent results, meaning that they can be used interchangeably.

2.10.2 Detailed discussion of individual stars

2.10.2.1 O-Type Stars

K2/B2: K2/B2 is the second brightest star in our sample ($F475W_{VEGA} = 20.24$ and $F336W_{VEGA} = 18.57$). Like K1, its locations on the UV and optical CMDs indicate it is likely an O star. Its spectrum is shown in Figure 2.8. We list its EW measurements in Table 2.3 and comment only on a subset of those features.

The spectrum shows the characteristics of a typical late-type O-star. We find emission line contamination in the Balmer series, which is not surprising given K2's location in the middle of an H II region. The narrow emission lines are particularly clear for Hα and Hβ and weaker in the Hγ. The 2D spectrum shows that emission is spatially extended, consistent with a nebular origin. In most cases, we can only derive upper limits of EWs for the absorption features. Thus, we can only roughly estimate the spectral type. Following the EW classification process described for K1, we find that K2 is an O9.7 V type star in all the schemes (Sota et al. 2011, Martins 2018, Castro et al. 2008).

When fitting the full spectrum using `The Payne`, we mask lines clearly affected by emission (e.g., the Hα feature and the center of the Hβ feature). The spectroscopic analysis yields log($T_{\rm eff}$)= 4.50 ± 0.01 dex and log(g)= 4.10 ± 0.02 dex, which is consistent with a late O-type MS star. We find a $v \sin i$= 95 ± 20 kms^{-1}, which is reasonable for a late O-type star. Using equations 1-3, we derive $M_{spec} = 27 \pm 6 M_\odot$ and $M_0 = 17 \pm 1 M_\odot$, and log($L/L_\odot$) = 4.72 ± 0.09 dex. Overall this agrees well with the EW measurements and the CMD location. We find the SED fitting yields log($T_{\rm eff}$)= 4.50 ± 0.01 dex and

Table 2.8: Photometric parameters determined using the BEAST and the PARSEC models. The columns are:(1) star name; (2) initial mass; (3) temperature; (4) surface gravity; (5) luminosity; (6) extinction parameter; (7) stellar age in log-space; (8) reduced χ^2 yielded by the BEAST; (9) number of *HST* bands used for the SED fitting, when the value is 4 we observed F275W, F336W, F475W and F814W. When the value is 6, we additionally observed F110W and F160W. Columns (2), (6) and (7) lists primary parameters, while columns (3), (4) and (5) list derived parameters.

Star	M_{ini}	$\log(T_{eff})$	$\log(g)$	$\log(L/L_\odot)$	A_v	log(Age)	χ^2	Nr. of filters	notes
	$M_\odot$								
(1)	(2)	(3)	(4)	(5)	(6)	(7)	(8)	(9)	(10)
K1	24 ± 3.67	4.59 ± 0.05	4.08 ± 0.14	5.02 ± 0.12	0.06 ± 0.03	6.80 ± 0.18	17	6	O9V
K2	16.8 ± 0.16	4.50 ± 0.01	3.88 ± 0.01	4.74 ± 0.01	0.03 ± 0.02	7.00 ± 0.07	13	4	O9.7 V
K3	13.3 ± 1.05	4.42 ± 0.02	3.67 ± 0.06	4.54 ± 0.07	0.10 ± 0.04	7.15 ± 0.09	7	6	B1.5 V
K7	15.9 ± 0.17	4.54 ± 0.01	4.24 ± 0.01	4.50 ± 0.02	0.08 ± 0.03	6.8 ± 0.07	21	4	O9.5 V
B4	16.3 ± 0.15	4.50 ± 0.01	3.93 ± 0.01	4.69 ± 0.01	0.03 ± 0.02	7.0 ± 0.07	13	6	B0V
B7	8.6 ± 0.08	4.34 ± 0.01	3.70 ± 0.01	3.99 ± 0.01	0.33 ± 0.07	7.5 ± 0.07	371	4	P-Cyg B1 V / Be1 V
B9	15.9 ± 0.15	4.54 ± 0.01	4.24 ± 0.01	4.50 ± 0.01	0.48 ± 0.02	7.00 ± 0.07	104	6	B2 V
B10	7.5 ± 0.16	4.33 ±0.02	3.72 ± 0.01	3.86 ± 0.01	0.38 ± 0.03	6.8 ± 0.07	80	6	B0.5 V
B11	4.7 ± 0.29	4.22 ±0.02	3.70 ± 0.03	3.23 ± 0.06	0.08 ± 0.03	7.60 ± 0.08	16	6	B2 V
B12	6.5 ± 2.05	4.30 ± 0.08	3.81 ± 0.14	3.57 ± 0.29	0.04 ± 0.04	7.70 ± 0.25	6	4	B1.5V
B13	10.9 ± 0.11	4.47 ±0.01	4.28 ± 0.01	4.05 ± 0.01	0.03 ± 0.03	7.00 ± 0.07	7	4	O9.7 V
B14	5.3 ± 0.90	4.27 ± 0.04	3.83 ± 0.08	3.37 ± 0.14	0.03 ± 0.02	7.9 ± 0.17	16	6	B3 V

Table 2.9: Photometric parameters determined using the BEAST and the MIST models with $v/vcrit$ = 0.0. The columns are:(1) star name; (2) initial mass; (3) temperature; (4) surface gravity; (5) luminosity; (6) extinction parameter; (7) stellar age in log-space; (8) reduced χ^2 yielded by the BEAST; (9) number of *HST* bands used for the SED fitting, when the value is 4 we observed F275W, F336W, F475W and F814W. When the value is 6, we additionally observed F110W and F160W. Columns (2), (6) and (7) lists primary parameters, while columns (3), (4) and (5) list derived parameters.

Star	M_{ini}	$\log(T_{eff})$	$\log(g)$	$\log(L/L_\odot)$	A_v	log(Age)	χ^2	Nr. of filters	notes
	$M_\odot$								
(1)	(2)	(3)	(4)	(5)	(6)	(7)	(8)	(9)	(10)
K1	19.0 ± 0.4	4.49 ± 0.01	3.87 ± 0.02	4.74 ± 0.01	0.03 ± 0.02	6.6 ± 0.07	18	6	O9V
K2	16.0 ± 0.2	4.44 ± 0.01	3.79 ± 0.01	4.57 ± 0.01	0.03 ± 0.02	6.8 ± 0.07	12	4	O9.7 V
K3	14.6 ± 1.1	4.41 ± 0.03	3.71 ± 0.10	4.48 ± 0.08	0.07 ± 0.05	6.9 ± 0.11	20	6	B1.5 V
K7	15.0 ± 0.3	4.47 ± 0.01	4.13 ± 0.02	4.31 ± 0.01	0.03 ± 0.02	5.6 ± 0.08	36	4	O9.5 V
B4	17.0 ± 0.5	4.48 ± 0.01	3.93 ± 0.05	4.59± 0.03	0.04 ± 0.02	6.6 ±0.12	13	6	B0V
B7	10.0 ± 0.2	4.33 ± 0.01	3.72 ± 0.01	3.98 ± 0.01	0.18 ± 0.03	7.2 ±0.07	230	4	P-Cyg B1 V / Be1 V
B9	14.4 ± 0.5	4.46 ± 0.01	4.13 ± 0.02	4.27 ± 0.04	0.40 ± 0.04	5.9 ± 0.28	107	6	B1.5 V
B10	13.4 ± 0.8	4.43 ± 0.02	4.03 ± 0.05	4.22 ± 0.05	0.45 ± 0.04	6.5 ± 0.25	73	6	B0.5 V
B11	11.3 ± 0.2	4.41 ± 0.01	4.15 ± 0.01	3.94 ± 0.01	0.13 ± 0.03	5.9 ± 0.10	9	6	B2 V
B12	10.6 ± 0.9	4.38 ± 0.03	4.03 ± 0.06	3.90 ± 0.10	0.05 ± 0.04	6.8 ± 0.43	3	4	B1.5V
B13	6.0 ± 0.1	4.59 ± 0.02	3.39 ± 0.02	4.34 ± 0.01	0.05 ± 0.03	7.9 ± 0.07	52	4	O9.7 V
B14	11.0 ± 0.2	4.40 ± 0.01	4.13 ± 0.01	3.91 ± 0.01	0.13 ± 0.03	6.2 ± 0.07	200	6	B3 V

$\log(g)= 3.85 \pm 0.02$ dex, which are also consistent with a late O-type star.

K4: K4 is among the brighter stars ($F475W_{VEGA}$ = 20.65 and $F336W_{VEGA}$ = 19.04) in our spectroscopic sample. On the CMD, it is located on the BHeB sequence in the optical, but appears on the MS in the UV-optical CMD. Its spectrum is shown in Figure 2.8. We list its EW measurements in Table 2.3 and comment only on a subset of those features. It is not located near a known H II region (Fig. 2.3).

Several of the spectral features suggest a Be-type star: He I, Mg II, Si III and Si IV are in absorption. The Balmer lines are strong in emission for Hβ and Hγ and we observe emission features within absorption for Hδ and Hϵ. Based on the EWs we classify K4 as Be1 V (Evans et al. 2015; Castro et al. 2008).

K4 only has measurements in 4 bands (2 UV and 2 optical), since the stars falls outside of the NIR footprint. This makes the composite photometry method not viable, since we cannot constrain the disk. Using the adapted spectroscopy method, we determine that $\log(T_{\rm eff})_{,star}$ = 4.45 ± 0.01 dex and $v \sin i$= 339 ± 10 kms^{-1}. This is inline with a early type Be star. The high $v \sin i$ is a key indicator that the star has to be a rotating MS star as opposed to a BHeB star. An evolved star would break apart at such high $v \sin i$ (e.g., Rivinius et al. 2013). Furthermore, the scenario is supported by Leščinskaitė et al. (2022) whose photometric analysis shows that K4 is a strong Hα emitter, similar to K6 and K8.

B4: B4 is the 3rd brightest star in the sample ($F475W$ = 20.40 and $F336W$ = 18.75). Its location in the optical and UV CMDs are typical of a MS star. Its spectrum is shown in Figure 2.8. We list its EW measurements in Table 2.3 and comment only on a subset of those features.

The spectra shows the characteristics of a late O-type/early B-type star: He I, He II, Si II, Si III and Si IV in absorption and emission. B4 shows weak emission in the wings of Hβ, Hγ, Hδ and Hϵ absorption lines. Hα is in absorption with weak narrow emission at the central wavelength. Based on the EW and the schemes by Lennon (1997), Evans et al. (2015) and Castro et al. (2008), we type this as a B0V type star.

We model the full spectrum of B4, but mask out pixels clearly affected by emission lines, as they are not captured by the TLUSTY models. Our spectroscopic fitting yields $\log(T_{\rm eff})= 4.46 \pm 0.01$ dex and $\log(g)= 3.75 \pm 0.04$ dex, which is consistent with a early B-type star. Using equations 1-3, we derive $M_{spec} = 15 \pm 2 M_{\odot}$ and $M_0 = 15 \pm 1 M_{\odot}$, and $\log(L/L_{\odot}) = 4.65 \pm 0.05$ dex. Overall, this aligns well with the EW measurements and the CMD location.

The results from SED fitting are consistent with the spectroscopic parameters. The SED fitting yields $\log(T_{\rm eff})= 4.50 \pm 0.01$ dex and $\log(g)= 3.91 \pm 0.01$ dex. The photometric parameters are also consistent with a late-type O star. However, given the cooler $\log(T_{\rm eff})$ from spectroscopy and the EW analysis from the spectra, we conclude the star is likely an

early B-type star.

K5: K5 ($F475W_{VEGA}$ = 20.78 and $F336W_{VEGA}$ = 19.19), like the previous stars, is located on the BHeB sequence in the optical, but appears on the MS in the UV-optical CMD. Its spectrum is shown in Figure 2.8. We list its EW measurements in Table 2.3 and comment only on a subset of those features.

The spectral features suggest a early Be-type star: He I is in absorption and emission. Mg II and Si III is in absorption. It is possible that He II is in absorption, but the features is nearly indistinguishable from the continuum. We do not detect any other absorption features for any other elements. This is likely because the fast rotation of the star has washed out these features. For the Balmer lines we find Hβ in emission, we note that the star is not near any H II regions. Hγ shows emission within the absorption profile. We further note that the Hδ feature appears to have emission nearly cancelling the absorption feature. Based on the presence of Si IV and the He I lines, using the classification scheme of Castro et al. (2008) we determine the star is likely an early Be2 V star. The Be-star scenario is supported by Leščinskaitė et al. (2022) which finds that K4 is a strong Hα emitter, similar to K6 and K8.

Strong emission in the Balmer lines and the high reduced χ^2 (> 300) in the photometry, lead us to adopt the adapted methods. We only have observations in 4 bands, making the composite photometric fitting not possible, since we cannot constrain the disk properties. Using the adapted spectroscopic method, we determine $\log(T_{\rm eff})_{,star}$ = 4.46 ± 0.02 dex and $v \sin i$= 370 ± 90 kms^{-1}. This is consistent with an early type Be star.

B5: B5 ($F475W_{VEGA}$ = 21.5 and $F336W_{VEGA}$ = 20.18) is located on the BHeB sequence in the optical CMD, but appears on the MS in the UV-optical CMD. Its spectrum is shown in Figure 2.8. We list its EW measurements in Table 2.3 and comment only on a subset of those features.

The spectrum shows the characteristics of a typical early/mid-type Be star. He I, Si II and Mg II are in absorption Hα is in emission, while Hβ shows a strong emission component within its absorption feature. The remaining Balmer lines are all in absorption with weak emission features. We estimate the stellar type of Be3 V using its EWs (Castro et al. 2008).

Balmer line emission and the large `BEAST` reduced χ^2 (> 200) hint at the presence of a disk. Using the adapted spectroscopic method (§2.5.3), we determine $\log(T_{\rm eff})$= 4.40 ± 0.01 dex and $v \sin i$= 165 ± 15 kms^{-1}. This is inline with a early to mid type Be star. Using the composite photometric method, we determine that the star has a $\log(T_{\rm eff})_{,star}$ = $4.38\pm^{0.13}_{0.04}$ dex and $\log(T_{\rm eff})_{,disk}$ = 3.74 ± 0.17, which is inline with the spectroscopic findings. Leščinskaitė et al. (2022) had identified B5 as a strong Hα emitter based on photometry.

K7/B6: K7/B6 ($F336W_{VEGA}$ = 18.57, $F475W_{VEGA}$ = 19.46) appears to be an O-type star based on its CMD location.Its spectrum is shown in Figure 2.8. We list its EW measurements in Table 2.3 and comment only on a subset of those features.

We observe both He I and He II in absorption. We further measure Mg II in absorption. Most Balmer lines appear in absorption; though the spectral region around Hα does not show a clear Gaussian absorption feature. However, due to the low resolution (R~1250), it is not clear if this is a data artifact or if there are other physical processes at work (e.g., stellar winds). The EW ratios suggest that K7 is an O9.7 (Sota et al. 2011) or O9.5 (Martins 2018) type star, with a luminosity class of V (Martins 2018). Lastly, using Castro et al. (2008), we determine the star to be an O9.5 V star. This fits well with the star's position in the CMD (See Fig. 4.2).

The median parameters from full spectral fitting for K7 are $\log(T_{\rm eff})$= 4.48 ± 0.01 dex and $\log(g)$= 4.04 ± 0.02 dex (Table 2.4). Like the EW ratios, these values indicate the K7 is a late-type O star. The derived $\log(g)$ is consistent with K7 being a MS star. We find a $v \sin i$ = 97 ± 20 kms^{-1}. Using equations 1-3, we derive M_{spec} = 13 ± 3$M_{\odot}$ and M_0 = 13 ± 1$M_{\odot}$, and $\log(L/L_{\odot})$ = 4.38 ± 0.08 dex . These values are in agreement with the classification derived from the EW measurements and its location on the CMD. The spectroscopic and photometric parameters for K7 are in broad agreement, although we observe an elevated $\log(g)$ value similarly to K1. The photometric parameters are $\log(T_{\rm eff})$= 4.52 ± 0.02 dex and $\log(g)$= 4.23 ± 0.05 dex, both analyses are consistent with this being an O-type star. We find that M_0 and M_{ini} as well as M_{spec} and M_{act}, are consistent with each other.

B7: B7 ($F475W_{VEGA}$ = 21.35 and $F336W_{VEGA}$ = 20.31) is amongst the bluest stars in the optical CMD, but in the UV the star appears to be amongst the reddest stars. Its spectrum is shown in Figure 2.8. We list its EW measurements in Table 2.3 and comment only on a subset of those features.

The star shows emission resembling a P-Cygni profile in each of its Balmer lines. The clearest P-Cygni feature is the Hβ line, since Hα shows a strong emission feature. The central wavelength of Hα falls in the blue-wing of the emission feature hinting at a P-Cygni profile. Hγ and Hδ on the other hand show narrow absorption features with very weak emission on the red side. We find He I, Mg II ,Si II, Si III, Si IV and C I are in absorption (See Table 2.3. We also find He I in emission, as well as N III, O II, C II. Based on the EW ratios and following Castro et al. (2008), we determine the star to be an early B1-type/Be1-type star.

The strong emission appears to be associated with the star, as opposed to being gaseous in origin. B7 is not near the known H II regions (See Fig.2.3). Due to the strong emission in the Balmer lines and the high reduced χ^2 ($\chi^2 > 300$) in the photometry, we adopt here

the alternative fitting methods introduced in §2.5.3. B7 only has measurements in 4 bands (2 UV and 2 optical), since the stars falls outside of the NIR footprint. This makes the composite photometry method not viable, since we cannot constrain the NIR to determine the nature of the star's SED profile.

Using this adapted spectroscopic method, we find $\log(T_{\rm eff})= 4.44 \pm 0.02$ dex, and $v \sin i= 125 \pm 11$ kms^{-1}(See Table 2.5).

K8: K8 ($F475W_{VEGA}$ = 21.45 and $F336W_{VEGA}$ = 19.88), like the previous star, is located on the BHeB sequence in the optical CMD, but appears on the MS in the UV-optical CMD. Its spectrum is shown in Figure 2.8. We list its EW measurements in Table 2.3 and comment only on a subset of those features.

The Keck spectrum of K8 is shown in Fig.,2.8. The spectral features suggest a early-type fast rotating Be star: We find He I, Si III and Si IV in absorption and He II in emission. The Balmer lines shows emission in Hβ. Hγ appears to show an emission feature within its absorption feature. Interestingly, Hδ feature is a very shallow absorption feature and lastly, we find Hϵ in absorption. All spectral features are quite shallow, indicating that there is significant rotation. Based on the detected upper limits for both He II and Si, we type the star as a early Be2 V. Similarly to K6, Leščinskaitė et al. (2022) had identified K8 as a strong H-α emitter. Due to the stars similarity to K6, both in spectroscopy and photometry, we use the described alternative method of fitting the data (See §2.5.3).

Using our adapted spectroscopic method, we determine that $\log(T_{\rm eff})= 4.44 \pm 0.03$ dex and $v \sin i= 290 \pm 10$ kms^{-1}. This is consistent with an early type Be star. Using the composite photometric method, we determine that $\log(T_{\rm eff})_{,star} = 4.51\pm^{0.04}_{0.06}$ dex and $\log(T_{\rm eff})_{,disk} = 3.64\pm^{0.10}_{0.04}$ dex, which is inline with the spectroscopic method.

B8: B8 is a faint star ($F475W_{VEGA}$ = 21.5 and $F336W_{VEGA}$ = 20.18) and is the reddest of those we observed with MMT. Its spectrum is shown in Figure 2.8. We list its EW measurements in Table 2.3 and comment only on a subset of those features.

The spectrum contain several unusual features. We observe only upper limit for He I in B8, and we find Mg II and Si II in absorption.

Hα and Hβ are in emission and both show a double peaked line profile. For the other Balmer lines are combined absorption and emission features, we observe a widened wing and narrow absorption within the emission lines. It is likely that emission in the wings is making line profiles shallower. Using the EWs, we classify the star as a Be3 V (Castro et al. 2008). Lastly, the distinct Balmer profiles suggest the star is most likely a shell star (i.e. a Be star viewed edge-on).

The unusual pattern of emission and absorption in the Balmer lines and the high χ^2(> 200) in the BEAST fitting suggest B8 may have a circumstellar disk.

Using the adapted spectroscopic method (§2.5.3), we determine that the star has

a $\log(T_{\rm eff})$= 4.42 ± 0.03 dex and $v \sin i$= 135 ± 80 kms^{-1}. This is inline with a early to mid type Be star. Using the composite photometric method, we determine that $\log(T_{\rm eff})_{,star}$ = $4.37\pm^{0.15}_{0.03}$ dex and $\log(T_{\rm eff})_{,disk}$ = $3.74\pm^{0.06}_{0.10}$ dex, which is inline with our previous findings. Interestingly, we would expect the $v \sin i$ to be higher given that we are likely looking at the star equator-on based on the doubled peaked profile in Hα. However, if the star is really viewed edge-on the $v \sin i$ value is surprisingly low. However, the uncertainty on our measurement are quite large, suggesting that the star could have a higher $v \sin i$ value more in line with expectation (e.g., Rivinius et al. 2013; Iqbal & Keller 2013; Arcos et al. 2018). Leščinskaitė et al. (2022) identified B8 as a strong Hα emitter. Despite the low $v \sin i$, the strong emission and spectral shape supports the classification of the star as a shell star.

B9: B9 is one of our fainter spectroscopic targets ($F475W$ = 21.67, $F336W$ = 20.25). Fig.,4.2 shows that B9 is located between the MS and the BHeB sequences. Its spectrum is shown in Figure 2.8. We list its EW measurements in Table 2.3 and comment only on a subset of those features.

The spectrum shows the characteristics of an early B-type star: We find He I, Si II, Si III and Mg II in absorption. The Hα appears in emission, while all other Balmer lines are in absorption. The Hα is marginally broader than what might be expected from purely gaseous emission, suggesting there may be a stellar contribution. The EW suggest that B9 is a B1.5 V in multiple classification schemes (Lennon 1997, Evans et al. 2015, and Castro et al. 2008).

We fit the full spectrum of B9 using `The Payne` and find $\log(T_{\rm eff})$= 4.45 ± 0.02 dex and $\log(g)$= 4.18 ± 0.08 dex, and $v \sin i$= 115 ± 20 kms^{-1}. Using equations 1-3, we derive M_{spec} = 15 ± 5$M_\odot$ and M_0 = 12 ± 2$M_\odot$, and $\log(L/L_\odot)$ = 4.26 ± 0.04. All in line with the rough classification described by the EW measurements and location in the CMD. The BEAST-based photometric parameters are $\log(T_{\rm eff})$= 4.49 ± 0.05 dex, $\log(g)$= 4.12 ± 0.68 dex and M_{ini} = 10.87 ± 6.13$M_\odot$. The parameters are consistent with the spectroscopic measurement.

B10: B10 ($F475W_{VEGA}$ = 21.7 and $F336W_{VEGA}$ = 20.35) is the faintest stars in our sample in the UV-optical CMD, but is brighter than several other stars in the optical-only CMD. Its spectrum is shown in Figure 2.8. We list its EW measurements in Table 2.3 and comment only on a subset of those features.

The spectrum shows the characteristics of a early B-type star with He I, Si III and Si IV in absorption. Hα is in strong emission, while Hβ and Hδ show modest emission within their absorption feature. Hγ and Hϵ are both in absorption. B10 is not near any known H II region, suggesting the emission is not likely due to nebular contamination. Based on the observed EWs we classify it as a B0.5 V (candidate Be) star.

We fit the full spectrum of B10 using The Payne and find $\log(T_{\rm eff})= 4.43 \pm 0.02$ dex, $\log(g)= 3.92 \pm 0.11$ dex, and $v \sin i= 141 \pm 25$ kms^{-1}. Using equations 1-3, we derive $M_{spec} = 11 \pm 6 M_{\odot}$ and $M_0 = 11 \pm 1 M_{\odot}$, and $\log(L/L_{\odot}) = 4.24 \pm 0.04$ dex. These all are consistent with the EW-based spectroscopic type and location on the CMDs.

The photometric parameters yield $\log(T_{\rm eff})= 4.47 \pm 0.03$ dex, $\log(g)= 4.02 \pm 0.07$ dex and $M_0 = 12.2 \pm 1.21 M_{\odot}$.

B11:B11 ($F475W_{VEGA} = 21.90$ and $F336W_{VEGA} = 20.25$) is the 2nd faintest star in the sample. Both in the optical-only and the UV-optical sample, it lies on the MS. Its spectrum is shown in Figure 2.8. We list its EW measurements in Table 2.3 and comment only on a subset of those features.

The spectrum shows the characteristics of an early B-type star. We find He I, Si II, Si III and Si IV in absorption. Most Balmer lines are in absorption with variable amounts of emission. For Hα, the strong emission nearly cancels out the absorption feature. Hβ and Hδ show nearly no emission in their absorption features. Although Hγ and Hϵ are predominantly in absorption, there is some emission in the blue wings. Taking the EWs, including upper limits at face value, we determine that the spectral type is a B2 type star (Evans et al. 2015, Castro et al. 2008).

Since B11 spectrum shows a SNR of <10, we cannot reliably recover the spectroscopic parameters. The photometric parameters are $\log(T_{\rm eff})= 4.27 \pm 0.04$ dex, $\log(g)= 3.81 \pm 0.06$ dex and $M_{ini} = 6.26 \pm 0.69 M_{\odot}$. The photometric are consistent with the stars position in the CMDs as well as the spectral type derived from the EW.

Given the SNR is ~10, we refrain from making any further speculations as to the origin of the emission.

B12: B12 is among the faintest stars in our sample ($F475W_{VEGA} = 21.75$ and $F336W_{VEGA} = 20.19$). Its location in the optical and UV CMDs are typical of a MS star. Its spectrum is shown in Figure 2.8. We list its EW measurements in Table 2.3 and comment only on a subset of those features.

The spectrum shows the characteristics of an early B-type star. He I, Si III and Si IV are detected in absorption. The Balmer lines show absorption features with emission for Hα, Hβ and Hγ. Overall, the emission within the star appears to be predominantly stellar, since the star is not near any know gas region. The emission feature overall appear quite weak in comparison to the other stars with emission in this sample. Lastly, based the He EW ratios, the presence of Si IV, and absence of Mg II we use the classification scheme of Castro et al. (2008) to conclude that the star is likely an B1.5V star.

We fit the full spectrum of B12 using The Payne. The parameters for the spectral fitting are listed in Table 2.4. For B12, we find $\log(T_{\rm eff})= 4.44 \pm 0.05$ dex and $\log(g)= 4.00 \pm 0.10$ dex. Using equations 1-3, we derive $M_{spec} = 8 \pm 4 M_{\odot}$ and $M_0 = 11 \pm 2 M_{\odot}$, and $\log(L/L_{\odot}) = 4.07 \pm 0.05$ dex. All in line with the rough classification described by the

EW measurements and location in the CMD. The photometric parameters yield $\log(T_{\rm eff})$= 4.34 ± 0.05 dex, $\log(g)$= 3.86 ± 0.08 dex and M_{ini} = 6.61 ± 1.21$M_{\odot}$.

B13: B13 ($F336W_{VEGA}$ = 20.25 and $F475W_{VEGA}$ = 21.9) is among the faintest stars in the optical-CMD, but is much brighter than several other stars in the UV-optical CMD. Its location on the UV and optical CMDs indicates it is likely a late-type O-type. Its spectrum is shown in Figure 2.8. We list its EW measurements in Table 2.3 and comment only on a subset of those features.

The spectrum shows the characteristics of a typical late-type O-star: He I and He II are in absorption. Most Balmer lines appear in absorption with light contamination; except $H\alpha$ which is fully in emission. The low SNR (SNR ∼ 12) makes is challenging to definitely classify this star. It is likely that B13 is a late O-type MS star. However, it may also be consistent with a early B-type star; we cannot rule this out. Based on the scheme applied thus far for EW we determine the star is an O9.7-B0 dwarf.

From full spectral fitting of B13, we find $\log(T_{\rm eff})$= 4.50 ± 0.02 dex, and $\log(g)$= 4.64 ± 0.06 dex. Using equations 1-3, we derive M_{spec} = 19 ± 4$M_{\odot}$ and M_0 = 12 ± 1$M_{\odot}$, and $\log(L/L_{\odot})$ = 4.07 ± 0.08. M_0 and M_{ini} are consistent, but M_{spec} appears to be too large, once again this is likely due to the high $\log(g)$ value. The emission in the Balmer lines might affect the $\log(g)$, since the parameter is the most sensitive to it. Nevertheless, these values are in line with the rough classification described by the EW measurements and location in the CMD.

SED fitting yields $\log(T_{\rm eff})$= 4.50 ± 0.01 dex and $\log(g)$= 4.37 ± 0.02 dex. Similarly to other O-stars, we find consistency in $\log(T_{\rm eff})$ and a slight discrepancy in $\log(g)$. M_0 and M_{ini} are consistent with one another.

Given that the star shows narrow emission features, poor spectroscopic fitting, and extended emission in the 2D spectra, we postulate that the star must have some nebular contamination.

B14: B14 ($F475W_{VEGA}$ = 21.9 and $F336W_{VEGA}$ = 20.40) is the faintest star in our sample in the optical-only CMD, but is brighter than several stars in the UV-optical CMD. In both cases it lies on the MS. Its spectrum is shown in Figure 2.8. We list its EW measurements in Table 2.3 and comment only on a subset of those features.

The spectrum shows the characteristics of a early/mid B-type star with emission in that He I features show both absorption and emission. We also find Mg II, Si II, Si III in absorption and [O II] in emission. B14 shows Hα is primarily present in absorption. Furthermore, we find that Hβ, Hγ and Hδ all show some potential emission in their wings. However, due to the low SNR (SNR ∼ 15) of the spectrum, the weak emission in the Balmer lines could be artifacts of the data. Based on the classification scheme previously employed for EWs, we determine the star is B3 star.

We fit the full Keck spectrum of B14 using `The Payne` and find $\log(T_{\rm eff})$= 4.39 ± 0.02 dex, $\log(g)$= 4.41 ± 0.08 dex, and $v \sin i$= 80 ± 15 kms^{-1}. Using equations 1-3,

we derive $M_{spec} = 24 \pm 5 M_{\odot}$ and $M_0 = 8 \pm 1 M_{\odot}$, and $\log(L/L_{\odot}) = 3.87 \pm 0.08$ dex. The spectroscopic $\log(g)$ value is likely too high, since it yields a high M_{spec} that is unreasonable for the stars position in the CMD (Fig. 2.2). In comparison, the photometric parameters are $\log(T_{\rm eff}) = 4.42 \pm 0.06$ dex, $\log(g) = 4.12 \pm 0.06$ dex, and $M_{ini} = 9.22 \pm 0.99 M_{\odot}$. $\log(T_{\rm eff})$ is in consistent between the two methods, while $\log(g)$ shows a discrepancy.

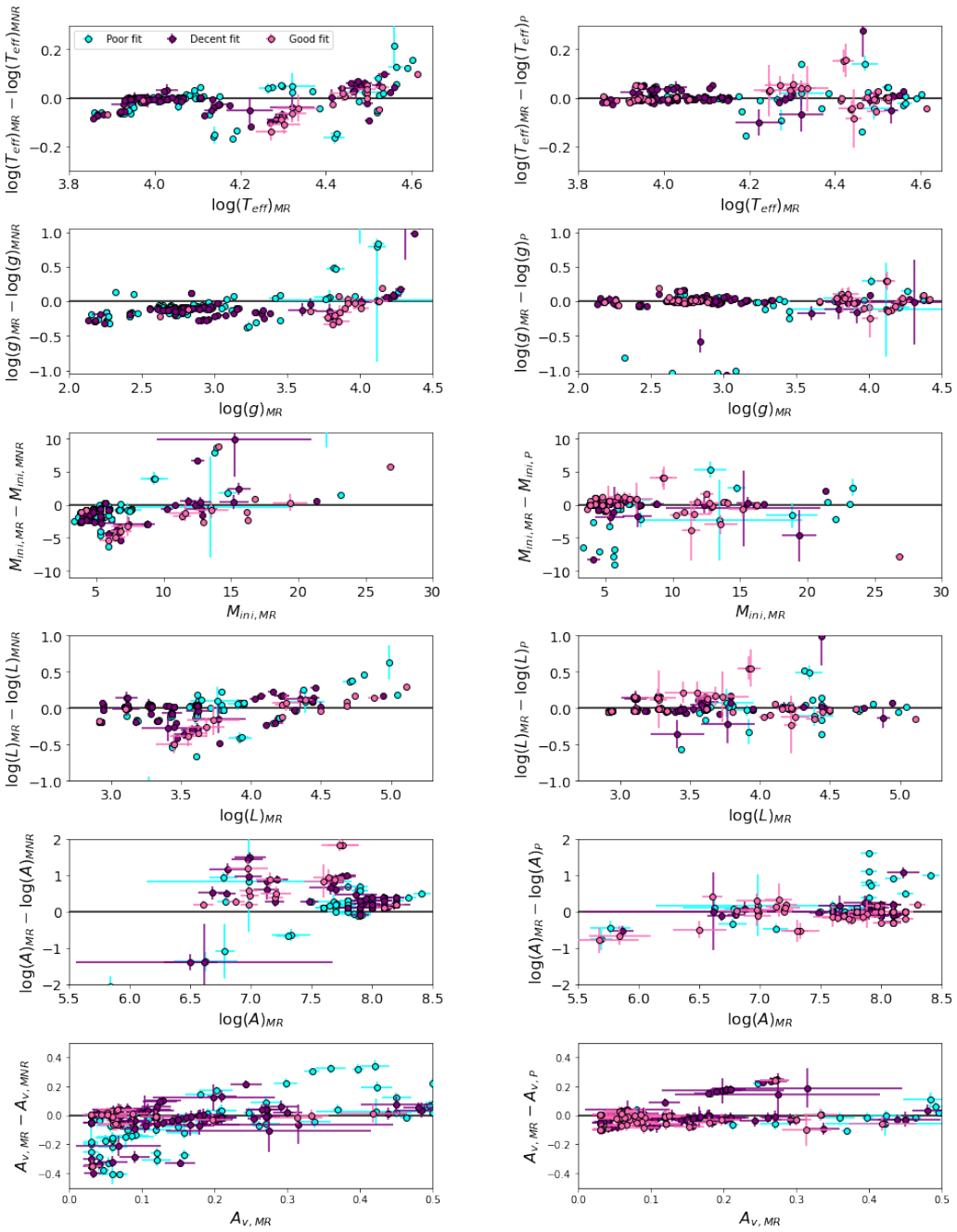


Figure 2.18: The figure shows a direct comparison between the parameters derived from the BEASTusing the different available evolutionary models. The left panels compare the MIST models with v/vcrit=0.4 (MR) and v/vcrit=0.0 (MNR). The right panels compare the MIST models with v/vcrit=0.4 (MR) to the PARSEC models (P). We plot the values for the stars in both our spectroscopic and photometric sample. The top two panels compare $\log(T_{\rm eff})$. The second two panels compare the $\log(g)$. The third two panels compare M_{ini}. The fourth panels compare $\log(L/L_{\odot})$. The fifth panels compare $\log(A)$. The bottom panels compare the $A_{\rm V}$. Stars with $\chi^2 < 20$ for both fits are pink (good fits), stars with $\chi^2 > 80$ in either fits are cyan (poor fits), all other stars are purple (decent fits).

Chapter 3

A Low Metallicity Massive Contact Binary Star System Candidate in WLM identified by Hubble and James Webb Space Telescope imaging

An earlier version of this article was previously published as Gull, Maude; Weisz, Daniel R.; El-Badry, Kareem; Henneco, Jan; Savino, Alessandro; Durbin, Meredith; Choi, Yumi; Cohen, Roger E.; Cole, Andrew A.; Correnti, Matteo; Dalcanto, Julianne J.; Gilbert, Karoline M.; Goldman, Steven R.; Guhathakurta, Puragra; McQuin, Kristen B. W.; Newman, Max J. B.; Skillman, Evan D.; Williams, Benjamin F. (2025) 'A Low Metallicity Massive Contact Binary Star System Candidate in WLM identified by Hubble and James Webb Space Telescope imaging', The Astrophysical Journal, Available at: Co-authors contributed the following parts: HST reductions as part of LUVIT (PIs: Gilbert and Boyer) products (Williams, Benjamin F.); HST multi-epoch photometry reductions (Savino, Alessandro); JWST photometry reductions (Durbin, Meredith); and a custom-made MESA grid (Henneco, Jan). The remaining co-authors provided feedback and comments on the manuscript. The first author (Gull, Maude) led, performed, created, and wrote the remaining reductions, analysis, figures, and texts.

3.1 Chapter Abstract

We present archival *HST* and *JWST* ultraviolet through near infrared time series photometric observations of a massive minimal-contact binary candidate in the metal-poor galaxy WLM ($Z = 0.14Z_{\odot}$). This discovery marks the lowest metallicity contact binary candidate observed to date. We determine the nature of the two stars in the binary by using the eclips-

ing binary modeling software (PHysics Of Eclipsing BinariEs; `PHOEBE`) to train a neural network to fit our observed panchromatic multi-epoch photometry. The best fit model consists of two hot MS stars ($T_1 = 29800^{+2300}_{-1700}$ K, $M_1 = 16^{+2}_{-3}\ M_\odot$, and $T_2 = 18000^{+5000}_{-5000}$ K, $M_2 = 7^{+5}_{-3}\ M_\odot$). We discuss plausible evolutionary paths for the system, and suggest the system is likely to be currently in a contact phase. Future spectroscopy will help to further narrow down evolutionary pathways. This work showcases a novel use of data of *JWST* and *HST* imaging originally taken to characterize RR Lyrae. We expect time series imaging from LSST, BlackGEM, etc. to uncover similar types of objects in nearby galaxies.

3.2 Introduction

Massive metal-poor binary star systems ($M_\star > 8M_\odot, Z_\star < 0.2\,Z_\odot$) are key to many open problems in astrophysics. At high-redshift, these massive binary systems may contribute significantly to the ultra-violet (UV) and optical spectral energy distributions (SEDs) of star-forming galaxies (e.g., Steidel et al. 2016; Eldridge & Stanway 2020, 2022). Across all redshifts, they are thought to be the likely progenitors for many gravitational wave sources (e.g., Spera et al. 2015; Abbott et al. 2016; Briel et al. 2023; Marchant & Bodensteiner 2024; Dorozsmai & Toonen 2024, and references therein).

Studies over the last decade have shown that most massive stars are in binary systems and will interact with their companions during their evolution (e.g., Sana et al. 2013; Rizzuto et al. 2013; Kobulnicky et al. 2014; Moe & Di Stefano 2015; Dunstall et al. 2015; Moe & Di Stefano 2017; Mahy et al. 2022; Offner et al. 2023; Marchant & Bodensteiner 2024). A star's evolutionary path is dramatically altered by the presence of a close companion (e.g., Paczyński 1967; Podsiadlowski et al. 1992; Langer 2012; Sana et al. 2013; Dunstall et al. 2015; Willcox et al. 2023). Interacting massive stars can lead to a variety of astrophysical phenomena such as X-ray binaries (e.g., Jones et al. 1973; Verbunt 1993; Tauris & van den Heuvel 2006), stripped-envelope supernovae (Wellstein & Langer 1999; Eldridge et al. 2013; Tauris et al. 2015; Laplace et al. 2021), and gravitational wave sources (e.g., Schneider et al. 2001; Tauris et al. 2017; Mandel & Farmer 2022), and they can play an important role in nucleosynthesis (e.g., Lattimer & Schramm 1976; Kasen et al. 2017; Margutti & Chornock 2021).

While there has been a tremendous effort to study massive binaries in the Local Group (LG), the lowest metallicity environment that has received significant attention is the SMC (e.g., Moe & Di Stefano 2013; Hilditch et al. 2005; Lamb et al. 2016; Mahy et al. 2020; Dufton et al. 2019; Bodensteiner et al. 2021; Rickard & Pauli 2023; Shenar et al. 2024). The physics of massive binary star systems (e.g., rotation, mass-loss) and the formation and evolution of their descendants (e.g., supernovae, gravitational wave sources) are likely to depend on metallicity such that the SMC is not sufficiently metal-poor to characterize the full extent of metallicity effects (e.g., Klencki et al. 2018; Gull et al. 2022; Ramachan-

dran et al. 2024; Telford et al. 2024; Shenar et al. 2024). Despite the clear importance of metallicity, there are very few observational studies for massive binaries in the sub-SMC metallicity regime ($Z_\star \leq 0.2\ Z_\odot$; Bodensteiner et al. 2021). Observing resolved massive stars in sub-SMC metallicity environments is challenging, due to large typical distances to star-forming dwarf galaxies ($D \gtrsim 1$ Mpc) with such metallicities, hence why only a few quantitative studies exist (e.g., Telford et al. 2021; Gull et al. 2022; Telford et al. 2023). Acquiring sufficiently high SNR spectra and photometry, even with our most powerful space- and ground-based facilities, is challenging owing to faintness and crowding in these environments. These issues are compounded for the study of time variations in spectra or photometry (i.e., time series data for eclipsing systems) for which high SNR data is needed for each epoch.

In this paper, we use the combined power of *HST* and *JWST* to provide the first detailed time series studies of a massive binary system in a sub-SMC metallicity dwarf galaxy. Specifically, it is the first study of a massive contact binary candidate in a galaxy more distant and metal-poor than the SMC. A contact binary is a pair of stars that are sufficiently close together such that they physically touch one another, i.e., both overfill their Roche Lobes, which are the Roche equipotential surfaces through the first Lagrange point (L1; (e.g., Pols 1994; Wellstein et al. 2001; Menon et al. 2021).

Massive contact binaries are complex systems, and their evolution, especially after the onset of the contact phase, is being actively explored, both theoretically (e.g., de Mink et al. 2007; Marchant et al. 2016; Hastings et al. 2020a; Fabry et al. 2022, 2023; Henneco et al. 2024) and observationally (Penny et al. 2008; Lorenzo et al. 2014; Almeida et al. 2015; Martins et al. 2017; Raucq et al. 2017; Abdul-Masih et al. 2019). While several candidates have been identified in surveys of the LMC and SMC (e.g., Balona 1992; Muraveva et al. 2014; Pawlak 2016), only $\sim$ 10 contact binaries have been studied in detail in the LMC ($\sim 50\% Z_\odot$) and $\sim$ 12 in the SMC ($\sim 20\% Z_\odot$) (Hilditch et al. 2005; North et al. 2010; Mahy et al. 2020; Abdul-Masih et al. 2021; Rickard & Pauli 2023; Wu et al. 2023; Chu-Qi et al. 2023). Owing to the observational challenges described above, none have been identified in more distant and/or metal-poor galaxies.

We focus on the galaxy Wolf–Lundmark–Melotte (WLM; also known as DDO221). WLM is a nearby, isolated dwarf with active star-formation ($D \sim 1$ Mpc, log(SFR) $\sim -2.24\ M_\odot\ \mathrm{yr}^1$; Karachentsev et al. 2013) with an average gas-phase metallicity of $\sim 14\%\ Z_\odot$ ($12 + log(O/H) = 7.83$; Lee et al. 2005). Several studies have explored aspects of its rich population of metal-poor massive stars (Massey et al. 2007a; Urbaneja et al. 2008; Tramper et al. 2011, 2014; Goldman et al. 2019; González-Torà et al. 2021; Telford et al. 2021; Bonanos et al. 2024), but, aside from Cepheids as distance indicators (Lee et al. 2021), none have explicitly focused on time series analysis of its massive star content.

Here, we have identified candidate massive contact binary systems (WLM-CB1) in time series imaging from archival *HST* and *JWST* observations that were originally designed for

the detection of RR Lyrae stars. Our goals in the following sections are to provide the first observational data point of massive contact binaries in a metal-poor galaxy beyond the Magellanic Clouds and to demonstrate the type of data and analysis needed to identify and characterize these types of systems in other nearby galaxies.

This paper is organized as follows. §4.3 presents our archival *HST* and *JWST* Early Release Science observations of WLM-CB1. §3.4 describes our analysis of the multi-band light curve observation, and using MESA. Finally, we discuss the results of our analysis and the future observations needed to confirm the nature of WLM-CB1 in §3.7.

Throughout this analysis we adopt the tip of the red giant branch distance measurement of 968^{+5}_{-7} kpc (μ = 24.93 mag) from Albers et al. (2019).

3.3 Photometry

To investigate the system (WLM−CB1), we use a combination of archival *HST* data and *JWST* early release science imaging. The footprints for our datasets are shown in Figure 3.1.

3.3.1 *HST* Imaging and Photometry

We use archival *HST* ACS/WFC imaging of WLM that was originally acquired for deep photometry and RR Lyrae studies (GO−13768; PI Weisz; Albers et al. 2019). These multi-epoch observations were carried out over a period of roughly 3 days. There are 24 exposures with ACS/WFC F475W and 26 exposures with ACS/WFC F814W. We summarize the observations in Table 3.1.

We further complement our dataset with multi-band photometry observed as part of a larger survey that includes LG dwarf galaxies (GO−15275; PI Gilbert). The WLM multi-band photometry additionally covers the following bands: WFC3/UVIS F275W and F336W which are part of the Local Ultraviolet to Infrared Treasury (LUVIT, (LUVIT Gilbert et al. 2025)) dataset. We use individual exposures of the WFC3/UVIS F275W and F336W photometric observations to obtain short NUV time series photometry from the dataset. Observations in each filter cover a time baseline of ∼30 min, are summarized in Table 3.1 as well.

The ACS/WFC F475W and ACS/WFC F814W multi-epoch observations were reduced using DOLPHOT (Dolphin 2000, 2016). For a given reference image footprint, DOLPHOT takes any exposure and reports a measurement of point-spread function photometry for every detected object. This method has been well-tested by previous LG *HST* resolved star studies (e.g., Dalcanton et al. 2009; Williams et al. 2014, 2019; Savino et al. 2022; Gull et al. 2022; Savino et al. 2023). We follow the same steps as Savino et al. (2022), who

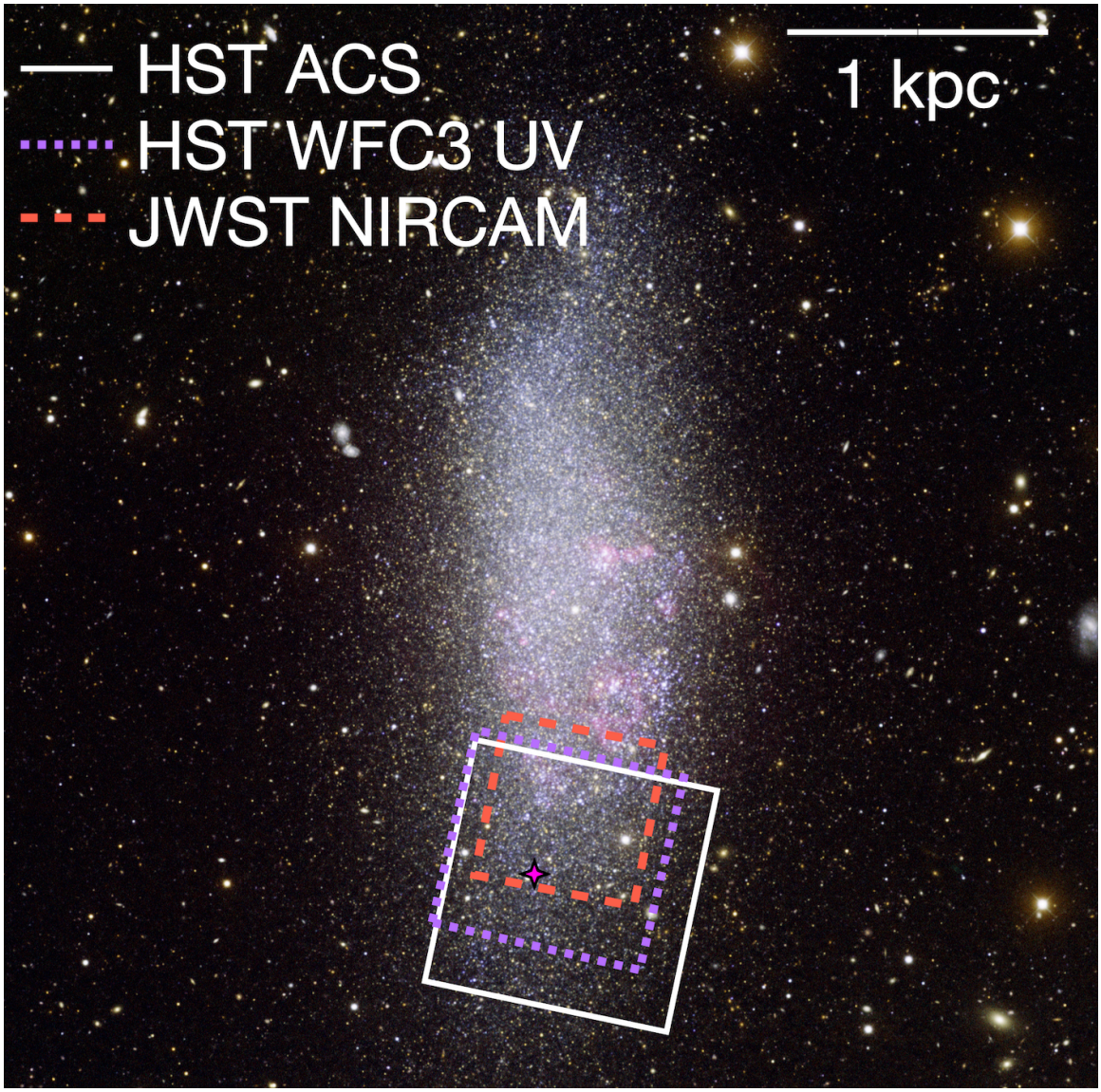


Figure 3.1: An optical ground-based image of WLM (credit: NOIRLab/NSF/AURA/CTIO/Local Group Survey Team and T.A. Rector (University of Alaska Anchorage)) with the *HST*/ACS, *HST*/WFC3, and *JWST*/NIRCAM footprints overplotted. The location of WLM-CB1 (RA: 00 02 00.23, DEC:15 31 05.20) is shown as a pink star. It falls within all three footprints.

base their DOLPHOT setup on Williams et al. (2014). For a more detailed discussion of the reduction we refer the reader to Williams et al. (2014) and Savino et al. (2022).

The LUVIT data collection and reduction was carried out separately using DOLPHOT

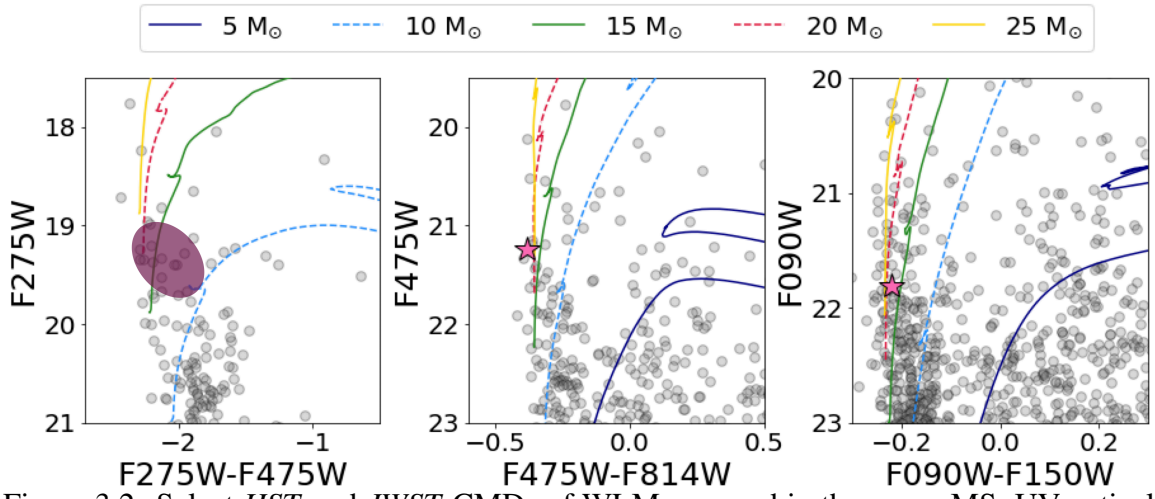


Figure 3.2: Select *HST* and *JWST* CMDs of WLM, zoomed in the upper MS: UV-optical (left), optical-only (middle), near-IR (right). WLM-CB1 is shown as a star symbol. The optical and near-IR values of WLM-CB1 reflect the maximum point on the optical and near-IR light curves i.e., maximum brightness of the system. Since we have no direct constraint initially on the the phase of the UV data point, we indicate likely CMD position by the shaded oval. We overplot select MIST tracks ([Fe/H]=−0.82, v/vcrit = 0.4, A_v = 0.10) for reference. Note that the 5 $M_\odot$ track falls off in the UV-optical CMD, due to its faintness in F275W. A visual comparison with the single-star models suggests a lower limit of $\sim$ 10 $M_\odot$ on the current mass of WLM-CB1.

as well and we refer the reader to the survey paper Gilbert et al. (2025) and Gull et al. (2022) for further details. We note that we only use the UV data points from the catalog.

Once the data are reduced, we apply the following quality cuts as outlined by Williams et al. (2014) to each epoch; (1) signal-to-noise $<$ 4 , (2) $\texttt{sharpness}^2 < 0.15, 0.2$ for WFC3/UVIS, and ACS/WFC respectively, (3) $\texttt{crowding} < 1.3, 2.25$ for WFC3/UVIS, and ACS/WFC, and (4) any DOLPHOT FLAG <= 2 are removed.

Figure 3.2 shows the upper part of the UV and optical color–magnitude diagrams (CMDs) of WLM generated by the LUVIT photometry, with WLM-CB1 highlighted. We overplot the rotating ($v/v_{\rm crit}$ = 0.4) MESA Isochrones and Stellar Tracks (MIST; Choi et al. 2016; Dotter 2016) for reference. We note that the MIST isochrones have not yet been updated with in-flight characteristics of *JWST* , which affects the bandpasses at the level of $\sim$ 0.05 mag. The system appears to be located on the main-sequence (MS) in each CMD, which indicates that at least one of the stars is likely a bright, blue MS star. The UV data only provides a single point, meaning without constraints on the period we do not know where in the light curve this data point falls, leading to some uncertainty in its position on the CMD.

3.3.2 *JWST* Imaging and Photometry

The *JWST* Resolved Stellar Populations Early Release Science (ERS) Program (DD-1334; PI D. Weisz; Weisz et al. 2023, 2024) obtained F090W/F150W/F277W/F444W NIR-Cam imaging of a field in WLM that spatially overlaps the *HST* imaging (McQuinn et al. 2024).

The extraction of time series data points from the *JWST* imaging required manual adjustments to the default *JWST* pipeline. The ERS program was not formally designed as a time-series program (i.e., specifically using the time series observation mode, TSO), as it required spatial dithers to sample the point spread function, which is not permitted in TSO mode. As a result, the *JWST* pipeline by default does not produce exposure level calibrated images needed for DOLPHOT. We therefore created them by re-running the pipeline manually with small changes. Specifically, we started with the Stage 1 `*_rateints` data products from the Mikulski Archive for Space Telescopes (MAST). We passed into the Stage 2 imaging pipeline[1] (`calwebb_image2` or `jwst.pipeline.Image2Pipeline`) to produce the fully calibrated `*_calints` products. We stopped our reduction here, and did not produce aperture photometry, yet. Instead we first created a series of individual"pseudo-cal" 2D images by splitting the `*_calints` products. This choice was made so that the data is compatible with our existing pre-processing routine for DOLPHOT (Dolphin 2000, 2016) input images. The "pseudo-cal" image files were supplemented by a table of integration times (FITS extension "INT_TIMES"), so that we retained the correct timestamps for each header.

A reduction from this point on was performed via the DOLPHOT package for NIRCam (Dolphin 2000, 2016; Weisz et al. 2024). We applied the following quality cuts to the per-epoch catalog as outlined in Section 3 of Warfield et al. (2023); (1) OBJECT_TYPE <= 2; (2) `sharpness`^{2} < 0.01 for both F090W and F150W; (3) `crowding` < 0.5 for both F090W and F150W; and (4) any FLAG <= 2. While the *JWST* photometry reaches magnitudes of $\sim$ 28 mag, we only highlight the relevant part of the upper CMD in Figure 3.2. We summarize the time-stamps of the individual multi-band photometric observation in Table 3.1.

3.4 Analysis

We first describe the discovery of WLM−CB1 in archival *HST* data, we then determine a credible period range of WLM−CB1 using multi-band Lomb-Scargle (L-S) periodogram provided with `astropy` (Astropy Collaboration et al. 2013, 2018, 2022; Vanderplas et al. 2012). Next, we use `PHOEBE` (PHysics Of Eclipsing BinariEs; Prša & Zwitter 2005; Prša

[1] https://jwst-pipeline.readthedocs.io/en/latest/jwst/pipeline/calwebb_image2.html

Table 3.1: Time-stamps of individual WLM-CB1 observations.

Filter	MJD	Magnitude	Uncertainty	Systematic Uncertainty
HST ACS/WFC F475W	57220.347346	21.619	0.005	0.03
HST ACS/WFC F475W	57220.410298	21.478	0.004	0.03
HST ACS/WFC F475W	57220.479904	21.354	0.004	0.03
...	...	...	...	...

Note. — This Table is published in its entirety in the machine readable format. A portion is shown here for guidance regarding its form and content.

et al. 2016; Horvat et al. 2018; Conroy et al. 2020; Jones et al. 2020), a mature software package that allows in-depth modeling of light and RV curves, to determine the parameters of the binary system. Below, we describe each step in more detail.

3.4.1 Discovery

We initially apply an additional magnitude cut to the *HST* archival data that filters for light-curves where the difference between the minimum and maximum reported magnitude in F475W and F814W is ≥ 0.1 mag. We then use multi-band L-S periodogram in astropy (Astropy Collaboration et al. 2013, 2018, 2022; Vanderplas et al. 2012) to find any light-curves in the *HST* archival data that may show periodic signal. We search over a range of periods from 0.2 to 3 days, with a step size of 0.001 days. The min-max range was set by the properties of our observations, which were taken for the purposes of studying RR Lyrae. The best candidates are then visually inspected, specifically whether the periodicity was visible and similar in nature in both bands. In addition the star in this paper, we detected an three other massive or intermediate mass eclipsing short-period binary candidates in WLM, which will be reported in a future study. We choose to focus on WLM-CB1 first as it is the brightest source.

Figure 3.3 shows the multi-band light curves of WLM−CB1. Photometric variations are already quite clear in F475W, F814W, F090W, and F150W, indicating this is not a normal, static, upper MS star. Although our data does not completely cover the entire phase, our sampling is still clearly rich in information. The overall shape of the light-curve suggest that the system could be a contact binary or near-contact (i.e., semi-detached) binary, hence why a quantitative analysis with `PHOEBE` is necessary to determine the exact nature of WLM-CB1.

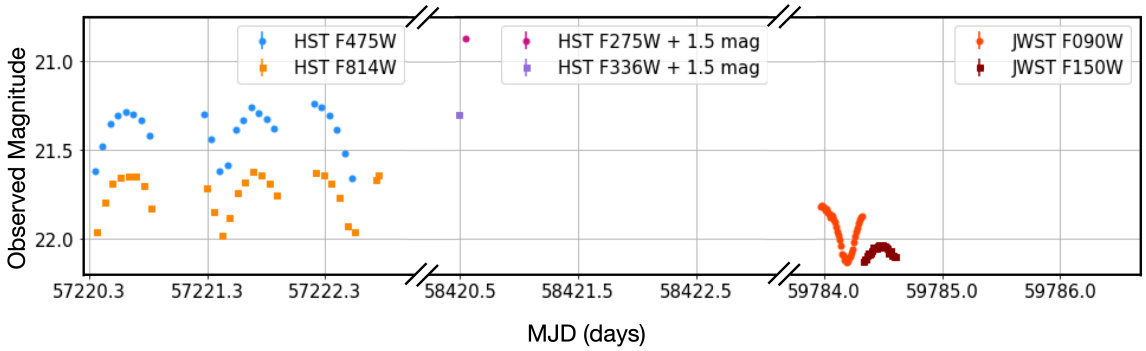


Figure 3.3: All *HST* and *JWST* observations of the WLM-CB1 used in this paper, shown in chronological order. Even without phase-folding, variability in the light curves is visible for the optical and near-IR bands. A constant offset has been added to the two UV data points in order to improve the dynamic range of the y-axis for illustrative purposes.

3.4.2 Period and Temperature Estimation

We use the multi-band Lomb-Scargle periodogram to estimate the period of WLM-CB1, now including the IR data points. The UV data points do not contribute to the period determination in the periodogram, due to the sparse coverage.

For the combined F475W, F814W, F090W and F150W photometry, the L-S power spectrum yields a period of 1.0934 days and a FWHM of 0.07. This period is the orbital period, since the original search only using F475W and F814W yielded another peak at 0.5467 days likely half the period. we note that the peak is broad, nearly rectangular, hence why bounds of our model grid for the period are chosen to be slightly larger than the uncertainty yielded by the FWHM.

In the absence of spectra, we use multi-band colors to infer a range of plausible temperatures for this system. We later use this range to inform our more detailed model grid for formal fitting. We choose to refer to the hotter star as the primary and the cooler star as the secondary. Specifically, we place WLM-CB1 on static CMDs (See Figure 3.2) using the peak magnitude for WLM-CB1 (when available). WLM-CB1 is located on the upper MS in the optical and IR CMD, close to the zero-age main sequence (ZAMS), suggesting a hot MS primary, since the primary will dominate the SED. In the UV, we shade the color-magnitude range in which the star is likely to be located, since we do not have the peak magnitude observed. While we cannot precisely place the peak magnitude, the location still suggests a hot system since it is on the MS. The secondary is unlikely to be a cool star, since the star would not appear on the MS on the near-IR CMD. We therefore assume that the stars must both be hot MS stars. Based on the color and magnitude of the peak light we estimate using the evolutionary tracks that the primary will have a temperature between $24,000$ K and $35,000$ K, which would be a late O-type or early B-type star. We allow the

secondary to reach the same maximum temperature; however, we allow it to be a late B-type star, which translates to a lower bound of $10,000$ K. Hence the temperature and mass range are quite broad, as might be expected when using only a photometric estimation. Furthermore, we can compare WLM-CB1 against mass tracks in the CMD. In each CMD, WLM-CB1 is located above the 10 $M_\odot$ track, and close to the 25 $M_\odot$ track in the optical and in the IR. Based on this we can infer that at least one of the stars is massive ($M_\star > 8M_\odot$) , while the secondary is either an intermediate mass or massive star ($M_\star > 3M_\odot$) .

3.4.3 Neural Net training and Setup

Though `PHOEBE` provides all the functionality needed to characterize our data, it is computationally expensive to embed and run it within a Markov chain Monte Carlo framework (e.g., Conroy et al. 2020; Ding et al. 2021, 2022), especially when fitting a great number of models to multiple observed light curves. Therefore, following Ding et al. (2021, 2022), we train a neural net framework to emulate `PHOEBE`, resulting in significantly reduced model generation time with minimal loss in accuracy.

Because it is not immediately clear whether WLM-CB1 is a true contact binary or a semi-detached system, we generated a model grid for each scenario in `PHOEBE`. At this point, the parameterization of `PHOEBE` does not allow for a smooth transition between detached (which includes semi-detached) and contact binary models, meaning the analysis has to be done separately for each physical scenario. We train different neural nets for each grid.

In what follows, we describe the fitting process for the single case of the contact binary, and note that we carried out an identical process for the detached model grid. We opt for a fully connected neural network (NN), using PyTorch (Paszke et al. 2019) and Optuna (Akiba et al. 2019). Third-light contributions (i.e., crowding from a background object, or an extra component in the system (tertiary)) are not invoked and neither are stellar spots.

For the contact binary model grids, we have the following physical parameters: temperature of the primary (T_1), mass of the primary (M_1), temperature ratio (T_2/T_1), inclination (Inc), mass ratio ($q = M_2/M_1$), period (P), fillout-factor (f) and extinction (A_V). For the detached system model grid, the `PHOEBE` parameters are: temperature of the primary (T_1), mass of the primary (M_1), radius of the primary (R_1), temperature of the secondary (T_2), radius of the secondary (R_2), inclination (Inc), mass ratio (q = M_2/M_1), period (P), and extinction (A_V). Our adopted parameter ranges are displayed in Table 3.2.

The temperature range of the primary and secondary was chosen based on CMD location, as explained in Section 3.4.2. Similarly, the mass ranges are informed by the location the system in the CMD above the 10 $M_\odot$ evolutionary track. The radius range is determined using average radii for MS stars observed in the SMC and sub-SMC galaxies. The period range was determined using the results from the periodogram, where we use the base of

Table 3.2: Basic information on the PHOEBE model grids used for the neural network. The columns are: (1) Model type; (2) Temperature of the primary (T_1); (3) Mass of the primary (M_1); (4) Temperature Ratio (T_2/T_1); (5) Inclination (Inc);(6) Mass ratio ($q = M_2/M_1$); (7) Period (P); (8) fillout-factor (f); (9) extinction (A_V); (10) Temperature of the secondary (T_2); (11) Radius of the Primary (R_1); (12) Radius of the secondary (R_2)

Mode	T_1	M_1	T_2/T_1	Inc	q	P	f	A_V	T_2	R_1	R_2
	K	$M_\odot$		deg		days			K	$R_\odot$	$R_\odot$
(1)	(2)	(3)	(4)	(5)	(6)	(7)	(8)	(9)	(10)	(11)	(12)
Contact	24000-35000	8-20	0.3-1.05	40-90	0.2-1.1	1.0-1.2	0.01-0.8	0.05-0.20	···	···	···
Detached	20000-35000	8-20	···	40-90	0.3-1.1	1.0-1.2		0.05-0.20	15000-29000	3.8-7.0	3.8-6.5

the peak in the L-S spectrum as our range. The inclination range is set to a lower limit of 40°, since observing a lower inclination would be unlikely given the depth of the eclipse. The mass-ratio is set at a lower cut-off of 0.2, since observing a smaller companion than this would be unlikely, as such a low-mass would not perturb the orbit of a massive star so much. We note that the upper limit is set to > 1 for mass-ratio and temperature ratio. Although we choose the brighter/more massive star to be the primary (i.e., subscript 1), we needed to ensure that the model can reliably recover a equal mass or equal temperature model.

We undertake the following steps to train our neural net. We manually add *HST* and *JWST* bands, which are not natively included in PHOEBE, using the atmosphere models of Castelli & Kurucz (2004). Using PHOEBE, we generate $\sim 45,000$ light curves for each filter in phase space. The light curves are generated by randomly sampling parameters within the ranges in Table 3.2. PHOEBE ensures that each combination of parameter yields a physical binary model. This yields a grid, where for each combination of parameters there are six associated light curves. PHOEBE light curves fluxes are converted to magnitudes using the `pyphot`[2] zero-points, and parameters and light curves are normalized to improve our computational efficiency. The optimal suggested set-up yielded by tuning the neural network is a total of 5 layers; one input layer, 3 hidden layers and one output layer. The suggested activation function is "Adam" (Kingma & Ba 2017), while the learning rate is 10^{-4} and the batchsize is set to 32. We use 80% of our sample to train and 20% to validate. Our median approximation error peaks under $\sim 10^{-3}$ for our normalized data set.

Using the trained neural network, we present the effects of each parameter on the light curve in Figure 3.4. We note that the full effects pf two parameters is not fully captured by a phase-spaced single-band light-curve: Period (P) and Attenuation (A_V). The Period, additionally to the modification of the brightness of the light-curve, also will fold the data and hence have an additional temporal effect. The attenuation can only be fully captured with panchromatic light-curve since the effect on each band will be different in accordance with the dust law applied. Furthermore Figure 3.4 shows nicely why from ground-based

[2]https://mfouesneau.github.io/pyphot/

photometry parameters like the temperatures of each star (T_1 and T_2/T_1), the inclination (*Inc*) and the fill-out factor (f) are easier to obtain. In contrast, the mass-ratio (q) has been notoriously difficult to obtain from light-curves due to the need for high-precision photometry, which thus far has only been possible with *HST* or *JWST*. Lastly, the mass and temperature of the primary seem to have similar effects on the single-band light curve, however, they will have different effects on the panchromatic light-curves, which allows us to disentangle the effects.

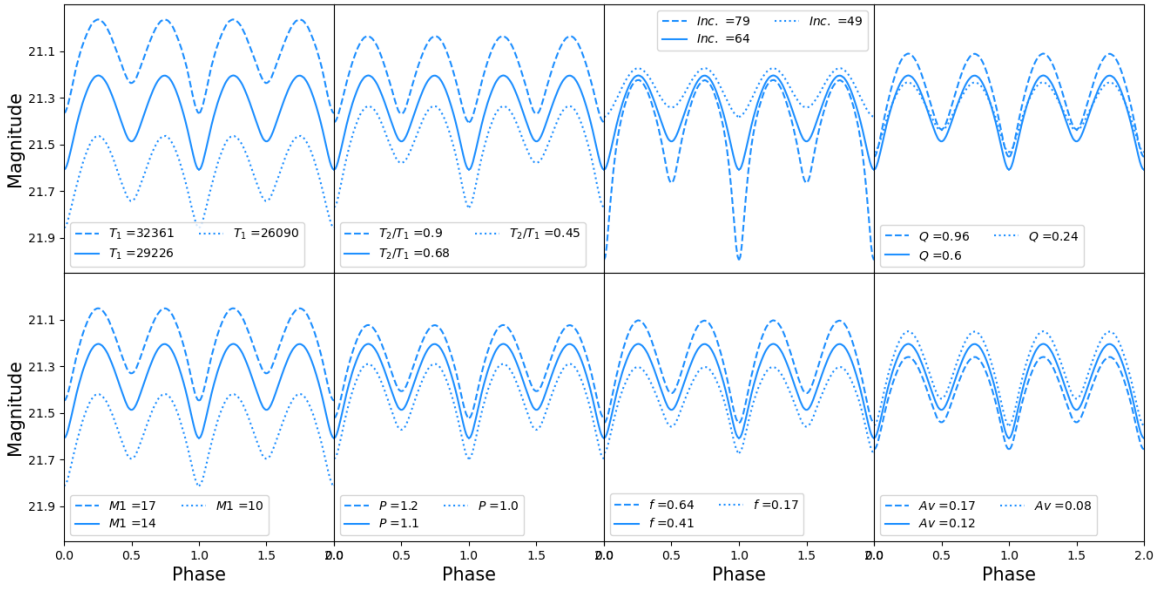


Figure 3.4: Synthetic F475W light-curves generated by the neural network trained on `PHOEBE`. The solid light-curve in each panel is the baseline model. Each panel shows the effects of a singular parameter being varied on the light-curve. It is evident that the mass-ratio has the smallest effect in the light-curve and can only be constrained by high-precision photometry such *HST* and *JWST*. We note that since this is in phase space, the effects of the period on the fitting is not fully captured, as it also folds the data into phase space.

3.4.4 Fitting using `UltraNest`

Given that our light curves do not sample a full phase, and we do not have spectra, it is probable that our likelihood surface will be multi-modal in period, and perhaps other parameters. Accordingly, we opt to use a nested sampling algorithm instead of Markov Chain Monte Carlo (MCMC) methods, the former of which is generally better at sampling complex posterior distributions.

For our analysis, we use the nested sampling Monte Carlo algorithm `MLFriends` (Buch-

ner 2016, 2019) as part of the `UltraNest` [3] package (Buchner 2021). UltraNest uses multiple clusters and has an adjustable step sampler, which allows us to explore the entire parameter space and find the highest probability mode. To perform the fitting, we use Ultranet's reactive nested sampling implementation. Reactive nested sampling differs from a nested sampling algorithm by adding new live-points closer to the peak of the posterior mass as opposed to uniformly over the entire posterior mass. This makes the computation overall more efficient by minimizing rejection points, and does not affect the final posterior distribution.

We use 400 live points, and, before running the algorithm, use the calibrator capabilities to obtain the optimal number of steps. Each live point takes $N_{param} \times 2^{11}$ steps, so that we converge and pass the relative jump distance and acceptable fraction criteria. Furthermore, we use the "*generate_mixture_random_direction*" step sampler. The advantage of using this "mixed" sampler, is that it randomly changes between region sampling and step sampling (Buchner 2021, 2023).

We present the resulting posterior distributions and quantiles in Figure 3.5. The strong peaks, with 0% valleys for the period, reflect the multi-modality of the posterior of the period. This means that instead of a smooth probability curve, the period probability is rather concertized; very narrow peaks will set the possible values. This implies that even a slight shift in period drastically worsens the fit of model to data.

To describe the system completely and compare it to evolutionary models, we report additional parameters. The parameters that are directly derived from our results are temperature of the secondary ($T_2 = T_1 \times T_2/T_1$), mass of the secondary ($M_2 = M_1 \times q$), and the semi-major axis (a). Using `PHOEBE` and the underlying atmosphere models we compute the radius of the primary (R_1), surface gravity of the primary ($\log(g)_1$), radius of the secondary (R_2) and surface gravity of the secondary ($\log(g)_2$). We present a summary of all fitted and derived parameters in Tables 3.3.

In Figure 3.6, we show light-curves from our data with the contact binary model light-curve generated by the median value (black) of the posterior distribution and 300 random draws from the posterior (color) overplotted . Overall, the data match the contact binary model extremely well, all data points are within the posterior bounds. The residuals are overall on the order of < 0.05 mag, nearing our precision limit. The largest difference is observed in the posterior distribution around the secondary dip; however, this is mostly reflective of the uncertainties in the secondary due to lack of data in this region of phase space. We do not present the semi-detached model here, since it yields a nearly identical median light curve, which would not be noticeably different by eye.

[3] https://johannesbuchner.github.io/UltraNest/

Table 3.3: Parameters yielded by the contact binary model of WLM-CB1 binary system.

Fitted parameter	
T_1 (K)	29800^{+2300}_{-1700}
T_2/T_1	$0.59^{+0.12}_{-0.14}$
Inc (degree)	68^{+4}_{-2}
$q = M_2/M_1$	$0.41^{+0.24}_{-0.14}$
M_1 ($M_\odot$)	16^{+2}_{-3}
P (days)	$1.0961^{+0.0066}_{-0.0036}$
f	$0.02^{+0.07}_{-0.03}$
A_V	$0.12^{+0.04}_{-0.04}$
Directly derived parameter	
T_2 (K)	18000^{+5000}_{-5000}
M_2 ($M_\odot$)	7^{+5}_{-3}
a ($R_\odot$)	$12.8^{+0.8}_{-1.1}$
PHOEBE derived parameter	
R_1 ($R_\odot$)	5.9
$\log(g)_1$ (dex)	4.11
R_2 ($R_\odot$)	3.9
$\log(g)_2$ (dex)	4.08

3.5 Results

WLM-CB1 is the first observed massive sub-SMC metallicity contact binary candidate. Our analysis suggests that WLM-CB1 is a massive contact binary consisting of a 16^{+2}_{-3} $M_\odot$ star (observational primary; WLM-CB1a) and a 7^{+5}_{-3} $M_\odot$ star (observational secondary; WLM-CB1b). The mass-ratio is $q = 0.41^{+0.24}_{-0.14}$. WLM-CB1a appears to be a MS star with $T_1 = 29800^{+2300}_{-1700}$ (K) and $\log(g)_1 = 4.11$, where T_1 is measured from the light curve and $\log(g)_1$ is inferred from the constraints provided by the filling factor and mass. Similarly WLM-CB1b appears to be a MS star with $T_2 = 17600^{+5000}_{-5100}$ (K) and $\log(g)_2 = 4.08$, which agrees well with its position on the multi-band CMDs. The system has a period of $1.0961^{+0.0066}_{-0.0036}$ days and an inferred semi-major axis of $12.8^{+0.8}_{-1.1}$ $R_\odot$. The fill-out factor is $0.02^{+0.07}_{-0.03}$, suggesting that the system is only minimally in contact; we will further discuss this below. The extinction is $A_V = 0.12^{+0.04}_{-0.04}$, this is only slightly higher than the overall measured foreground extinction of WLM (McQuinn et al. 2024).

In Figure 3.6, we show the observed light curves and those from the median values of the sampling and the posterior assuming a contact binary model. It is clear that the low sampling in the UV and the lack of coverage of the secondary eclipse drive the uncertainty. We find the data to be well-described by our contact binary model, as shown by the generally small residuals. The fillout factor is $f = 0.02^{+0.07}_{-0.03}$, which is low. As described in

Bradstreet (2005), a fillout factor greater than 0 qualifies a system as a contact system. However, a system with $-0.1 \lesssim f \lesssim 0$ would alter the classification to a near contact or semi-detached system. As evident in Figure 3.5, the fillout factor is nearing the edge of the allowed range for a contact model, which would raise the concern that the model is not a contact binary. We therefore repeat the analysis assuming a (semi-) detached model.

Quantitatively, we find little difference in the recovered physical parameters, i.e., all parameters in common are within $1-\sigma$ of one another. The sole exception is the mass-ratio, which agreed at $1.5-\sigma$. Statistically, the Bayesian evidence computed for each model was nearly identical ($logZ = -40.1 \pm 0.2$ vs $logZ = -40.8 \pm 0.2$). The natural log of the Bayesian factor is less than one, indicating the current available data is not sufficiently constraining to differentiate between these physical scenarios.

The median values for the detached model suggest that WLM-CB1a fills its Roche Lobe, while WLM-CB1b is nearing Roche Lobe overflow. This would suggest that the system would be a semi-detached. However,the suggested mass-ratio yields peculiar mass for WLM-CB1b given the suggested temperature and radius. Under the assumption that WLM-CB1b is a semi-detached system, WLM-CB1b would be extremely under-luminous compared to a similar mass star. Lastly, a lower mass-ratio in the semi-detached model would push the system to be a contact binary system with the current set of derived parameters for the semi-detached model. Given these circumstances, we cannot fully rule out a semi-detached model; however, these factors indicate that a contact system seems qualitatively more likely. We further explore these scenario using more formal stellar modeling.

3.6 Stellar Evolution Modeling of WLM-CB1 Using MESA

We use the 1D stellar structure and evolution code MESA (r12778; Paxton et al. 2011, 2013, 2015, 2018, 2019) to explore potential evolutionary paths of WLM-CB1. We use the assumptions in Henneco et al. (2024), except for the metallicity (14% $Z_{\odot}$), which is from Telford et al. (2021). We briefly summarize the Henneco et al. (2024) assumptions. Even though we use a lower metallicity, we still employ the Solar helium fraction (Asplund et al. 2009). Models are assumed to be hydrostatic, and we use the approx21 nuclear network. Stars are allowed to rotate in MESA's shellular approximation and are initially synchronized with the orbital period. We impose no fixed mass-transfer efficiency. Hence, mass transfer only becomes non-conservative when the accretor star spins up to its critical rotation rate. The tidal synchronisation rate is computed through the scheme of Hurley et al. (2002) and the orbital angular momentum evolves through mass loss from the system and spin-orbit coupling. Orbits are assumed to be circular. We use the wind mass-loss rates derived by Vink et al. (2001) since our models have surface temperatures above 11 kK.

We include mixing at several levels. Convective mixing is included via the mixing length theory (Böhm-Vitense 1958; Cox & Giuli 1968) with a mixing length parameter

of $\alpha_{\rm mlt} = 2.0$. We employ the Ledoux criterion to determine which regions are unstable to convection. Thermohaline mixing is included with an efficiency of $\alpha_{\rm th} = 1.0$ and semi-convection with an efficiency of $\alpha_{\rm sc} = 10.0$. Rotational mixing and diffusion of angular momentum are covered by the inclusion of the Goldreich-Schubert-Fricke instability, Eddington-Sweet circulation, Spruit-Tayler dynamo, and the secular and dynamic shear instabilities. We use the Spruit-Tayler dynamo to account for additional diffusion of angular momentum. The strength of mixing of chemical elements is scaled by a factor of $f_{\rm c} = 1/30$, and the sensitivity of rotational instabilities to composition gradients, which have a stabilizing effect, is set to a value of $f_\mu = 0.1$. Convective boundary mixing at the interface between the convective core and radiative envelope is handled through the step-overshoot scheme. In this scheme, we extend the convective core by $0.2\,H_{\rm P}$, with $H_{\rm P}$ the pressure scale height. We compute the mass transfer rate through MESA's `contact` scheme. This is a composite scheme that uses MESA's `roche_lobe` scheme for semi-detached systems and the mass-transfer scheme from Marchant et al. (2016) for contact binaries. The `roche_lobe` scheme sets the mass-transfer rate such that the donor star remains within its Roche lobe at every timestep. We stick to the original `contact` scheme by Marchant et al. (2016), that is, we do not model the tidal deformation and energy transfer in the common envelope as done in Fabry et al. (2022) and Fabry et al. (2023).

We explored possible evolutionary scenarios of WLM-CB1 by first estimating a reasonable range of starting conditions for the MESA calculations (total mass, initial mass ratio and initial separation). Assuming conservative mass transfer[4], we used a fixed value in the uncertainty range of the current-day total mass of WLM-CB1 as a starting point and varied the mass ratio and initial separation, with the latter limited to account only for Case-A mass transfer (see "sweep 1" in Table 3.4). We limited the initial mass ratio to $q_{\rm i} > 0.3$ given that mass transfer is typically unstable for lower-mass-ratio systems (see, e.g., Henneco et al. 2024 since the model assumptions are the same as in this work). We repeated this for a different value of the total mass ("sweep 2" in Table 3.4), this time restricting the initial mass ratios to $q_{\rm i} > 0.5$, with steps of 0.05 in $q_{\rm i}$ instead of 0.1 in the previous sweep. This restriction of $q_{\rm i}$ stems from the fact that no stable, long-lived (nuclear-timescale) contact binaries were found at lower $q_{\rm i}$ in the first sweep. By analyzing the results from the second sweep, we zoomed in on the most promising regions of the initial parameter space for which the models best fit our observational constraints (see "zoom 1", "zoom 2" and "zoom 3").

We emphasize that the goal of this exercise was to explore plausible evolutionary scenarios. It is, by no means, an exhaustive modeling effort to map out all possible scenarios. A more comprehensive modeling efforts would explore the initial binary parameter space in terms of the total mass, initial mass ration and initial separation in a systematic way. This approach is computationally non-trivial and beyond the scope of this work.

[4]We find that models in this initial separation range have conservative mass transfer, but do allow for mass transfer to become non-conservative by means of the spin-up of the accretor, as mentioned above.

Table 3.4: Parameter ranges of the different initial binary parameter sweeps and zoom-ins for the MESA models.

name	no. models	total mass $M_\odot$	q_i	a_i $R_\odot$
sweep 1	84	20.61	0.3–0.9	9.16–26.85
sweep 2	225	23.07	0.5–0.9	10.25–25.60
zoom 1	15	18.00–21.60	0.8	11.00–12.00
zoom 2	3	19.80	0.8	10.25–10.75
zoom 3	3	20.25–20.70	0.8	10.50–10.75

Lastly, the MESA models themselves have no constraint on whether the system is in contact or (semi-)detached; we are therefore simultaneously exploring whether the parameters match a contact or (semi-)detached point in the suggested MESA evolution. To compare the MESA models to our observed system, we search the model grid for simultaneous match between of the observational parameters (P, q, M_1, M_2, R_1, R_2, T_1, T_2, $\log(g)_1$, $\log(g)_2$) and a singular instance in the evolutionary models (i.e., a point in a system's evolution, where the system has the same binary properties as WLM-CB1). We use the uncertainties reported in Table 3.3, and use 0.5 uncertainty for R_1, R_2, $\log(g)_1$, and $\log(g)_2$. We note that keeping R_1, R_2, $\log(g)_1$, and $\log(g)_2$ free does not yield any additional matches.

In the initial search, we are not able to find any direct matches. The closest match requires either a relaxation on the lower bound of M_1 from $3M_\odot$to $3.3M_\odot$or a relaxation on the upper bound of T_2 from 5000 K to 5800 K. The evolutionary path with the closest match suggests an initial mass (M_p) of 11 or 11.25 $M_\odot$ for the more massive component at ZAMS, initial mass-ratio (q_i) of 0.8, and initial binary separation (a_i) of 10.75 $R_\odot$. We show the MESA model $M_p = 11.25$, $q_i = 0.8$, $a_i = 10.75$ in Figure 3.8. Interestingly, all evolutionary paths for which we find a match with WLM-CB1 paint the same picture: The two stars are born relatively close to each other and experience an initial short period of contact and extreme fully conservative mass transfer early in their evolution. This implies that WLM-CB1a was initially the less massive star and accreted mass from WLM-CB1b, until the mass ratio was reversed, so that now WLM-CB1a is the more massive star. This short-lived exchange is then followed by a prolonged near-contact phase (5-7 Myr), until ultimately the two stars once again fill their Roche-lobes and enter a contact phase once again.

In each evolutionary path, the solution matching our observed parameters suggests that WLM-CB1 current evolutionary state is the re-entrance to the contact phase. In this scenario, this evolutionary stage could explain why, compared to other observed contact systems so far, it may have a smaller mass-ratio. Furthermore this could also explain why determining the exact nature of WLM-CB1 is difficult, as it could be in such a transitional

phase. We note that, with the current period, we were not able to find a system in the definitively semi-detached phase that was able to match our observable, even with slightly relaxed constraints. Lastly, the two closest matches suggest that, after a contact phase, WLM-CB1 would likely merge because of orbital decay caused by mass loss through the outer Lagrange points (Marchant et al. 2021; Henneco et al. 2024).

Recently (Telford et al. 2024), reported that the Vink et al. (2001) predicted mass-loss rates appear to be too large for sub-SMC metallicity massive stars. For a sub-set of models we tested the Björklund et al. (2021) prescription for mass-loss rates (See comparison Fig. 3.7). For WLM-CB1 the binary interaction dominates the evolution, and we see no significant differences between Vink et al. (2001) and Björklund et al. (2021), except for a slight shift in timescale (14.81 Myr and 14.78 Myr). We note that in a higher mass regime, where mass-loss can be more significant, the mass-loss recipe may play a more significant role.

We also explored the effects of changing the metallicity of our system slightly, by using the same initial conditions but varying the metallicity. The evolutionary path is qualitatively similar at lower metallicity ($\sim$ 10%, See Fig. 3.7). At higher metallicity ($\sim$ 20%), the system has reversed its mass ratio not once but twice. This illustrates the sensitivity of binary evolution to metallicity and that systematic studies of these sub-SMC metallicity regimes are necessary to truly capture the physics in metal-poor environments (e.g., Götberg et al. 2017; Klencki et al. 2020).

Finally, we note that while our modeling suggests a merger is likely, it is not the only plausible outcome. It is possible that this system could survive its contact phase past the main-sequence ultimately evolving into a stripped star binary system. More detailed exploration of this possibility requires improved data (e.g., more UV data points, better cadence to constrain the period, time series radial velocities, rotational velocity, mass-loss), as well as a larger model grid that includes more subtle physical effects (e.g., tidal distortion or energy transport), and a more thorough investigation of the effects sub-SMC metallicity on binary evolution would certainly be useful.

As mentioned above, we acknowledge that this is only a small subset of plausible physical scenarios and our point is more illustrative than conclusive. We have assumed that the system primarily experiences conservative mass transfer, due to the observational suggestions that both stars are main-sequence stars and hence experience Case A mass-transfer. In some cases (e.g., wider Case A systems, Case-B and -C systems with at least one evolved star) this mass-transfer could be non-conservative, which is a possibility not explored in this paper, but an idea we can pursue in future work.

3.7 Discussion

3.7.1 WLM-CB1: a contact binary candidate

WLM-CB1 is the first sub-SMC metallicity contact binary candidate in the literature. Since there is currently no other confirmed sub-SMC metallicity contact binary we can only compare our system to literature examples of contact systems and semi-detached systems in the LMC and SMC and one Milky Way system (See Figure 3.9). In this comparison, WLM-CB1 seems to be right at the boundary of semi-detached and contact systems, though the sample of known systems is small ($\sim$ 50). Qualitatively, below a $P < 1.2$ days we find that out of the 20 systems in this sample, 16 are contact binaries, while 2 are semi-detached and 2 are undetermined. The frequency suggests that a contact system classification for WLM-CB1, which has a period of $P = 1.0961^{+0.0066}_{-0.0036}$ days. If we apply the period cut and a mass-ratio cut at q <0.7, we find that 4 of the 6 systems that pass this cut are contact binaries. When looking at the total mass of the system vs. period, it appears that if we draw a line through V382 Cyg (Milky Way system, $f \sim 0.1$ or $f \sim 1.1$ if 1 = contact; Abdul-Masih et al. 2021) and SSN 7 (SMC, $R_1/R_{RL} = 1.01$ and $R_1/R_{RL} = 1.03$), which are both marginal contact systems, the majority of systems falling on or below this empirical line (including our system) are contact systems. Overall, our comparison to observations in the literature favors a contact system as opposed to a semi-detached system. However, we remain cautious as we are in a small sample regime, which is not uniform (i.e., various metallicities, masses and stellar types).

Theoretical studies (e.g., Fabry et al. 2024; Menon et al. 2024) have recently aimed to predict the likely ranges of parameters for contact binary systems in higher metallicity regimes (MW, LMC, SMC). While some predictions suggest that contact binaries favor equal mass configurations, it appears that initial assumptions can influence the results greatly (Fabry et al. 2024). This is inline with observations of massive contact binaries (e.g., Abdul-Masih et al. 2022) in this metallicity regime, which find unequal-mass contact binaries and do not find evidence that they are quickly evolving towards an equal-mass configuration.

As noted we present WLM-CB1 as a contact binary candidate, since the fitting to observations does not statistical prefer a contact system vs. a near-contact/semi-detached system. We emphasize that follow-up observations as well as a more holistic analysis of the sub-SMC binary population is necessary to draw a definitive conclusion and confirm the true nature of this candidate. An increased sample of in detail studied contact binaries, which should soon be available through Vera C. Rubin Observatory's Legacy Survey of Space and Time (Rubin/LSST) (e.g., Ivezić et al. 2019; Street et al. 2023; Hambleton et al. 2023) and BlackGEM (Groot et al. 2022), would shed light on the distribution of binaries in the SMC and the lowest metallicity regime.

More data is required to more precisely constrain the nature of WLM-CB1. Notably

the lack of temporally extended UV data and coverage of the second dip drives larger uncertainties in the fitting (e.g., Figure 3.6. UV data points at the minima are a high priority.

Spectroscopically, time-series radial velocity measurements of the system would constrain the masses and mass ratio to a higher certainty (See Figure 3.10). The estimated ΔRV of 90 kms^{-1} difference between the two scenarios should be resolvable even in a low-resolution (R$\sim$2000) spectrum. Given the inferred inclination angle from the light curves and the close distance between the two stars, there is a chance to observe the system as a spectroscopic binary. To capture the ΔRV of 30 kms^{-1} difference for the secondary and disentangle the effects of both stars a medium-resolution spectra is a preferred option. Observing the spectral features of both stars, from emission lines to metal abundances, would provide further constraints on the evolutionary stage of the system. Comparison between photometry and spectroscopy will become increasingly important as we enter an era of time domain photometry and aim to study large populations of binaries yielded by these surveys. In the advent of time-series survey telescopes like the Rubin/LSST, BlackGEM, and instruments more sensitive to hot, blue objects, such as UVEX (Kulkarni et al. 2021) and CUBES (Evans et al. 2023), WLM-CB1 showcases how we will soon be able to routinely probe binary evolution of massive stars in the lowest metallicity regimes.

3.8 Acknowledgments

MG thanks the referee for helpful discussions, feedback or comments. MG thanks Sabrina Drammis, Jessica Lu and Jacqueline Blaum for the helpful discussion. MG acknowledges support of the UC Berkeley Cranor Fellowship and the Schweizerische Studienstiftung. Support for this work was provided by NASA through grants GO-15275, GO-15921, GO-16149, GO-16162, GO-16717, AR-15056, AR-16120, HST-HF2-51457.001-A, and JWST-DD-1334 from the Space Telescope Science Institute, which is operated by AURA, Inc., under NASA contract NAS5-26555.

This research used the Savio computational cluster resource provided by the Berkeley Research Computing program at the University of California, Berkeley (supported by the UC Berkeley Chancellor, Vice Chancellor for Research, and Chief Information Officer).

This work is based on photometric observations made with the NASA/ESA Hubble Space Telescope, obtained from the data archive at the Space Telescope Science Institute. STScI is operated by the Association of Universities for Research in Astronomy, Inc. under NASA contract NAS 5-26555. The HST data presented in this article can be obtained from the Mikulski Archive for Space Telescopes (MAST) at the Space Telescope Science Institute. The WLM-CB1 and WLM-CB1 UV observations analyzed can be accessed via [doi: 10.17909/v5pa-y253]https://doi.org/10.17909/v5pa-y253 and [doi: 10.17909/xxwx-ca38]https://doi.org/10.17909/xxwx-ca38, respectively. The JWST data can also be obtained from the MAST. The observations are part of the ERS JWSTSTARS High Level

Science product and can be accessed via (Weisz, Dan 2024).

This work made extensive use of NASA's Astrophysics Data System Bibliographic Services.

Software: `astropy` (Astropy Collaboration et al. 2013, 2018, 2022), `astrML` (Vanderplas et al. 2012), `corner` (Foreman-Mackey 2016), `DOLPHOT` (Dolphin 2016), `matplotlib` (Hunter 2007), `numpy` (Harris et al. 2020), `MESA` (Paxton et al. 2011, 2013, 2015, 2018, 2019), `Optuna` (Akiba et al. 2019), `PHOEBE` (Prša et al. 2016; Horvat et al. 2018; Conroy et al. 2020; Jones et al. 2020), `pyphot`, `PyTorch` (Paszke et al. 2019), `UltraNest` (Buchner 2021),

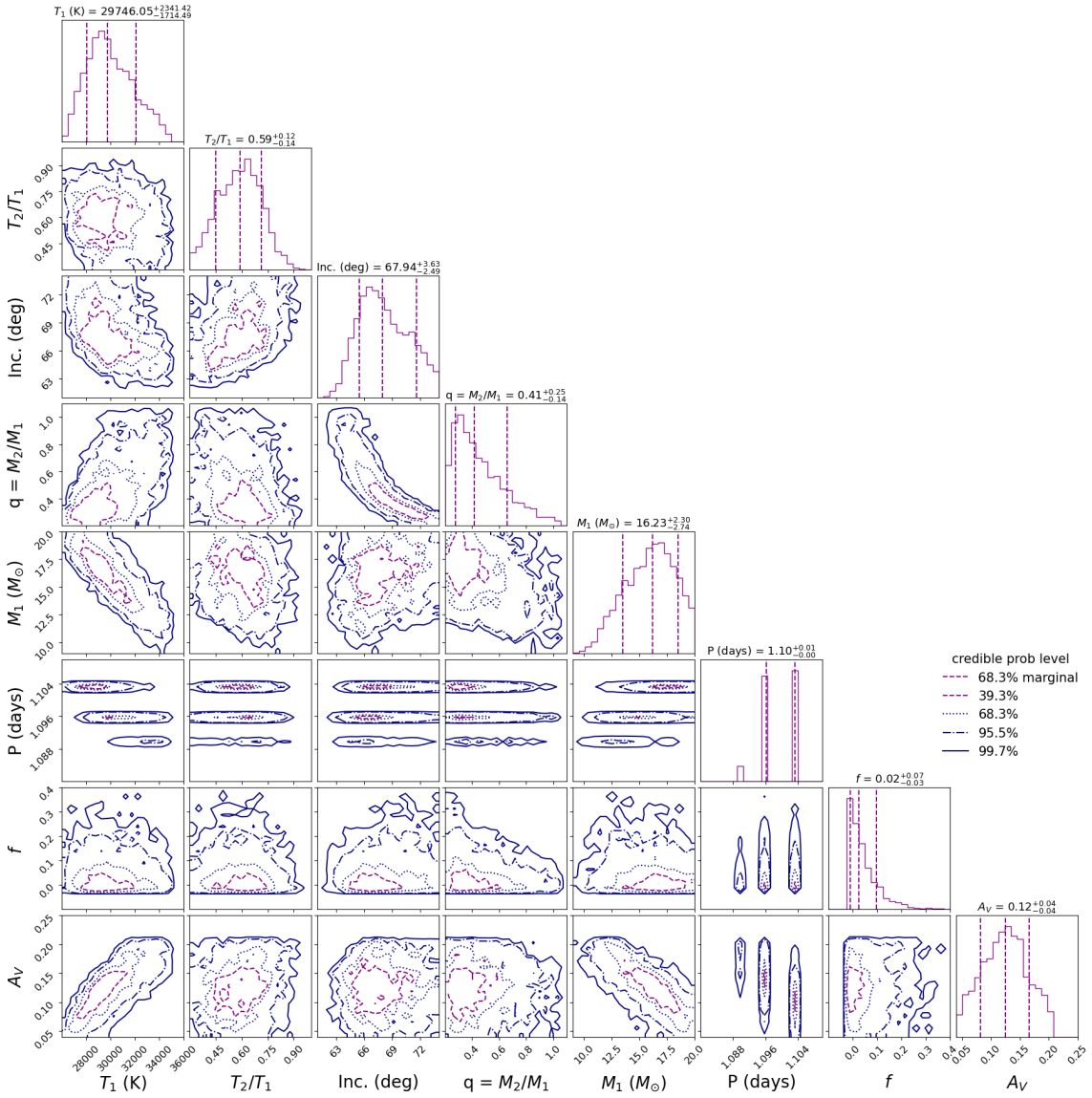


Figure 3.5: A corner plot showing samples of the posterior from our "ultranest" fitting of WLM-CB1. For the marginalized 1D distributions, we indicate the median and 25th and 75th percentiles. The period clearly shows the mutli-modal nature of the posterior distribution. The lack of any data in the secondary dip, along with a paucity of UV data, contribute to broad constraints on temperature ratio, mass, and mass-ratio. This would be better recovered with the addition of spectroscopy. There is a correlation between temperature of the primary, mass of the primary and dust, as all parameters affect the light-curve similarly (See Figure 3.4).Because the fill-out factor is hitting the edge of its parameter space we consider this to be a minimal contact binary.

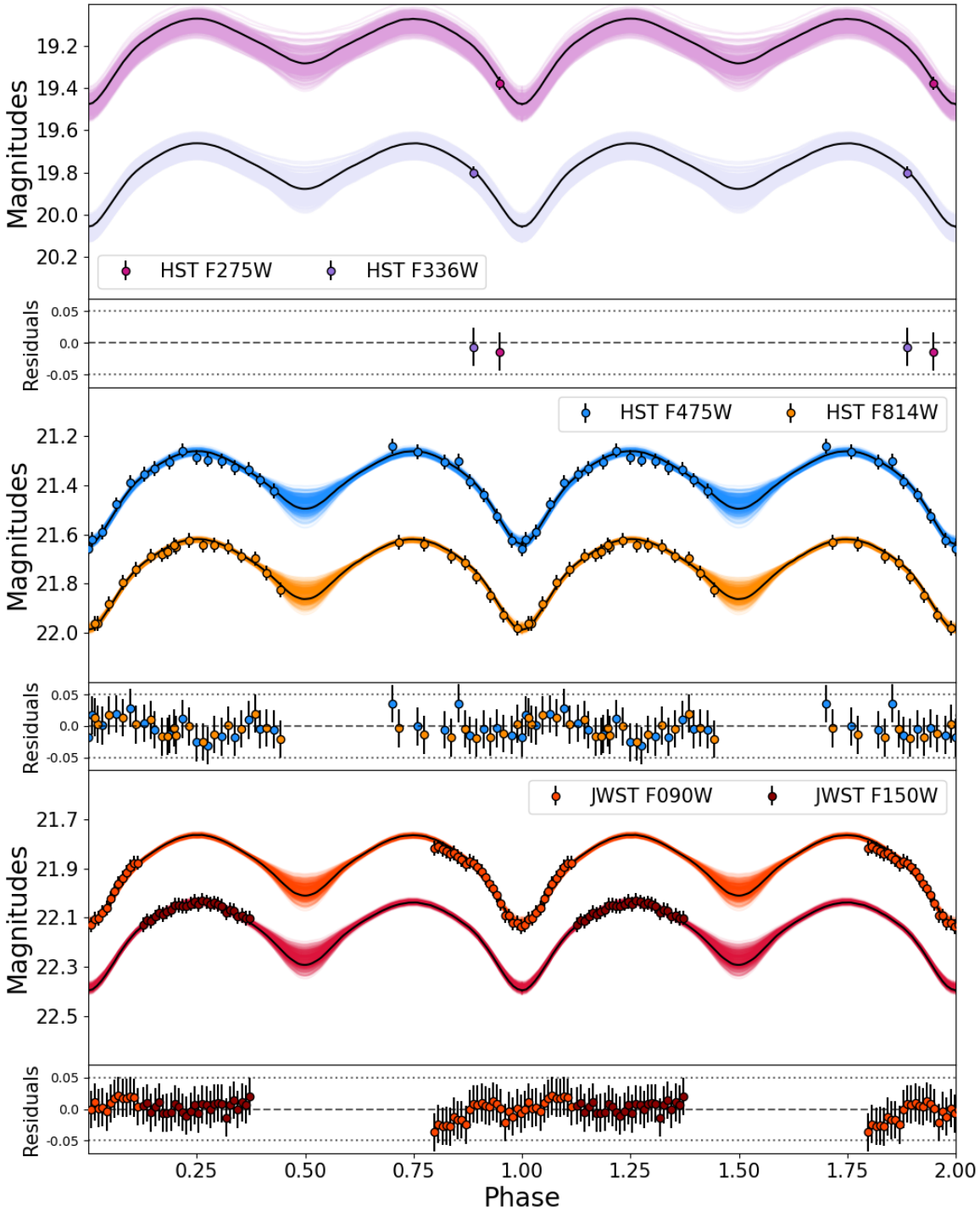


Figure 3.6: Multi-band observed (points) and model light curves (black lines) for WLM-CB1. We also plot 300 draws from the posterior as individual colored lines. Residuals for each set of filters are plotted below the light curves. The models generally provide an excellent fit to the observed light curves. The largest uncertainties are near the minima and the UV, for which there is sparse sampling.

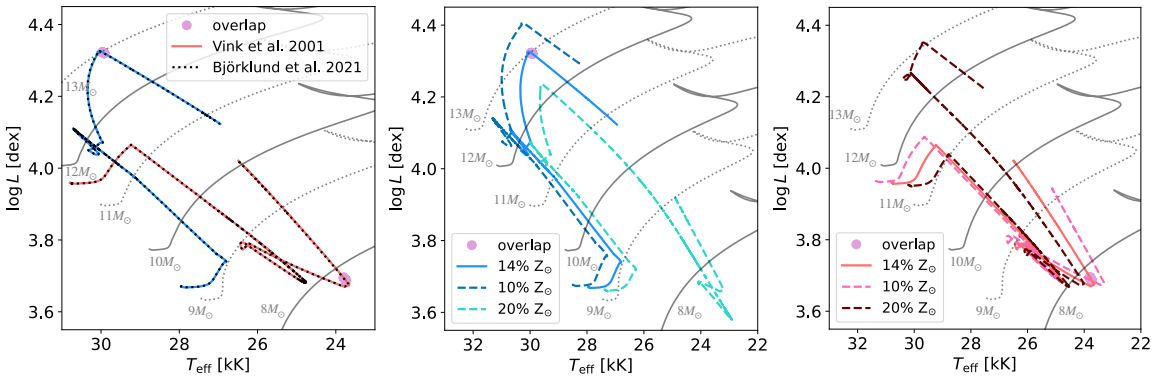


Figure 3.7: Evolutionary tracks yielded by MESA for our best match evolutionary path with initial primary mass (M_p) of 11.25 $M_\odot$ for the more massive component at ZAMS, initial mass-ratio (q_i) of 0.8, and initial binary separation (a_i) of 10.75 $R_\odot$. **Left:** The evolutionary tracks of WLM-CB1a (blue) and WLM-CB1b (red, M_p) are shown compared to MIST single star evolutionary tracks (grey lines). The pink dots indicate the area where the current observables match. It is evident from the figure that the initial mass exchange occurs soon after the ZAMS, that the second mass exchanges also occurs on the MS and that in this particular scenario the system merges on the MS. We also overplot the evolutionary tracks computed by MESA assuming the Björklund et al. (2021) wind prescription (black dashed line) to illustrate that in this very weak wind regime the binary interaction dominates the evolution of the stars. **Center and Right:** The evolutionary tracks yielded by MESA for a system with the aforementioned initial conditions (M_p=11.25 $M_\odot$, q_i=0.8, a_i=10.75 $R_\odot$) at different metallicities of 14% $Z_\odot$ (WLM), 10% $Z_\odot$(metal-poor), and 20% $Z_\odot$(SMC). While the evolutionary tracks are qualitatively similar between the 14% $Z_\odot$ and 10% $Z_\odot$ track, there is a clear difference to the higher metallicity (20% $Z_\odot$) track, which experiences an additional mass transfer. The sensitivity to metallicity in binary evolution is clearly illustrated here, emphasizing the need for systematic exploration of binaries in the sub-SMC metallicity regime. It also shows that caution is necessary when extrapolating from the SMC to lower metallicity regimes.

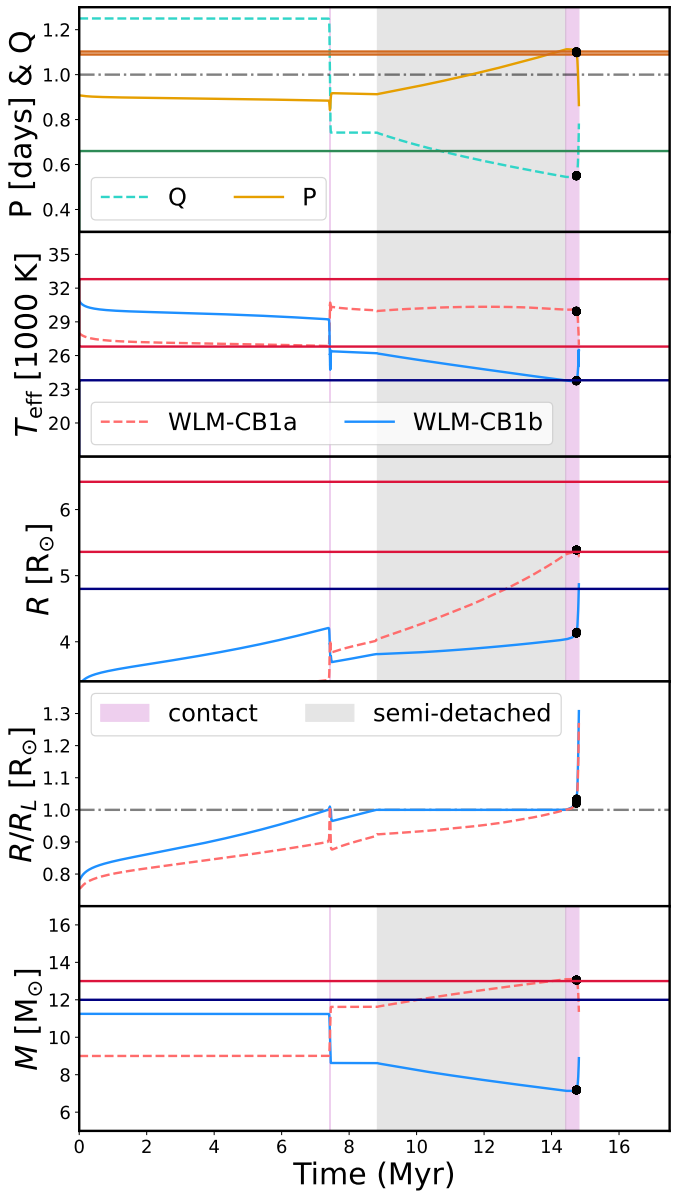


Figure 3.8: Best model of the evolutionary path WLM-CB1 that is consistent with current observations. The initial parameters of this model are the Mass of the primary (Mp) = 11.25 $M_\odot$, mass-ratio (q) = 0.8 and binary separation (a_i) = 10.75. The instance of overlap between the models and the observational parameters are marked by black dots. The limits given by the observational uncertainties are horizontal solid lines (crimson for WLM-CB1a and navy for WLM-CB1b). As seen in the 4th row, each evolutionary path suggests that both stars have filled their Roche Lobe ($R/R_L \geq 1$ at the observed point of their evolution). The scenario suggest a previous drastic short-lived mass transfer/contact phase, where the mass-ratio is flipped (light pink vertical line). The matches between models and observation suggest that WLM-CB1 just re-entered a contact phase (pink) after a prolonged near contact phase (semi-detached, grey), hence why the definitive nature of WLM-CB1 is hard to determine.

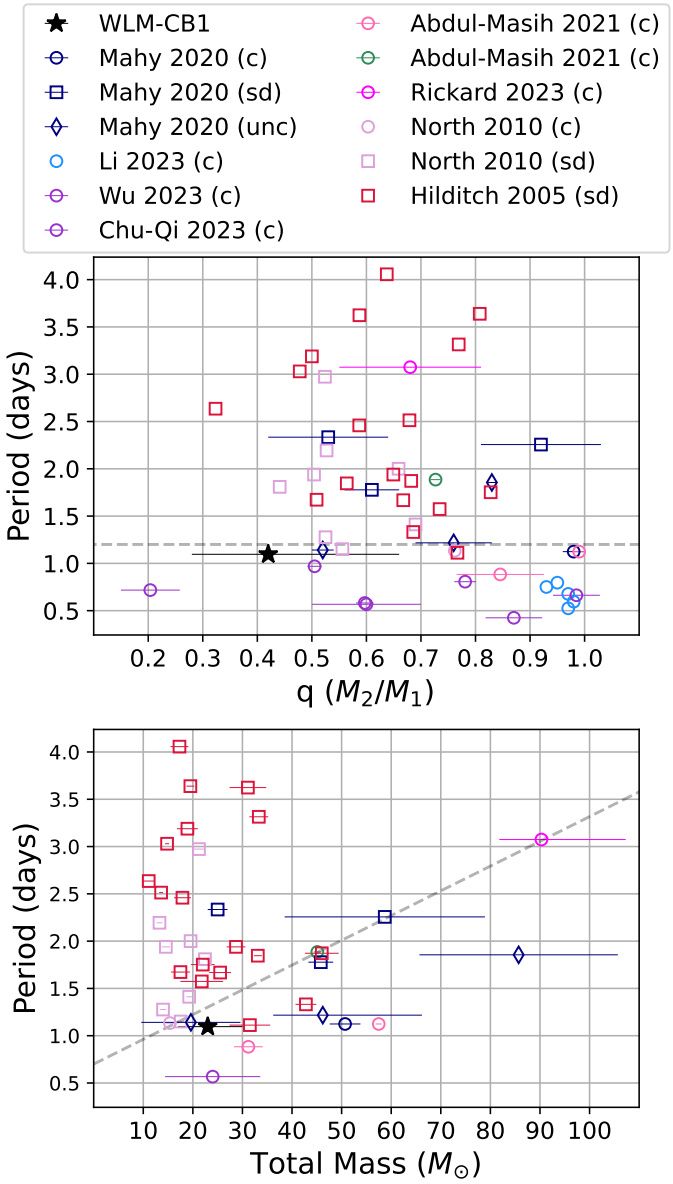


Figure 3.9: Overview of the observed mass ratio (q) and period (top) and of the observed total mass and period (bottom) of the contact binaries (circles) or semi-detached binaries (squares) in the LMC (blue hues) and SMC (purple/pink hues). We also plot system that are not clearly distinguished between the two (diamonds). WLM-CB1 (black star) appears to be in a regime where the transition from semi-detached to contact binary occurs based on the current observational sample. In the top panel, the gray line indicated $P = 1.2$ days, to illustrate that the majority of the systems below that line are contact binaries. In the bottom panel, the gray line is a visual guide to show that if a line is draw through the marginal contact binaries in literature (V382 Cyg (MW green), $f \sim 0.1$; Abdul-Masih et al. 2021) and SSN 7 ($R_1/R_{RL} = 1.01$ and $R_1/R_{RL} = 1.03$; Rickard & Pauli 2023) all observed contact system to this date fall on or below that line. We further note that the SMC appears to show a wider range of observed mass-ratios, though this may be an effect introduced by observational bias or the small sample.

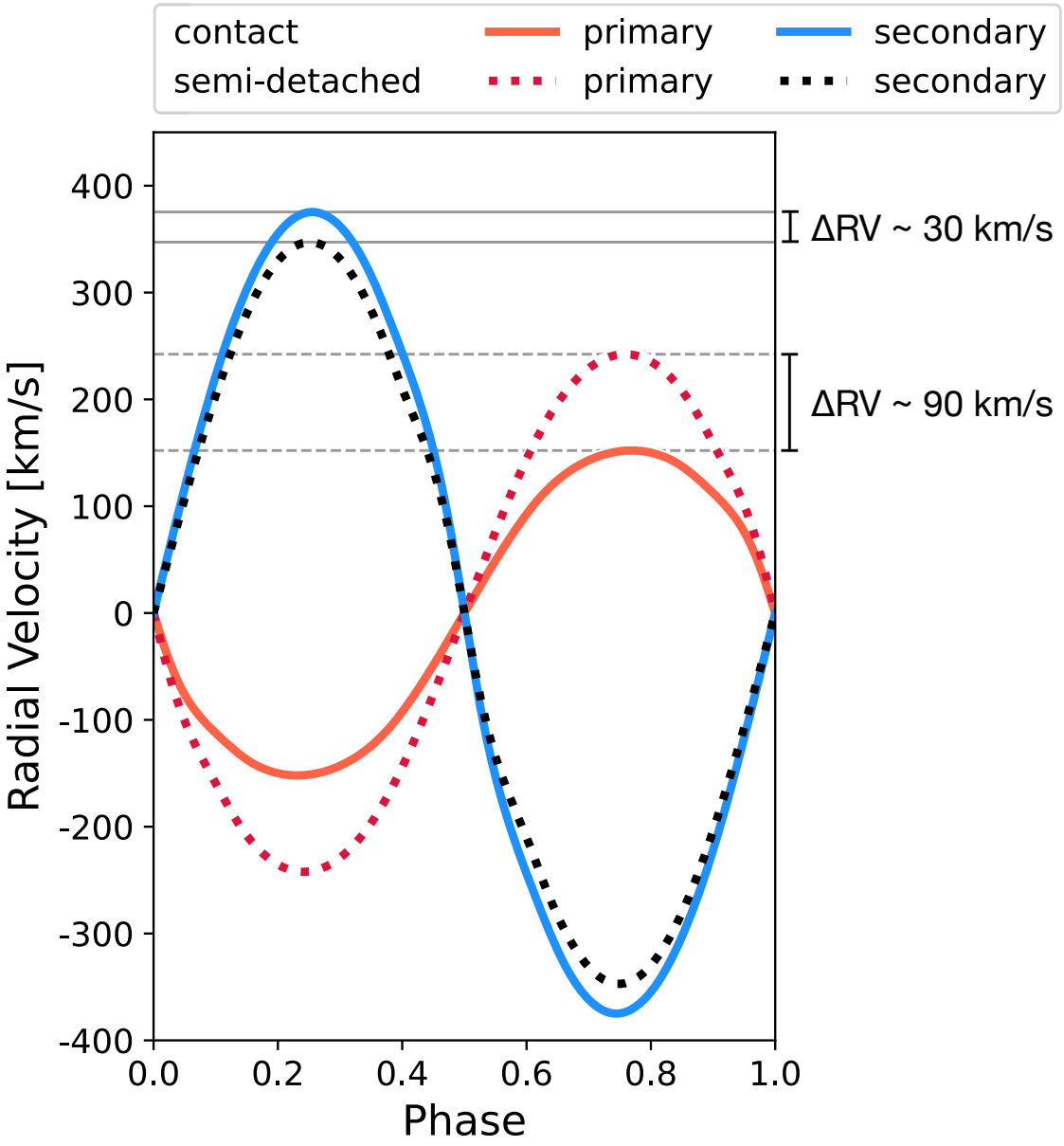


Figure 3.10: Synthetic Radial Velocity curves obtained by the PHOEBE code. We compute the expected radial velocity curves using the parameters obtained by the analysis. The solid lines represent the expected curves yielded by the contact fit, whereas the dotted lines are the expected curves yielded by the semi-detached fit. The velocity of the primary is more affected by the difference in parameters, since the difference is primarily introduces by the mass-ratio, i.e., in the semi-detached case the secondary is more massive than in the contact case, therefore the orbital velocity of the primary is larger.

Chapter 4

Photometric study of the massive star content in Sextans A

This article has not been published yet. Future co-authors contributed the following parts: HST reductions as part of LUVIT (PIs: Gilbert and Boyer) products (Williams, Benjamin F.) and the ASTs as part of LUVIT products (Choi Yumi). The first author (Gull, Maude) led, performed, created, and wrote the remaining reductions, analysis, figures, and texts.

4.1 Chapter Abstract

We present a study of the metal-poor massive star population in the Local Group dwarf galaxy Sextans A. We use panchromatic photometry of the Local Ultraviolet and Infrared Treasury (LUVIT) in combination with the Bayesian Extinction and Stellar Tool (`BEAST`) to characterize the massive stars by deriving stellar parameters with uncertainties. Additionally, we complement our dataset with GALEX FUV and Hα imaging to understand the spatial distribution of the massive stars found in our analysis. We address the importance of the UV in studying these stars and highlight the current shortcomings when it comes to massive binaries and future improvements. We find 369 massive main-sequence stars (median present-day mass: $M_{act,p50} > 8M_{\odot}$ and surface gravity: $\log(g)_{p50} > 3.7$ dex [cgs]) for which we find a $\chi^2 < 10$ fit. We compare our sample to existing observed spectra, with which we find overall good agreement, but we can explain most discrepancies when present. We identify 94 stripped star candidates due to their UV excess (bluewards of the zero-age main sequence) in the F225W-F475W CMD, the F275W-F475W CMD, and the F336W-F475W CMD. Furthermore, we identify OBe candidates through IR excess in the photometry and Hα excess. We find a putative fraction of OBe stars of 15% for M > 8 $M_{\odot}$, 25% for M > 15 $M_{\odot}$, and 63% for M > 20 $M_{\odot}$. This high fraction of OBe stars is in line

with expectations at low metallicity and may have implications for the effect of metallicity on binary interaction and mass transfer.

4.2 Introduction

Across the universe, metal-poor massive stars influence astrophysical phenomena and dominate the light of star-forming galaxies beyond the Local Group. The stellar physics, evolution, and final fates of massive stars can change drastically as a function of mass and metallicity, significantly impacting their environment and host galaxy. However, due to the dearth of spectroscopic data in the lowest metallicity regime, most of our theories remain loosely constrained empirically. Significant uncertainties thus persist in our understanding of massive stars, especially at low metallicities, which in turn makes the interpretation of the high-redshift Universe results delivered by JWST challenging (e.g. Bunker et al. 2023; Cameron et al. 2023; Senchyna et al. 2024; Castellano et al. 2024; Topping et al. 2024b,a).

A tremendous effort has been invested in studying these stars in the Local Group both photometrically and spectroscopically. Primarily, the SMC has been studied extensively (e.g., VLT-FLAMES Survey; Evans et al. (2006); Mokiem et al. (2006); Trundle et al. (2007); Hunter et al. (2008, 2009); Ritchie et al. (2010); Dunstall et al. (2011), RIOTS4; Lamb et al. (2016); Oey et al. (2018), ULYSSES; Roman-Duval et al. (2020); Vink et al. (2023); Sana et al. (2024); Sander et al. (2024); Martins et al. (2024); Ramachandran et al. (2024); Bernini-Peron et al. (2024) and just recently through BLOeM (e.g., Shenar et al. 2024; Bestenlehner et al. 2025; Patrick et al. 2025; Bodensteiner et al. 2025; Villaseñor et al. 2025; Britavskiy et al. 2025). However, SMC metallicity does not capture true low metallicity environments beyond our Local Group ($Z < 10\%Z_{\odot}$). In the past decade, the metallicity limit for massive stars in the Local Group has been pushed to sub-SMC metallicity by tremendous spectroscopic efforts (e.g., Camacho et al. 2016; Evans et al. 2019; Garcia et al. 2019a; Telford et al. 2021; Ramachandran et al. 2021; Lorenzo et al. 2022; Gull et al. 2022; Telford et al. 2024; Mintz et al. 2025). However, due to distances to these star-forming sub-SMC metallicity galaxies, the closest being ~700 kpc, these massive stars are faint and challenging to observe in large quantities. Our current spectroscopic capabilities do not allow for spectroscopic studies beyond a couple of dozen stars at a time, making it challenging to study massive stars as an entire population. In recent years, panchromatic photometry has emerged as a promising avenue to provide baseline insights into this elusive population and a scientifically motivated target list for dedicated spectroscopic follow-up. Additionally, comparing spectroscopically and photometrically derived stellar parameters provides a crucial test-bed for our stellar atmosphere and evolutionary models. Lastly, panchromatic photometry allows us to study these stars beyond our current spectroscopic capabilities, expanding the number of extremely metal-poor star-forming galaxies within our observational reach.

Here we present an in-depth quantitative panchromatic photometric study of the metal-poor massive stars in the Local Group galaxy Sextans A (Z$\sim$ 6% $Z_{\odot}$, D $\sim$ 1.3 Mpc). Sextans A is known to host a plethora of massive stars (Dohm-Palmer et al. 2002b). The galaxy has been previously photometrically inspected by Dohm-Palmer et al. (1997, 2002b); Dolphin et al. (2003); Massey et al. (2007b,a); Bianchi et al. (2012); however, none of these studies provide stellar parameters for the massive stars. Spectroscopically, Lorenzo et al. (2022) published an extensive qualitative analysis of OB stars in Sextans A, two stars were observed as part of ULYSSES, and in-depth spectroscopic medium-resolution studies of individual stars were only recently published (Telford et al. 2024). However, only one star currently has stellar parameter provided (S3; Telford et al. 2024). Our panchromatic photometric study comes at an optimal time by providing detailed stellar parameters derived from photometry as the field ramps up its spectroscopic effort to investigate the metal-poor massive stars in Sextans A. The paper is organized as follows. In §4.3, we describe the multi-wavelength *HST* observations and data reduction. In §4.4, we detail the process of measuring stellar properties from the *HST*-based spectral energy distributions (SEDs), then highlight the importance of UV filters, and discuss the shortcomings of the Bayesian Extinction and Stellar Tool (`BEAST`) in regards to massive binaries. In §4.5, we present our results, provide a detailed discussion of the fitting results and massive star population, comparison to literature, stripped star candidates, and Be star candidates.

4.3 HST Photometry

We use the HST data collected as part of the Local UltraViolet and Infrared Treasury (LUVIT) data products. The LUVIT data collection and reduction were carried out separately using DOLPHOT, and we refer the reader to the survey paper Gilbert et al. (2025) and Gull et al. (2022) for further details. We briefly summarize the reduction here. The footprints for our datasets are shown in Figure 4.1.

The LUVIT data of Sextans A consists of *HST* UV, optical, and NIR broad-band imaging. Optical imaging in the WFPC2 F555W and F814W filters acquired as part of GO-7496 (PI E. Skillman) (Dohm-Palmer et al. 2002a), and supplemented by new WFC3/UVIS F225W, F275W, F336W, F475W and F814W (GO-15275 (PI K. Gilbert) & GO-16104 (PI J. Roman-Duval)) and WFC3/IR F110W and F160W (GO-16162 (PI M. Boyer) imaging . In addition to the LUVIT photometry, we also reduce the HST/ACS F658N imaging of GO-17 PI Gull. To summarize the filter coverage, we provide Table 4.1 and a mapping to Sextans A in Figure 4.1.

To reduce the HST data, the photometric reduction pipelines for *HST* simultaneous *N*-band photometry (Williams et al. 2014, 2021) were utilized and improved (see Gilbert et al. 2025, for details).

For a given reference image footprint, DOLPHOT reports measurements of point-

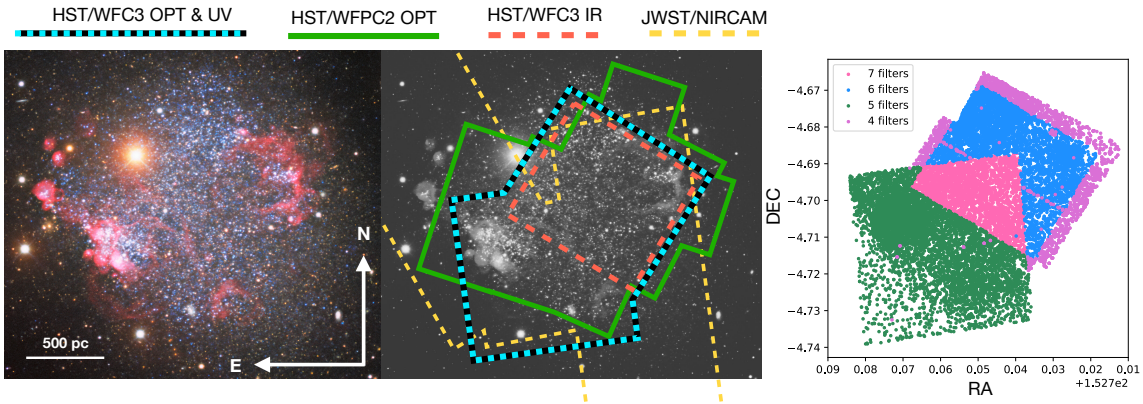


Figure 4.1: Optical image (left: color, right:bw) of Sextans A with the Nicholas U. Mayall 4-meter Telescope at Kitt Peak National Observatory. Left: We indicate the directions of North and East and a distance scale of 500pc. Middle: Footprints of the HST imaging produced by the LUVIT Survey (Gilbert et al. 2025) and JWST/NIRCAM observations (JW 2391 PI: Roman-Duval and JW 1619 PI: Boyer) are overlaid on the optical image. The turquoise footprint shows the HST UV observations, the green and black footprint shows the HST optical observations, the red footprint denotes the HST IR footprint, and the yellow footprint indicates the JWST/NIRCAM observations. Right: We plot the filter coverage with corresponding coordinates. Stars filter coverage is color-coded in the following way: pink;7, blue;6, green; 5 and purple;4. (credit: KPNO/NOIRLab/NSF/AURA Data obtained and processed by: P. Massey (Lowell Obs.), G. Jacoby, K. Olsen, & C. Smith (AURA/NSF) Image processing: T.A. Rector (University of Alaska Anchorage/NSF NOIRLab), M. Zamani (NSF NOIRLab) & D. de Martin (NSF NOIRLab)

spread-function photometry for every object detected on any exposures. The measurements include the flux, flux uncertainty, magnitude in the Vega system, signal-to-noise ratio (S/N), and various photometry quality metrics. Quality cuts are applied to the DOLPHOT output catalog of all objects identified: 1) with S/N $\geq$ 4; (2) with crowding $<$ 1.3 and $<$ 2.25 for UV and optical/IR filters, respectively; and (3) with square of sharpness (SHARP^2) $<$ 0.15 and $<$ 0.2 for UV/IR and optical filters, respectively, producing the "GST" catalog. These quality cuts were applied in each band independently. Additionally, objects associated or impacted by diffraction spikes after the GST cuts are removed using the median filter technique to identify impacted regions and culling the objects belonging to the regions (Gilbert et al. 2025). Even though the photometric depth reaches a couple of magnitudes fainter than the old main-sequence (MS) turn-off, we limited our stellar SED modeling to the bright targets of our interest by applying the following cut: $F475 < 24$ dex.

Artificial star tests (ASTs) are used to compute the photometric accuracy, precision, and completeness. See Gilbert et al. (2025) for more details.

Figure 4.2 shows select UV and optical CMDs of Sextans A. The CMDs are close to 50% or above of the completeness limit. We overplot the rotating (v/vcrit=0.4) MESA Isochrones & Stellar Tracks (MIST) (Dotter 2016; Choi et al. 2016) for reference. We shift the tracks to the JAGB distance modulus of μ=25.71 mag reported by Lee et al. (2024) and A_v = 0.122 mag, consistent with the foreground maps of NASA/IPAC Extragalactic Database.

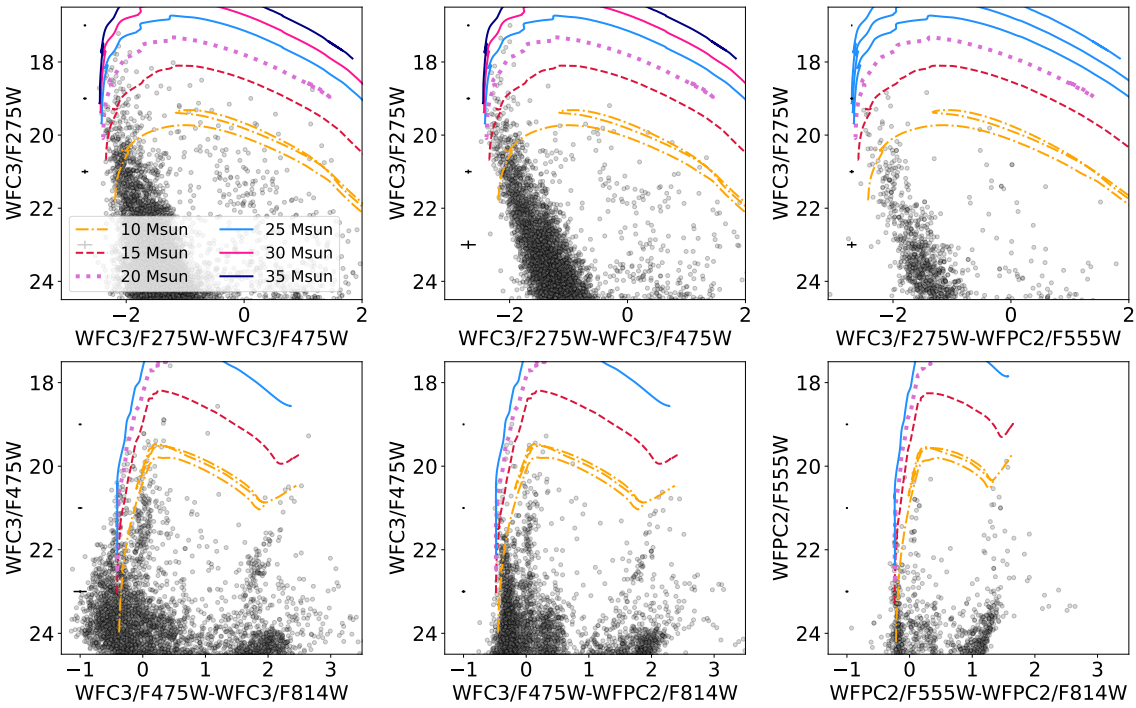


Figure 4.2: Select *HST*-based UV-optical (top) and optical-only (bottom) CMDs of Sextans A. For reference, we overplot select MIST tracks ([Fe/H] =−1.0, v/vcrit=0.4, A_v = 0.09). We also indicate the typical errors for each CMD in the left-hand of each subplot.

4.4 Analysis

In this section, we describe our analysis of the panchromatic photometry using the `BEAST`, we discuss our simulations for each filter combination, and the impact on stellar parameters determination for massive stars when the UV filters are absent. Lastly, we describe the shortcomings of the `BEAST` regarding massive binaries.

4.4.1 BEAST fitting

We fit the panchromatic photometry from the *HST* broad-band multi-wavelength imaging (F225W, F275W, F336W, F475W, F814W, F110W, F160W) with the Bayesian Extinction and Stellar Tool (`BEAST`; Gordon et al. 2016) to infer physical properties of the stars in Sextans A. In short, the `BEAST` uses Bayesian inference to simultaneously model individual stars' stellar and line-of-sight dust properties while considering the observational biases arising from noise and crowding.

A detailed technical description of the `BEAST` can be found in Gordon et al. (2016). The `BEAST` has also been used to study properties of nearby low-metallicity dwarf galaxies and their stellar content (e.g., Choi et al. 2020; Gull et al. 2022; Lindberg et al. 2025)

Here we briefly outline the steps taken for this `BEAST` fitting. First, a physics model grid is created by mapping a stellar evolution library (1) to a stellar atmospheric model (2) using the following parameters; (1) initial mass M_{ini}, age A, and metallicity Z and (2) effective temperature $\log(T_{\rm eff})$, surface gravity $\log(g)$ and metallicity Z.

The stellar atmosphere models are split into a lower temperature regime (i.e., A-type and cooler), where stars are fit with local thermodynamic equilibrium models from Castelli & Kurucz (2004), and a higher temperature regime, where stars are paired with non-local thermodynamic equilibrium (non-LTE) atmospheres from the TLUSTY OSTAR and BSTAR grids (Lanz & Hubeny 2003, Lanz & Hubeny 2007). We opt to fix the distance of our stars to the galaxy distance, and a dust model then extinguishes the intrinsic light. For the dust model, we opt to choose an SMC-like attenuation curve with $R_V = 2.74$ (Gordon et al. 2003) and allow $A_{\rm V}$ to vary from a minimum of $A_V = 0.00$ mag to a maximum of $A_V = 2.0$ mag. Furthermore, we split our observations and artificial star tests (ASTs) catalog into three density bins using the spatial density information. Using the resulting ASTs, we create an observational noise model for each resulting dust extinguished stellar model.

As mentioned for the analysis of the stars in Sextans A, we adopt a fixed distance modulus of $\mu = 25.71 \pm 0.15$ mag. Second, we use the PARSEC stellar evolutionary models (Bressan et al. 2012; Chen et al. 2014, 2015; Fu et al. 2018). Finally, we adopt a metallicity of $Z = 0.06$ $Z_\odot$ throughout the paper based on the metallicity measurement of Berg et al. (2012). We report the median value (_p50) and the uncertainty computed from the 68% confidence interval (i.e., 0.5∗(_p84-_p16)) of a marginalized 1D posterior probability distribution function (PDF) for each parameter. Throughout the analysis we report following parameters: effective temperature ($\log(T_{\rm eff})$, $\log_{10}(T/[K])$), surface gravity ($\log(g)$, $\log_{10}[cgs]$) , attenuation ($A_{\rm V}$, mag) , initial mass (M_{ini}, $M_\odot$), present day mass (M_{act}, $M_\odot$), luminosity ($\log(L)$, $\log_{10}(L/[L_\odot])$), age ($\log(A)$, $\log_{10}(A/[yr])$) and radius (R, $R_\odot$). Example `BEAST` fits are in Gull et al. (2022); Lindberg et al. (2025).

As shown in Figure 4.1, not all stars have seven filter (F225W-F160W) coverage; a subset of stars have only 4-5 filters (no *HST* IR). We split the LUVIT catalog by filter coverage, creating 12 sub-catalogs. These sub-catalogs are all fit independently in the `BEAST` with

Table 4.1: Filter Combinations

# Filters	F225W	F275W	F336W	F475W	WFPC2 F555W	WFC3 F814W	WFPC2 F814W	F110W	F160W	N Stars
7	✓	✓	✓	✓	···	✓	···	✓	✓	2642
6	···	✓	✓	✓	···	✓	···	✓	✓	3
5	···	✓	✓	✓	···	✓	···	···	···	6456
4	···	✓	✓	✓	···	✓	···	···	···	6
6	···	✓	✓	✓	···	··· ✓	✓	✓	✓	4505
5	✓	✓	✓	✓	···	··· ✓	✓	···	···	1
4	✓	✓	✓	✓	···	··· ✓	✓	···	···	1221
6	···	✓	✓	···	✓	···	✓	✓	✓	53
5	✓	✓	✓	···	✓	···	✓	···	···	1
4	···	✓	✓	···	✓	···	✓	···	···	106

Note. — Summary of various filter combinations of the Sextans A data used in this work. When the data overlaps, we choose the WFC3 values over the WFPC2 values.

the corresponding ASTs, which will have the same coverage as the data catalog. Whenever possible, we use the seven filter fit for our analysis, then in decreasing order with a preference for WFC3 F475W and F814W filter coverage over WFPC2 F555W and F814W. We only fit stars with at least two UV filter coverages. The various filter combinations are described in Table 4.1.

We divide the resulting photometric SED fitting results into three groups based on the χ^2 values to facilitate discussion and comparison. Fits with $\chi^2 < 10$ are considered good fits, $10 < \chi^2 < 100$ are decent fits, and $\chi^2 > 100$ are poor fits. These χ^2 divisions are based on qualitative assessment of the fits, following other BEAST papers in the literature (e.g., Van De Putte et al. 2020; Gull et al. 2022). They are meant to be used qualitatively to facilitate discussion.

4.4.2 The Importance of the UV

The UV is particularly sensitive to the properties of massive MS stars. We simulate stars based on our Sextans A observations and noise model and the ASTs to quantify the effects on the fitting in the absence of UV photometry. Using the `BEAST` we can generate this simulated catalog, and fit it through the same infrastructure as our real stars. The simulated data is generated with fixed distance, metallicity, and extinction curve (Rv). We start with the seven filter fit and remove a UV filter for each run, until F475W (optical) is our bluest filter. We compare each resulting `BEAST` output to the simulated input parameters in Figure 4.3. We break up the discussion into the individual rows:

- **Masses: M_{act} and M_{ini}**: Massive MS stars are generally hot (> 25 kK), which means the filter most sensitive to their stellar properties will be the UV filters. For an apparently single star, the `BEAST` can recover the input masses within 1σ for stars up

to 55 $M_\odot$, with uncertainties slightly increasing with increasing mass. As we remove all the UV data, we see the recovery of the input worsen; in fact, the mass is underestimated by the BEAST. While removing F225W and F275W generally leads to larger scatter, we are in the small number regime above 20 $M_\odot$, and therefore the large peaks can be driven by a single outlier.

- **Temperature and Surface Gravity:** $\log(T)$ **and** $\log(g)$: The temperature and surface gravity input is accurately recovered. The sole exception is the hot temperature end, where we observe a slight underestimation of the hottest temperature. This divergence is unsurprising, as even F225W will be in the Rayleigh-Jeans tail for hotter stars. As we remove the UV filters, two trends happen. First, the BEAST overestimates $\log(T) \sim 3.8$ and $\log(T) \sim 4.2$; additionally, it underestimates temperature higher than $\log(T) \sim 4.3$. The latter is because the optical bands fall on the Rayleigh-Jeans tail for hot stars, making them relatively insensitive to temperatures. For surface gravity, we find a large scatter of input-output as we remove the UV filter. Similarly to temperature, we find an overestimation to underestimation transition here at $\log(g) \sim 3.5$, which is likely to reconcile the overestimated temperatures with the underestimated mass and the input SED.

- **Luminosity and Radius:** $\log(L)$ **and** *Radius*: The input luminosity is well recovered by BEAST when 7-band coverage is available. When the F225W and F275W bands are removed, the BEAST overestimates the luminosity of stars with$<$ 4.1; this may be related to the divergence from the input parameters observed in A_V. As the UV can no longer be used to constrain the overall attenuation, the luminosity will drive the scaling of the SED and may be anchored to high luminosities. When removing all UV bands, the BEAST consistently underestimates the input luminosity for stars with$>$ 3.6. Again, this aligns with the expectation that these bright sources will likely be hot sources, for which the UV is the most sensitive. The notable exception are Yellow supergiants (YSG) and Red Supergiants (RSG), however, these are a minority of sources in our simulated data. For radius, we see an increase of scatter as we remove bands, and only a slight underestimation of the radius for stars with $radius >$ 150 $R_\odot$.

- **Age and Extinction:** *Age* **and** *Av*: We find that for the stellar ages the BEAST underestimates the age of the oldest stars (Age$>$ 500 Myr), even when using all 7 filters. As we remove the UV bands, the BEAST overestimates the age of young stars. For extinction, we find that input and output are overall consistent; however, they experience a slight underestimation of input by the BEAST as we move above $A_V \sim 1.25$ for all simulated data with at least one NUV band. Without UV filters, the uncertainty on the A_V increases significantly, and is overestimated for low A_V and underestimated for high A_V.

Overall, it is evident that UV photometry is crucial in the study of massive MS stars and that F225W is sufficient to describe apparently single stars up to $\sim 55\ M_{\odot}$.

4.4.3 Shortcomings of the BEAST in regards to massive binaries

Binaries and binary interaction are omnipresent among massive stars. Observations and predictions suggest that the binary fraction of stars with $M_* > 8\ M_{\odot}$ ranges from 85% to 100% (Sana et al. 2012; Moe & Di Stefano 2017; Offner et al. 2023). In de Mink et al. (2014), the authors simulated the effects of binarity on an observed massive star population of a young cluster ($\sim 2\ Myr$), assuming a binary fraction of $\sim 70\%$. They predict that $\sim 22\%$ will be effectively single (they may have companions, but they are too far or too small to matter), $\sim 28\%$ will be post-interaction products (mergers, semi-detached systems, stars that have gained mass). In contrast, the remaining $\sim 50\%$ will be pre-interaction binaries. They note that changing initial conditions can vary these relations. For example, increasing the binary fraction to 100% will lead the binary products to increase to $\sim 36.8\%$, but decreasing metallicity will lead to a fraction of $\sim 26.5\%$. Other major drivers of uncertainty are primary mass distribution, mass-ratio distribution, and orbital period distribution. All these distributions are observationally unconstrained at the metallicity of Sextans A. Physical assumptions (e.g., accretion efficiency, angular momentum loss) may also affect this ratio. In the context of our panchromatic photometry analysis of Sextans A, the stellar evolution and atmosphere models used throughout this study are single-star models. Given what we know about massive stars and binarity, it is clear that these will not be adequate models or assumptions for all stars. We briefly discuss here which shortcomings in particular will be problematic. For the $\sim 20\%$ apparently single stars, the `BEAST` assumptions are adequate. For the pre-interaction binaries, we can encounter four fitting scenarios. First, for some systems, the primary will still be photometrically so dominant that the `BEAST` fit with the uncertainties on our measurements will adequately capture the primary. Second, twin binaries, expected to make up $3\% - 14\%$ (Moe & Di Stefano 2017), will likely yield a good χ^2 value for the `BEAST` fit, since the SED will be indistinguishable from a star with similar temperature but larger mass (See Figure 4.4). In that case, the `BEAST` will mistake the twin system as a more massive single star. Third, in the case of eclipsing binaries, the `BEAST` will yield a poor χ^2 value (> 100 in most cases) for short-period binaries. The individual data points are likely not measured in-phase, hence the variations will lead to large enough divergence from a single star SED that the `BEAST` will yield a bad fit (detectable eclipsing binaries ($\sim 1 - 5\%$)). The last scenario concerns pre-interaction binary configurations not covered yet. The more the stars in the system diverge in type, the higher the χ^2 value will be (See Figure 4.4). Therefore, a subset will likely still fall in the good χ^2 regime (< 10), while a subgroup will fall in the decent χ^2 regime (< 100). The remaining will fall within the bad χ^2 regime. Future studies may want to consider fitting two stellar SEDs to systems

falling within the $10 < \chi^2 < 100$ regime to determine if a better fit can be recovered. For all of the aforementioned binary scenarios, the masses of the stars are overestimated in the worst-case scenario. For the post-interaction binaries and products, a subset will yield bad χ^2 values (e.g., classical Be stars with disk in line-of-sight, stripped stars). However, a subgroup of post-interaction stars will appear as single stars, yielding a decent or good χ^2 value. In that case, the stellar parameters may not truly capture the star's actual parameters. Post-interaction mass gainers can appear over-luminous for their mass. In contrast, mass donors may appear under-luminous for their mass. In both these cases, fitting a single star atmosphere model will yield erroneous stellar parameters, even when recovering a good χ^2 value. To first degree, the temperature is likely the only reliable parameter in this case.

Our `BEAST` fit report that for stars with $\log(L) > 3.5$ (luminosity of $\sim$ B4-type star) $\sim$ 44% stars are recovered with $\chi^2 < 10$, while $\sim$ 32% stars are recovered with $10 < \chi^2 < 100$. The remaining $\sim$ 24% show $\chi^2 > 100$. Overall, this aligns with the expectations for the issues described above. Of the $\sim$ 44% stars with good χ^2 value, it is likely that $\sim$ 10% – 20% are not well captured by the current underlying models.

The accuracy of panchromatic photometry can be compared to low-resolution spectra; however, to capture all the physical phenomena of metal-poor massive stars, higher-resolution spectra are necessary to improve our current understanding of stellar astrophysics in this regime.

4.5 Massive stars in Sextans A

We find 369 massive stars with $M_{act,p50} > 8M_{\odot}$ and $\log(g)_{p50} > 3.7$ in our panchromatic analysis with $\chi^2 < 10$ (502; $\chi^2 < 100$). No other cuts have been applied thus far. For this part of the discussion, we will first focus on the main-sequence stars, as massive stars beyond the main-sequence are not always well captured by current evolutionary models due to the physical phenomena like binarity and rotation, which can heavily impact their evolution at low metallicity (See Section 4.4.3). Figure 4.5 shows the sample of massive main-sequence stars. We find 5(11) above 30 $M_{\odot}$, 8(41) between 20 $M_{\odot}$ and 30 $M_{\odot}$, and 233(183) between 10 $M_{\odot}$ and 20 $M_{\odot}$. Lastly, we have one star with $\chi^2 < 100$ between 60 $M_{\odot}$ and 70 $M_{\odot}$ and 4 between 40 $M_{\odot}$ and 50 $M_{\odot}$. No spectra exist for 350(464) of the massive stars. Above 25 $M_{\odot}$ 4(9) out of the 6(25) currently have low resolution spectra (Lorenzo et al. 2022), and one star has medium resolution spectra (Telford et al. 2021). In Figure 4.5, we plot the massive MS in our sample and show the massive star candidates identified by (Lorenzo et al. 2022), including giants and supergiants, which are not all MS stars. We note that on the upper end of the HR diagram (LogL> 4.5), most stars in both panels are located in reasonable areas based on their spectral type. Exceptions include stars marked as binary candidates, which, as explained in the previous section, may have misleading stellar parameters despite their good χ^2 values. In particular, the B

III type star appearing to the right of the supergiants in the left panel may appear more luminous in the BEAST fit due to extra light contamination from the secondary. The lower end of the HR diagram shows more peculiar placements of stars for their spectral type. We note that a subset of these stars, particularly the O V star residing to the right of the main-sequence, are spectra that are reported with quite low S/N, which may have led to a spectral misclassification, especially for stars in crowded regions. Lastly, the HR diagram shows four stars classified as supergiants residing on the MS. We find that in Lorenzo et al. (2022) these stars (s053,s073,s075,s116) are all described to have contaminated spectra, either a blend of SB2, which may make the luminosity classification harder or low S/N, which may impact spectral typing. We will make further comparisons to the literature in the next subsection.

We compare the age distribution of the massive stars with $\log(A)_{p50} < 7.50$ to ground-based Hα and GALEX observations (See Figure 4.6). We note that the stellar population here does not include $\chi^2 > 10$ fits, which may include OBe stars and stripped stars, which could power the intensity in both the Hα and FUV (See Section 4.7.1 and 4.7.2). Overall, the young stellar population traces the FUV and Hα intensities well. The largest HII region (A) is well traced by the young stellar population and the UV intensity, although the Hα emission is slightly more extended than the FUV. On the other hand, the upper right part of the region seems to show some higher FUV intensity, but does not show strong Hα, despite showing some young stars in this region. Although we note a young B-type star may contribute to the overall UV flux, but not necessarily ionize the Hα region significantly. Spatial resolution in the region is limited, which is why we cannot isolate the exact sources contributing to the majority of the high intensity in the FUV at this time. In the future, UVEX (Kulkarni et al. 2021) will provide a slightly clearer image. Region B shows significantly less Hα emission than the number of young stars and FUV intensity in this region. While a very clustered high intensity Hα region exists near the top right, the FUV intensity and the young stellar population are far more extended. As mentioned, these may all be B stars; alternatively, the star formation in region B could have depleted most of the gas in that region. Region C similarly to Region A appears to be traced by both the FUV and the young stellar population. Although again we find a pocket, where young stars and a high intensity FUV region exist, Hα emissions are lacking. Lastly, Region D appears very diffuse, which is also reflected in the limited FUV emission and sparse young stellar population. We do find a handful of young stars not near any Hα emission or high FUV intensity region. Near region B, we find four very young stars not associated with any Hα nor high FUV luminosity. There are also two near region C, and one is seemingly in the galaxy's center. Two reasons can explain the lack of Hα emission near these young stars. Although stars are thought to form in clustered environments (Lada & Lada 2003; Krumholz et al. 2019), it is not uncommon to find massive stars isolated in the field (Oey

et al. 2018; Dorigo Jones et al. 2020; Vargas-Salazar et al. 2020; Gull et al. 2022; Vargas-Salazar et al. 2025). One plausible explanation is that they belong to a small cluster, which depleted all the surrounding gas in its formation and therefore cannot ionize or excite any nearby gas, which would lead to Hα emission. Alternatively, these stars may be runaway stars, i.e., stars that were ejected from their birth cluster due to dynamical interactions (Oey et al. 2018; Vargas-Salazar et al. 2020). These mechanisms primarily rely on binaries driving ejections, either through supernova explosions of one of the companions (binary supernova scenario) or close encounter with a binary system (dynamical ejection scenario). It is worth pointing out that we are only plotting young stars for which the `BEAST` yielded $\chi^2 < 10$; therefore, several young stars typically associated with runaway phenomena (i.e., OBe stars Dallas et al. (e.g., 2022); Rocha et al. (e.g., 2024)) are not included in this discussion. Lastly, we find some sources of high Hα intensity not near any H II region. While this is speculative, common sources of strong Hα emission not associated with extended gas regions are binary interactions and binary products (e.g., OBe stars and stripped stars, Section 4.7). Explaining the sources for ionizing radiation and UV luminosity at high redshift remains challenging, partly due to the limited local empirical constraints. Sextans A, and a handful of other sub-10% $Z_{\odot}$Local Group galaxy, are our some of our best local testbeds for these far away galaxies, As evident in Figure 4.6, the distances to these galaxies prevent shallow ground-based observations (Hα) or low-resolution instruments (GALEX FUV) from capturing more than the brightest features. From a photometric perspective, the HST photometry is crucial to characterize these stars, especially in the UV (See Section 4.4.2. Future UV-sensitive space-based missions like UVEX, or the Habitable World Observatory (HWO), if the UV capabilities are supported, would provide much-needed tools to tackle these outstanding questions at high redshift.

4.6 Comparison to Literature

4.6.1 Spectral Types

Spectral Typing can be a useful qualitative tool to describe massive stars for which only low-resolution spectra exist. As higher resolution spectra become available, stellar parameters are updated and spectral types corrected. However, even low-resolution spectra can be observationally expensive for metal-poor massive stars. A more cost-effective alternative for this initial spectral characterization is panchromatic photometry (Gull et al. 2022). In particular, for most single appearing massive stars, the photometric stellar parameters and spectroscopic stellar parameters appear consistent, and outliers can, in most cases, be flagged in the panchromatic photometry. A subset will not appear as suspicious in the panchromatic photometry (See Section 4.4.3. However, the vetting sample is currently still limited to a dozen stars. We further test this method by comparing

a subset of our derived panchromatic stellar parameters to the spectral typing of Lorenzo et al. (2022). We focus on the early-type (O-B3) stars. First, we use the commonly used spectral type versus effective temperature relationship. We divide the stars that yield χ^2 < 100 into two luminosity classes (dwarfs and giants) using the derived log(g) values. Any star with log(g) > 3.70 is designated a dwarf, while stars between 3.70 > log(g) > 2.50 are designated as a giant. We do not include a comparison of the supergiants. We end up with 22 dwarfs and 32 (sub)giants in our sample, with spectral types reported in Lorenzo et al. (2022). In addition to our data, we include commonly used observational relation between spectral type and temperature reported by Dufton et al. (2019) for the SMC and the theoretical prediction for the relationship reported by (Lorenzo et al. 2025) for sub-SMC metallicity. Of the 22 dwarfs, we derive slightly lower temperatures for a given spectral type. However, for most of them, the error bars fall within the uncertainties derived by (Lorenzo et al. 2025). We find four clear outliers showing lower temperatures than expected for the reported spectral type in Lorenzo et al. (2022). These stars are s001, s002, s020 and s026. We note that for s001 and s002, we derive a χ^2 value of 24.5 and 18.7, respectively. This may be unsurprising as Lorenzo et al. (2022) flagged s001 as a potential double-lined spectroscopic binary (SB2) system and noted strong He II absorption and nebular emission. Both stars may have companions undetected by the `BEAST`, especially if the companion is hotter and less massive, since it could easily hide in the photometry. s020 is classified as either a double-lined spectroscopic binary (SB2) or a blend, and s026 is considered a potential blend. The `BEAST` fits yield χ^2 < 10. The disagreement here could be explained by the lack of resolution in the spectra, compared to the high spatial resolution in the photometry. We find eight stars for the 32 (sub)giants that significantly deviate from the theoretical relation. The temperatures derived for the stars s010, s013, s034, s051, s052, and s057 are too cool, while s049 and s050 are too hot. s010 has very low S/N and resolution, and s034 also has low S/N and is classified as an O-type star despite the absence of He II 4686. We note that s051 and s052 are classified as supergiants in Lorenzo et al. (2022), and the `BEAST` yields χ^2 of 35 and 29, respectively. It has been previously suggested that stellar atmosphere models do not capture supergiants adequately (McQuinn et al. 2011; Gull et al. 2022), so this may be a plausible explanation for the discrepancy seen here. Neither the s013 spectra nor the `BEAST` fit suggest any peculiarities. s050 appears to be a potential binary, while s049 is another supergiant; both may not be captured well by the underlying models used in the `BEAST`, despite yielding good χ^2 values. To summarize, 18/22 of the dwarf appear in good agreement, while 24/34 of the (sub)giants are in good agreement, we note that the sub(giants) generally have lower quality spectra. Overall, the `BEAST` recovers temperatures that align with the spectral typing from low-resolution spectra.

We also explore the luminosity classes reported in Lorenzo et al. (2022) to their position

in the CMD and the derived surface gravities from the BEAST in Figure 4.8. We also include S3 (s029) analyzed in Garcia et al. (2019a); Telford et al. (2024); Furey et al. (2025), which we will discuss in Section 4.6.2. In the optical, distinguishing between various surface gravities is nearly impossible as they blend, especially in the high mass regime. However, in the NUV-optical CMD, we see a clearer trend for the surface gravities. Although the surface gravity values depend on the underlying stellar atmosphere models, the trend across the CMD will be accurate for most stars. We find that the majority of dwarfs (denoted as V) identified by Lorenzo et al. (2022) fall on the 4.5 dex > $\log(g)_{p50}$ > 3.7 dex range of the CMD. However, three stars classified as dwarfs appear red-ward of the main-sequence. We note that in Lorenzo et al. (2022) it is remarked that one was observed with the 1.5 slit (very low resolution R< 1000), one seemed to be a blend (potential binary), while the last star doesn't have any special remarks, but is quite faint. Furthermore, we find that three (s003,s024,s043) stars marked as dwarfs and on the main-sequence in the 4.5 dex > $\log(g)_{p50}$ > 3.7 dex region in the NUV-Optical CMD appear in the 3.0 dex > $\log(g)_{p50}$ > 2 dex region in the optical only CMD. In Gull et al. (2022), this phenomenon was described as typical for Be-type stars. The spectra of s003 show Hβ and Hγ emission, as well as relatively shallow He I line, potentially indicating high $v \sin i$, spectral features typically associated with Oe/Be stars. We discuss these further in Section 4.7.2. Some stars identified as supergiants (I) appear blue-wards of the core Helium burning sequence (cHeB). The cHeB may not be well calibrated, as underlying assumptions in the evolutionary tracks can greatly impact its location. We only comment on the faintest bluest five sources, which Lorenzo et al. (2022) comments on potential contamination by either a nearby star or nebula that may have impacted the luminosity class determination. Lastly, we comment on the brightest star in the optical CMD (s106), Lorenzo et al. (2022) identified the star as a potential binary, we find that the BEAST fit yields a bad χ^2 value, meaning a single star SED does not capture the SED of this star, further supporting the claim that this may be a massive binary system.

4.6.2 S3 – s029

S3 (s029) is one of the most studied stars at sub-10% $Z_\odot$massive stars. The star was first observed with (R~ 1000) as part of Garcia et al. (2019a) study of hot stars in Sextans A, and then observed at low resolution (R~ 1000) in Lorenzo et al. (2022), at R~ 6000 resolution in the UV as part of Telford et al. (2021) and at medium resolution (R~ 4000) in the optical as part of Telford et al. (2024); Furey et al. (2025). A challenging problem for the star has been that the photometrically derived parameters disagree with the spectroscopically derived parameters. In Garcia et al. (2019a), the star was identified as an O9 V star, although they note that the derived luminosity seemed closer to a III type star. In Lorenzo et al. (2022), the star was classified as an 08.5 III star and denoted as an SB1 candidate. Telford

et al. (2024) higher resolution optical and UV spectra, could not confirm this claim, and reclassified the star as an O9 V star. The main parameter divergence lies in the surface gravity value and, therefore, in the masses. In Telford et al. (2024) the spectroscopic surface gravity $\log(g) = 3.9 \pm 0.1$, which suggest a spectroscopic mass of $49\ ^{+30}_{-19}\ M_{\odot}$ and in Furey et al. (2025) it was derived to be $\log(g) = 4.18^{+0.14}_{-0.08}$, which suggest a spectroscopic mass of $77.8\ ^{+25}_{-12}\ M_{\odot}$. In contrast, the photometric 3.5±0.1 was in Telford et al. (2024), which yielded a photometric mass of 21 $M_{\odot}$. Our `BEAST` fit, which yields $\chi^2 < 10$, suggest a surface gravity of $3.73^{+0.12}_{-0.08}$ and mass of $25.08^{+4.87}_{-2.29}\ M_{\odot}$. Surprisingly, we find consistent luminosity values throughout with $\log(L) = 5.1$ (photometry Telford et al. 2021), $\log(L) = 5.15$ (spectra Telford et al. 2024), $\log(L) = 5.18^{+0.05}_{-0.04}$ Furey et al. (2025) and $\log(L) = 5.24^{+0.12}_{-0.09}$ for our `BEAST` fit. Current evolutionary tracks suggest that the masses derived in Furey et al. (2025) and Telford et al. (2024) are too high for its derived luminosity and temperature, making the star under-luminous for its mass, as the authors point out. The tension arises from the difference in surface gravity measured between spectroscopy and photometry, as the spectroscopic mass strongly depends on surface gravity measurements. We note that the photometric surface gravity is model-dependent. While we cannot further comment on the spectroscopy other than higher resolution or multi-epoch spectra may shed more light on this disagreement, we can further investigate the photometry. In Figure 4.8, we show the position of S3–s029. The NUV-optical CMD falls within the $4.00 < \log(g)_{p50} < 3.5$ range of surface gravity values. In the optical, it does indeed appear closer to the main-sequence, but as explained in Section 4.6.1 $4.50 < \log(g)_{p50} < 3.0$ overlap in this region of the CMD. Although S3 behaves like a standard apparently single star, we remain cautious as binaries and binary products can easily hide in photometry (See Chapter 3). We perform one last test, integrating the light of all the HST sources within the KCWI PSF ($\sim$ 1 arcsec) and rerun the `BEAST`. We find a slightly higher χ^2 value, but still acceptable, and a slightly higher mass ($\sim 1-2\ M_{\odot}$), but the remaining parameters are relatively consistent with the previous measurement. This is because S3 is a relatively isolated source, and still dominates the flux compared to its neighboring sources. It is unclear at this point if S3 is just a peculiar source (binary or binary product) or whether the single star models are culprits and need to be adjusted at low metallicity. The former appears more likely since the expectancy is that massive stars are in binaries or experience binary interaction. Photometrically, monitoring the source with time-series photometry would provide the chance to observe variability. Fortunately, the Vera Rubin Observatory Legacy Survey of Space and Time (LSST) will map out the southern sky every two weeks over the next ten years. S3 is bright enough to be reliably observed by LSST, so we should expect to be able to monitor S3 for any brightness changes. Spectroscopically, we require both multi-epoch spectra to monitor for a companion and higher-resolution, higher S/N spectra to measure the surface gravity to higher precision.

4.7 Stripped star and OBe star candidates

This section discusses stripped star candidates and Be star candidates, which are considered major products of binary interaction. Predictions currently estimate that ~ 30% of massive stars will experience some "stripping" (Sana et al. 2012), which may result in binary products referred to as stripped stars. These stripped stars are thought to be an important stepping stone towards compact object binaries (e.g., Kalogera et al. 2007; de Mink & Belczynski 2015; Tauris et al. 2017; Kruckow et al. 2018) and one of the prime candidates to explain the hardest ionizing photons observed in starforming galaxies at high-redshift due to their longevity and abundance (Götberg et al. 2018). There are currently no observations on the relationship between abundance of stripped stars and metallicity; on the other hand, Be stars are thought to increase in abundance with a decrease in metallicity (Peters et al. 2020; Schootemeijer et al. 2022). While other explanations for the formation of Be stars exist, one of the leading theories is that they are binary products (e.g., Kriz & Harmanec 1975; Pols et al. 1991; Bodensteiner et al. 2020). As the mass gainer, they increase their angular momentum, causing them to reach high rotational velocities near their break-up velocity, leading to the formation of a disk. In either case, these stellar objects warrant more attention and detailed observations. This section presents stripped star candidates, OBe star candidates, and preliminary Be star fractions.

4.7.1 Stripped star candidates

Recently, Ludwig et al. (2025) showed how to identify stripped star candidates in space-based Swift-Ultraviolet Optical Telescope (UVOT) photometry. They identified 522 candidate stripped stars in the LMC and 298 in the SMC. They recover stripped stars spectroscopically identified by Drout et al. (2023). Using a similar approach, we use the NUV-Optical CMD to identify stars that are bluewards of the ZAMS (See Figure 4.9). We find 190 stars bluewards of the MS in the F225W-F475W CMD, 215 in the F275W-F475W CMD, and 454 in the F336W-F475W CMD. We find 94 stars being blueward in all three CMDs, making them the most promising candidates. This may not be surprising as recent modeling predicts a decrease in hot stripped stars as a function of decreasing metallicity and decreasing star formation (Hovis-Afflerbach et al. 2025).

In Lorenzo et al. (2022), seven stars were identified as potential stripped stars. We have six stars in our observational footprint: s004, s005, s007, s015, s023, and s129. All but two stars show $\chi^2 < 10$ values for their fit, and all show $\chi^2 < 40$ values. When plotted on the CMD in the optical-only (F475W-F814W), we find that the three stars (s005, s015, and s129) appear bluewards of the ZAMS. While s129 appears to show a good `BEAST` fit, s005 and s015 show higher χ^2 values, ~ 14 and ~ 38, respectively. It would not be surprising that these stars are binary systems with a stripped star companion, as the primary star could

easily hide the stripped star contribution to the flux Drout et al. (2023); Ramachandran et al. (2023, 2024); Ludwig et al. (2025). Although the 94 stars constitute the most promising single star candidates, we note that detecting them through UV excess may be more complicated for stripped stars in binaries if their companion is a hot massive star. A subset of recently observed and modeled stripped stars shows that they can overlap with the main-sequence (Dutta & Klencki 2024, See Figure 4.9). While certainly photometric candidates remain crucial for follow-up, the stripped stars overlapping on the main-sequence will only be revealed by measuring surface gravity, chemical abundances, and rotational velocities in their spectra.

The photometry allows us to observe the spatial distribution of the stripped star candidates in Sextans A and comment on what we could learn about stripped star evolution and runaways from this sample. The stripped star candidates are spatially distributed throughout the galaxy, with a higher density around the H II regions. This clustering in H II regions is expected as they are thought to primarily be formed through interaction with other massive binaries. This behavior was also observed by Ludwig et al. (2025) for their LMC and SMC sample. An interesting question poses itself: what is the binary fraction of stripped stars in H II regions and in situ? Assuming stripped stars at low metallicity are formed through binary interaction (winds are too weak at low metallicity Telford et al. 2024), we would expect the majority of these systems to have companions. Additionally, stripped stars in the field are most likely, similar to other massive stars, ejected from their cluster through some dynamical mechanism. Given the timescale and formation theory of stripped stars, the expectation would be that in situ stripped stars are primarily ejected through a dynamical ejection scenario. In this case, they most likely would still have a companion, and we would observe a similar binary fraction between the stripped stars found in H II regions and the field. However, finding more single stripped stars in the field compared to the H II regions would pose significant challenges in our understanding of stripped star formation.

The formation and evolution of stripped stars, especially at low metallicity, remain highly uncertain. Understanding the true fraction of stripped star in Sextans A may hold key information about their influence on their host galaxy. As previously noted, models predict a decrease in hot stripped stars as a function of decreasing metallicity and decreasing star formation. The comparison between the LMC (522), SMC (298) and Sextans A (94), may indeed be a reflection of this prediction. However, stripped star do not necessarily have to be very hot, or fully stripped to be able to ionize their surrounding environment (Drout et al. 2023; Götberg et al. 2023). Determining the true fraction of stripped star in a given galaxy is crucial as stripped stars are popular sources to explain the ionization in high-redshift star-forming galaxies (Götberg et al. 2020). Building a census of stripped stars across all the low-metallicity star-forming galaxies in our nearby universe would allow us to probe the effects of star formation and metallicity on stripped stars. While not straight-forward,

a good handle on the relations between distributions of stripped stars and star-formation or metallicity, could allows to extrapolate to the high-redshift environments and provide clearer constraints on the likelihood of stripped stars dominating the ionization of these early star-forming galaxies.

Overall, higher resolution follow-up and potential HST UV spectra for the brightest candidates are warranted, and continued candidate detection through UV photometry is necessary, as these stripped stars are crucial to astrophysical phenomena.

4.7.2 Be stars fraction and candidates

Gull et al. (2022) showed that Be stars can be photometrically identified by detecting an IR excess compared to stars near the main sequence in the UV CMD. We repeat this analysis for the stars in Sextans A. Using the evolutionary tracks, we identify the end of the main-sequence in the UV. We then apply two different ways to identify potential OBe stars. First, we identify stars that fall redwards at the MS's end in the optical CMD. Second, we use the `BEAST` simulated photometry resulting from the fitting. Specifically, we compare the observed F814W magnitude to the simulated F814W magnitude, and identify all the stars that show more than two sigma excess in the observed magnitude compared to the suggested magnitude based on the `BEAST`. In Figure 4.10, we show the results of applying these cuts, and observe a similar behavior to Leo A; a subset of MS stars in the UV appear to pollute the BHeB sequence. NIR excess is not the only signature of OBe stars in photometry. They can also be identified using Hα imaging. Hence, we plot the emission-line stars identified through Hα imaging by Massey et al. (2007a) and stars we detected with strong Hα in our F656N observations. Using good χ^2 stars, we determine the cutoff for ~8 $M_\odot$, ~15 $M_\odot$ and ~20 $M_\odot$ in F275W magnitude. Using these cutoffs we find that above ~ 8 $M_\odot$ the OBe fraction is 15% (counting identified emission-line stars), above ~ 15 $M_\odot$ the OBe fraction is 25% and above ~ 20 $M_\odot$ the OBe fraction is 63%. This increase in OBe fraction across mass and metallicity follows similar findings as in Peters et al. (2020). We also find relatively good agreement with the ~ 27% derived in Schootemeijer et al. (2022). It is particularly striking that for ~ 20 $M_\odot$ nearly half the OB stars may be OBe stars, although we remain careful that other types of systems could pollute this fraction, and we remain in a small number statistics realm for the most massive stars.

Eleven stars have derived `BEAST` masses between 41 − 81 $M_\odot$ and fall within our OBe star candidate category. We note that seven of these stars show bad χ^2 but constitute half of the brightest OBe candidates. It is not entirely clear what the true mass of these systems is, as the bad χ^2 value indicates that the `BEAST` attempted to increase Av and luminosity to match the observed SED. The UV CMD suggests they are more likely in the 20 − 40 $M_\odot$ range; however, assuming they are binary products or experience

drastic rotational velocities, this remains highly speculative. We find that nine of the stars identified as OBe candidates through color cuts are also observed in Lorenzo et al. (2022), and, from the Hα emission, we find fifteen stars with overlap. For the stars identified through color cuts, most notably are 's003', 's024', and 's132', which show broad appearing emission lines in $H\beta$ and $H\gamma$. We further note that the remaining spectral features in 's003' and 's024' appear quite shallow, which could indicate high rotational velocity, another typical observable for OBe stars. Furthermore, 's045' is noted to have some broad absorption features and emission in Hβ, making it a viable candidate in combination with the photometry. 's049' was identified as an emission line star in Massey et al. (2007a), but is classified as a supergiant in Lorenzo et al. (2022). This star may be a supergiant with emission lines (sgB[e]); however, only higher resolution spectra may answer this question. 's069' is classified as a potential binary system. We note that Hβ emission is present, and the authors note the potential presence of a hot companion. This is particularly interesting as OBe stars are thought to have stripped star companions, making 's069' a potential candidate for such a system. We find no particularities in the spectra for 's043' and 's073', however, for some OBe stars only Hα will be in emission, so further spectroscopic or deeper photometric follow-up is needed. Lastly, 's076' and 's079' have low S/N spectra, making further comments difficult. Among the stars identified through Hα emission, we find that 's022', 's023', 's045', 's071', and 's115' all show emission in the Balmer lines and some broad shallow absorption lines. For 's023', the author suggests a projected rotational velocity $v \sin i$ 300 km s-1; additionally, they mark it as a system with potentially a hot companion. Once again, it would not be unlikely to find an OBe + stripped star system. 's054' and 's042' show broad absorption features but do not seem to indicate any emission in $H\beta$ and $H\gamma$. 's143' and 's161' show $H\beta$ emission, but otherwise low S/N. Similarly, 's027, 's058', 's019' and 's157' have low S/N spectra, which makes further comments on the spectra difficult. 's011' appears to be a binary system, it is unclear whether the Hα emission is rising from binary interact, or circumbinary material, or if one of the stars is infact a OBe star. Lastly, 's036' appears unsuspicious in the stacked spectra and is classified as an O I star. The Hα emission could originate through other mechanisms than disks; however, it is also not uncommon for OBe stars to turn on or turn off their emission, hence further follow-up of this source would provide more clarity.

Additionally, a multi-epoch spectroscopic survey of these stars would provide much-needed insight into their formation. Under the assumption that OBe stars are formed in binary interactions, one should expect a lack of OBe+MS binaries, and the most likely companions for OBe stars should be stripped to compact stars (e.g., Wang et al. 2024). But observing multiplicity properties similar to OB counterparts, would imply that these stars are formed through single star effects (high rotators at birth; Bodenheimer (1995), efficient angular momentum drives them close to critical velocity end of MS; Ekström et al. (2012);

Hastings et al. (2020b)) (Sana et al. 2011; Banyard et al. 2022). Recent results in the SMC seem to confirm a lack of OBe+MS binaries (Bodensteiner et al. 2025). It remains to be seen if this holds in the lowest metallicity environments, as rotation on the MS may play a more critical role. We note further that the increase of OBe stars at low metallicity may also be related to the inefficient stripping, causing the predicted lack of hot stripped stars. It may be the case that in higher metallicity environments, we observe more post-interaction systems, while in low metallicity environments, interacting systems are more likely to be observed. Hence, determining whether OBe stars have stripped star companions could improve our understanding of their formation and increased occurrence at low metallicity.

To determine the exact fraction, we will need the full deep Hα imaging (GO-17438 PI: Gull) or spectroscopic follow-up to constrain further binary parameters of these crucial stepping stones in the evolution of massive stars and binaries.

4.8 Conclusion

We present a panchromatic photometric characterization of the metal-poor massive star content in Sextans A. Our findings from the LUVIT observations are as follows:

- We analyze the bright stars ($F475W < 24$) in Sextans A using the LUVIT *HST* photometry. We perform SED fitting using the `BEAST` for all stars in the sample.
- We show that the `BEAST` SED fitting can reliably recover stars up to $\sim 55 M_{\odot}$, when UV (HST/F225W) photometry is present. We show that as the UV filters are removed, the SED fitting accuracy suffers greatly for massive stars.
- We identify 369 massive stars with $M_{ini,p50} > 8$ and $\log(g)_{p50} > 3.7$ with $\chi^2 < 10$ (502:$\chi^2 < 100$). Most of the identified massive stars cluster around H II regions and overlap with FUV GALEX observations. However, we find a subset of seemingly isolated stars, which could be potential runaway star candidates.
- Using the spectral-typing in Lorenzo et al. (2022), we compare the `BEAST` derived temperatures versus spectral type to the theoretical prediction of the relation as derived in Lorenzo et al. (2025) and the observed relation in the SMC of Dufton et al. (2019). We find that for the 22 dwarf-type stars, our derived parameters agree with the relationship, except for four outliers that appear to show signs of binarity, which may impact the `BEAST` fit. However, they seem to trend towards slightly lower temperatures overall than predicted by the relationship. For the 32 (sub) giant-type stars, we find eight stars that deviate from the predicted relationship. Two stars have low resolution spectra, which may make the spectral typing less reliable, one star appears to be in a binary and one star shows no apparent signs explaining the discrepancy.

The remaining four stars seem to be classified as supergiants in Lorenzo et al. (2022). Supergiants are currently not well captured by the BEAST, which is likely the source of disagreement in this case.

- We compare the identified massive stars to existing literature on the massive star content in Sextans A (Camacho et al. 2016; Garcia et al. 2019a; Telford et al. 2021, 2024). Most spectroscopically observed stars that also yield a good χ^2 value for their photometric fit show good agreement (i.e., fall on expected locations in the HR diagram and CMD for given parameters and spectral type). In most cases, disagreements can be explained by binarity, low spatial resolution spectra, or low S/N spectra. We investigate s3-s029 in greater detail and rule out that the flux contribution of unresolved nearby sources in the spectroscopy is driving the disagreement between the spectroscopic and photometric mass.

- We identify 94 promising stripped star candidates. We find that the majority cluster is in HII regions, but in-field sources also appear to exist. We postulate that there is a decrease of UV-detected stripped star candidates with decreasing metallicity and star-formation rate (LMC: 522, SMC: 298, Sextans A: 94) as predicted by theory.

- We show indications that the OBe star fraction increases at low metallicity. We obtain OBe star fractions of 15%,25% and 63% above 8 $M_\odot$, 15 $M_\odot$ and 20 $M_\odot$, respectively. We comment on the eleven OBe stars with the highest derived BEAST mass. A comparison with spectra suggests that most of these stars are truly OBe stars.

This study highlights the utility of panchromatic photometry in characterizing the general population of metal-poor massive stars in nearby dwarf galaxies. While the photometry cannot replace medium to high resolution spectra, it is a cost-effective alternative to identify the highest priority targets for different science goals.

4.9 Acknowledgments

MG acknowledges support of the UC Berkeley Cranor Fellowship and the Schweizerische Studienstiftung. Support for this work was provided by NASA through grants GO-15275, GO-15921, GO-16149, GO-16162, GO-16717, AR-15056, AR-16120, HST-HF2-51457.001-A, and JWST-DD-1334 from the Space Telescope Science Institute, which is operated by AURA, Inc., under NASA contract NAS5-26555.

This research used the Savio computational cluster resource provided by the Berkeley Research Computing program at the University of California, Berkeley (supported by the UC Berkeley Chancellor, Vice Chancellor for Research, and Chief Information Officer).

This work is based on photometric observations made with the NASA/ESA Hubble Space Telescope, obtained from the data archive at the Space Telescope Science Institute. STScI is operated by the Association of Universities for Research in Astronomy, Inc. under NASA contract NAS 5-26555. The HST data presented in this article can be obtained from the Mikulski Archive for Space Telescopes (MAST) at the Space Telescope Science Institute.

This work made extensive use of NASA's Astrophysics Data System Bibliographic Services. NED `astropy` (Astropy Collaboration et al. 2013, 2018, 2022),`DOLPHOT` (Dolphin 2016), `matplotlib` (Hunter 2007), `numpy` (Harris et al. 2020), `pyphot`

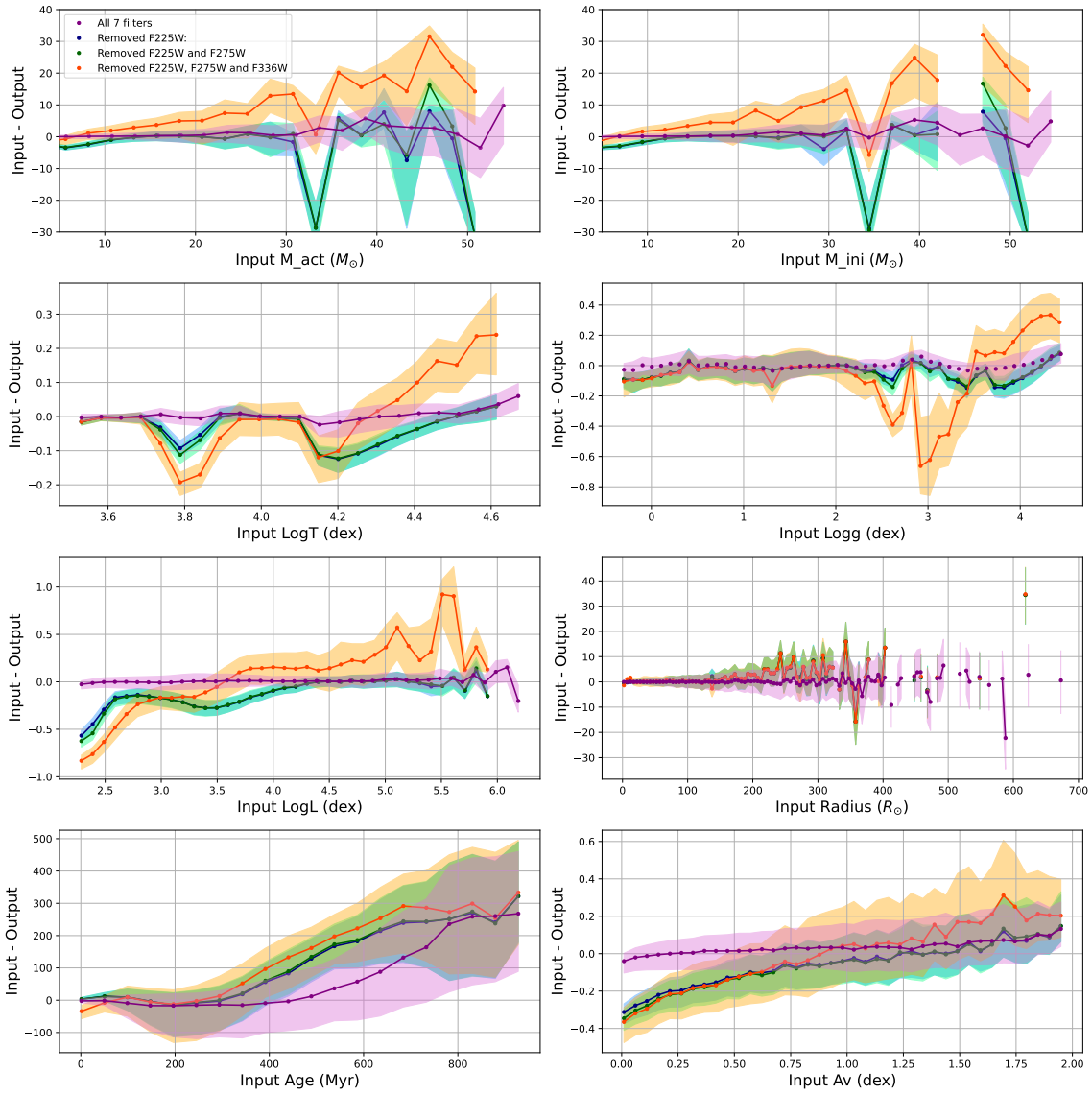


Figure 4.3: The medium $\pm 1\sigma$ difference between the BEAST output (Output) and simulated parameters (Input) for 45'000 stars. We compare the difference as a function of removing a filter in the NUV until we have only optical and IR bands. For single stars, we recover the parameters (M_{act},M_{ini},log(g),log(L),Av) for massive stars up to 55 $M_\odot$ consistently. We find that even with 7-bands available, the BEAST tends to fit slightly younger ages to the oldest stars in the population (Age > 500 Myr). Additionally, we find that at the hot end of log(T), the BEAST starts to underestimate the temperature, which is unsurprising as the hotter temperature pushes the SED of the star into a regime less sensitive to the NUV-Optical photometry. The output parameters struggle to recover the true parameters as blue filters get removed. In particular, the BEAST underestimates mass, which was also noted in Lindberg et al. (2025). Especially when no UV filters are available (No F225W, F275W, F336W), recovering the properties of massive stars is not realistic.

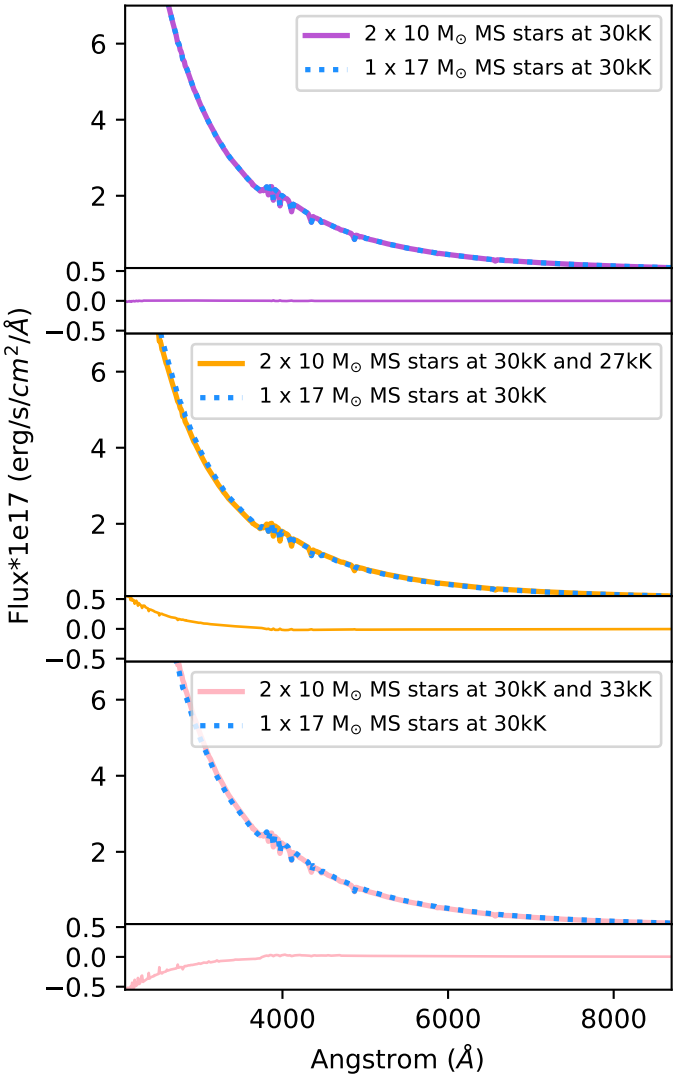


Figure 4.4: We show synthetic spectra of massive stars and binaries. The top panel shows the spectra of a twin binary system consisting of two 10 $M_\odot$ MS stars, each with T_{eff} = 30kK (purple). We overplot the spectra of a single 17 $M_\odot$ MS star with T_{eff} = 30kK (blue). The two spectra are nearly indistinguishable; inspecting the residual, we see nearly no difference between the two SEDs. Only if we were to zoom in on the spectral features would we see minimal differences in the depth of the lines, which is unlikely to be captured by photometry alone. The middle and lower panel repeat the exercise, but the companion is once cooler (middle), once hotter (bottom). We note that in the optical ($\lambda > 4000$ Angstrom), there is nearly no difference between the binary and the single star. However, the UV reveals a deviation covered by our HST photometry and will yield a less-than-optimal χ^2.

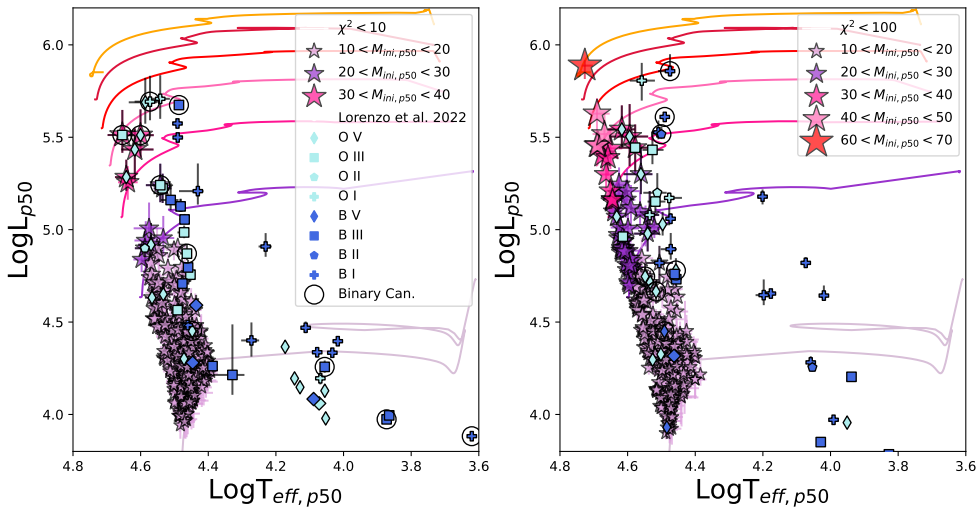


Figure 4.5: Hertzsprung-Russel diagram of the main-sequence massive stars in Sextans A. We overplot Parsec evolutionary tracks. The circles are stars where the BEAST yields $\chi^2 < 10$, whereas the squares represent $10 < \chi^2 < 100$. The stars are color-coded by their mass range, and the size of the stars is scaled to their mass. Additionally, we overplot the stars in Lorenzo et al. (2022) sample with their spectral and luminosity type. O-stars are in light blue, while B stars are in dark blue. We also circle stars marked as potential binary candidates by the author. We note that several stars that appear at odd locations for their spectral type are amongst the faintest stars in the sample, and the low S/N may have complicated the spectral typing.

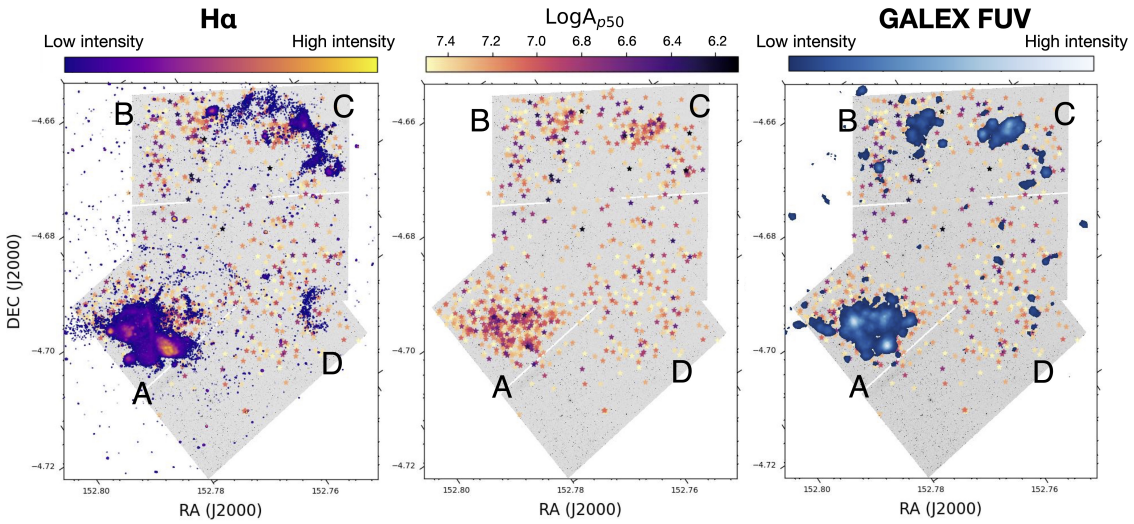


Figure 4.6: The Sextans A HST WFC3/F475W footprint overplotted with the stars fitted with the BEAST that yield a good fit ($\chi^2 < 10$) color-coded by$\log(A)_{p50} < 7.50$. Intensity maps of Hα emission from ground-based imaging are overplotted in the left plot, color-coded by intensity. Intensity maps of the UV as observed by GALEX are overplotted in the right plot. The HII regions (A, B, C, D) overlap with the young stellar population and the high intensity part of the UV map; however, some young stars appear in the field.

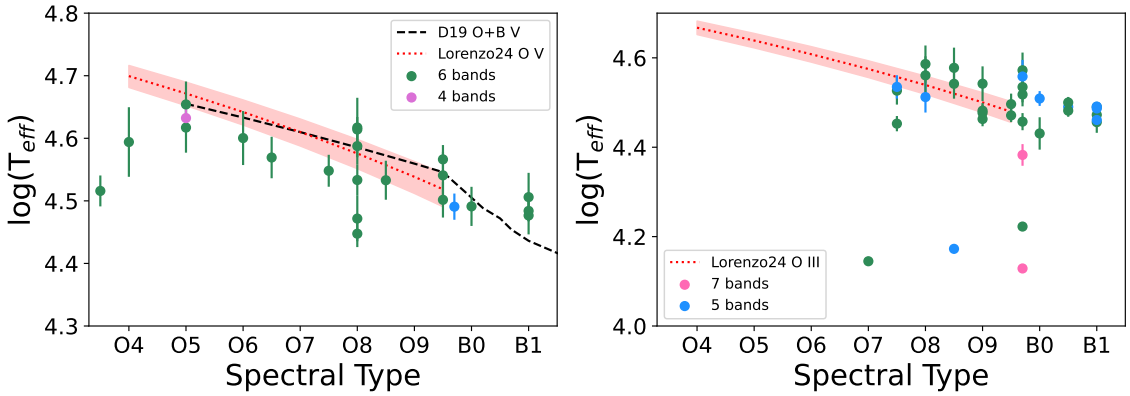


Figure 4.7: $\log(T_{\rm eff})$ is plotted vs. Spectral Type for early-type (O-B3) stars in our sample. The $\log(T_{\rm eff})$ values are taken from our `BEAST` fit, while the Spectral Types are the types reported in (Lorenzo et al. 2022). We classify stars with $\log(g)_{p50} > 3.70$ as dwarfs (left), and $2.50 < \log(g)_{p50} < 3.70$ as giants. We note that these classifications are based on the photometry alone and must be confirmed by spectra. The stars are color-coded by the number of filters they were observed in. We compare our stars ($\chi^2 \leq 100$) with the theoretical $\log(T_{\rm eff})$ is plotted vs. Spectral Type relation derived by (Lorenzo et al. 2025) as well as the $\log(T_{\rm eff})$ scale derived by Dufton et al. (2019) (dashed line, D19). The stars appear to follow the relationship within error bars, except for four dwarfs and six sub-giants.

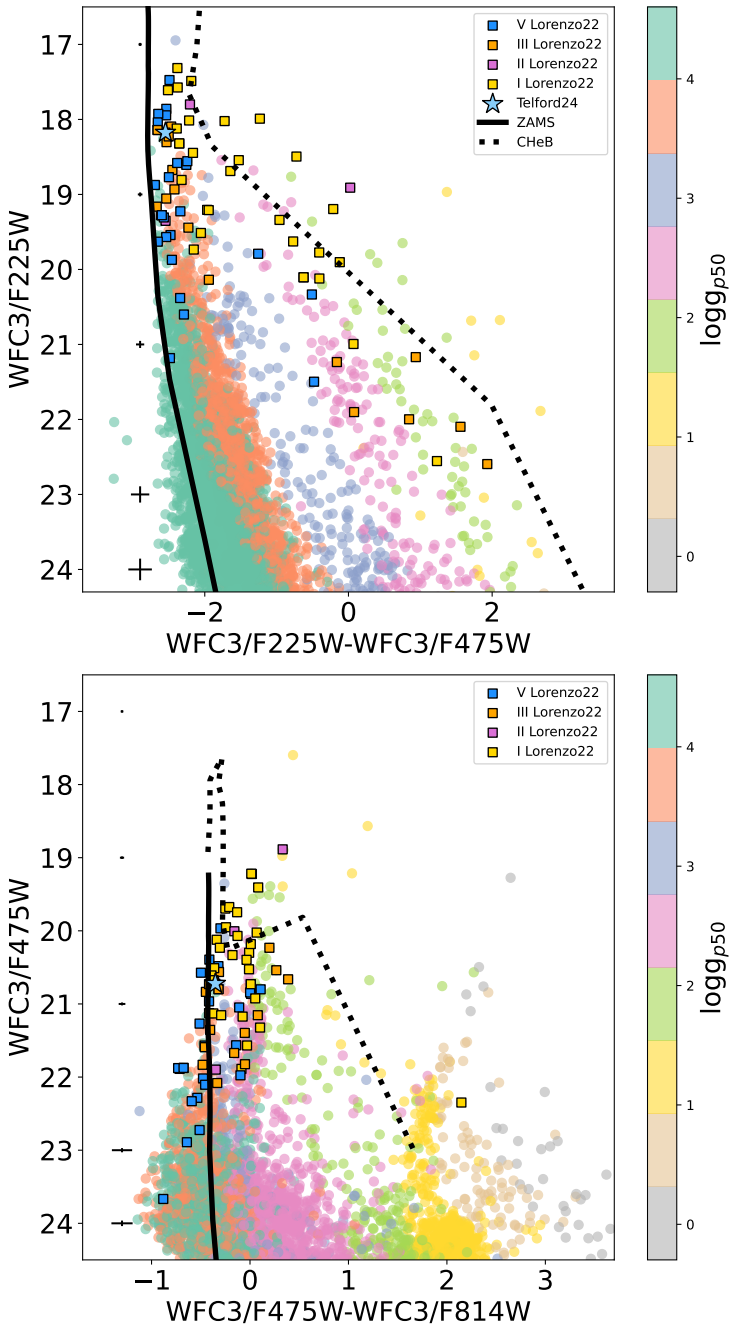


Figure 4.8: We show NUV-Optical (top) and Optical-only (middle and bottom) CMDs of Sextans A. The stars are color-coded by the $\log(g)_{p50}$ values obtained by the BEAST fit. Furthermore, we overplot the stars observed in Telford et al. (2021) (star) and Lorenzo et al. (2022) (squares), the latter of which are color-coded by their Luminosity class based on the R$\sim$ 1000 spectra in Lorenzo et al. (2022). In the optical, distinguishing between surface gravity and luminosity class is challenging; however, the NUV-Optical CMD paints a clearer picture. Most stars are placed on the CMD as expected based on their luminosity class, with a couple of outliers.

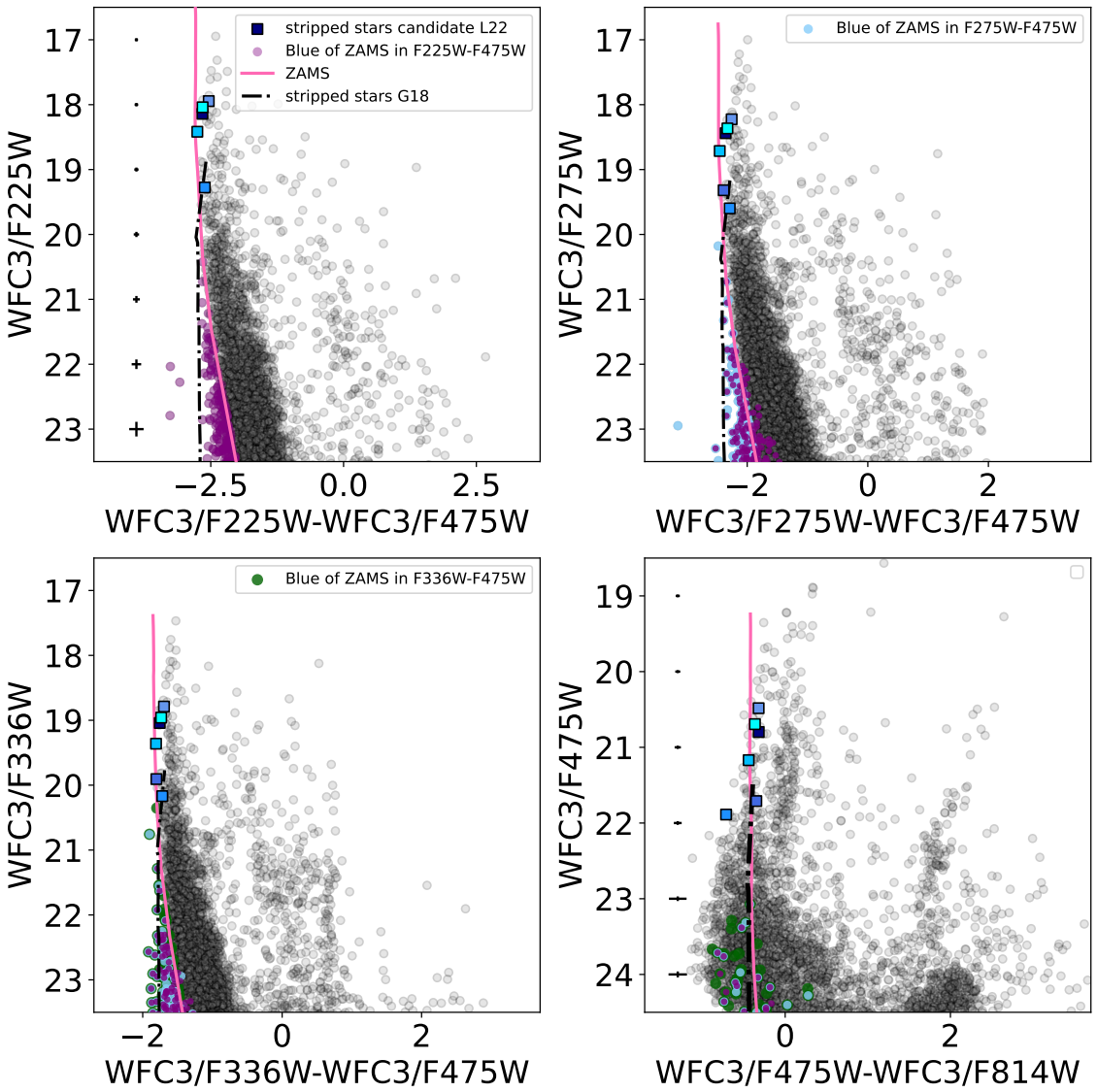


Figure 4.9: UV-optical (both top and bottom left) and optical (bottom right) *HST*-based CMDs of Sextans A. We overplot the ZAMS (pink, solid) as well as the stripped star core He burning (cHeb) sequence (black, dashed Götberg et al. 2018). Stars to the left of the ZAMS in the NUV-optical are plotted as purple (F225W-F475W), light blue (F275W-F475W), and green (F336W-F475W). Lastly, we plot the stars identified as stripped star candidates by Lorenzo et al. (2022). Additionally, three stars to the left of the cHeb (black) appear to be true sources upon further investigation. Two sources identified by Lorenzo et al. (2022) appear bluer than the ZAMS in the optical-only, but otherwise on the ZAMS in the other CMDs. However, two stars appear on top of the cHeb in all other CMDs. Higher S/N and resolution optical or UV spectra are necessary to ultimately confirm these stars' nature.

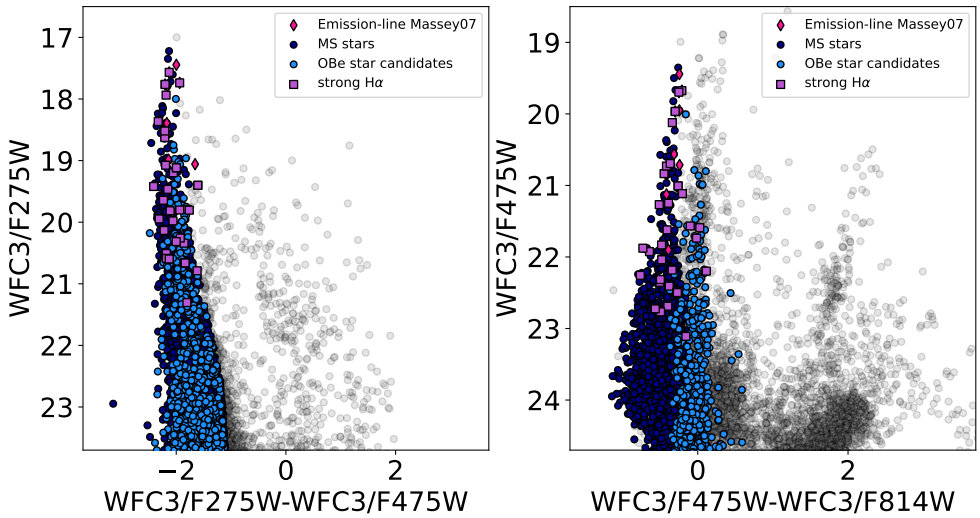


Figure 4.10: UV-optical (left) and optical (right) *HST*-based CMDs of Sextans A. Using the BEAST fit, we identify the area of the CMD where main-sequence OB stars show up in the UV-optical CMD and color-code the stars with navy. We additionally plot the emission-line stars identified by Massey et al. (2007a) (pink) and stars identified as strong Hα emission in GO-17438 (PI: Gull) (purple). Using the BEAST fit, we identify stars on the MS in the UV and show more than 2σ difference between the observed F814W flux and the BEAST predicted F814W flux. Additionally, we apply color cuts to identify stars with potential IR excess in the CMD. These two groups of stars are our OBe star candidates. In Gull et al. (2022), some stars showing this behavior were identified as Be-type stars, while one was identified as a partially stripped star candidate with a companion (Senchyna, Götberg, Gull et al. in prep). We find a OBe fraction of $\sim$ 15% in Sextans A for stars $F275W > 22.9$, a OBe fraction of $\sim$ 25% for stars $F275W > 21$ and a OBe fraction of $\sim$ 63% for stars $F275W > 19.5$. Although confirmation through deep Hα imaging (GO-17438 PI: Gull) or spectroscopic follow-up is needed.

Chapter 5

Concluding Remarks

The work presented in this thesis provides one of the most extensive studies of the lowest metallicity massive stars found in our Local Group. This chapter will summarize key findings and contributions to the fields and highlight future avenues.

For this thesis, I compiled and analyzed the most extensive quantitative spectroscopic study of the metal-poor massive stars at sub-10% $Z_{\odot}$ (Chapter 2). Using archival HST and JWST imaging, I discovered the lowest-metallicity contact binary candidate to date (Chapter 3). And lastly, I conducted the largest quantitative photometric study of massive stars in a sub-10% $Z_{\odot}$ galaxy (Chapter 4).

At the start of this PhD project, observations and quantitative analyses of metal-poor massive stars ($Z_{*} < 0.1\ Z_{\odot}$) in the Local Group were scarce (See Chapter 1), limiting our ability to test models and theories empirically. To address this dire need for empirical evidence and answer the fundamental question: "What are the properties of the massive metal-poor star population in the lowest metallicity regime?" I spectroscopically observed and analyzed 18 stars in the nearby dwarf galaxy Leo A. Leo A is one of the most metal-poor ($\sim 0.05\ Z_{\odot}$) and closest (D$\sim$ 800 kpc) star-forming dwarf galaxies. Aiming to obtain a uniform sample of main-sequence (MS) stars, I used the panchromatic photometry from the Local Ultraviolet and Infrared Treasury (LUVIT) to select the brightest, bluest objects in the UV Color-Magnitude Diagram (CMD). Due to the need for quantitative analysis methods that are scalable to larger samples in the future, I am among the first to have applied machine learning to the spectral analysis of massive stars (Chapter 2). Using my neural network, I recovered the stars' temperatures, surface gravities, and radial velocities. This resulted in one of the most extensive quantitative analyses of metal-poor massive stars with Z$< 0.1\ Z_{\odot}$. Future work will include a more extensive neural network that will be able to measure helium and key metal abundances (C, N, O, Mg, Si).

With the panchromatic photometry at hand, I explored the reliability of high-precision photometry (like HST, JWST, or UVEX) to study metal-poor stars beyond our spectro-

scopic limits and to test our current spectral energy distribution (SED) modeling and evolutionary tracks. To analyze the photometry, I utilized the Bayesian Extinction And Stellar Tool (BEAST), which fits model SEDs to panchromatic photometry. Two-thirds of the sample yielded robust measurements (see outliers following paragraph) and good agreement between the spectroscopically and photometrically derived temperature, luminosity, and surface gravity when using stellar evolutionary models, showing the potential of panchromatic photometry as a reliable tool. When comparing the spectroscopic mass to the photometric mass, I found three outliers on the higher mass end; however, two are likely binaries due to the radial velocity variations in the available spectra. Future work will include time-series spectroscopy to confirm the binary nature of these stars.

As part of my Chapter 2, I have analyzed the lowest metallicity sample of Be stars, making up the outliers that did not yield robust measurements in the original analysis. Be stars are rapidly rotating MS B-type stars surrounded by a disk, giving rise to emission (e) and IR excess Rivinius et al. (2013). The BEAST identified them as outliers but was unable to characterize them. However, I was able to recover the parameters of the star and disk by creating a new fitting routine. I discovered that Be stars may pollute the blue helium core burning (BHeB) sequence at low metallicity, despite appearing on the MS in the UV CMD. (See Chapters 2 and 4). This is a significant finding as the BHeB sequence is used to constrain recent star formation in galaxies. My HST program (HST Cycle 31 proposal (GO-17438)) is a follow-up to these findings. My primary science goal is to test models and prevalence predictions of Be stars at sub-SMC metallicity as a function of age and position on the HR diagram. Be stars are cornerstones in the evolution of massive stars and potentially in the formation of compact binaries (Marchant & Bodensteiner 2023), yet their formation is still debated. It is unclear whether they result from mass transfer in binary systems where the gain in angular momentum spins them up to high rotational velocities or are born with very high rotation rates (Rivinius et al. 2013; Marchant & Bodensteiner 2023). Be stars are yet another clue in the evolution of massive stars, and their potential significant fraction hints at the importance of rotation or binarity in the low metallicity regime.

With an increased interest in binaries at low metallicity, I decided to search for metal-poor binaries in photometric archives. Outside the SMC, there is no population study of metal-poor massive binaries nor observational constraints on their prevalence. While no dedicated time-series photometry program has yet focused on sub-SMC metallicity binaries, such programs exist for other variable objects (e.g., RR Lyrae, Cepheids). I realized that using these datasets provided a unique opportunity to detect short-period, time-varying binaries. I supplemented archival HST data with LUVIT data and the JWST Resolved Stellar Populations Early Release Science Program (Weisz et al. 2023) data. I discovered the lowest metallicity contact binary to date by using the archival data and decomposing the stacked LUVIT UV and JWST IR exposures into their single-epoch observations to

produce time-series photometry (See Chapter 3). The resulting panchromatic photometry enabled me to derive fundamental characteristics of the contact binary system using my neural network trained on a model grid generated by PHOEBE (Jones et al. 2020), a light curve modeling tool.

Contact binaries are two stars that fill their Roche Lobe and exchange mass and energy. They are crucial laboratories of binary evolution and interaction and are potential progenitors to mergers, gamma-ray bursts, or even gravitational wave events. To understand the evolutionary path of this contact binary candidate, I compared my observations with MESA (Paxton et al. 2011, 2013, 2015, 2018, 2019; Jermyn et al. 2023) evolutionary path models. I found that the best match scenario suggests that the system was previously semi-detached and is now in contact again before it will eventually merge. I used the model to predict the system's orbital velocity, enabling future radial velocity measurements to confirm its nature and evolutionary path. With observations coming later this year, I will be able to confirm my prediction and understand this system even better. Additionally, I have identified a dozen other short-period massive binary candidates, for which I will perform the same type of study. Both my discovery and methods will be pivotal in my planned work and in future endeavors to study the metal-poor massive binary populations at a large scale.

Realizing the untapped potential of the available panchromatic photometry, I decided to undertake a novel quantitative study of the metal-poor massive stars in Sextans A. This last chapter leverages the UV through IR photometry of LUVIT and shallow Hα imaging to characterize the massive star population at low metallicity. I show that UV filters like HST/F225W and HST/F275W are paramount to the photometric study of massive stars. I address the shortcomings of the `BEAST` as it fits single star models to populations I expect to be predominantly in primaries and show which results are reliable and which must be examined more carefully. Future work on this will include folding in the capabilities to fit binary systems within the `BEAST` framework, allowing us to capture the whole population of massive stars at higher accuracy. I identify 369 massive star candidates with reliable stellar parameters. This number is increased to 502 when considering stars in the second-best-fit category. Of most interest are the 5(19) candidates above 30 $M_{\odot}$, as these stars would constitute the most massive sub-SMC metallicity massive stars or binaries observed so far. Obtaining medium-resolution spectra will be crucial to gain insight into these stars. Comparing the stellar parameters to spectral types derived from low-resolution spectra, I find that the stellar parameter return parameters align with the expectations based on their spectral types. The outliers found in the comparison are often stars showing signs of binarity, binary products, or stars with very low resolution (R$<$ 1000) and SNR ($<$ 25) spectra. Additionally, I identify 94 promising stripped star candidates and postulate a decrease in UV-detected stripped star candidates with decreasing metallicity and star formation as pre-

dicted by theoretical models. Furthermore, I show early indications of an increasing OBe fraction with decreasing metallicity. Future works will include detailed photometric modeling of the stripped star and OBe star candidates to characterize this population of binary products. This extensive catalog will aid the community in selecting high-priority spectroscopic targets and provide an overview of the massive star content in this galaxy. Future plans include using archival and LSST data to monitor the massive binary candidates for photometric variations to identify eclipsing binaries. A key question remains to be answered: What is the binary fraction and binary parameter distribution at low metallicity?

The discovery space in the field remains ample. My thesis lays the groundwork to characterize metal-poor massive stars and their population. It started to test our understanding of stellar physics in this regime and current SED models and evolutionary tracks. It set the first observational constraints on rotation and binarity in the metal-poor regime. In the long term, my catalogs will form the baseline for future time-series photometry studies, spectroscopic follow-up, and the photometric standard for metal-poor massive stars. The observational constraints on and evidence for the metal-poor massive stars and binary population in this thesis supply a crucial ingredient for astronomers' modeling and studying the star-forming galaxies being discovered with JWST across cosmic time. By continuing to characterize the stellar physics of metal-poor massive stars and binaries, I aim to shed light on the pathways in the lowest metallicity regime that lead to transients and compact object mergers, giving rise to GW. Metal-poor massive stars are a fundamental ingredient to many astrophysical phenomena, theoretically and observationally, and their study is therefore consequential for all astrophysics.

Bibliography

Aasi, J., Abbott, B. P., Abbott, R., et al. 2014, Physical Review D, 90, 062010, publisher: APS ADS Bibcode: 2014PhRvD..90f2010A

Abbott, B. P., Abbott, R., Abbott, T. D., et al. 2016, Phys. Rev. Lett., 116, 061102

Abdul-Masih, M., Escorza, A., Menon, A., Mahy, L., & Marchant, P. 2022, A&A, 666, A18

Abdul-Masih, M., Sana, H., Sundqvist, J., et al. 2019, ApJ, 880, 115

Abdul-Masih, M., Sana, H., Hawcroft, C., et al. 2021, A&A, 651, A96

Akiba, T., Sano, S., Yanase, T., Ohta, T., & Koyama, M. 2019, in Proceedings of the 25th ACM SIGKDD International Conference on Knowledge Discovery and Data Mining

Albers, S. M., Weisz, D. R., Cole, A. A., et al. 2019, MNRAS, 490, 5538

Almeida, L. A., Sana, H., de Mink, S. E., et al. 2015, ApJ, 812, 102

Alongi, M., Bertelli, G., Bressan, A., & Chiosi, C. 1991, A&A, 244, 95

Arcos, C., Kanaan, S., Chávez, J., et al. 2018, MNRAS, 474, 5287

Asplund, M., Grevesse, N., Sauval, A. J., & Scott, P. 2009, ARA&A, 47, 481

Astropy Collaboration, Robitaille, T. P., Tollerud, E. J., et al. 2013, A&A, 558, A33

Astropy Collaboration, Price-Whelan, A. M., Sipőcz, B. M., et al. 2018, AJ, 156, 123

Astropy Collaboration, Price-Whelan, A. M., Lim, P. L., et al. 2022, ApJ, 935, 167

Aver, E., Berg, D. A., Olive, K. A., et al. 2021, J. Cosmology Astropart. Phys., 2021, 027

Balona, L. A. 1992, MNRAS, 256, 425

Banyard, G., Sana, H., Mahy, L., et al. 2022, A&A, 658, A69

Barbá, R. H., Gamen, R., Arias, J. I., & Morrell, N. I. 2017, in The Lives and Death-Throes of Massive Stars, ed. J. J. Eldridge, J. C. Bray, L. A. S. McClelland, & L. Xiao, Vol. 329, 89

Bellinger, E. P., de Mink, S. E., van Rossem, W. E., & Justham, S. 2024, The Astrophysical Journal, 967, L39, publisher: IOP ADS Bibcode: 2024ApJ...967L..39B

Berg, D. A., Skillman, E. D., Marble, A. R., et al. 2012, ApJ, 754, 98

Berger, T. A., Kudritzki, R.-P., Urbaneja, M. A., et al. 2018, ApJ, 860, 130

Bernini-Peron, M., Sander, A. A. C., Ramachandran, V., et al. 2024, A&A, 692, A89

Bestenlehner, J. M., Crowther, P. A., Bronner, V. A., et al. 2025, MNRAS, 540, 3523

Bianchi, L., Efremova, B., Hodge, P., Massey, P., & Olsen, K. A. G. 2012, AJ, 143, 74

Bianchi, L., & Garcia, M. 2002, ApJ, 581, 610
Björklund, R., Sundqvist, J. O., Puls, J., & Najarro, F. 2021, A&A, 648, A36
Blaauw, A. 1961, Bull. Astron. Inst. Netherlands, 15, 265
Bodenheimer, P. 1995, ARA&A, 33, 199
Bodensteiner, J., Shenar, T., & Sana, H. 2020, A&A, 641, A42
Bodensteiner, J., Sana, H., Wang, C., et al. 2021, A&A, 652, A70
Bodensteiner, J., Sana, H., Wang, C., et al. 2021, Astronomy & Astrophysics, 652, A70, publisher: EDP Sciences
Bodensteiner, J., Heida, M., Abdul-Masih, M., et al. 2022, The Messenger, 186, 3, aDS Bibcode: 2022Msngr.186....3B
Bodensteiner, J., Shenar, T., Sana, H., et al. 2025, A&A, 698, A38
Böhm-Vitense, E. 1958, ZAp, 46, 108
Bonanos, A. Z., Tramper, F., de Wit, S., et al. 2024, A&A, 686, A77
Bouret, J. C., Lanz, T., Hillier, D. J., et al. 2003, ApJ, 595, 1182
—. 2015, MNRAS, 449, 1545
Bouret, J. C., Lanz, T., Martins, F., et al. 2013, A&A, 555, A1
Bouret, J. C., Martins, F., Hillier, D. J., et al. 2021, A&A, 647, A134
Bradstreet, D. H. 2005, Society for Astronomical Sciences Annual Symposium, 24, 23
Bresolin, F., Pietrzyński, G., Urbaneja, M. A., et al. 2006, ApJ, 648, 1007
Bresolin, F., Urbaneja, M. A., Gieren, W., Pietrzyński, G., & Kudritzki, R.-P. 2007, ApJ, 671, 2028
Bressan, A., Marigo, P., Girardi, L., et al. 2012, MNRAS, 427, 127
Briel, M. M., Stevance, H. F., & Eldridge, J. J. 2023, MNRAS, 520, 5724
Britavskiy, N., Mahy, L., Lennon, D. J., et al. 2025, A&A, 698, A40
Brown, W. R., Geller, M. J., Kenyon, S. J., & Kurtz, M. J. 2007, ApJ, 666, 231
Buchner, J. 2016, Statistics and Computing, 26, 383
—. 2019, PASP, 131, 108005
—. 2021, The Journal of Open Source Software, 6, 3001
Buchner, J. 2023, in MaxEnt 2022, MaxEnt 2022 (MDPI)
Bunker, A. J., Saxena, A., Cameron, A. J., et al. 2023, Astronomy and Astrophysics, 677, A88
Calzetti, D., Lee, J. C., Sabbi, E., et al. 2015, AJ, 149, 51
Camacho, I., Garcia, M., Herrero, A., & Simón-Díaz, S. 2016, A&A, 585, A82
Camacho, I., García, M., Urbaneja, M. A., & Herrero, A. 2017, in The Lives and Death-Throes of Massive Stars, ed. J. J. Eldridge, J. C. Bray, L. A. S. McClelland, & L. Xiao, Vol. 329, 389
Cameron, A. J., Katz, H., Rey, M. P., & Saxena, A. 2023, Monthly Notices of the Royal Astronomical Society, 523, 3516
Castellano, M., Napolitano, L., Fontana, A., et al. 2024, The Astrophysical Journal, 972,

143
Castelli, F., & Kurucz, R. L. 2004, A&A, 419, 725
Castro, N., Oey, M. S., Fossati, L., & Langer, N. 2018, ApJ, 868, 57
Castro, N., Herrero, A., Garcia, M., et al. 2008, A&A, 485, 41
Castro, N., Crowther, P. A., Evans, C. J., et al. 2021, A&A, 648, A65
Chen, Y., Bressan, A., Girardi, L., et al. 2015, MNRAS, 452, 1068
Chen, Y., Girardi, L., Bressan, A., et al. 2014, MNRAS, 444, 2525
Chevalier, R. A. 2012, The Astrophysical Journal, 752, L2, publisher: IOP ADS Bibcode: 2012ApJ...752L...2C
Choi, J., Conroy, C., & Byler, N. 2017, ApJ, 838, 159
Choi, J., Dotter, A., Conroy, C., et al. 2016, ApJ, 823, 102
Choi, Y., Dalcanton, J. J., Williams, B. F., et al. 2020, ApJ, 902, 54
Chu-Qi, W., Fu-Xing, L., Sheng-Bang, Q., et al. 2023, PASP, 135, 094202
Clarke, C. J., & Pringle, J. E. 1992, MNRAS, 255, 423
Cole, A. A., Skillman, E. D., Tolstoy, E., et al. 2007, The Astrophysical Journal, 659, L17–L20
Conroy, K. E., Kochoska, A., Hey, D., et al. 2020, ApJS, 250, 34
Conti, P. S., & Alschuler, W. R. 1971, ApJ, 170, 325
Costa, G., Bressan, A., Mapelli, M., et al. 2021, MNRAS, 501, 4514
Cox, J. P., & Giuli, R. T. 1968, Principles of stellar structure
Crowther, P. A. 2022, ULLYSES and Complementary Surveys of Massive Stars in the Magellanic Clouds, publication Title: arXiv e-prints ADS Bibcode: 2022arXiv220708690C
Dalcanton, J. J., Williams, B. F., Seth, A. C., et al. 2009, ApJS, 183, 67
Dallas, M. M., Oey, M. S., & Castro, N. 2022, ApJ, 936, 112
de Mink, S. E., & Belczynski, K. 2015, ApJ, 814, 58
de Mink, S. E., Langer, N., Izzard, R. G., Sana, H., & de Koter, A. 2013, The Astrophysical Journal, 764, 166, publisher: IOP ADS Bibcode: 2013ApJ...764..166D
de Mink, S. E., Pols, O. R., & Hilditch, R. W. 2007, A&A, 467, 1181
de Mink, S. E., Sana, H., Langer, N., Izzard, R. G., & Schneider, F. R. N. 2014, The Astrophysical Journal, 782, 7, publisher: IOP ADS Bibcode: 2014ApJ...782....7D
de Mink, S. E., Sana, H., Langer, N., Izzard, R. G., & Schneider, F. R. N. 2014, ApJ, 782, 7
de Wit, W. J., Oudmaijer, R. D., & Vink, J. S. 2014, Advances in Astronomy, 2014, 270848
de Wit, W. J., Testi, L., Palla, F., & Zinnecker, H. 2005, A&A, 437, 247
Degroote, P., Aerts, C., Samadi, R., et al. 2010, Astronomische Nachrichten, 331, 1065, aDS Bibcode: 2010AN....331.1065D
Ding, X., Ji, K., Li, X., et al. 2022, AJ, 164, 200
Ding, X., Ji, K.-F., & Li, X.-Z. 2021, PASJ, 73, 786
Dohm-Palmer, R. C., Skillman, E. D., Mateo, M., et al. 2002a, AJ, 123, 813

—. 2002b, AJ, 123, 813
Dohm-Palmer, R. C., Skillman, E. D., Saha, A., et al. 1997, AJ, 114, 2514
Dolphin, A. 2016, DOLPHOT: Stellar photometry, Astrophysics Source Code Library, record ascl:1608.013
Dolphin, A. E. 2000, PASP, 112, 1383
Dolphin, A. E., Saha, A., Skillman, E. D., et al. 2003, AJ, 126, 187
Dorigo Jones, J., Oey, M. S., Paggeot, K., Castro, N., & Moe, M. 2020, ApJ, 903, 43
Dorozsmai, A., & Toonen, S. 2024, MNRAS, 530, 3706
Dotter, A. 2016, ApJS, 222, 8
Drout, M. R., Götberg, Y., Ludwig, B. A., et al. 2023, Science, 382, 1287
Drout, M. R., Götberg, Y., Ludwig, B. A., et al. 2023, Science, 382, 1287, aDS Bibcode: 2023Sci...382.1287D
Dufton, P. L., Evans, C. J., Hunter, I., Lennon, D. J., & Schneider, F. R. N. 2019, A&A, 626, A50
Dunstall, P. R., Brott, I., Dufton, P. L., et al. 2011, A&A, 536, A65
Dunstall, P. R., Brott, I., Dufton, P. L., et al. 2011, Astronomy and Astrophysics, 536, A65, aDS Bibcode: 2011A&A...536A..65D
Dunstall, P. R., Dufton, P. L., Sana, H., et al. 2015, A&A, 580, A93
Dutta, D., & Klencki, J. 2024, A&A, 687, A215
Earl, N., Jones, C., Kerzendorf, W., et al. 2019, astropy/specutils: v0.6
Ekström, S., Georgy, C., Eggenberger, P., et al. 2012, A&A, 537, A146
Ekström, S. 2021, Frontiers in Astronomy and Space Sciences, 8, 53, aDS Bibcode: 2021FrASS...8...53E
Ekström, S., Meynet, G., Chiappini, C., Hirschi, R., & Maeder, A. 2008, Astronomy and Astrophysics, 489, 685, aDS Bibcode: 2008A&A...489..685E
El-Badry, K., Wetzel, A., Geha, M., et al. 2016, ApJ, 820, 131
Eldridge, J. J., Fraser, M., Smartt, S. J., Maund, J. R., & Crockett, R. M. 2013, MNRAS, 436, 774
Eldridge, J. J., Izzard, R. G., & Tout, C. A. 2008, MNRAS, 384, 1109
Eldridge, J. J., & Stanway, E. R. 2020, arXiv e-prints, arXiv:2005.11883
—. 2022, ARA&A, 60, 455
Eldridge, J. J., & Stanway, E. R. 2022, Annual Review of Astronomy and Astrophysics, 60, 455, aDS Bibcode: 2022ARA&A..60..455E
Eldridge, J. J., Stanway, E. R., Xiao, L., et al. 2017, Publications of the Astronomical Society of Australia, 34, e058, aDS Bibcode: 2017PASA...34...58E
Eldridge, J. J., & Tout, C. A. 2004, MNRAS, 353, 87
Emerick, A., Bryan, G. L., & Mac Low, M.-M. 2018, ApJ, 865, L22
Evans, C., Marcolino, W., Bouret, J.-C., & Garcia, M. 2023, Experimental Astronomy, 56, 537

Evans, C. J., Bresolin, F., Urbaneja, M. A., et al. 2007, ApJ, 659, 1198
Evans, C. J., Lennon, D. J., & Smartt, S. J. 2006, 353, 41, conference Name: Stellar Evolution at Low Metallicity: Mass Loss, Explosions, Cosmology Place: eprint: arXiv:astro-ph/0508645 ADS Bibcode: 2006ASPC..353...41E
Evans, C. J., Lennon, D. J., Smartt, S. J., & Trundle, C. 2006, A&A, 456, 623
Evans, C. J., Lennon, D. J., Smartt, S. J., & Trundle, C. 2006, Astronomy and Astrophysics, 456, 623, aDS Bibcode: 2006A&A...456..623E
Evans, C. J., Taylor, W. D., Hénault-Brunet, V., et al. 2011, Astronomy and Astrophysics, 530, A108, aDS Bibcode: 2011A&A...530A.108E
Evans, C. J., Kennedy, M. B., Dufton, P. L., et al. 2015, A&A, 574, A13
Evans, C. J., Castro, N., Gonzalez, O. A., et al. 2019, A&A, 622, A129
Fabry, M., Marchant, P., Langer, N., & Sana, H. 2023, A&A, 672, A175
—. 2024, arXiv e-prints, arXiv:2410.21394
Fabry, M., Marchant, P., & Sana, H. 2022, A&A, 661, A123
Farrell, E., Groh, J. H., Meynet, G., & Eldridge, J. J. 2022, MNRAS, 512, 4116
Ferland, G. J., Chatzikos, M., Guzmán, F., et al. 2017, Rev. Mexicana Astron. Astrofis., 53, 385
Foreman-Mackey, D. 2016, The Journal of Open Source Software, 1, 24
Foreman-Mackey, D., Hogg, D. W., Lang, D., & Goodman, J. 2013, PASP, 125, 306
Frebel, A., & Norris, J. E. 2015, Annual Review of Astronomy and Astrophysics, 53, 631–688
Fu, X., Bressan, A., Marigo, P., et al. 2018, MNRAS, 476, 496
Furey, C., Telford, O. G., de Koter, A., et al. 2025, A&A, 698, A9
Gaia Collaboration, Arenou, F., Babusiaux, C., et al. 2023, Astronomy and Astrophysics, 674, A34, aDS Bibcode: 2023A&A...674A..34G
Gaia Collaboration, Panuzzo, P., Mazeh, T., et al. 2024, Astronomy and Astrophysics, 686, L2, aDS Bibcode: 2024A&A...686L...2G
Garcia, M. 2018, MNRAS, 474, L66
Garcia, M., & Herrero, A. 2013, A&A, 551, A74
Garcia, M., Herrero, A., Najarro, F., Camacho, I., & Lorenzo, M. 2019, MNRAS, 484, 422
Garcia, M., Herrero, A., Najarro, F., Camacho, I., & Lorenzo, M. 2019a, Monthly Notices of the Royal Astronomical Society
Garcia, M., Herrero, A., Najarro, F., Lennon, D. J., & Alejandro Urbaneja, M. 2014, ApJ, 788, 64
García, M., Herrero, A., Najarro, F., Lennon, D. J., & Urbaneja, M. A. 2015, in New Windows on Massive Stars, ed. G. Meynet, C. Georgy, J. Groh, & P. Stee, Vol. 307, 41
Garcia, M., Evans, C. J., Bestenlehner, J. M., et al. 2019b, Massive stars in extremely metal-poor galaxies: A window into the past, arXiv:1908.04687 [astro-ph.IM]
Georgy, C., Saio, H., & Meynet, G. 2021, A&A, 650, A128

Gilbert, K. M., Choi, Y., Boyer, M. L., et al. 2025, ApJS, 276, 8
Ginsburg, A., & Mirocha, J. 2011, PySpecKit: Python Spectroscopic Toolkit
Godart, M., Simón-Díaz, S., Herrero, A., et al. 2017, Astronomy and Astrophysics, 597, A23, aDS Bibcode: 2017A&A...597A..23G
Goldman, S. R., Boyer, M. L., McQuinn, K. B. W., et al. 2019, ApJ, 877, 49
González-Torà, G., Davies, B., Kudritzki, R.-P., & Plez, B. 2021, MNRAS, 505, 4422
Gordon, K., Larson, K., McBride, A., et al. 2022, karllark/dust_extinction: NIRSpectralExtinctionAdded, Zenodo
Gordon, K. D., Clayton, G. C., Misselt, K. A., Landolt, A. U., & Wolff, M. J. 2003, ApJ, 594, 279
Gordon, K. D., Fouesneau, M., Arab, H., et al. 2016, ApJ, 826, 104
Götberg, Y., de Mink, S. E., & Groh, J. H. 2017, A&A, 608, A11
Götberg, Y., de Mink, S. E., Groh, J. H., et al. 2018, A&A, 615, A78
Governato, F., Brook, C., Mayer, L., et al. 2010, Nature, 463, 203
Grassitelli, L., Fossati, L., Langer, N., et al. 2016, A&A, 593, A14
Grevesse, N., Asplund, M., Sauval, A. J., & Scott, P. 2010, Ap&SS, 328, 179
Groh, J. H., Ekström, S., Georgy, C., et al. 2019, A&A, 627, A24
Groh, J. H., Ekström, S., Georgy, C., et al. 2019, Astronomy and Astrophysics, 627, A24, aDS Bibcode: 2019A&A...627A..24G
Groot, P. J., Bloemen, S., Vreeswijk, P. M., et al. 2022, in Society of Photo-Optical Instrumentation Engineers (SPIE) Conference Series, Vol. 12182, Ground-based and Airborne Telescopes IX, ed. H. K. Marshall, J. Spyromilio, & T. Usuda, 121821V
Gull, M., Weisz, D. R., Senchyna, P., et al. 2022, ApJ, 941, 206
Gull, M., Weisz, D. R., Senchyna, P., et al. 2022, The Astrophysical Journal, 941, 206, publisher: IOP ADS Bibcode: 2022ApJ...941..206G
Gull, M., Weisz, D. R., El-Badry, K., et al. 2024, arXiv e-prints, arXiv:2410.16393
Gull, T. R., & Sofia, S. 1979, ApJ, 230, 782
Götberg, Y., De Mink, S. E., McQuinn, M., et al. 2020, Astronomy & Astrophysics, 634, A134
Götberg, Y., Drout, M. R., Ji, A. P., et al. 2023, The Astrophysical Journal, 959, 125, publisher: IOP ADS Bibcode: 2023ApJ...959..125G
Hack, W. J., Cara, M., Sosey, M., et al. 2020, spacetelescope/drizzlepac: Drizzlepac
Hambleton, K. M., Bianco, F. B., Street, R., et al. 2023, PASP, 135, 105002
Harris, C. R., Millman, K. J., van der Walt, S. J., et al. 2020, Nature, 585, 357
Hastings, B., Langer, N., & Koenigsberger, G. 2020a, A&A, 641, A86
Hastings, B., Wang, C., & Langer, N. 2020b, A&A, 633, A165
Hawcroft, C., Sana, H., Mahy, L., et al. 2023, X-Shooting ULLYSES: Massive stars at low metallicity. III. Terminal wind speeds of ULLYSES massive stars, publication Title: arXiv e-prints ADS Bibcode: 2023arXiv230312165H

Heap, S. R., Lanz, T., & Hubeny, I. 2006a, The Astrophysical Journal, 638, 409, publisher: IOP ADS Bibcode: 2006ApJ...638..409H
—. 2006b, The Astrophysical Journal, 638, 409–432
Heger, A., Fryer, C. L., Woosley, S. E., Langer, N., & Hartmann, D. H. 2003, ApJ, 591, 288
Henneco, J., Schneider, F. R. N., & Laplace, E. 2024, A&A, 682, A169
Herrero, A., Kudritzki, R. P., Vilchez, J. M., et al. 1992, A&A, 261, 209
Herrero, A., Puls, J., & Najarro, F. 2002, A&A, 396, 949
Hilditch, R. W., Howarth, I. D., & Harries, T. J. 2005, MNRAS, 357, 304
Hillier, D. J., & Lanz, T. 2001, in Astronomical Society of the Pacific Conference Series, Vol. 247, Spectroscopic Challenges of Photoionized Plasmas, ed. G. Ferland & D. W. Savin, 343
Hoogerwerf, R., de Bruijne, J. H. J., & de Zeeuw, P. T. 2000, ApJ, 544, L133
Hopkins, P. F., Quataert, E., & Murray, N. 2011, MNRAS, 417, 950
Horvat, M., Conroy, K. E., Pablo, H., et al. 2018, ApJS, 237, 26
Hosek, Matthew W., J., Kudritzki, R.-P., Bresolin, F., et al. 2014, ApJ, 785, 151
Hovis-Afflerbach, B., Götberg, Y., Schootemeijer, A., et al. 2025, A&A, 697, A239
Hummer, D. G., & Storey, P. J. 1987, MNRAS, 224, 801
Hunter, D. A., Ficut-Vicas, D., Ashley, T., et al. 2012, AJ, 144, 134
Hunter, I., Lennon, D. J., Dufton, P. L., et al. 2008, Astronomy and Astrophysics, 479, 541, aDS Bibcode: 2008A&A...479..541H
Hunter, I., Dufton, P. L., Smartt, S. J., et al. 2007, Astronomy and Astrophysics, 466, 277, aDS Bibcode: 2007A&A...466..277H
Hunter, I., Brott, I., Lennon, D. J., et al. 2008, ApJ, 676, L29
Hunter, I., Brott, I., Langer, N., et al. 2009, A&A, 496, 841
Hunter, I., Brott, I., Langer, N., et al. 2009, Astronomy and Astrophysics, 496, 841, aDS Bibcode: 2009A&A...496..841H
Hunter, J. D. 2007, Computing in Science & Engineering, 9, 90
Hurley, J. R., Tout, C. A., & Pols, O. R. 2002, MNRAS, 329, 897
Iqbal, S., & Keller, S. C. 2013, MNRAS, 435, 3103
Ivezić, Ž., Kahn, S. M., Tyson, J. A., et al. 2019, ApJ, 873, 111
Jermyn, A. S., Bauer, E. B., Schwab, J., et al. 2023, ApJS, 265, 15
Ji, A. P., Beaton, R., Chakrabarti, S., et al. 2019, Astro2020 Science White Paper: Local Dwarf Galaxy Archaeology, arXiv:1903.09275 [astro-ph.GA]
Jie, J., Zhu, C., & Lv, G. 2015, arXiv e-prints, arXiv:1505.03182
Jones, C., Forman, W., Tananbaum, H., et al. 1973, ApJ, 181, L43
Jones, D., Conroy, K. E., Horvat, M., et al. 2020, ApJS, 247, 63
Kalogera, V., Belczynski, K., Kim, C., O'Shaughnessy, R., & Willems, B. 2007, Phys. Rep., 442, 75

Kansky, J., Chilingarian, I., Fabricant, D., et al. 2019, PASP, 131, 075005
Karachentsev, I. D., Makarov, D. I., & Kaisina, E. I. 2013, AJ, 145, 101
Kasen, D., Metzger, B., Barnes, J., Quataert, E., & Ramirez-Ruiz, E. 2017, Nature, 551, 80
Kaufer, A., Venn, K. A., Tolstoy, E., Pinte, C., & Kudritzki, R.-P. 2004, AJ, 127, 2723
Kennicutt, Robert C., J. 1998, ARA&A, 36, 189
Kennicutt, R., Engelbracht, C., Begum, A., et al. 2007, The Local Volume Legacy Survey, Spitzer Proposal ID #40204
Kingma, D. P., & Ba, J. 2017, Adam: A Method for Stochastic Optimization, arXiv:1412.6980 [cs.LG]
Kirby, E. N., Rizzi, L., Held, E. V., et al. 2017, ApJ, 834, 9
Klencki, J., Moe, M., Gladysz, W., et al. 2018, A&A, 619, A77
Klencki, J., Nelemans, G., Istrate, A. G., & Pols, O. 2020, A&A, 638, A55
Kobulnicky, H. A., Kiminki, D. C., Lundquist, M. J., et al. 2014, ApJS, 213, 34
Kriz, S., & Harmanec, P. 1975, Bulletin of the Astronomical Institutes of Czechoslovakia, 26, 65
Kruckow, M. U., Tauris, T. M., Langer, N., Kramer, M., & Izzard, R. G. 2018, MNRAS, 481, 1908
Krumholz, M. R., McKee, C. F., & Bland-Hawthorn, J. 2019, ARA&A, 57, 227
Kubátová, B., Szécsi, D., Sander, A. A. C., et al. 2019, A&A, 623, A8
Kudritzki, R.-P., Urbaneja, M. A., Bresolin, F., et al. 2008, ApJ, 681, 269
Kulkarni, S. R., Harrison, F. A., Grefenstette, B. W., et al. 2021, arXiv e-prints, arXiv:2111.15608
Lada, C. J., & Lada, E. A. 2003, ARA&A, 41, 57
Lamb, J. B., Oey, M. S., Segura-Cox, D. M., et al. 2016, ApJ, 817, 113
Lamers, H. J. G. L. M., & Cassinelli, J. P. 1999, Introduction to Stellar Winds
Langer, N. 2012, ARA&A, 50, 107
Langer, N., & Maeder, A. 1995, A&A, 295, 685
Lanz, T., & Hubeny, I. 2003, The Astrophysical Journal Supplement Series, 146, 417–441
Lanz, T., & Hubeny, I. 2007, ApJS, 169, 83
Laplace, E., Justham, S., Renzo, M., et al. 2021, A&A, 656, A58
Larsen, S. S., de Mink, S. E., Eldridge, J. J., et al. 2011, A&A, 532, A147
Lattimer, J. M., & Schramm, D. N. 1976, ApJ, 210, 549
Lazzarini, M., Williams, B. F., Durbin, M., et al. 2021, ApJ, 906, 120
Lee, A. J., Freedman, W. L., Madore, B. F., et al. 2021, ApJ, 907, 112
Lee, A. J., Monson, A. J., Freedman, W. L., et al. 2024, ApJ, 967, 22
Lee, H., Skillman, E. D., & Venn, K. A. 2005, ApJ, 620, 223
Lejeune, T. 2002, in Astronomical Society of the Pacific Conference Series, Vol. 274, Observed HR Diagrams and Stellar Evolution, ed. T. Lejeune & J. Fernandes, 159
Lennon, D. J. 1997, A&A, 317, 871

Leščinskaitė, A., Stonkutė, R., & Vansevičius, V. 2022, A&A, 660, A79
Li, G.-W. 2021, ApJS, 253, 54
Lindberg, C. W., Murray, C. E., Yanchulova Merica-Jones, P., et al. 2025, ApJ, 982, 33
Liu, B., Sibony, Y., Meynet, G., & Bromm, V. 2021, Monthly Notices of the Royal Astronomical Society, 506, 5247, publisher: OUP ADS Bibcode: 2021MNRAS.506.5247L
Lorenzo, J., Negueruela, I., Baker, A. K. F. V., et al. 2014, A&A, 572, A110
Lorenzo, M., Garcia, M., Castro, N., et al. 2025, MNRAS, 537, 1197
Lorenzo, M., garcia, M., Najarro, F., et al. 2022, arXiv e-prints, arXiv:2207.09700
Lorenzo, M., Garcia, M., Najarro, F., et al. 2022, Monthly Notices of the Royal Astronomical Society, 516, 4164, publisher: OUP ADS Bibcode: 2022MNRAS.516.4164L
Ludwig, B., Drout, M. R., Gotberg, Y., Lang, D., & Laroche, A. 2025, arXiv e-prints, arXiv:2505.18632
Mac Low, M.-M., & Ferrara, A. 1999, ApJ, 513, 142
Madau, P., & Dickinson, M. 2014, Annual Review of Astronomy and Astrophysics, 52, 415, aDS Bibcode: 2014ARA&A..52..415M
Madau, P., & Dickinson, M. 2014, ARA&A, 52, 415
Maeder, A., & Meynet, G. 2000, Annual Review of Astronomy and Astrophysics, 38, 143, aDS Bibcode: 2000ARA&A..38..143M
—. 2002, 485, 49, conference Name: Stellar Structure and Habitable Planet Finding ADS Bibcode: 2002ESASP.485...49M
Maeder, A., Meynet, G., & Hirschi, R. 2005, in Astronomical Society of the Pacific Conference Series, Vol. 336, Cosmic Abundances as Records of Stellar Evolution and Nucleosynthesis, ed. I. Barnes, Thomas G. & F. N. Bash, 79
Mahy, L., Rauw, G., De Becker, M., Eenens, P., & Flores, C. A. 2015, A&A, 577, A23
Mahy, L., Almeida, L. A., Sana, H., et al. 2020, A&A, 634, A119
Mahy, L., Lanthermann, C., Hutsemékers, D., et al. 2022, A&A, 657, A4
Mandel, I., & Farmer, A. 2022, Physics Reports, 955, 1, aDS Bibcode: 2022PhR...955....1M
Mandel, I., & Farmer, A. 2022, Phys. Rep., 955, 1
Marchant, P., & Bodensteiner, J. 2023, The Evolution of Massive Binary Stars, publication Title: arXiv e-prints ADS Bibcode: 2023arXiv231101865M
Marchant, P., & Bodensteiner, J. 2024, ARA&A, 62, 21
Marchant, P., Langer, N., Podsiadlowski, P., Tauris, T. M., & Moriya, T. J. 2016, A&A, 588, A50
Marchant, P., Pappas, K. M. W., Gallegos-Garcia, M., et al. 2021, A&A, 650, A107
Margutti, R., & Chornock, R. 2021, ARA&A, 59, 155
Markova, N., & Puls, J. 2015, in New Windows on Massive Stars, ed. G. Meynet, C. Georgy, J. Groh, & P. Stee, Vol. 307, 117
Markova, N., Puls, J., & Langer, N. 2018, A&A, 613, A12

Martayan, C., Floquet, M., Hubert, A. M., et al. 2007a, A&A, 472, 577
Martayan, C., Frémat, Y., Hubert, A. M., et al. 2007b, A&A, 462, 683
Martayan, C., Hubert, A. M., Floquet, M., et al. 2006, A&A, 445, 931
Martins, F. 2018, A&A, 616, A135
Martins, F., Mahy, L., & Hervé, A. 2017, A&A, 607, A82
Martins, F., & Palacios, A. 2021, Astronomy and Astrophysics, 645, A67, aDS Bibcode: 2021A&A...645A..67M
Martins, F., & Palacios, A. 2021, A&A, 645, A67
Martins, F., Schaerer, D., Hillier, D. J., & Heydari-Malayeri, M. 2004, A&A, 420, 1087
Martins, F., Bouret, J. C., Hillier, D. J., et al. 2024, X-Shooting ULLYSES: Massive stars at low metallicity – V. Effect of metallicity on surface abundances of O stars, publication Title: arXiv e-prints ADS Bibcode: 2024arXiv240501267M
Martins, F., Bouret, J. C., Hillier, D. J., et al. 2024, A&A, 689, A31
Massey, P. 2003, ARA&A, 41, 15
Massey, P., McNeill, R. T., Olsen, K. A. G., et al. 2007a, AJ, 134, 2474
Massey, P., Olsen, K. A. G., Hodge, P. W., et al. 2007b, AJ, 133, 2393
Massey, P., Puls, J., Pauldrach, A. W. A., et al. 2005, ApJ, 627, 477
Massey, P., Zangari, A. M., Morrell, N. I., et al. 2009, ApJ, 692, 618
McEvoy, C. M., Dufton, P. L., Evans, C. J., et al. 2015, A&A, 575, A70
McQuinn, K. B. W., Skillman, E. D., Dalcanton, J. J., et al. 2012, ApJ, 759, 77
—. 2011, ApJ, 740, 48
McQuinn, K. B. W., B. Newman, M. J., Savino, A., et al. 2024, ApJ, 961, 16
Menon, A., Pawlak, M., Lennon, D. J., Sen, K., & Langer, N. 2024, arXiv e-prints, arXiv:2410.16427
Menon, A., Langer, N., de Mink, S. E., et al. 2021, MNRAS, 507, 5013
Metzger, B. D. 2022, The Astrophysical Journal, 932, 84, publisher: IOP ADS Bibcode: 2022ApJ...932...84M
Meyer, D. M. A., Mackey, J., Langer, N., et al. 2014, MNRAS, 444, 2754
Meynet, G., Ekström, S., Maeder, A., et al. 2008, in American Institute of Physics Conference Series, Vol. 990, First Stars III, ed. B. W. O'Shea & A. Heger, 212
Meynet, G., & Maeder, A. 2002, Astronomy and Astrophysics, 390, 561, aDS Bibcode: 2002A&A...390..561M
Meynet, G., & Maeder, A. 2002, A&A, 390, 561
Meynet, G., Maeder, A., Choplin, A., et al. 2017, in 14th International Symposium on Nuclei in the Cosmos (NIC2016), ed. S. Kubono, T. Kajino, S. Nishimura, T. Isobe, S. Nagataki, T. Shima, & Y. Takeda, 010401
Mintz, A., Telford, O. G., Kirby, E. N., et al. 2025, arXiv e-prints, arXiv:2503.19020
Moe, M., & Di Stefano, R. 2013, ApJ, 778, 95
—. 2015, ApJ, 810, 61

Moe, M., & Di Stefano, R. 2017, The Astrophysical Journal Supplement Series, 230, 15, publisher: IOP ADS Bibcode: 2017ApJS..230...15M
Moe, M., & Di Stefano, R. 2017, ApJS, 230, 15
Mokiem, M. R., Martín-Hernández, N. L., Lenorzer, A., de Koter, A., & Tielens, A. G. G. M. 2004, A&A, 419, 319
Mokiem, M. R., de Koter, A., Evans, C. J., et al. 2006, A&A, 456, 1131
Mokiem, M. R., de Koter, A., Evans, C. J., et al. 2006, Astronomy and Astrophysics, 456, 1131, aDS Bibcode: 2006A&A...456.1131M
Muraveva, T., Clementini, G., Maceroni, C., et al. 2014, MNRAS, 443, 432
Nagarajan, P., Weisz, D. R., & El-Badry, K. 2021, arXiv e-prints, arXiv:2111.06899
Noels, A., Godart, M., Salmon, S. J. A. J., et al. 2015, 307, 470, conference Name: New Windows on Massive Stars Place: eprint: arXiv:1409.1765 ADS Bibcode: 2015IAUS..307..470N
North, P., Gauderon, R., Barblan, F., & Royer, F. 2010, A&A, 520, A74
Oey, M. S., King, N. L., & Parker, J. W. 2004, AJ, 127, 1632
Oey, M. S., Lamb, J. B., Kushner, C. T., Pellegrini, E. W., & Graus, A. S. 2013, ApJ, 768, 66
Oey, M. S., Dorigo Jones, J., Castro, N., et al. 2018, ApJ, 867, L8
Offner, S. S. R., Moe, M., Kratter, K. M., et al. 2023, 534, 275, conference Name: Protostars and Planets VII Place: eprint: arXiv:2203.10066 ADS Bibcode: 2023ASPC..534..275O
Offner, S. S. R., Moe, M., Kratter, K. M., et al. 2023, in Astronomical Society of the Pacific Conference Series, Vol. 534, Protostars and Planets VII, ed. S. Inutsuka, Y. Aikawa, T. Muto, K. Tomida, & M. Tamura, 275
Ott, J., Stilp, A. M., Warren, S. R., et al. 2012, AJ, 144, 123
Paczyński, B. 1967, Acta Astron., 17, 355
Paszke, A., Gross, S., Massa, F., et al. 2019, PyTorch: An Imperative Style, High-Performance Deep Learning Library, arXiv:1912.01703 [cs.LG]
Patrick, L. R., Lennon, D. J., Britavskiy, N., et al. 2019, A&A, 624, A129
Patrick, L. R., Lennon, D. J., Najarro, F., et al. 2025, A&A, 698, A39
Pawlak, M. 2016, MNRAS, 457, 4323
Paxton, B., Bildsten, L., Dotter, A., et al. 2011, ApJS, 192, 3
Paxton, B., Cantiello, M., Arras, P., et al. 2013, ApJS, 208, 4
Paxton, B., Marchant, P., Schwab, J., et al. 2015, ApJS, 220, 15
Paxton, B., Schwab, J., Bauer, E. B., et al. 2018, ApJS, 234, 34
Paxton, B., Smolec, R., Schwab, J., et al. 2019, ApJS, 243, 10
Penny, L. R., & Gies, D. R. 2009, ApJ, 700, 844
Penny, L. R., Ouzts, C., & Gies, D. R. 2008, ApJ, 681, 554
Peters, M., Wisniewski, J. P., Williams, B. F., et al. 2020, AJ, 159, 119

Podsiadlowski, P., Joss, P. C., & Hsu, J. J. L. 1992, ApJ, 391, 246
Pols, O. R. 1994, A&A, 290, 119
Pols, O. R., Cote, J., Waters, L. B. F. M., & Heise, J. 1991, A&A, 241, 419
Prochaska, J. X., Hennawi, J., Cooke, R., et al. 2019, pypeit/PypeIt: Releasing for DOI
Prša, A., & Zwitter, T. 2005, ApJ, 628, 426
Prša, A., Conroy, K. E., Horvat, M., et al. 2016, ApJS, 227, 29
Puls, J., Vink, J. S., & Najarro, F. 2008, Astronomy and Astrophysics Review, 16, 209, publisher: Springer ADS Bibcode: 2008A&ARv..16..209P
Ramachandran, V., Klencki, J., Sander, A. A. C., et al. 2023, A&A, 674, L12
Ramachandran, V., Oskinova, L. M., & Hamann, W. R. 2021, Astronomy and Astrophysics, 646, A16, aDS Bibcode: 2021A&A...646A..16R
Ramachandran, V., Oskinova, L. M., & Hamann, W. R. 2021, A&A, 646, A16
Ramachandran, V., Hamann, W. R., Oskinova, L. M., et al. 2019, A&A, 625, A104
Ramachandran, V., Sander, A. A. C., Pauli, D., et al. 2024, X-Shooting ULLYSES: Massive Stars at low metallicity VIII. Stellar and wind parameters of newly revealed stripped stars in Be binaries, publication Title: arXiv e-prints ADS Bibcode: 2024arXiv240617678R
Ramachandran, V., Sander, A. A. C., Pauli, D., et al. 2024, A&A, 692, A90
Ramírez-Agudelo, O. H., Sana, H., de Mink, S. E., et al. 2015, A&A, 580, A92
Ramírez-Agudelo, O. H., Sana, H., de Koter, A., et al. 2017, A&A, 600, A81
Raucq, F., Gosset, E., Rauw, G., et al. 2017, A&A, 601, A133
Renzo, M., Zapartas, E., de Mink, S. E., et al. 2019, A&A, 624, A66
Rickard, M. J., & Pauli, D. 2023, A&A, 674, A56
Ricotti, M., Polisensky, E., & Cleland, E. 2022, MNRAS, arXiv:2205.07911 [astro-ph.GA]
Ritchie, B. W., Clark, J. S., Negueruela, I., & Langer, N. 2010, A&A, 520, A48
Ritchie, B. W., Stroud, V. E., Evans, C. J., et al. 2012, Astronomy and Astrophysics, 537, A29, aDS Bibcode: 2012A&A...537A..29R
Ritossa, C. 1996, MNRAS, 281, 970
Rivet, J.-P., Siciak, A., de Almeida, E. S. G., et al. 2020, Monthly Notices of the Royal Astronomical Society, 494, 218
Rivinius, T., Carciofi, A. C., & Martayan, C. 2013, Astronomy and Astrophysics Review, 21, 69, publisher: Springer ADS Bibcode: 2013A&ARv..21...69R
Rivinius, T., Carciofi, A. C., & Martayan, C. 2013, A&A Rev., 21, 69
Rizzuto, A. C., Ireland, M. J., Robertson, J. G., et al. 2013, MNRAS, 436, 1694
Robertson, B. E. 2021, arXiv e-prints, arXiv:2110.13160
Robertson, B. E., Ellis, R. S., Furlanetto, S. R., & Dunlop, J. S. 2015, ApJ, 802, L19
Rocha, K. A., Kalogera, V., Doctor, Z., et al. 2024, ApJ, 971, 133
Roman-Duval, J., Proffitt, C. R., Taylor, J. M., et al. 2020, Research Notes of the American Astronomical Society, 4, 205, publisher: IOP ADS Bibcode: 2020RNAAS...4..205R
Roman-Duval, J., Proffitt, C. R., Taylor, J. M., et al. 2020, Research Notes of the American

Astronomical Society, 4, 205
Roman-Duval, J. C., Aloisi, A., Britt, C., et al. 2021, ULLYSES NGC 3109 COS Spectroscopy, HST Proposal. Cycle 28, ID. #16511
Ruiz-Escobedo, F., Peña, M., Hernández-Martínez, L., & García-Rojas, J. 2018, MNRAS, 481, 396
Russeil, D., Adami, C., Bouret, J. C., et al. 2017, A&A, 607, A86
Sabín-Sanjulián, C., Simón-Díaz, S., Herrero, A., et al. 2017, A&A, 601, A79
Sana, H., James, G., & Gosset, E. 2011, MNRAS, 416, 817
Sana, H., de Mink, S. E., de Koter, A., et al. 2012, Science, 337, 444, publisher: American Association for the Advancement of Science
Sana, H., de Mink, S. E., de Koter, A., et al. 2012, Science, 337, 444
Sana, H., de Koter, A., de Mink, S. E., et al. 2013, A&A, 550, A107
Sana, H., Tramper, F., Abdul-Masih, M., et al. 2024, X-Shooting ULLYSES: Massive Stars at low metallicity II. DR1: Advanced optical data products for the Magellanic Clouds, publication Title: arXiv e-prints ADS Bibcode: 2024arXiv240216987S
Sana, H., Tramper, F., Abdul-Masih, M., et al. 2024, A&A, 688, A104
Sander, A. A. C., Bouret, J. C., Bernini-Peron, M., et al. 2024, X-Shooting ULLYSES: Massive Stars at low metallicity – IV. Spectral analysis methods and exemplary results for O stars, publication Title: arXiv e-prints ADS Bibcode: 2024arXiv240703137S
Sander, A. A. C., Bouret, J. C., Bernini-Peron, M., et al. 2024, A&A, 689, A30
Santolaya-Rey, A. E., Puls, J., & Herrero, A. 1997, A&A, 323, 488
Sanyal, D., Langer, N., Szécsi, D., -C Yoon, S., & Grassitelli, L. 2017, A&A, 597, A71
Savino, A., Weisz, D. R., Skillman, E. D., et al. 2022, ApJ, 938, 101
—. 2023, ApJ, 956, 86
Schlafly, E. F., & Finkbeiner, D. P. 2011, ApJ, 737, 103
Schlegel, D. J., Finkbeiner, D. P., & Davis, M. 1998, ApJ, 500, 525
Schneider, F. R. N., Ramírez-Agudelo, O. H., Tramper, F., et al. 2018, A&A, 618, A73
Schneider, R., Ferrari, V., Matarrese, S., & Portegies Zwart, S. F. 2001, MNRAS, 324, 797
Schoettler, C., de Bruijne, J., Vaher, E., & Parker, R. J. 2020, MNRAS, 495, 3104
Schootemeijer, A., Lennon, D. J., Garcia, M., et al. 2022, A&A, 667, A100
Schulte-Ladbeck, R. E., Hopp, U., Drozdovsky, I. O., Greggio, L., & Crone, M. M. 1995, The Astronomical Society of the Pacific, 107, 375
Senchyna, P., Plat, A., Stark, D. P., et al. 2024, The Astrophysical Journal, 966, 92
Shenar, T., Bodensteiner, J., Sana, H., et al. 2024, A&A, 690, A289
Sibony, Y., Georgy, C., Ekström, S., & Meynet, G. 2023, Astronomy and Astrophysics, 680, A101, aDS Bibcode: 2023A&A...680A.101S
Sibony, Y., Shepherd, K. G., Yusof, N., et al. 2024, Grids of stellar models with rotation VIII: Models from 1.7 to 500 $M_\odot$ at metallicity $Z = 10^{-5}$, publication Title: arXiv e-prints ADS Bibcode: 2024arXiv240706739S

Simón-Díaz, S., & Herrero, A. 2007, A&A, 468, 1063
Skillman, E. D., Kennicutt, R. C., & Hodge, P. W. 1989, ApJ, 347, 875
Smartt, S. J. 2009, Annual Review of Astronomy and Astrophysics, 47, 63–106
Smith, N. 2014, ARA&A, 52, 487
Sota, A., Maíz Apellániz, J., Morrell, N. I., et al. 2014, ApJS, 211, 10
Sota, A., Maíz Apellániz, J., Walborn, N. R., et al. 2011, ApJS, 193, 24
Spera, M., Mapelli, M., & Bressan, A. 2015, MNRAS, 451, 4086
Stark, D. P., Richard, J., Siana, B., et al. 2014, MNRAS, 445, 3200
Steidel, C. C., Strom, A. L., Pettini, M., et al. 2016, ApJ, 826, 159
Stinson, G. S., Dalcanton, J. J., Quinn, T., Kaufmann, T., & Wadsley, J. 2007, ApJ, 667, 170
Stonkutė, R., & Vansevičius, V. 2022, ApJS, 259, 6
Storey, P. J., & Hummer, D. G. 1995, MNRAS, 272, 41
Street, R. A., Li, X., Khakpash, S., et al. 2023, ApJS, 267, 15
Tauris, T. M., Langer, N., & Podsiadlowski, P. 2015, MNRAS, 451, 2123
Tauris, T. M., & van den Heuvel, E. P. J. 2006, in Compact stellar X-ray sources, Vol. 39, 623
Tauris, T. M., Kramer, M., Freire, P. C. C., et al. 2017, The Astrophysical Journal, 846, 170, publisher: IOP ADS Bibcode: 2017ApJ...846..170T
Tauris, T. M., Kramer, M., Freire, P. C. C., et al. 2017, ApJ, 846, 170
Telford, G., Berg, D., Chisholm, J., & McQuinn, K. B. W. 2021, A Family Portrait of the O Stars in the Extremely Metal-Poor Galaxy Sextans A, HST Proposal. Cycle 29, ID. #16767
Telford, O. G., Chisholm, J., McQuinn, K. B. W., & Berg, D. A. 2021, The Astrophysical Journal, 922, 191, publisher: IOP ADS Bibcode: 2021ApJ...922..191T
Telford, O. G., Chisholm, J., McQuinn, K. B. W., & Berg, D. A. 2021, ApJ, 922, 191
Telford, O. G., Chisholm, J., Sander, A. A. C., et al. 2024, Observations of Extremely Metal-Poor O Stars: Weak Winds and Constraints for Evolution Models, arXiv:2407.20313 [astro-ph]
Telford, O. G., Chisholm, J., Sander, A. A. C., et al. 2024, ApJ, 974, 85
Telford, O. G., McQuinn, K. B. W., Chisholm, J., & Berg, D. A. 2023, ApJ, 943, 65
Ting, Y.-S., Conroy, C., Rix, H.-W., & Cargile, P. 2019, ApJ, 879, 69
Topping, M. W., Stark, D. P., Senchyna, P., et al. 2024a, Deep Rest-UV JWST/NIRSpec Spectroscopy of Early Galaxies: The Demographics of CIV and N-emitters in the Reionization Era
—. 2024b, Monthly Notices of the Royal Astronomical Society, 529, 3301
Tramper, F., Sana, H., de Koter, A., & Kaper, L. 2011, ApJ, 741, L8
Tramper, F., Sana, H., de Koter, A., Kaper, L., & Ramírez-Agudelo, O. H. 2014, A&A, 572, A36

Trundle, C., Dufton, P. L., Hunter, I., et al. 2007, A&A, 471, 625
Trundle, C., Dufton, P. L., Hunter, I., et al. 2007, Astronomy and Astrophysics, 471, 625, aDS Bibcode: 2007A&A...471..625T
Urbaneja, M. A., Kudritzki, R.-P., Bresolin, F., et al. 2008, ApJ, 684, 118
van Buren, D., & McCray, R. 1988, ApJ, 329, L93
Van De Putte, D., Gordon, K. D., Roman-Duval, J., et al. 2020, ApJ, 888, 22
van Zee, L., Skillman, E. D., & Haynes, M. P. 2006, ApJ, 637, 269
Vanderplas, J., Connolly, A., Ivezić, Ž., & Gray, A. 2012, in Conference on Intelligent Data Understanding (CIDU), 47
Vargas-Salazar, I., Oey, M. S., Barnes, J. R., et al. 2020, ApJ, 903, 42
Vargas-Salazar, I., Oey, M. S., Eldridge, J. J., et al. 2025, ApJ, 988, 146
Venn, K. A., Tolstoy, E., Kaufer, A., & Kudritzki, R. P. 2004, in Origin and Evolution of the Elements, ed. A. McWilliam & M. Rauch, 58
Verbunt, F. 1993, ARA&A, 31, 93
Villaseñor, J. I., Sana, H., Mahy, L., et al. 2025, A&A, 698, A41
Vink, J. S. 2022, Annual Review of Astronomy and Astrophysics, 60, 203, aDS Bibcode: 2022ARA&A..60..203V
—. 2024, Stellar Winds, publication Title: arXiv e-prints ADS Bibcode: 2024arXiv240616517V
Vink, J. S., de Koter, A., & Lamers, H. J. G. L. M. 2001, A&A, 369, 574
Vink, J. S., & Sander, A. A. C. 2021, MNRAS, 504, 2051
Vink, J. S., Mehner, A., Crowther, P. A., et al. 2023, Astronomy and Astrophysics, 675, A154, aDS Bibcode: 2023A&A...675A.154V
Vink, J. S., Mehner, A., Crowther, P. A., et al. 2023, A&A, 675, A154
Virtanen, P., Gommers, R., Oliphant, T. E., et al. 2020, Nature Methods, 17, 261
Wang, C., Bodensteiner, J., Xu, X.-T., et al. 2024, ApJ, 975, L20
Wang, F. Y. 2013, A&A, 556, A90
Warfield, J. T., Richstein, H., Kallivayalil, N., et al. 2023, Research Notes of the American Astronomical Society, 7, 23
Waters, L. B. F. M. 2010, in Astronomical Society of the Pacific Conference Series, Vol. 425, Hot and Cool: Bridging Gaps in Massive Star Evolution, ed. C. Leitherer, P. D. Bennett, P. W. Morris, & J. T. Van Loon, 267
Weidner, C., & Vink, J. S. 2010, A&A, 524, A98
Weisz, D. R., McQuinn, K. B. W., Savino, A., et al. 2023, ApJS, 268, 15
Weisz, D. R., Dolphin, A. E., Savino, A., et al. 2024, ApJS, 271, 47
Weisz, Dan. 2024, JWST Resolved Stellar Populations Early Release Science ("JWST-STARS")
Wellstein, S., & Langer, N. 1999, A&A, 350, 148
Wellstein, S., Langer, N., & Braun, H. 2001, A&A, 369, 939

Willcox, R., MacLeod, M., Mandel, I., & Hirai, R. 2023, The Astrophysical Journal, 958, 138, publisher: IOP ADS Bibcode: 2023ApJ...958..138W
Willcox, R., MacLeod, M., Mandel, I., & Hirai, R. 2023, ApJ, 958, 138
Williams, B. F., Hillis, T. J., Blair, W. P., et al. 2019, ApJ, 881, 54
Williams, B. F., Lang, D., Dalcanton, J. J., et al. 2014, ApJS, 215, 9
Williams, B. F., Durbin, M. J., Dalcanton, J. J., et al. 2021, ApJS, 253, 53
Wofford, A., Vidal-García, A., Feltre, A., et al. 2021, MNRAS, 500, 2908
Wu, C., Qian, S., Li, F., et al. 2023, PASJ, 75, 358
Xiang, M., Rix, H.-W., Ting, Y.-S., et al. 2022, A&A, 662, A66
Young, D. R., Smartt, S. J., Mattila, S., et al. 2008, A&A, 489, 359
Young, L. M., & Lo, K. Y. 1996, ApJ, 462, 203
Zinnecker, H., & Yorke, H. W. 2007, Annual Review of Astronomy and Astrophysics, 45, 481, aDS Bibcode: 2007ARA&A..45..481Z
Zorec, J., & Briot, D. 1997, A&A, 318, 443